Investigating the Physical Properties of Planetary Surfaces using the Huygens Penetrometer

Thesis

UNRESTRICTED

Investigating the Physical Properties of Planetary Surfaces using the Huygens Penetrometer

Karl R. Atkinson
September 2008

A thesis submitted to The Open University
in the subject of Planetary and Space Sciences for the
degree of Doctor of Philosophy

Submitted: 30 Sept 2008
Doty award: 8 April 2009

Planetary and Space Sciences Research Institute
The Open University

To my father

Abstract

The Huygens probe landed on the unknown surface of Titan on 14 January 2005. Onboard, a small, protruding hemispherical-tipped penetrometer, ACC-E, part of the Surface Science Package, impacted the surface returning a short ~20 ms force signature of the mechanical resistance of the ground. The purpose of this thesis is to examine the response of an identical penetrometer to various terrestrial target materials and provide an insight into the penetrometer's performance and assess its capability.

Signatures collected at the Huygens impact speed of both natural and artificial material targets in the laboratory are examined using various descriptive statistical measures. Structural and textural properties are identified and the penetrometer's response to granular targets, both wet and dry, is examined. Mitigation of the effects of target boundaries and velocity dependence of the signatures are both considered.

Terrestrial fieldwork penetrometry is presented that demonstrates that even for short penetration depths the sensor is capable of distinguishing several types of geological surface features. A physical model extended for layered targets is presented and applied to laboratory data.

Using the results from the laboratory and fieldwork, together with more specific experiments, a possible interpretation of the signature returned from Titan is presented and discussed within the context of recent findings from other investigations.

Acknowledgements

There are many people who have helped me in various ways during this study.

I am indebted to my supervisors for their support and advice; Professor John Zarnecki for giving me the opportunity to work on such an exciting project, Dr Tim Ringrose and Dr Martin Towner for reading through and making sense of my work. My thanks also to Mark Leese and the other members of the SSP team, Dr Mark Paton for helping compile the initial material catalogue and the department technical staff with particular mention to Mike Muckelow and Nick Alderidge for their advice and assistance with electrical circuits and Chris Hall who helped transform my mechanical widgets from ideas on scraps of paper to practical working devices. Particular thanks also to Dr Axel Hagermann for his friendship, tolerance and helpful words of advice during trying times.

I am also grateful to Dr. Gunter Kargl from the Space Research Institute in Graz, for his help in understanding the finer points of the ACC-E electronics and Professer Helmut Schweiger and Alexander Zöhrer from the Institute for Soil Mechanics and Foundation Engineering at the Technical University in Graz for kindly allowing me to attend a crash-course in soil mechanics and discussing possible modeling approaches. During this period the enthusiasm and encouragement of Vaclev Racinsky was greatly appreciated.

I would also thank Brian Speyer of DRS digital imaging Ltd, Dr Emma Taylor and Dr Andrew Ball for their help organizing the high speed photography session, the staff of

Century Dynamics for allowing me to attend their AUTODYN finite element impact modeling course and Geoff Bradshaw for helping work around the bugs in the system.

My appreciation also to Dave Marsden of WBB minerals Ltd. for supplying the test sands, Dr Yoseph Arraya for explaining practical methods of measuring their moisture content and Dr Diane Johnson for imaging their grains. Thanks also to my fellow students who throughout my studies have supported and encouraged me.

Finally, to Mum, Dad, Susan and Aggie without whose support this would have been impossible.

Contents

Chapter 4. Identifying granular target materials

Chapter 5. Field testing

Chapter 6. Penetrometry modelling

Chapter 7. Analysis of the Titan penetrometry signature

List of Figures

List of Tables

List of Acronyms

ACC-E	Accelerometer-external (Penetrometer)
ACC-I	Accelerometer-internal (SSP)
ACP	Aerosol Collector and Pyrolyser
A/D	Analogue to Digital
ADC	Analogue to Digital Converter
ANOVA	Analysis Of Variance
API-S	Acoustic Properties Instrument (SSP)
API-V	Acoustic Properties Instrument (SSP)
ASP	Apollo Simple Penetrometer
CPT	Cone Penetration Testing
DC	Direct Current
DEN	Density (SSP subsystem)
DISR	Descent imaging spectral radiometer
DFT	Discrete Fourier Transform
DLI	Downward looking imager (DISR)
DLVS	Downward-Looking Visible Spectrometer (DISR)
DWE	Doppler Wind Experiment
EMC	Electromagnetic Compatibility
ESA	European Space Agency
FEM	Finite Element Model
FFT	Fast Fourier Transform
FIFO	First In First Out
FM	Flight Model
FS	Flight Spare
GCMS	Gas Chromatograph mass spectrometer
HASI	Huygens Atmospheric Structure Instrument
HSD	Honestly Significant Difference. A multiple comparison test.
ISS	Imaging Science Subsystem
LB	Leighton Buzzard
MRI	Medium Resolution Imager (DISR)
NASA	National Aeronautics and Space Administration
NEO	Near Earth Objects

OU	Open University
PSSRI	Planetary and Space Sciences Research Institute
PTFE	Teflon
PZR	Accelerometers (HASI)
PZT	Lead Zirconate Titanate. ACC-E penetrometer ceramic crystal.
RAL	Rutherford Appleton Laboratory
REF	Refractometer (SSP subsystem)
SLI	Side looking imager
SRP	Self Recording Penetrometer
SSP	Surface Science Package
THP	Thermal properties sensor (SSP)
TIL	Tilt sensor (SSP)
UTC	Coordinated Universal Time
VIMS	Visual and Infrared mapping spectrometer

Publications and Conference presentations

Publications:

Zarnecki, J. C., Leese, M. R., Hathi, B., Ball, A. J., Hagermann, A., Towner, M. C., Lorenz, R. D., Mcdonnell, J. A. M., Green, S. F., Patel, M. R., Ringrose, T. J., Rosenberg, P. D., Atkinson, K. R., Paton, M. D., Banaszkiewicz, M., Clark, B. C., Ferri, F., Fulchignoni, M., Ghafoor, N. A. L., Kargl, G., Svedhem, H., Delderfield, J., Grande, M., Parker, D. J., Challenor, P. G. and Geake, J. E. (2005). A soft solid surface on Titan as revealed by the Huygens Surface Science Package. *Nature* 438: 792-795.
Contribution: compiled initial material catalogue and assisted in interpretation of sensor return data.

Kargl, G., Zohrer, A., Komle, N. I., Ball, A. J., Ringrose, T. J., Paton, M. D., Atkinson, K. R., Towner, M. C. and Klapper, K. L. (2005). The detection of small-scale structures in planetary surface materials with ground-penetrating instruments. *Proceedings of the 3rd International Planetary Probe Workshop, Anavyssos, Attica, Greece.*
Contribution: Discussions on best methods for consistent target preparation.

Baldwin, E. C., Taylor, E. A., Ball, A. J., Atkinson, K.R., Hayhurst, C. (2006) Initial results from hydrocode modeling of the impact of SMART-1 on the lunar surface. *Proceedings of the 2nd Internationational Workshop on Penetrometry in the Solar System (IWPSS2), Graz, Austria.*
Contribution: Assisted in setting up initial AUTODYN model and discussions on appropriate target material parameters.

Presentations:

Atkinson, K. R., Zarnecki, J. C., Ringrose, T. J., Ball, A. J., Green, S. F., Hagermann, A., Hathi, B., Kargl, G., Leese, M. R., Lorenz, R. D., Patel, M. R., Paton, M. D., Rosenberg, P. D., Towner, M. C., "Investigating Titan's surface through penetrometry" *poster presented at the Cassini/Titan Workshop "Titan after the Huygens and First Cassini Encounters", May 2005, Heraklion, Crete, Greece.*

Atkinson, K. R., Ball, A. J., Hagermann, A., Kargl, G., Leese, M. R., Lorenz, R. D., Ringrose, T. J., Towner, M. C., Zarnecki, J. C., "Examining the surface mechanical properties of Titan at the Huygens probe landing site" *talk given at the 2nd Internationational Workshop on Penetrometry in the Solar System (IWPSS2), September 2006, Graz, Austria.*

Preface

This thesis investigates the ability of a penetrometer to determine and identify *in situ* the physical properties of a planetary surface material. It is motivated by the successful landing on the surface of Titan of the Huygens probe and the subsequent return of data from a unique penetrometry measurement of the hitherto unknown surface. Titan surface knowledge is a central theme throughout this thesis although given the limited flight data, penetrometry of terrestrial surfaces are also explored so that a fair assessment of this sensor can be made. The thesis is organized as follows:

The first chapter gives a brief history of the use of penetrometry in planetary exploration. The state of Titan knowledge before the arrival of the Cassini-Huygens mission is described with particular emphasis on information pertinent to unveiling the unknown surface. An overview of the mission and its scientific objectives is given. The Surface Science Package ACC-E penetrometer and other key instruments on board the Huygens probe and Cassini orbiter are described.

The second chapter gives a brief account of the entry and descent of the Huygens probe through the Titanian atmosphere. The penetrometer data collected on impacting with the ground are presented together with other instrument results and their implications for understanding the nature of the surface. Signal limitations and the possibility of penetrometer catastrophic failure are also addressed. Chapter 3 provides a description of the laboratory work before and immediately after the Huygens landing event. The development of a portable drop rig to facilitate both laboratory and fieldwork experiments and the building of a laser based penetrometer velocity measurement system are both detailed. Calibration, noise and sampling rate issues and laboratory data processing of a duplicate Huygens penetrometer made by the author is presented.

Chapter 4 considers descriptive statistical measures to classify penetrometry signatures. Experiments carried out in the laboratory to investigate the response of the penetrometer to different targets made of natural and artificial materials are set out. Incidental high-speed camera work is also shown. A description of fieldwork carried out to examine penetrometry of natural targets at several sites is given in chapter 5 and the ability of the penetrometer to determine material textural properties and structure is explored. Chapter 6 discusses some of the efforts made to model the penetration process and describes an extension of a physical penetration model to layered targets.

Further experiments specific to the understanding of the Titan surface are reported and the results of these together with knowledge gained from earlier laboratory and fieldwork are used in chapter 7 to provide a possible interpretation of the surface material impacted at the Huygens landing site.

The thesis ends with a final discussion and points to further work that could be addressed. The appendices that follow catalogue the laboratory drops carried out solely by the author and various Octave programs written.

1 Introduction

1.1 Sensing the physical properties of planetary surfaces

Measuring the physical properties of a planetary surface has been of importance since the beginning of *in situ* planetary exploration with the soft landing of the Surveyor 1 spacecraft on the Moon in 1966. These properties allow the nature and history of an unknown target surface to be constrained, and can indicate the physical processes that shaped it.

Penetration is one way in which the mechanical and structural properties of a surface can be sensed. Mechanical properties are those associated with the response of a material to an applied force, such as strength or abrasion resistance, whereas structural properties refer to the way in which a material is arranged and organised. For example, a finger pushed into sand senses the resistance and the granular structure of the material. The process in which the penetration characteristics of a body impacting into a surface are measured is known as penetrometry.

In planetary exploration, useful penetrometry investigations have sometimes been opportunistic using equipment not intended for the task. Examples include evidence of the compressible and powdery nature of the lunar regolith from flagpole penetrations and measurements of the impressions left by astronaut boots (Mitchell *et al.*, 1972; Perko, 2007) to the ongoing investigation of the range of Martian soils determined using the wheel tracks of the MER Spirit and Opportunity rovers (Richter *et al.*, 2005).

Other missions have carried instruments specifically for penetrometry measurement. A penetrometer is a device that is driven into the target surface by a purely axial force (unlike a drill that use rotating, lateral force) (Glaser *et al.*, 2006). This is achieved by various means including gravitational free fall, an internal hammering device (e.g. as used in a mole) or by an accelerator such as an explosive charge (Mitzutani, 1999). Measurements of the final depth reached, rate of penetration or force on the tip enable the mechanical resistance and texture of the target to be determined. A similar device, a penetrator, is a rigid body the primary purpose of which is to emplace other instruments into a surface. It may also function as a penetrometer if its payload includes instruments to measure mechanical resistance (Lorenz and Ball, 1999).

An important factor to be considered is the velocity at which the impacting body hits the target surface. Lorenz and Ball (1999) consider dynamic penetrometry to cover impact speeds between 0.1 and 1000 m s^{-1}. These boundaries are necessarily somewhat arbitrary with the hypervelocity regime occurring above this, and the related quasi-static penetrometry (where velocity effects are largely neglected) below this range. The recent end of mission impact of the lunar investigation spacecraft SMART-1 cannot be considered to be penetrometry as although its impact speed was within this range, no measurement of the impact resistance or final depth reached was made.

1.2 History of planetary penetrometry

Planetary penetrometry developed from terrestrial geotechnical methods, specifically the Dutch Cone Penetration Tests (CPT) (Lunne *et al.*, 1997). Penetrometry investigations have been attempted (both successfully and unsuccessfully) on several planetary bodies. The first use of penetrometry in planetary exploration was the use of strain gauges on the landing legs of Surveyor 1 that measured the peak axial force as the

spacecraft soft landed on the surface of the Moon in 1966. Comparing the force on each leg suggested that the surface material properties were horizontally homogeneous on the scale of the lander (Christensen *et al.*, 1966).

The Soviet Luna 13 Moon mission (1966) carried a conical penetrometer that was pushed into the ground by an explosive charge with the final depth measured by a potentiometer. This device penetrated the surface to a depth of 4.5 cm into a material consistent with a dense granular soil or a granular soil with a small amount of cohesion between its grains (Cherkasov, 1968b). Two further missions, Luna 17 (1970) and Luna 21 (1973), carried Lunakhod rovers each with a shear vane device and cone sampling penetrometer capable of repeated insertion to a maximum depth of 10 cm as they traversed the lunar surface. Over 1000 measurements were taken by the Lunakhod rovers and analysis of the penetrometery allowed the shear strength parameters of the lunar soil for different surfaces (e.g. crater rims and walls and the intercrater surface) to be constrained (Carrier *et al.*, 1991).

Further lunar penetrometery investigations occurred with the advent of the manned Apollo programme. A cone penetrometer, the Apollo Simple Penetrometer (ASP), was used by astronauts on Apollo 14 (1971) to investigate the penetration resistance of the lunar soil. It consisted of a thin 68 cm long aluminium rod with a 30° apex angle cone tip that was pushed into the soil using first one hand and then both hands (Mitchell *et al.*, 1971). This procedure was then repeated twice at points located 4 m apart with the depth of penetration recorded. These data, together with estimates of the driving force imparted by the astronaut, were used for comparison with previous Surveyor

measurements of soil strength parameters and it was noted that in general the lunar soil density and strength increased with depth (Mitchell *et al.*, 1972).

The variation of penetration resistance with depth for lunar regolith is probably complicated by several factors such as layering, soil pockets that change the bulk density of the material, the distribution of grain sizes and the cohesion of the soil (Mitchell *et al.*, 1971). Subsequent Apollo 15 (1971) and 16 (1972) investigations used an improved Self-Recording Penetrometer (SRP) which inscribed a gold plated drum to record the penetration resistance of a 30° apex cone (Carrier *et al.*, 1991). In general the investigations found a good correlation between the SRP resistance and an x-ray of a returned core-tube sample containing surface material that varied from fine grained to coarse rock fragments (Mitchell *et al.*, 1973).

Other successful penetration investigations have been carried out on Venus by the Venera 13 and 14 landers (1982). These craft carried 'conical rotodynamic punches'- conical penetration tips on a spring-loaded arm. Subsequent analysis showed that at the Venera 13 site the punch entered the soil some 32 mm indicating a load-carrying (bearing) capacity of 0.26-1 MPa. This result is thought to indicate a crumbly possibly highly porous soil structure (Kemurdzhian *et al.*, 1983). At the Venera 14 site, the punch impacted a surface of consolidated rock and only entered 7 mm giving an estimated bearing capacity of 65-250 MPa. The analysis using terrestrial analogues (Table 1.1) indicated that the surface was similar to terrestrial tuff type rock (Kemurdzhian *et al.*, 1983).

Depth of penetration of punch (cm)	Load-carrying capacity, (daN cm^{-2}=0.1 MPa)	Type of soil	Terrestrial analogues
<0.5	>400	Solid rocks	Basalts, granites
0.5-2	40-400	Foamed porous rocks, reworked rocky soils	Tuffs, rocks full of cracks
2-7	1-40	Cohesive products of chemical reworking and weathering of rocks. Strongly compacted grainy material which consolidated	Heavy clays loamy, clays, compacted dusty sand
>7	<1	Crumbly deposits of grainy material, regolith	Gravel, sand, ground basalt

Table 1.1 Categorisation of the mechanical properties of the main types of soil and terrestrial analogues within the Venera 13 and Venera 14 conical rotodynamic punch measurement range (Kemurdzhian et al., 1982).

From this brief history and the summary table of key missions (Table 1.2), it can be seen that penetrometry has been used to investigate several different planetary bodies with varying degrees of success. Mars, in particular, has proved to be a difficult target with no successful direct penetrometry investigation to date. This has often been due to the failure of the spacecraft or launch vehicle. A comprehensive review of planetary penetrometry can be found in Ball and Lorenz (1999).

1.3 Titan's surface before Cassini-Huygens

Titan is Saturn's largest moon and the second largest in the solar system after Jupiter's heavily cratered moon Ganymede. First discovered by Dutch astronomer Christiaan Huygens in 1655, it is unique in the solar system as the only moon with a dense atmosphere. This atmosphere has kept the moon's surface hidden from observation and is key to understanding the surface of Titan.

The suggestion that Titan could hold onto an atmosphere was made by Sir James Jeans in 1925 (Jeans, 1925). Using his kinetic theory of gases he predicted that any atmosphere of Titan must consist of molecules heavier than hydrogen or helium, both of which would escape the moon's gravity.

Mission	Target and type of device	Measurement	Aim	Comments
Surveyor 1 (Christensen *et al.*, 1966)	Moon (soft landing) Strain gauges	Axial force on each landing leg shock absorber	Characterize surface material	First successful lunar penetrometry measurement, June 1966.
Luna 17 & 21 (Perko, 2007) (Ball and Lorenz, 1999)	Moon Cone penetrometer (and shear vane)	Penetration resistance with depth	Characterize variations in lunar soil properties	Penetrometers carried on Lunakhod 1 & 2 rovers. November 1970 & January 1973
Apollo 14 Apollo Simple Penetrometer (ASP) Apollo 15 & 16 Self Recording Penetrometer (SRP) (Mitchell *et al.*, 1972)	Moon non-instrumented manual cone penetrometer	Depth- Pushed in manually by astronaut, using one hand then both hands.	Provide an indication of local soil variability and stratigraphy	February 1971. July 1971 & April 1972.
Venera 13 & 14 (Kemurdzhian *et al.*, 1983)	Venus Conical rotodynamic punch	Depth Pushed in by spring-loaded mechanical lever	Characterize the physical and mechanical properties of the Venusian surface.	Successfully returned data March 1982.
Mars 96 penetrators (Surkov and Kremnev, 1998)	Mars Penetrator instrumented with accelerometer	Deceleration (depth) Impact ~70 ms^{-1} Depth 4-6 m	Characterize the physical and mechanical characteristics of the Martian soil and rock	Launch failure November 1996
DS-2 (Smrekar *et al.*, 1999)	Mars Penetrator instrumented with accelerometer	Deceleration (depth) Impact 190 ms^{-1} Depth 0.2-0.6 m	Determine hardness of regolith. Presence or absence of 10cm polar dust and ice layers	No signal received on arrival at Mars December 1999
Beagle 2 (Richter *et al.*, 2001)	Mars Self hammering mole	Penetration rate	Estimate vertical profile of regolith strength	No signal received on arrival at Mars December 2003
Huygens ACC-E, ACC-I (Lorenz *et al.*, 1999) (Zarnecki *et al.*, 2002)	Titan Instrumented Penetrometer, Accelerometer	Force on penetrometer tip Deceleration	Identify surface material. Compressive properties of surface	Successful data return January 2005
Rosetta Lander ANC-M (Kömle *et al.*, 1997; Kömle *et al.*, 2001) PEN-M (Seiferlin *et al.*, 1999)	Comet 67P/Churyumov-Gerasimenko anchoring harpoon with accelerometer Hammering penetrometer	Deceleration Depth	Measure strength with depth. Verify the existence and strength of surface layers (ANC-M). Mechanical strength of soil (PENM).	Expected to arrive at comet in 2014.

Table 1.2 Summary of key missions in which penetrometry measurements were made or attempted.

Telescopic observations made by Gerard Kuiper in 1943-44 first confirmed the existence of an atmosphere when he observed methane absorption bands on Titan. He incorrectly suggested that the orange colour of the moon was due to the action of the atmosphere on the surface in a process analogous to oxidation (Kuiper, 1944). Carl Sagan (1972) later proposed that Titan's atmosphere had methane cloud layers that when irradiated by ultraviolet (UV) light would produce complex organic molecules with a characteristic red colour.

In November 1980 Voyager 1 made a close flyby of Titan. It was hoped that the surface of the moon might be seen through broken clouds; however the onboard cameras returned disappointing images showing a surface entirely hidden by thick layer of haze (Rages and Pollack, 1983).

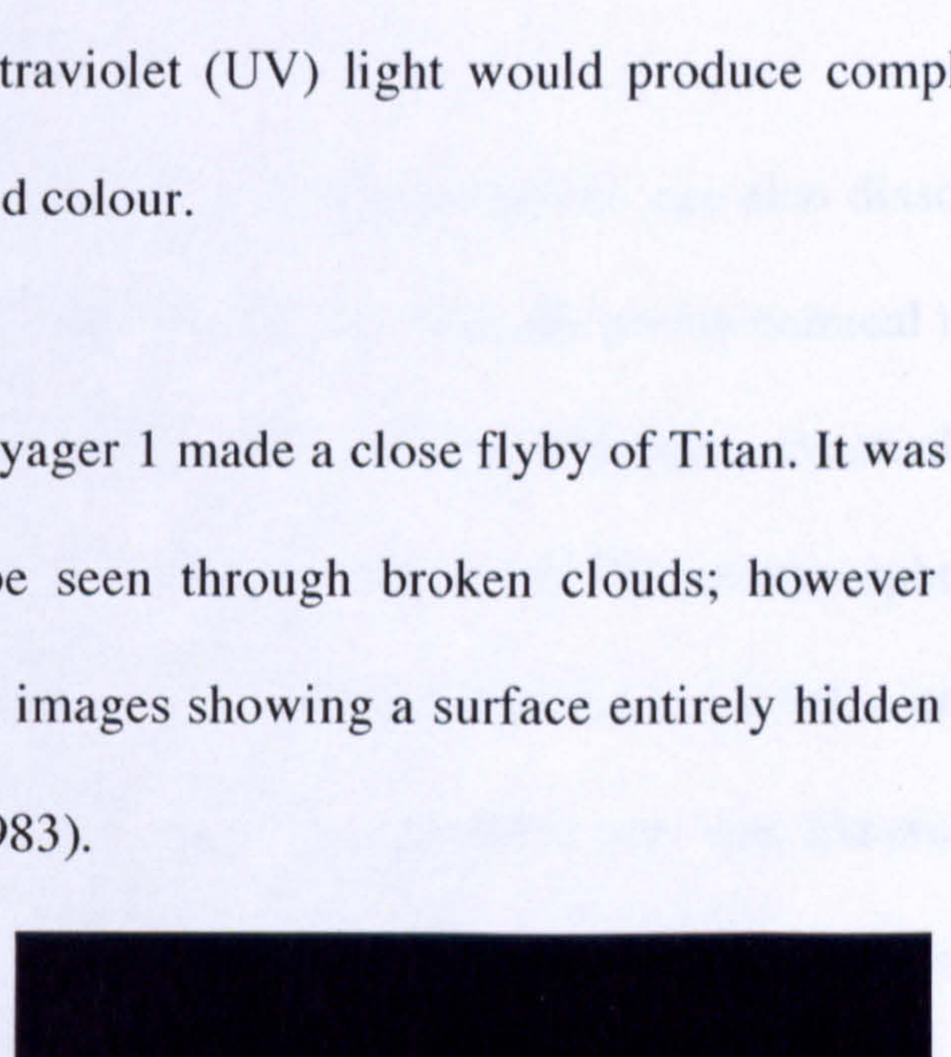

Figure 1.1 Titan imaged by Voyager 1 in 1980 (Source: NASA)

The aerosols that form this haze are produced high in the stratosphere by the action of UV radiation from the Sun on one of the primary constituents of the atmosphere,

methane. This UV sunlight has sufficient energy to break up the methane molecules, allowing them to recombine into larger, more complex molecules. This photochemical process, known as UV photolysis, is irreversible as the dissociation of the methane releases hydrogen that escapes from the atmosphere (Lunine and Stevenson, 1983). It has been hypothesized that this hydrogen, unable to escape the gravitational attraction of Saturn may form a torus roughly centered on Titan's orbit (Ip, 1993; McDonough and Brice, 1973a).

Energetic electrons from Saturn's magnetosphere can also dissociate the methane and nitrogen molecules, adding other products to the photochemical mix. The hydrocarbons and other complex molecules produced by this process eventually condense into solid particles, known as 'tholins', that are suspended in the atmosphere and are responsible for Titan's orange colour. It is thought that these particles collide with each other producing larger particles, that form droplets that are eventually deposited on the surface of Titan (Yung and Allen, 1984). Laboratory experiments have synthesised analogues of these organic compounds from simple binary mixtures of methane and nitrogen irradiated by UV sources. These laboratory-produced tholins have similar spectral properties to the upper atmospheric haze of Titan (Khare and Sagan, 1973).

The Voyager 1 flyby of Titan was followed by a second, more distant pass by the Voyager 2 spacecraft in August 1981. The Voyager flybys provided very little direct information about the nature of Titan's surface, however they did allow the abundances of the main gaseous constituents of the atmosphere, nitrogen and methane, to be constrained and gave an indication of the composition of Titan. Measurements of the signal strength received from the Voyager 1 spacecraft as it flew past Titan allowed the

surface radius of the moon to be more accurately determined as 2575.0 ± 0.5 km. Using this result and the measured mass gave the moon a mean density of 1.881 ± 0.002 g cm^{-3} (Lindal *et al.*, 1983). This relatively low density implies that Titan is not a purely rocky body (silicate rocks have a density of 2.5-3 g cm^{-3}) but must be a combination of rock and ice (density of water ice is ~1 g cm^{-3}). A simple model of the moon might consist of a thick mantle of water ice overlying a denser rocky core (Coustenis and Taylor, 1999). At the surface this ice may be covered in the tholin photolysis products deposited from the atmosphere.

The important relationship between the atmosphere and its influence on the surface has been highlighted by theoretical models of the atmosphere. One of the first complete models of the photochemistry of Titan using the Voyager data was that proposed by Yung (1984). This model predicted that photolysis produced a net loss of methane from the atmosphere of 4×10^{-13} g $cm^{-2}s^{-1}$ which, assuming this rate to be constant over time, would lead to an accumulated loss of 5.6×10^{4} g cm^{-2} over the age of the solar system, 4.5 billion years (Yung and Allen, 1984). This is approximately 400 times the abundance observed today, which implies that there must be some other source of methane or Titan's atmosphere would have depleted its entire inventory in ~10^{7} years. Therefore it is thought that Titan must be replenishing its atmospheric methane. The model also predicted that the heavier photolysis products would fall on the surface producing an approximately 1 km thick layer (Yung and Allen, 1984).

Possible sources of methane include direct delivery by external supply such as comets, although this theory is not currently favoured (Kress and McKay, 2004); the methane is probably resupplied to the atmosphere by some store or reservoir on or in Titan's

surface. This store could take the form of a global methane ocean as the triple point of methane (90.7 K at 1.6 bar) occurs close to the measured Titan surface temperature of 94 K. A simple, single component methane ocean was however calculated to produce an atmospheric saturation inconsistent with Titan's atmospheric temperature profile as measured by Voyager 1 (Lindal *et al.*, 1983). This led to the proposal of oceans containing other photolysis products such as ethane and propane which are less volatile than methane and would combine with it, producing an ocean with a lower vapour pressure, that would be both consistent with the saturation data and provide a long term source for photolysis (Flaser, 1983; Lunine and Stevenson, 1983). Tidal arguments put forward by Sagan and Dermott (1982) placed constraints on the coverage of any oceans. Titan is observed to have a small orbital eccentricity, and they therefore argued that a liquid surface layer would have substantial tidal currents generated by Saturn that would act to reduce orbital energy. These would then eliminate the orbital eccentricity currently observed unless the surface was essentially dry (with only small unconnected lakes) or completely covered in a global ocean.

Radar evidence later shed doubt on the possibility of a global ocean. Titan's thick atmosphere inhibits observations of the surface at optical wavelengths; however there are a few spectral 'windows' in the near-IR and radar bands where the atmosphere is more transparent. Radar observations by Muhlemann *et al.* (1995) showed strong scattering that would not be consistent with a (relatively) smooth global ocean surface. These observations did not rule out large lakes of liquid hydrocarbons; however this evidence prompted the suggestion that the methane ocean supply might be hidden in an aquifer of subsurface caverns and pore space (Stevenson, 1990, 1992). Its release could

take the form of volcanic activity e.g. cryovolcanism or some kind of outgassing process.

Observations of Titan carried out using the large Arecibo radio telescope showed sharp specular echoes, consistent with a smooth (possibly liquid covered) surface. These were seen in around 75% of the returned spectra covering a thin region around 26°S latitude (Campbell *et al.*, 2003). The polarization ratio (the ratio of the received signal polarized in the opposite sense or same sense with respect to the transmitted signal) was also measured and found to be low. This indicated that Titan did not have a strong coherent backscatter effect as occurs on clean icy surfaces such as the Galilean satellites of Jupiter, which have much higher polarization ratios and stronger radar reflectivity. This apparent lack of ice could be due to either additional material such as ammonia/organic impurities or textural effects (e.g. few scattering cracks) that make the ice more radar-absorbing (Lorenz and Lunine, 2005).

Investigations of Titan in the near-infrared using Earth-based telescopes with adaptive optics have examined the albedo of the surface and found variations confirming that Titan has a varied surface (Griffith, 1993; Lemmon *et al.*, 1993). Using the Hubble Space Telescope allowed relative albedo maps of Titan to be produced showing the heterogeneity of the surface as distinct 'bright' and 'dark' regions (Smith *et al.*, 1996). It was speculated that the 'bright' regions could be caused by methane rainfall washing organic 'dark' material from raised terrain leaving cleaner less soluble ice (Griffith *et al.*, 1991).

Rainfall on Titan is unlikely to be mechanically strongly erosive as raindrops would fall only slowly through its high density, low gravity atmosphere, however it has been suggested that rare but violent rain storms could exist on Titan and cause substantial erosion (Lorenz and Lunine, 2005). A simplified schematic of the process that could shape the surface of Titan is shown in figure 1.2. A summary of Titan properties is given in table 1.3.

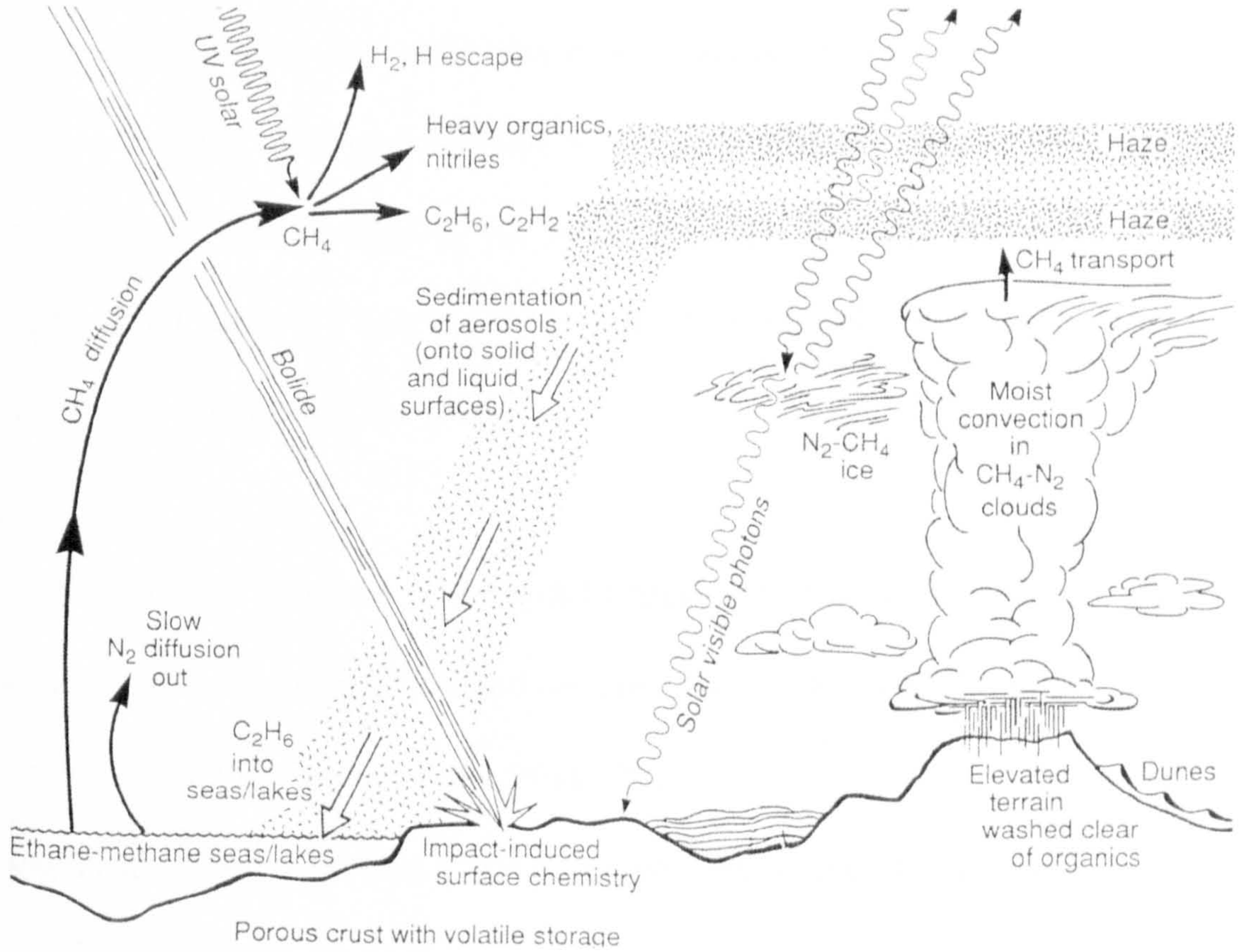

Figure 1.2 Simplified diagram of Titan's surface and atmospheric interactions (adapted from (Lunine, 1993).

	Titan	Earth
Orbital period (days)	15.94 (Saturn)	365.25 (Sun)
Rotation period	15.95 days	23h 56m
Surface radius (km)	2575	6378
Mass (kg)	1.35×10^{23}	5.97×10^{24}
Mean density (kg m^{-3})	1880	5515.3
Surface gravity (m s^{-2})	1.35 (0.14g)	9.81 (1g)
Surface temperature (K)	~94 (-179 °C)	287 (14 °C)
Surface pressure (kPa)	150 (1.5 bar)	101.3 (1.0 bar)
Primary atmospheric constituents	Nitrogen (90-97%), Methane (~2%)	Nitrogen (78.08%), Oxygen (20.94%)

Table 1.3 Summary of the physical and orbital data for Titan (Coustenis and Taylor, 1999) and Earth.

1.4 Description of the Cassini-Huygens mission

The joint NASA/ESA Cassini-Huygens mission was launched on 15th October 1997 with the goal of exploring Saturn and its moons. The mission is focused on the exploration of Titan with the inclusion of a probe, Huygens, to perform an *in situ* investigation of Titan's atmosphere and the nature of its surface.

The spacecraft consists of the Cassini orbiter and the Huygens probe. The orbiter, in addition to carrying the Huygens probe to Titan and acting as a relay for the probe data, has an array of instrumentation for remote global sensing observations of Titan's atmosphere and surface. These are measurements with global coverage that supplement the *in situ* data acquired by the probe.

The purpose of the Huygens probe was to make detailed investigation of the physical properties, chemical composition and dynamics of Titan's atmosphere and characterize the surface of the local area of the landing site.

The scientific objectives for the Cassini-Huygens mission with regard to Titan are :

- Determine the composition of the atmosphere and determine the isotope ratios of the abundant elements, constraining the formation and evolution of Titan.
- Detect more complex organic molecules and investigate the energy sources for the atmospheric chemistry. Investigate the formation and composition of aerosols and the cloud physics.
- Measure wind speeds and global temperatures. Search for lightning discharges.
- Determine the properties of the surface including its topography and composition. Infer Titan's internal structure.

- Study the ionization of the upper atmosphere and its interaction with the magnetosphere of Saturn.

(Lebreton and Matson, 2002)

1.4.1 Description of key instruments on Cassini and Huygens

The instrument payload on the Huygens probe comprises of six instruments. Their locations on the probe are shown in Figure 1.3.

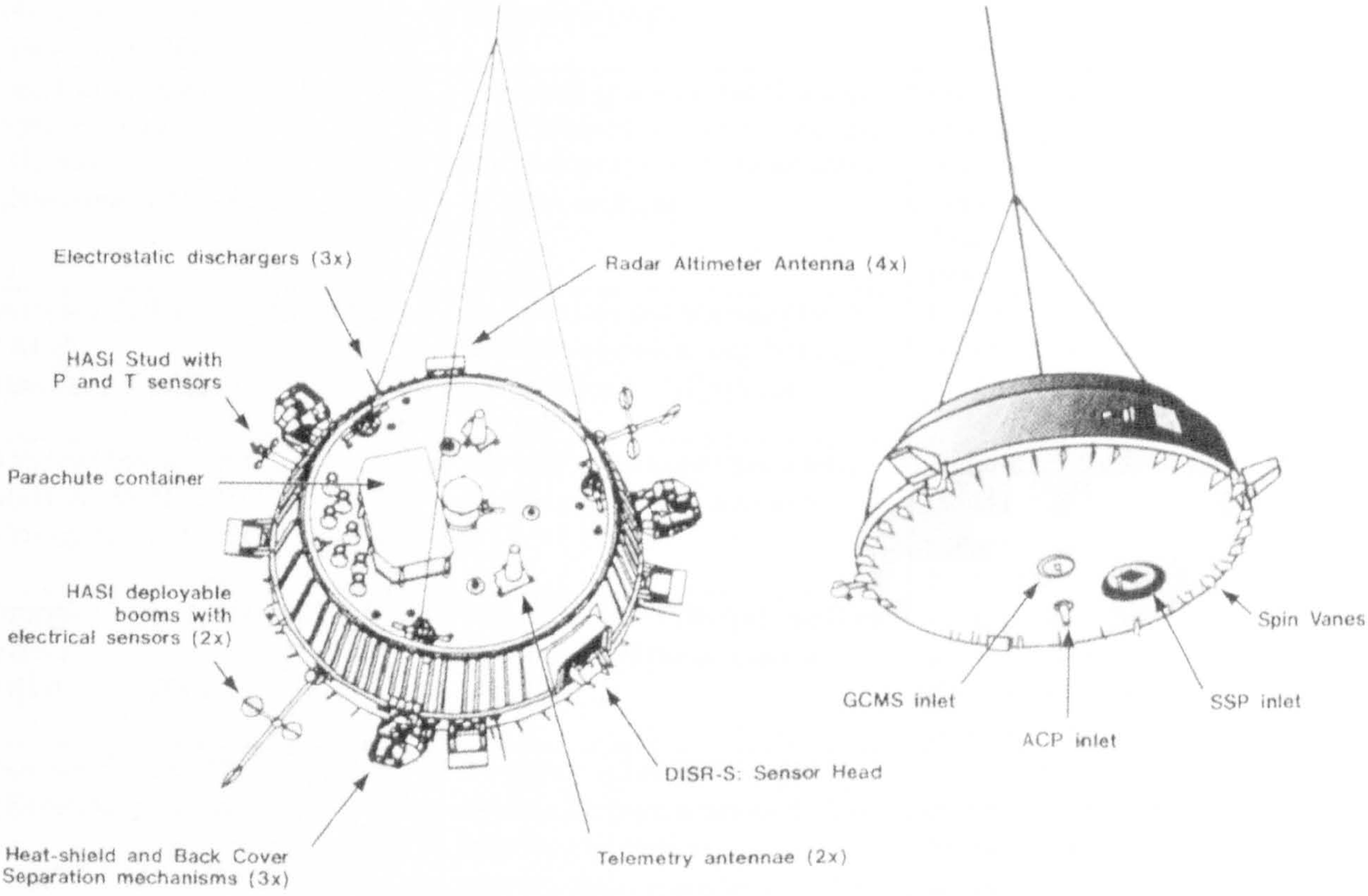

Figure 1.3 Top and bottom views of the Huygens probe showing locations of six instruments. From Lebreton and Matson (2002).

The instruments on Huygens and those on Cassini for remote surface investigation are summarised in Table 1.4 with their scientific objectives.

Cassini orbiter		
Instrument	*Measurement*	*Scientific objective*
Visual and Infrared mapping spectrometer (VIMS) (Brown *et al.*, 2004)	Imaging spectrometers operating in the near infrared.	Search for lightning and volcanism and observe the surface of Titan.
Imaging Science Subsystem (ISS) (Porco *et al.*, 2004)	Image surface using wide and narrow angle CCD imaging cameras	Map the surface in near-infrared spectral windows. Provide clues about nature and composition of surface materials.
Cassini Radar (RADAR) (Elachi *et al.*, 1991)	Transmit microwave pulses to surface and measure return time and intensity of echo.	Determine if oceans exist on Titan. Investigate surface geologic features and topography.
Huygens probe		
Instrument	*Measurement*	*Scientific objective*
Huygens Atmospheric Structure Instrument (HASI) (Ferri *et al.*, 2002)	3 axis accelerometer Relaxation probe	Measure entry deceleration.
Gas Chromatograph Mass Spectrometer (GCMS) (Niemann *et al.*, 2002)	Chemical species identification. Separation of mixtures using gas chromatograph and identification by mass analysis.	Identify and quantify abundance of atmospheric constituents. Analyse vaporised surface samples. Analysis of ACP samples (see below).
Aerosol Collector and Pyrolyser (ACP) (Israël *et al.*, 2002)	Acquire two aerosol samples at different altitudes, step heating, then passing to GCMS for analysis	Collect, and determine chemical composition of aerosols.
Descent Imager and Spectral Radiometer (DISR) (Tomasko *et al.*, 2002)	Upward/downward photometer. Visible and IR spectrometry	Atmospheric composition and cloud structure. Distribution of aerosols. Surface spectral reflectance. Imaging.
Doppler Wind Experiment (DWE) (Bird *et al.*, 2002)	Measurement of Doppler shift of signal from probe to Cassini orbiter.	Measure the velocity and direction of zonal winds with altitude in the atmosphere. Probe descent dynamics.
Surface Science Package (SSP) (Zarnecki *et al.*, 2002)	9 separate sensors making various measurements including impact acceleration, penetrometry, speed of sound in atmosphere and density and refractive index of any liquid.	Characterize the physical nature of the surface at the landing site. Measure thermal, optical, acoustic and electrical properties of any ocean. Measure abundance of major ocean constituents.

Table 1.4 Summary of instruments on the Huygens probe and key instruments on Cassini with surface science applicability.

1.4.2 The ACC-E penetrometer

The Surface Science Package (SSP) includes an instrumented penetrometer, designated 'ACC-E' or Accelerometer-external for historical reasons, as part of its array of sensors. The function of this sensor is to provide a qualitative identification of a terrestrial analogue material (Lorenz, 1994) for Titan's surface in the event of a (soft) solid

landing. The penetrometer was designed to measure forces ranging from a few newtons up to a limit of 2000 N. Impact loads higher than this would probably have caused a failure of the probe (Lorenz *et al.*, 1994). No scientific return was expected from the penetrometer in the case of a liquid landing as the force on the tip would be below the trigger threshold of the sensor (Zarnecki *et al.*, 1997).

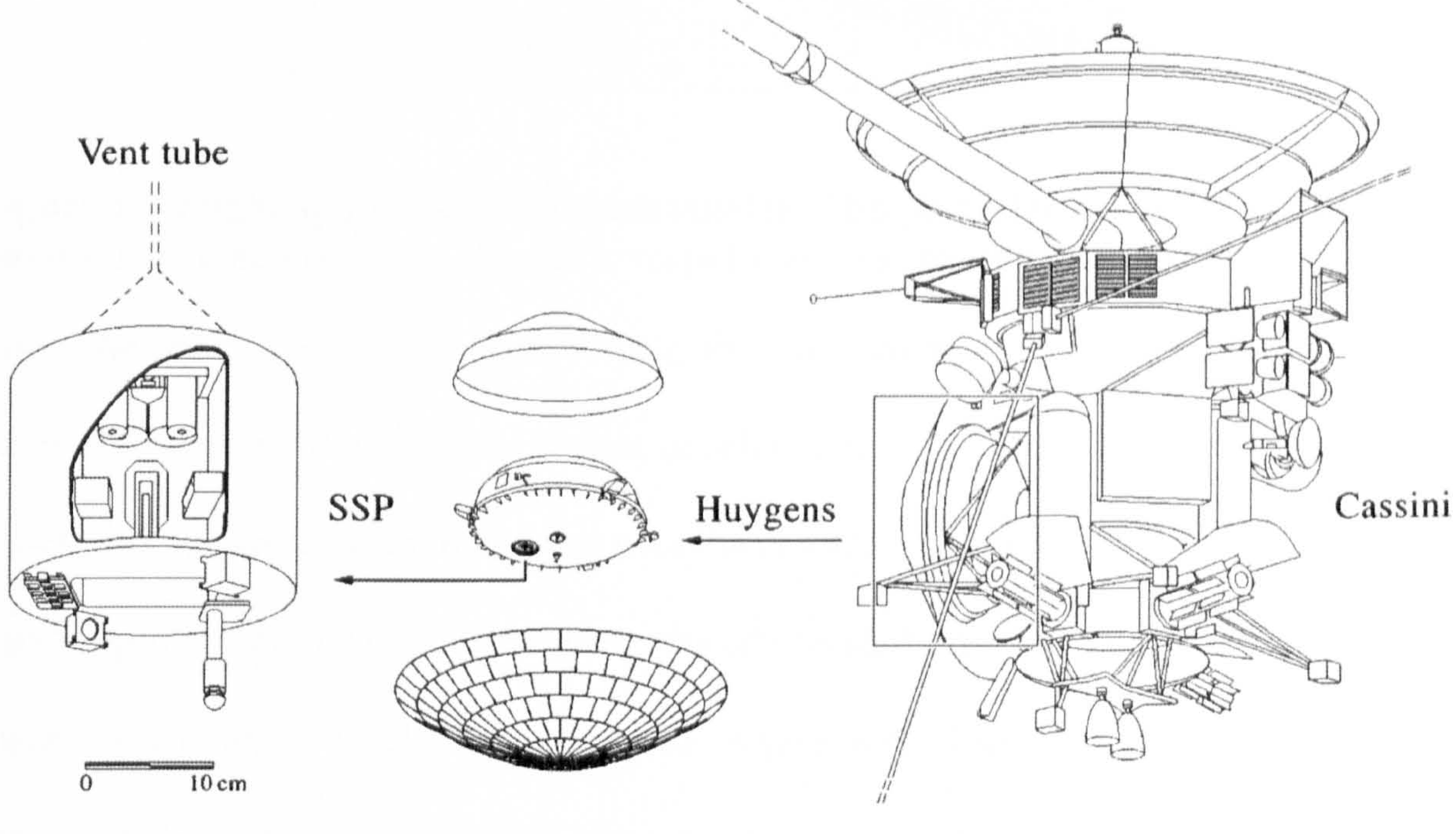

Figure 1.4 Schematic showing location of the Surface Science Package penetrometer on board the Huygens probe. From Zarnecki *et al.* (2002).

The penetrometer consists of a PZT-5A (donor-doped lead zirconate titanate ceramic) piezoelectric element sandwiched between a 14 mm diameter hemispherical titanium tip and an aluminium pylon (Figure 1.5 and Figure 1.6). This element generates a charge proportional to the stress placed on it, enabling it to act as a force transducer thereby allowing a direct measurement of the mechanical resistance of the material encountered.

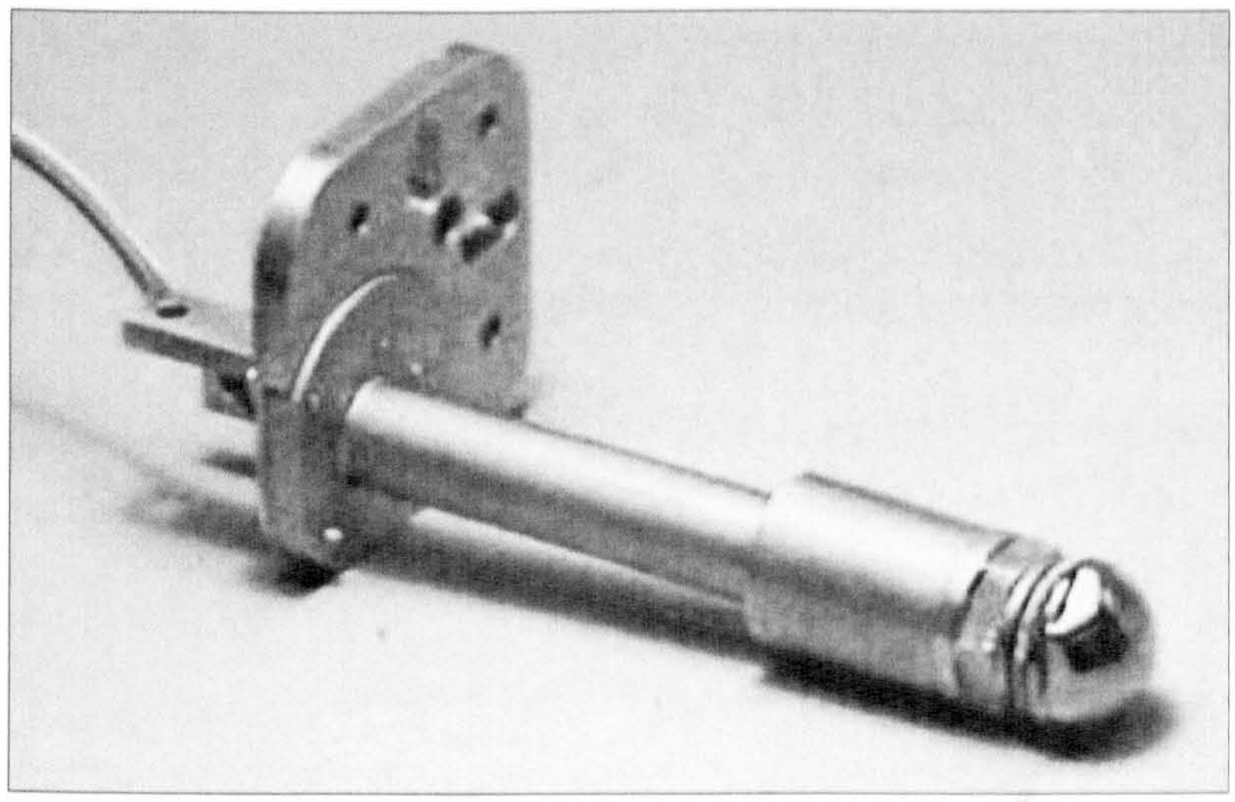

Figure 1.5 Flight spare ACC-E penetrometer. The piezoelectric crystal is the white band sandwiched between the dark vespel washers directly behind the tip.

Since the probe has a flexible foredome, this measurement has an advantage over the other SSP sensor, the internal impact accelerometer (ACC-I), for measuring surface material properties; by mounting the transducer as far forward as possible on the end of a pylon protruding out of the foredome, the effects of the SSP and probe structure on the measurement were considerably reduced. There were limits on the positioning and length of the penetrometer due to the crystal being located close behind a heat shield (Lorenz *et al.*, 1994) .

The sensor was sampled at a rate of 10 kHz and this, together with the expected impact velocity V on Titan of ~5 m s^{-1}, gives a theoretical depth resolution of 1 mm after accounting for Nyquist's theorem:

$$2 f_{Nyquist} = 10000 Hz$$

$$\Rightarrow T = \frac{1}{f_{Nyquist}} = 2 \times 10^{-4} s$$

$$S_{feature} = VT = 5 ms^{-1} \times 2 \times 10^{-4} s = 1 \times 10^{-3} m$$

where $f_{Nyquist}$ is the Nyquist frequency, T is the period and $S_{feature}$ is the theoretical depth resolution. This resolution was intended to allow the possibility of identifying layers in the surface or particle size if the surface was granular (Zarnecki *et al.*, 1997).

The tip was made hemispherical to make the penetrometer less sensitive to an unknown impact angle. It provides a simpler mechanical impulse response than a conical tip with fewer ringing modes and allows faster impact detection producing a quicker initial rise in the impact signature (Lorenz *et al.*, 1994). The sensitivity of the piezoelectric crystal was found to fall by a factor of ~1.8 when tested at liquid nitrogen temperatures of 77 K, close to Titan's surface temperature of 94 K.

For the purposes of producing a surface material catalogue and identifying a Titan surface analogue, the author constructed two replica penetrometers in accordance with the original assembly procedure instructions (Lorenz, 1994). This was an intricate task as three wires (a 'sense','common' and a third wire 'stim' designed for in-flight sensor health checks) needed to be soldered onto the piezoelectric crystal with minimal contact and then looped around into the tip shaft (Figure 1.7). The assembly was then attached to an aluminium collar and torqued to specification (being careful not to shear the delicate soldered joints while doing so!). The resistance and ratio of capacitances between the three connections was then checked to meet specification to ensure the crystal and contacts had not been damaged.

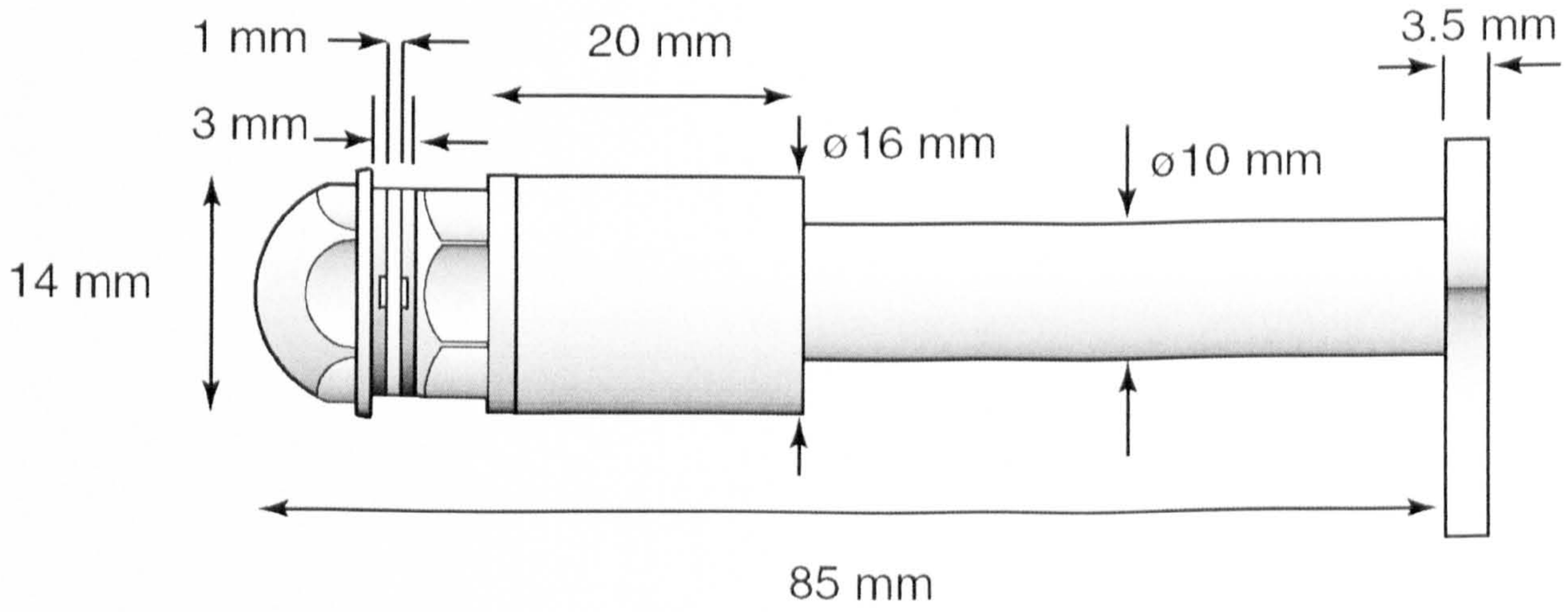

Figure 1.6 ACC-E penetrometer dimensions including small attachment base plate.

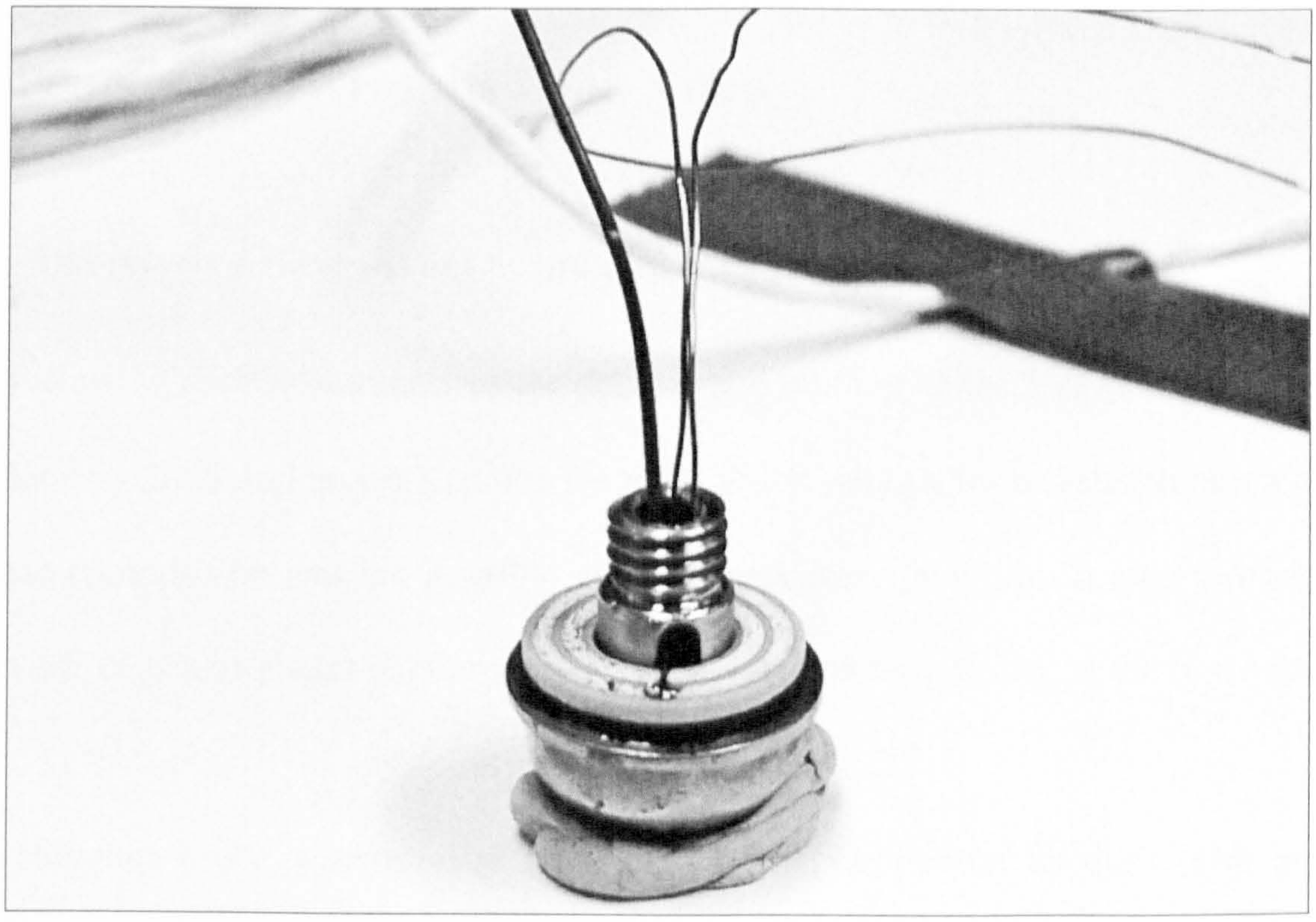

Figure 1.7 Tip and piezoelectric crystal during assembly. The two concentric rings are the 'sense' and 'stim' electrodes (the 'common' electrode is on the underside of the crystal). All solder joints needed to have very low profiles to fit within small grooves in the dark vespel washers.

2 Penetrometry results from Titan

2.1 Overview of Huygens entry and descent

The following section summarises the descent and landing of the Huygens probe on the 14th January 2005 and reviews results from the probe relating to the interpretation of the surface composition and the possible physical processes in action. It also provides an overview of penetrometer data processing and considers the validity of the flight data.

The Huygens probe was released from the Cassini Orbiter on its third orbit around Saturn on the 25th December 2004. During the following ~20 day coasting period the probe was in a dormant state with only three redundant timers active and counting down to a time 4 hours and 23 minutes before expected entry into Titan's atmosphere. At this time, the probe was woken up and on-board computers and sensors activated. At 09:05:53 UTC (Coordinated Universal Time reported with respect to the probe) the probe arrived at the defined interface altitude of 1,270 km, above which no significant atmospheric drag was expected, and then started to enter the upper atmosphere of Titan. Protected by its heatshield, the probe made a ballistic entry at a speed of 6 km s^{-1}, and slowed to 400 m s^{-1} in less than 5 minutes (Lebreton *et al.*, 2005). The starting time of the descent sequence, T_0, occurred nearly 5 minutes later at 09:10:21 UTC when a mortar was fired that pulled out a pilot parachute removing the back cover of the probe. The main parachute deployed two seconds later at an altitude of 155 km and this was followed after 30 seconds by the separation of the heat shield from the front of the probe. The on-board transmitter was then switched on thirteen seconds later. An overview of the descent sequence can be seen in Figure 2.1.

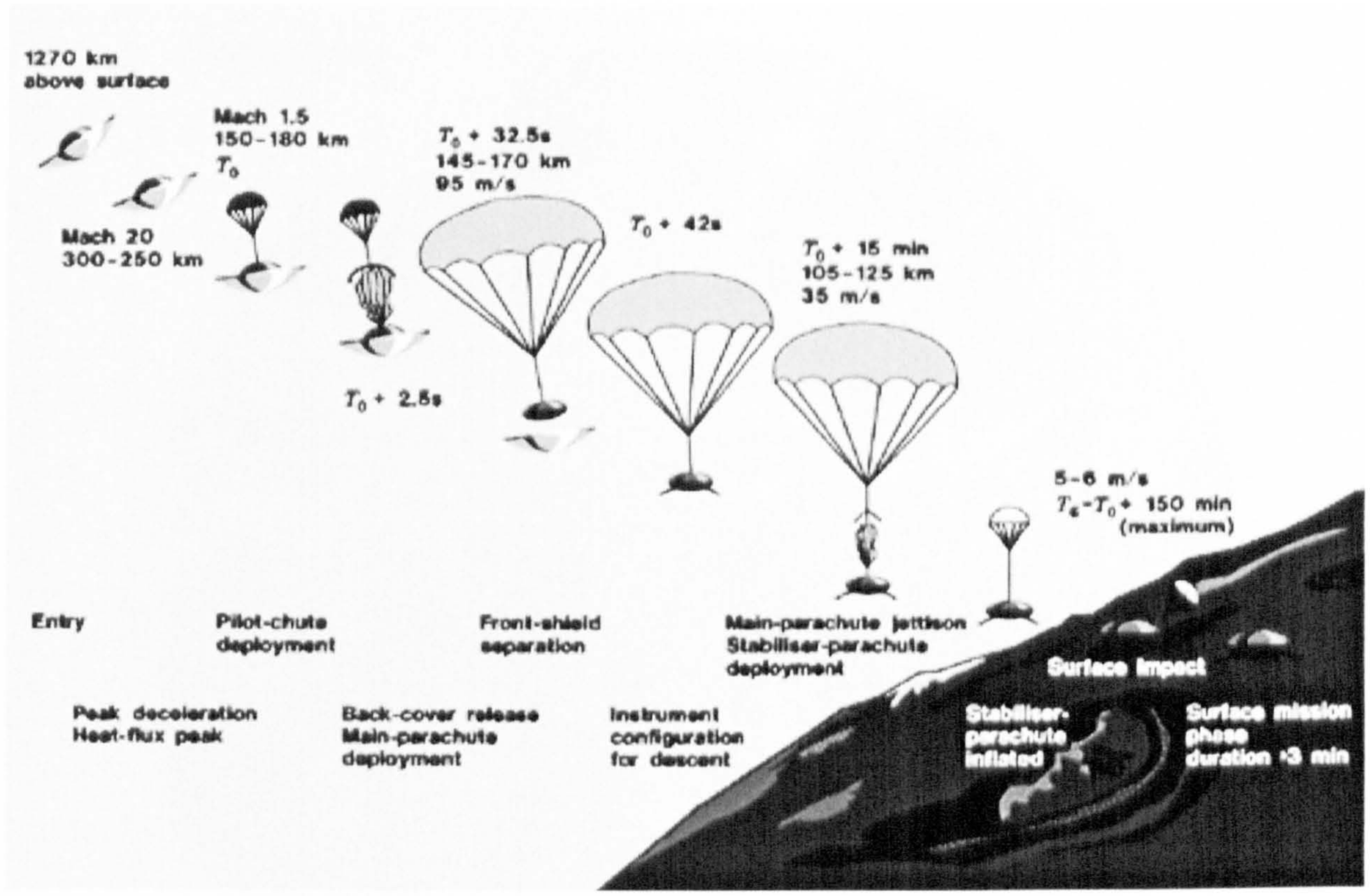

Figure 2.1 Diagram of the Huygens descent sequence from entering the upper atmosphere at an altitude of 1270 km to the impact with the surface some 2 hours 27 minutes later. From Lebreton and Matson (2002)

During the 2 hour 27 minute descent through the thick hazy atmosphere of Titan, the Descent Imaging Spectral Radiometer (DISR) collected imagery from various directions as the probe rotated. Combining these images allowed panoramas to be made. The first panorama, using images taken at altitudes between 49 and 20 km, shows that the probe descended over a boundary between 'bright' and 'dark' regions.

From a lower panorama at 8 km altitude, narrow dark channels cut into the brighter region and fall into two distinct types; dendritic rainfall drainage channels to the north-west contrast with short stubby channels in the west (Figure 2.2). These short channels are interpreted as possible sapping, spring-fed channels or arroyos, intermittently dry channels (Tomasko *et al.*, 2005).

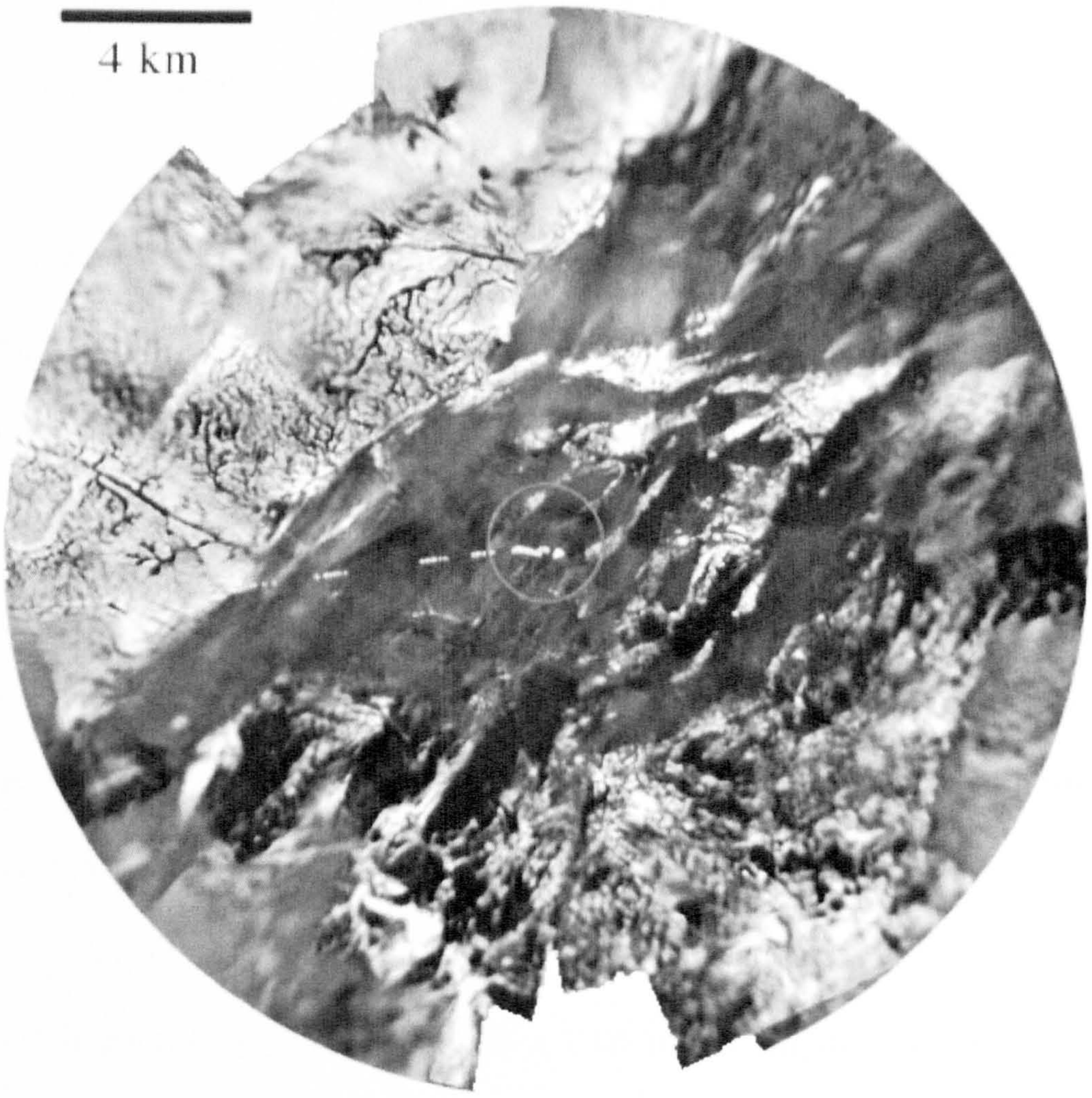

Figure 2.2 Panoramic mosaic projected at 8 km using images collected by the DISR camera as the probe descended between an altitude of 17 and 8 km. The probe crosses a boundary between the 'bright' and 'dark' regions. Dendritic channels can be seen to the north-west contrasting the shorter linear channels in the west. From Tomasko *et al.* (2005).

Stereo analysis of the dendritic region indicates that this terrain is higher than a dark 'lakebed' region that these channels appear to join. Measurements of the surface reflectivity using the Downward-Looking Visible Spectrometer (DLVS) show that the brighter highland areas are redder than the neighbouring dark regions with redness decreasing further from the boundary. It has been suggested by Tomasko *et al.* (2005) that this could indicate that lower albedo material is washed off the highland regions

into the 'lakebed' via the drainage channels, leaving the brighter material of local origin, implying that this material is bedrock.

As the probe descended through the atmosphere, the Gas Chromatograph-Mass Spectrometer (GCMS) measured the mole fraction of methane. This was found to increase gradually below an altitude of 32 km reaching a peak value of 4.92×10^{-2} at an altitude of 8 km and remained constant until impact with the surface (Niemann *et al.*, 2005). A similar value, within experimental uncertainties, of 3.5% was derived from the speed-of-sound measurements made by Surface Science Package (Hagermann *et al.*, 2007). A relative methane humidity of approximately 45% was found at the surface (Niemann *et al.*, 2005), too low for fog.

The probe impacted the surface at 4.60 ± 0.05 m s^{-1}, slightly slower than expected (Towner *et al.*, 2006; Zarnecki *et al.*, 2005). The impact triggered the penetrometer at T_0+8869.7598 seconds followed by the activation of the Surface Science Package piezoelectric accelerometer ACC-I (Accelerometer-Internal), 9.7 ms later. This accelerometer measurement agrees (within the timing uncertainties) with a similar measurement by a piezoresistive accelerometer, PZR-X, of the Huygens Atmospheric Structure Instrument (HASI) (Fulchignoni *et al.*, 2005; Zarnecki *et al.*, 2005).

Images of the surface taken with the DISR cameras (Figure 2.3) suggest a surface shaped by fluvial processes. Rounded pebbles 10-15 cm in size lie on top of a fine darker grained substrate material with a smallest detectable size of 3 mm, the resolution limit of the imager (Tomasko *et al.*, 2005). It is likely that these pebbles are made of water ice given the spectroscopic and radar evidence (Campbell *et al.*, 2003; Griffith *et*

al., 2003). A gap in the pebble distribution between the foreground and background, aligned with 'streamers' of dark material occurring off these pebbles suggests a liquid may have flowed from left to right in the image.

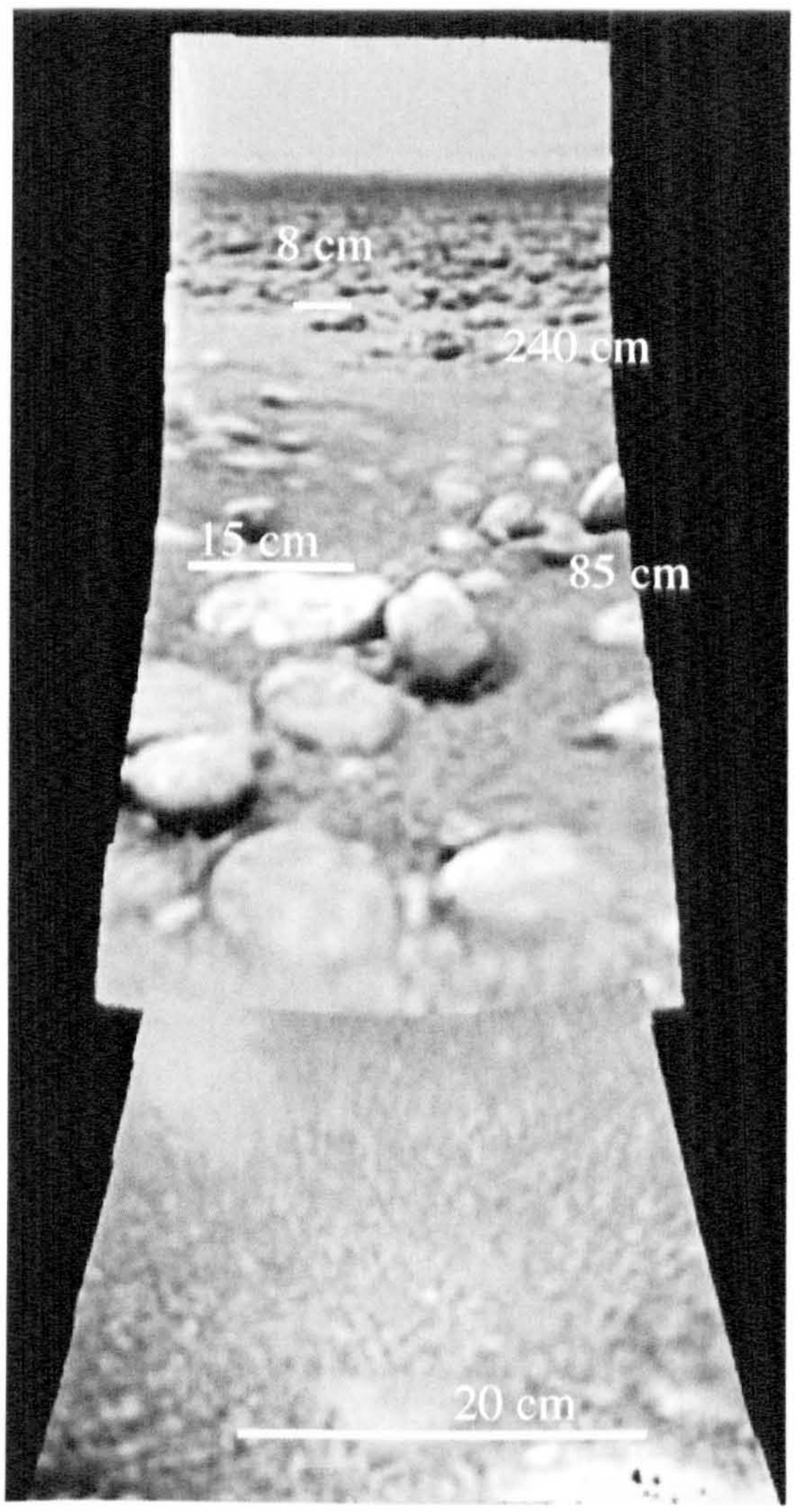

Figure 2.3 A combined image of the surface of Titan taken with the Side Looking Imager (SLI) and Medium Resolution Imager (MRI) of the DISR camera. No liquids are seen; however numerous rounded pebbles, most likely eroded by fluid transport, litter the surface. The pebble free channel dividing the foreground and background also indicates fluvial activity and parallel trails of dark material can be seen flowing off nearby pebbles. The underlying substrate material is composed of what appears to be a darker, finer granular material. The smallest measurable size of these grains is 3 mm, the limiting resolution of the imager. Approximate sizes of two pebbles and distances from camera are marked. From Tomasko *et al.* (2005)

After impacting the surface, the GCMS inlet port was either in direct contact with the surface material or in close proximity. Within two minutes of impact, the amount of methane detected increased by about 40% while the detection of nitrogen, the major atmospheric constituent, remained constant. This increase in methane continued for a further 50 minutes before dropping to 25% above pre-impact level. This suggests that liquid methane may be mixed with the surface material and was evaporated by the GCMS inlet line heater until the liquid became depleted (Niemann *et al.*, 2005). Recent modelling of the thermal environment of the inlet supports this possibility, indicating that the heated GCMS inlet may have evaporated a small quantity of methane in the local material (Lorenz *et al.*, 2006).

Further clues about Titan's surface come from the reflectance spectrum of the surface material taken after landing. This shows a relatively low brightness and a nearly linear decrease in reflectivity above 830 nm. A simulated combination of coarse grained low-temperature water ice, yellow tholins and a spectrally neutral dark component provides a reasonable reflectance spectrum match for this unusual material although it fails to reproduce the absence of weak H_2O bands in the quasi-linear slope. The large grained water ice is responsible for the quasi-linear slope and reducing the grain size would not suppress these H_2O bands. This implies that another material mixed with the ice is responsible for the suppression of these bands (Tomasko *et al.*, 2005).

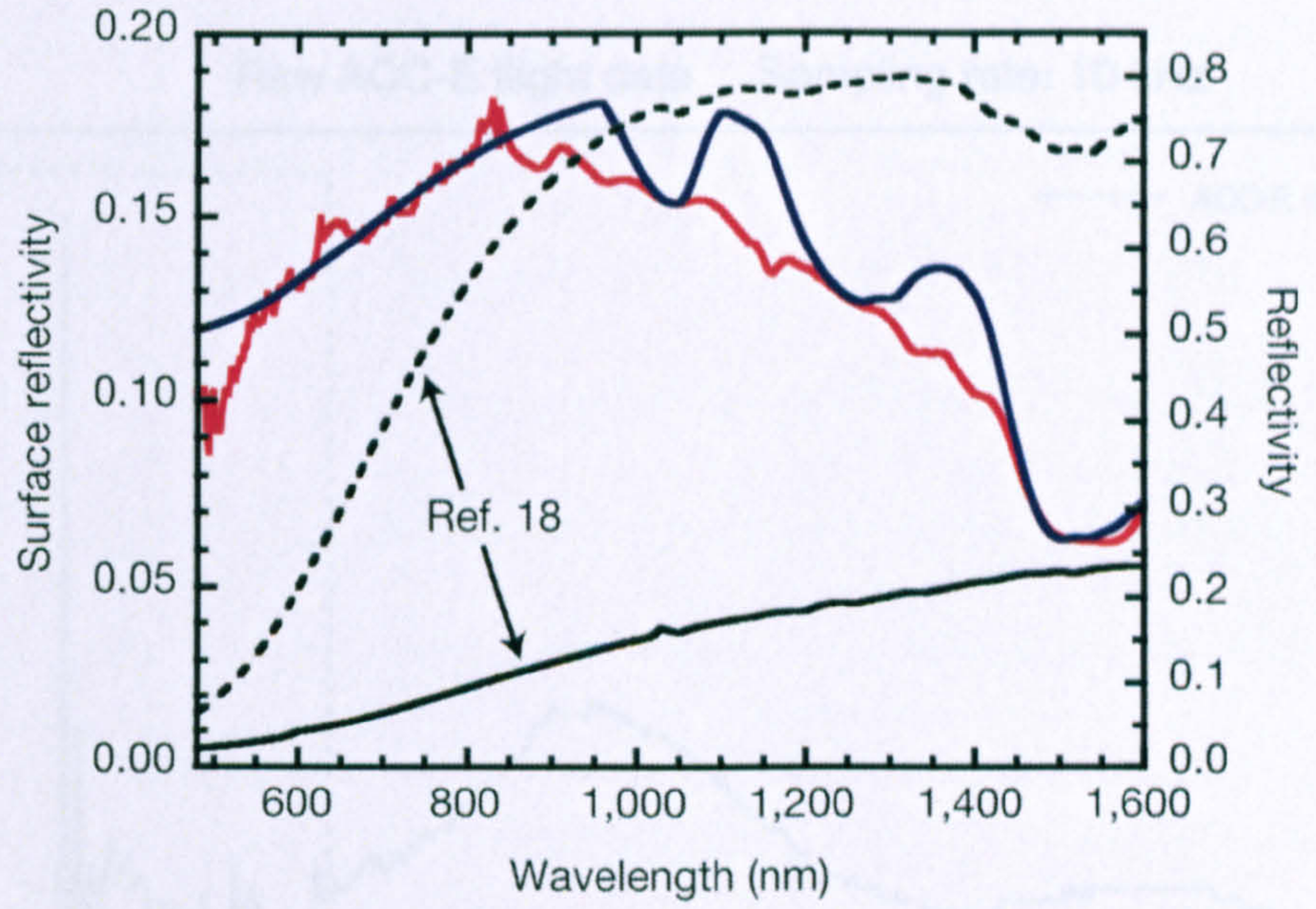

Figure 2.4 Reflectivity of Titan's surface measured by the DISR instrument after landing (red line). Comparison with a simulation (blue line) of a mixture of large grained water ice, tholin and a spectrally neutral dark component are shown. *Ref. 18* in the graph refers to other experiments with two different types of tholins- see Tomasko *et al.* (2005).

2.2 Flight data results from the ACC-E penetrometer

The flight penetrometry record from the impact of the Huygens probe with the surface of Titan consists of 512 samples of data at a sampling rate of 10 kHz. The record starts with 46 zero force samples and by design the First In First Out (FIFO) buffer of 512 samples is frozen 6.4 ms (64 samples) after a preset voltage threshold is exceeded (Lorenz, 1994). The raw penetrometery signature returned from the surface is shown in Figure 2.5.

For the purposes of analysis, only the region of 'clean' penetration (shown in the dashed box) is considered. The arrival of the probe structure to the right of this brings structural interactions which makes this further data unusable.

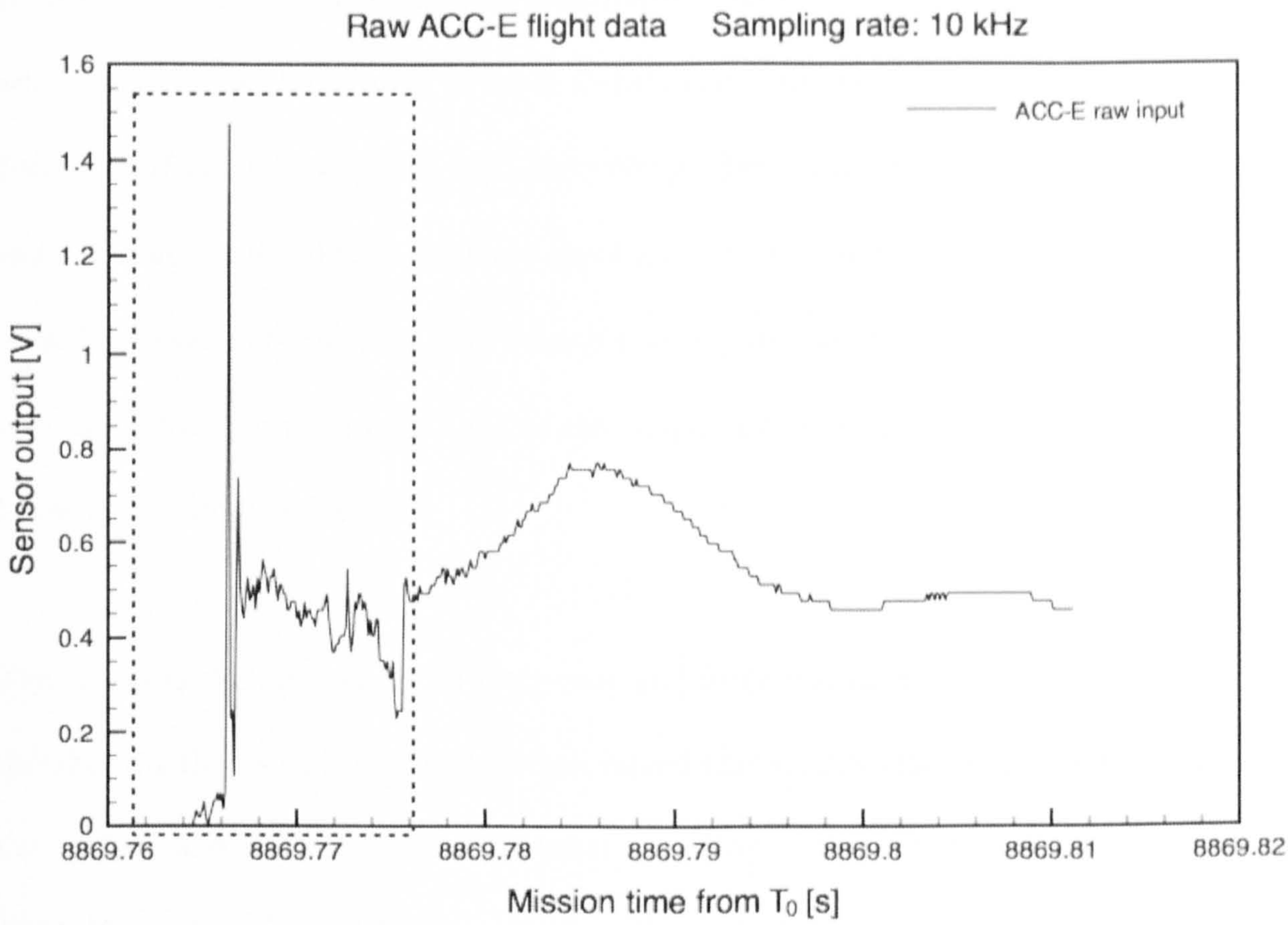

Figure 2.5 Complete raw penetrometer signature. Sensor output (related to force) is shown against mission time from T_0 prior to signal processing and calibration. The dashed box indicates the 'clean' part of the signature before the signal becomes corrupted by the arrival of the probe's foredome structure to the right of this box.

2.2.1 Signal processing

The response of the conditioning electronics and possible noise sources must be accounted for before any impact signature can be analysed. The path from signal generation to recovery of the force signature is as follows:

The piezoelectric crystal in the penetrometer generates an electric charge, Q, proportional to the force applied on the tip. This signal is then passed through several onboard conditioning electronic elements starting with a charge amplifier that converts the charge into a voltage. This is then pre-amplified by a pseudo-logarithmic amplifier with signal magnitude dependent gain that is approximated by three linear segments. The chosen amplification branch depends on the voltage input and is defined by two

predefined transition points. The logarithmic amplifier was used in the design to accommodate the large range of input signals that could be generated from the possible forces. In effect, this maps the high-end voltages generated by a very hard impact onto a smaller range and reduces the force resolution. In the case of the flight data returned from Huygens, only the high gain branch was required as the force on the penetrometer was at the low (softer impact) end of the range. For laboratory data analysis, all three branches are implemented.

The signal is then passed to an integrator and filter that detects when a preset voltage threshold is first reached. A flag is then raised that signals that the probe has impacted the surface and freezes the penetrometer sampling buffer 6.4 ms later (Lorenz *et al.*, 1994; Zarnecki *et al.*, 1997). The signal is then routed through an anti-aliasing filter that removes frequencies above the Nyquist frequency[1] (for the penetrometer, this is 5 kHz; half the sampling frequency) that cannot be resolved and would corrupt the correctly sampled data. In the case of the flight data, the output of the filter is then digitized using an 8-bit analogue to digital converter (ADC) and is stored ready for transmission. Figure 2.6 shows the signal path from the sensor to transmission and the data processing path required to recover the original signal.

---

[1] Nyquist's sampling theorem requires that for any sampled signal to be perfectly reconstructed it must be sampled at a rate a least twice that of the highest frequency it contains (Schwartz and Shaw, 1975).

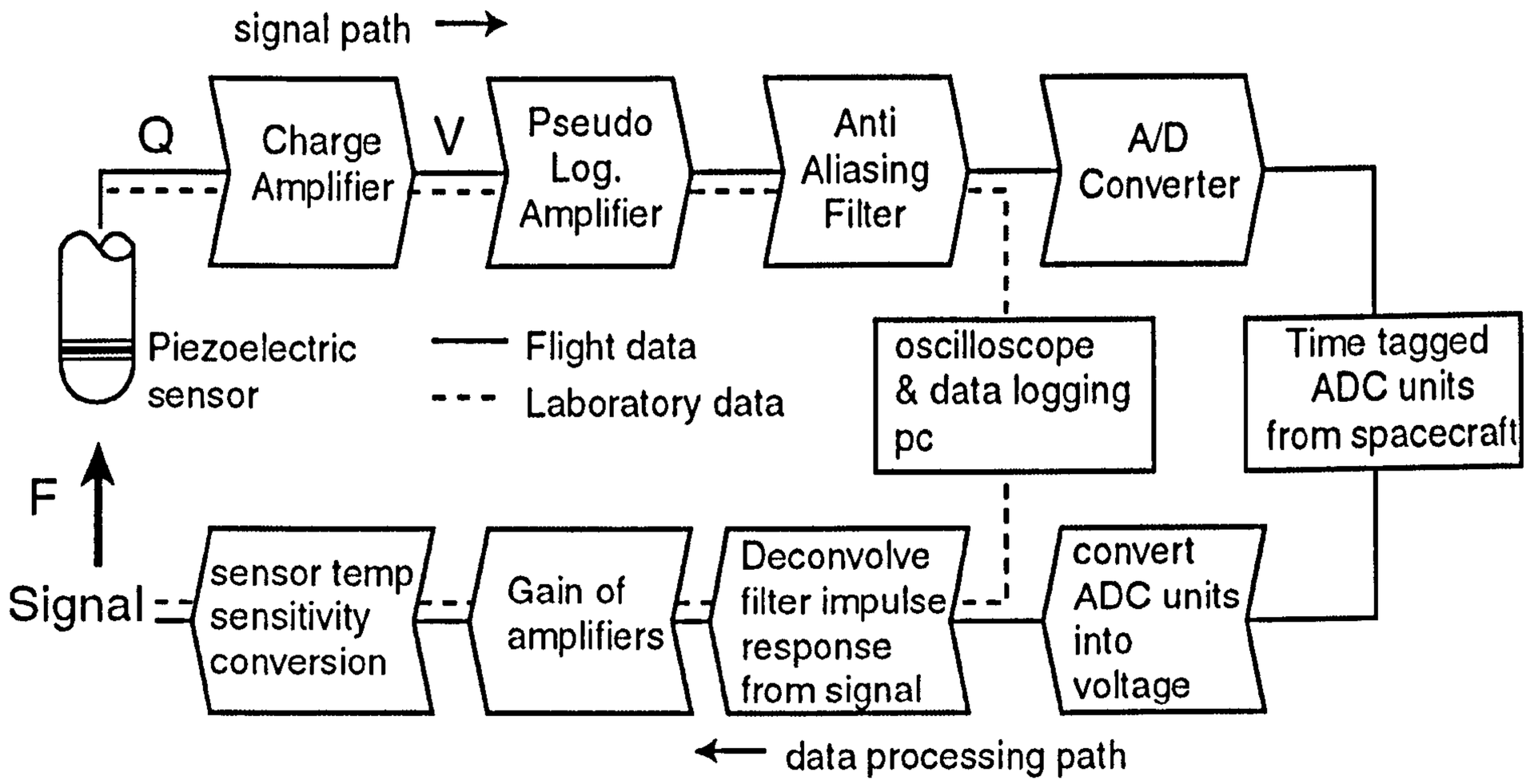

Figure 2.6 Schematic diagram of signal and data processing paths for the flight data and also for the examination of laboratory data. Adapted from Kargl *et al.* (2005).

An examination of the ACC-E front end conditioning electronics (Kargl *et al.*, 2005) suggested that the gain of both the charge amplifiers and pseudo logarithmic amplifier is not critically frequency dependent. This allows a linear relationship between the output voltage and applied force to be used subject to calibration of the piezoelectric sensor. The anti-aliasing filter does however have a significant effect on the signal shape at different frequencies: for frequencies nearing the corner frequency of the filter a phase shift occurs which distorts the signal (Kargl *et al.*, 2005).

Another significant issue is brought about by the sharp shape of the filter to attenuate the unwanted higher frequencies. This leads to a ringing effect in the output when steep (i.e. high frequency containing) signals are input into the filter. The effect can be seen in the response to an impulse as shown in Figure 2.7.

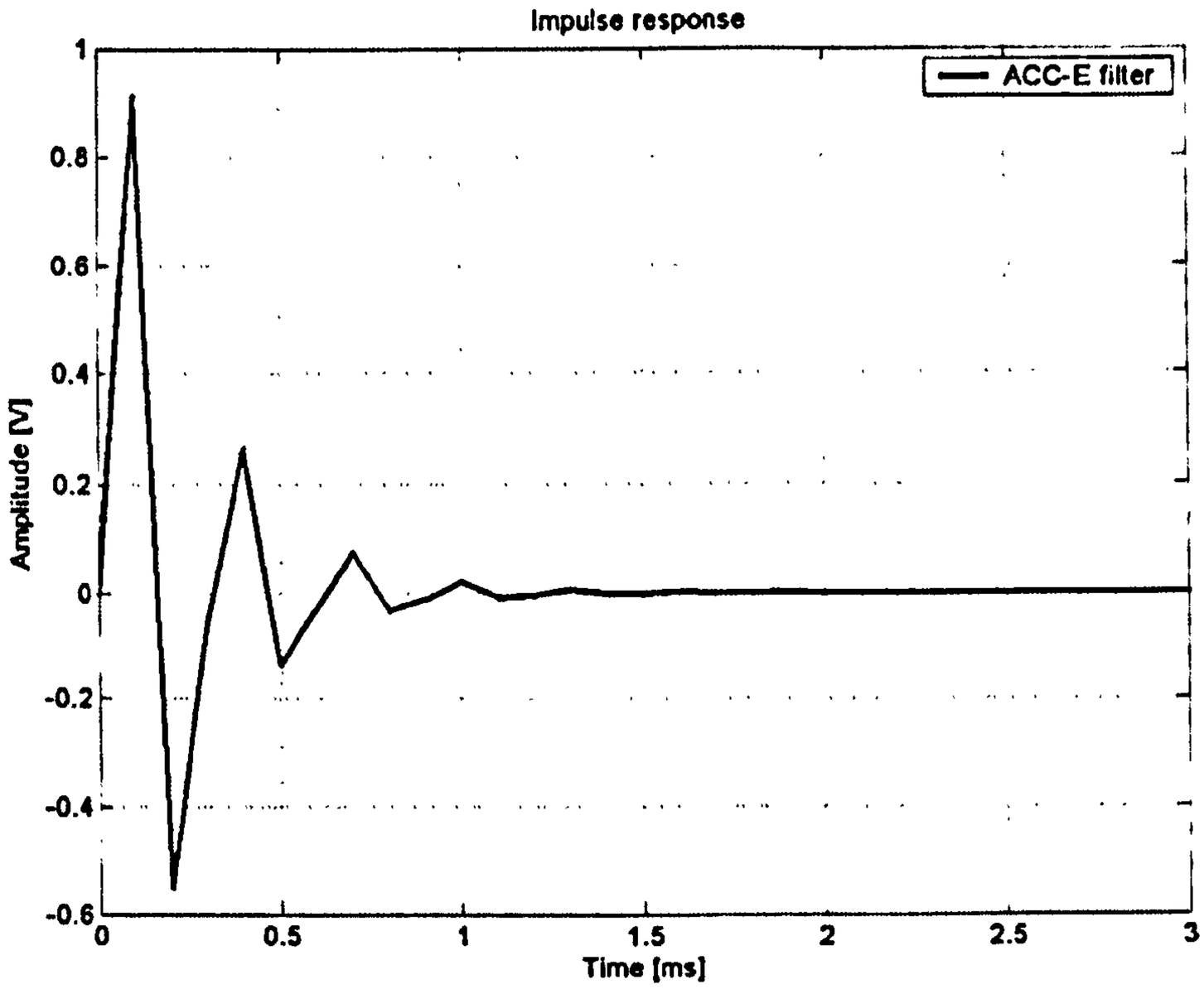

Figure 2.7 Response of ACC-E anti-aliasing filter to a 1 volt input impulse at a 10 kHz sampling rate. Ringing can be seen caused by the filter's sharp attenuation of high frequencies. From Kargl *et al.* (2005).

Since most dynamic penetrometry signatures contain impulses which would produce this effect, it is important that the influence of the filter is removed. This can be done by deconvolving the signal with the impulse response of the filter (Kargl *et al.*, 2005). This technique, used on the flight data, has also been applied to all laboratory data.

2.2.2 Penetrometer catastrophic failure

Impact with the unknown surface of Titan may have been sufficiently hard to cause a catastrophic failure of the penetrometer and this needs to be considered when analysing the returned data. There have been numerous laboratory drops into many materials and on only two occasions was the pylon of the penetrometer observed to have bent slightly. In both cases the sensor continued to function afterwards requiring only the aluminium pylon to be replaced. Interestingly, the damage occurred in the same place, at the

bottom of the pylon where it joins the base. Examination of this point shows that it is a sharp join resulting in a stress raiser[2].

The pylon of the engineering model penetrometer was compared to the laboratory pylons manufactured later, and found to have a small 0.4 mm radius at this join. This has very little effect on strengthening the join and was probably left by the machining process. Penetrometer design documentation (Lorenz, 1994) indicates that the original pylon had the same diameter as the hemispherical tip and that later the shank of the pylon was reduced in a revised design presumably to decrease the overall mass of the SSP instrument. Despite this revision, a failure of the penetrometer pylon on impact with the surface of Titan is unlikely for several reasons; the decelerations measured by onboard accelerometers indicate that the probe landed on a soft material and this is confirmed by the continued operation of the probe on the surface. Furthermore, the discontinuity seen at the end of the 'clean' penetration signal (dashed box region in Figure 2.5) corresponds very closely with the arrival of the electromagnetic compatibility (EMC) screen at the surface, 55 mm later at the 4.6 m s^{-1} constant impact speed.

Finally, on both occasions bending of the laboratory penetrometer occurred after many successful drops had been carried out. This suggests that in addition to existance of the stress raiser, fatiguing of this point by repeated loading and unloading may also be responsible. Clearly this potential failure mode is not applicable to the flight penetrometer which impacted its target surface only once.

---

[2] This is a point where stresses are concentrated.

2.2.3 Limitations of the flight data

The penetrometry flight record of Titan consists of 512 samples of data, although the useful proportion of this is smaller. This is due to the physical restrictions placed on the length that the flight penetrometer could extend beyond the rest of the spacecraft structure. The total length of the penetrometer was restricted by the heat shield attached to the front of the probe that protects it from the intense heat of atmospheric entry. A small recess in this shield was permitted to allow the penetrometer to extend forward slightly (Lorenz *et al.*, 1994), however the restriction still limited the maximum length of the penetrometer to 88 mm. Further reductions in useful length also occurred at the other end of the penetrometer; electric discharge protection in the form of lightweight metallic mesh Electromagnetic Compatibility (EMC) screen reduced the length of the pylon and tip assembly from 88 mm to 55 mm. These were unfortunately necessary design constraints that could not be further mitigated. A cross section through the probe is shown in Figure 2.8.

Sampling rate restrictions were placed on the penetrometer due to the limitations in data storage and transmission. This limits the frequency content of the signature which may restrict the size of particle that may be seen. This effect is investigated and will be discussed later. A further limitation of the data is the existence of only one penetrometer. This restricts the data to a sampling of only one area of the local surface and denies the possibility of making comparisons both to confirm the correct operation of the penetrometer and to examine the local homogeneity of the regolith.

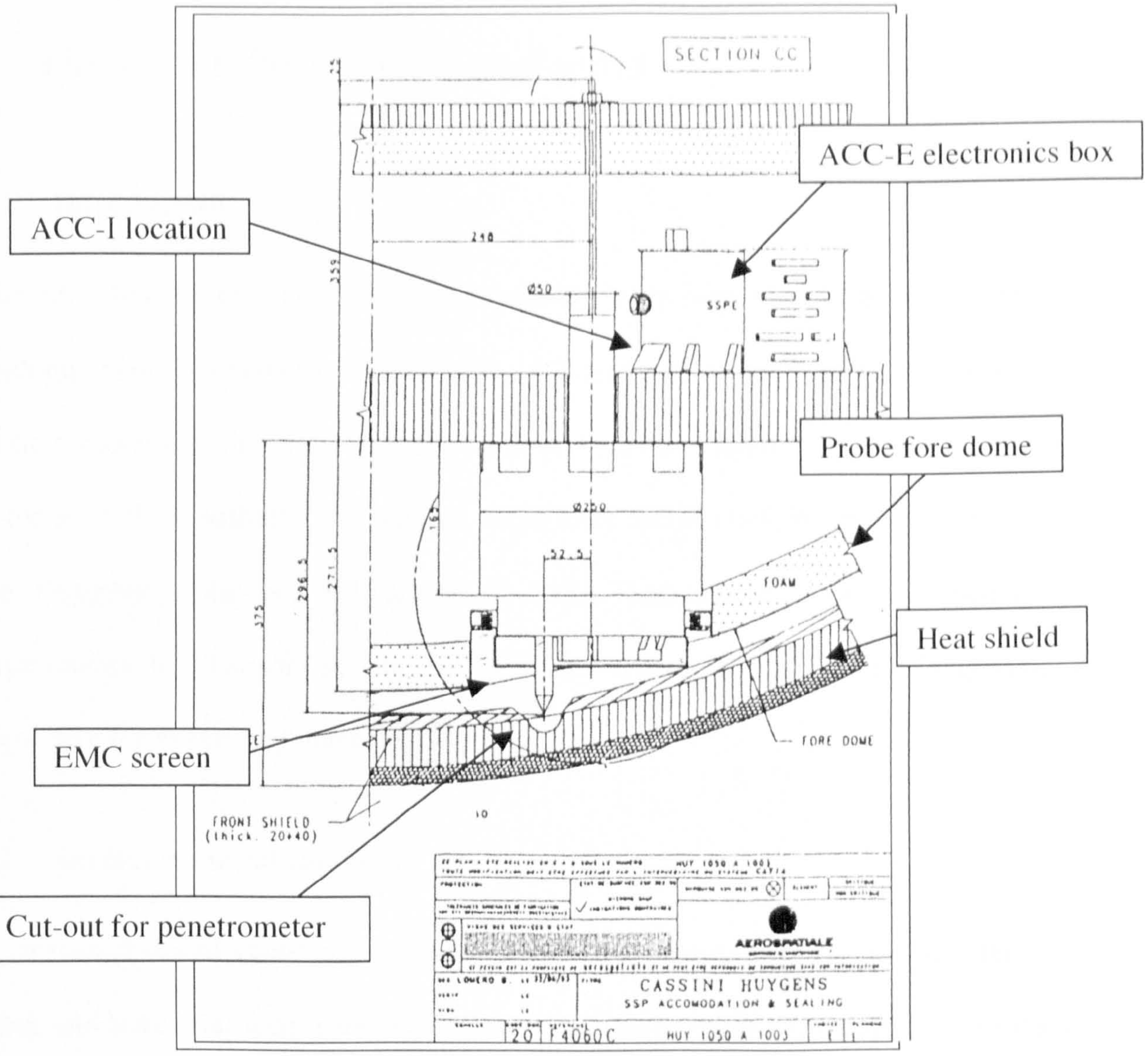

Figure 2.8 Cross section of the Huygens probe showing the location of the Surface Science package, ACC-E penetrometer , fore dome and heat shield. The useful length of the penetrometer was restricted by the heat shield and by the EMC screen attached to the front of the SSP Top Hat. (ESA document)

3 The search for physical analogues

3.1 Introduction

The objective of the laboratory penetrometer study was to find terrestrial physical analogue materials that are representative of Titan's unknown surface, should the probe make a successful landing. The preparation of a surface material catalogue was initiated at the start of the author's PhD studies, some three months before the expected arrival of the Huygens probe on the surface of Titan. Subsequent work has focussed on experiments to characterise the penetrometer more accurately and investigate its capability for examining planetary surfaces.

3.2 Surface material catalogue

A surface material catalogue to allow visual comparison between surface data from Titan and terrestrial analogues was prepared in conjunction with another PhD student Mark Paton at the end of 2004 using a drop rig originally designed for penetrometry of Near Earth Objects (NEOs). Some 30 drops into various materials including loose and compacted sand, fine and coarse gravel, and molasses were made. Following the successful landing of the Huygens probe further laboratory drops were carried out with target selection input from several members of the Surface Science Package (SSP) team. This effort culminated in the publication Zarnecki *et al.* (2005).

3.2.1 The Near Earth Object (NEO) drop rig

This section briefly describes the design of the Near Earth Object (NEO) drop rig used to produce the surface material catalogue. A detailed description, including development and operation can be found in Paton (2005).

The drop rig consists of a weighted baseplate attached, via a system of two chain loops and several cogs, to a counterweight. In the absence of other forces, the counterweight balances the acceleration of the plate due to gravity and the system is at rest. Using an actuator coupled to the chains, the chain loops can be moved manually, raising the baseplate above the target material container. A third set of accelerating weights is coupled to the chain loops as shown in Figure 3.1. When the actuator is released, this third weight unbalances the system causing the baseplate to accelerate downwards. Immediately prior to impact the accelerating weight hits the floor and is decoupled from the chain system so that the baseplate once again experiences no accelerating force and hits the target material with constant velocity.

By considering the mass of the weighted baseplate, m_1, counterweight, m_2, and accelerating weight, m_3, it can be shown that the impact speed of the rig is given by (Paton, 2005):

$$v = \sqrt{2s\left(\frac{(m_1 - m_2 + m_3)g - F_f}{(m_1 + m_2 + m_3 + m_4)}\right)} \qquad \textbf{(Equation 3.1)}$$

The masses m_1, m_2 and m_3 are 54.4, 55.7 and 27.0 kg respectively in the balanced configuration. The chain weight m_4, of 3.5 kg does not contribute to the acceleration. Further terms in the equation are, F_f, the dynamic friction of the rig (found to be approximately 15 N (Paton, 2005)) and s, the height the accelerating weights fall before being decoupled. When this height is at its maximum of 1.45 m, this gives a maximum impact speed of 2.2 m s^{-1}.

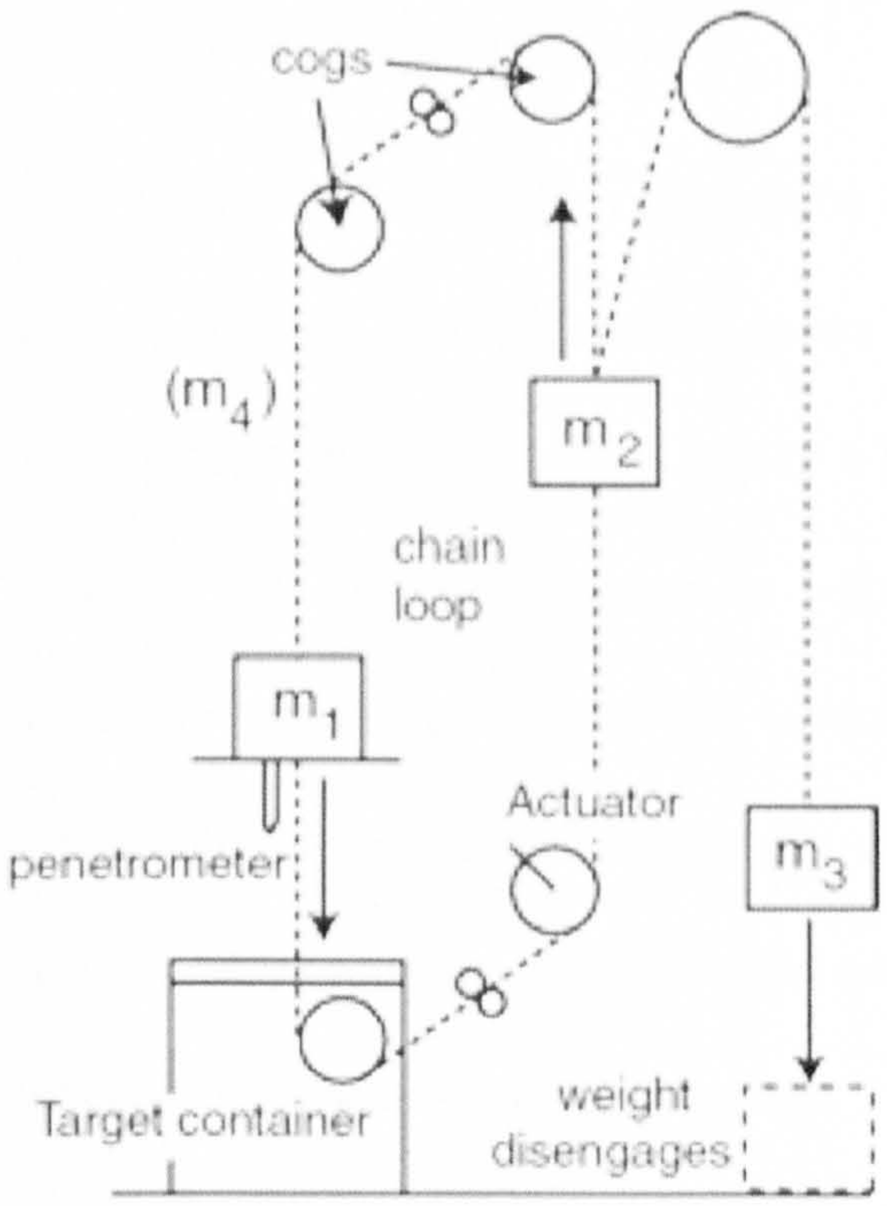

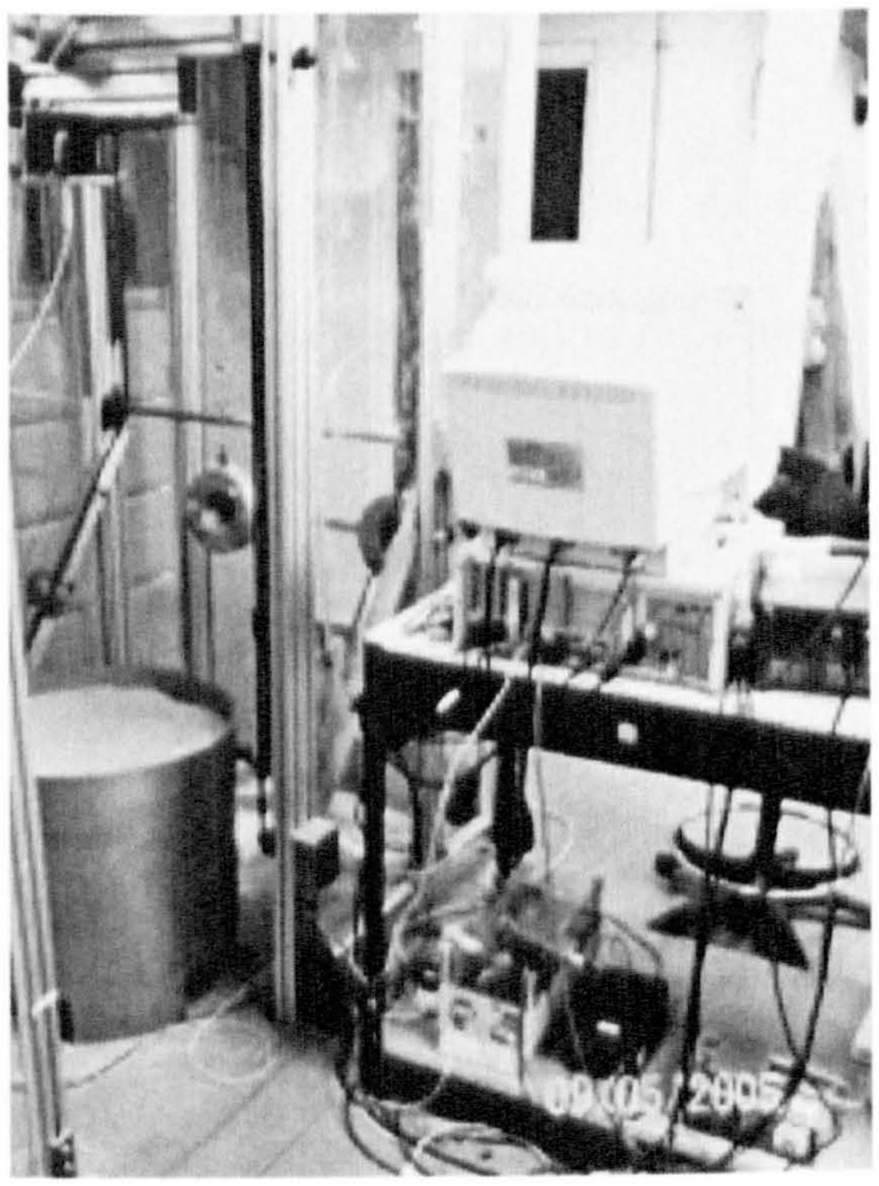

Figure 3.1 Schematic diagram of the NEO drop rig. The weight m_3 is used to accelerate the balanced chain loop weight system of m_1 and m_2. The mass m_3 impacts the floor disengaging it from the chain loop system immediately prior to the penetrometer impact. For balanced weights m_1=m_2, the penetrometer enters the target at constant speed.

For the purposes of creating the Titan surface material catalogue, the speed of impact was increased to a maximum of 3.7 m s^{-1}, 74% of the expected Titan impact speed of 5 m s^{-1}. This was achieved by removing most of the mass m_2. This allowed the falling baseplate to accelerate faster however, on impact it was no longer at zero acceleration due to the unbalanced weight configuration.

The impact speed for each drop was confirmed by using a shaft encoder connected to a chain cog that gave a series of pulses as the baseplate dropped. By using an electronic counter and slowly raising the baseplate over a known fixed distance, it was possible to determine the distance travelled between shaft encoder pulses. This allowed the shaft encoder pulses, recorded on the oscilloscope with each drop, to be used to calculate the impact velocity of the penetrometer.

3.2.2 Catalogue experiments

Until the landing of the Huygens probe in January 2005, very little was known about the surface of Titan. The uncertainty in the type of surface that was expected is reflected in the design of the SSP. In the event of a liquid landing, the tiltmeter sensors (TIL) would measure any bobbing motion, a refractometer (REF) would measure the liquid's refractive properties while the acoustic sounder/altimeter (API-S) could examine topography of a solid surface or floor of a liquid body. The penetrometer however, was directed at examining a likely solid surface with possible returns for a soft, possibly cohesive hydrocarbon coated surface. In the months leading up to the landing, a wide range of targets were used with some being necessarily speculative. Figure 3.3 at the end of this section shows some of the test drops.

With the NASA Voyager probe evidence for a likely icy body, various hard granular materials such as sand and gravels of different shapes, sizes were chosen to represent this. Water ice at the frigid -180°C surface temperatures of Titan would be much harder than ice on Earth (experiments indicate the Mohs' hardness of water ice increases from 2 near its freezing point to approximately 6 at -79°C, equivalent to orthoclase feldspar (Blackwelder, 1940, Nesje and Dahl, 2000). Terrestrial rock analogues were therefore considered to represent this well. Very little is known about the physical properties of tholins or how they might behave when deposited. In an attempt to examine this, analogue drops were carried out into viscous molasses and soft, plastically deforming modelling clay. Other materials tested included porous brittle Foamglas (a cometary analogue discussed later) and fine glass powder.

3.3 Discussion of Huygens ACC-E results

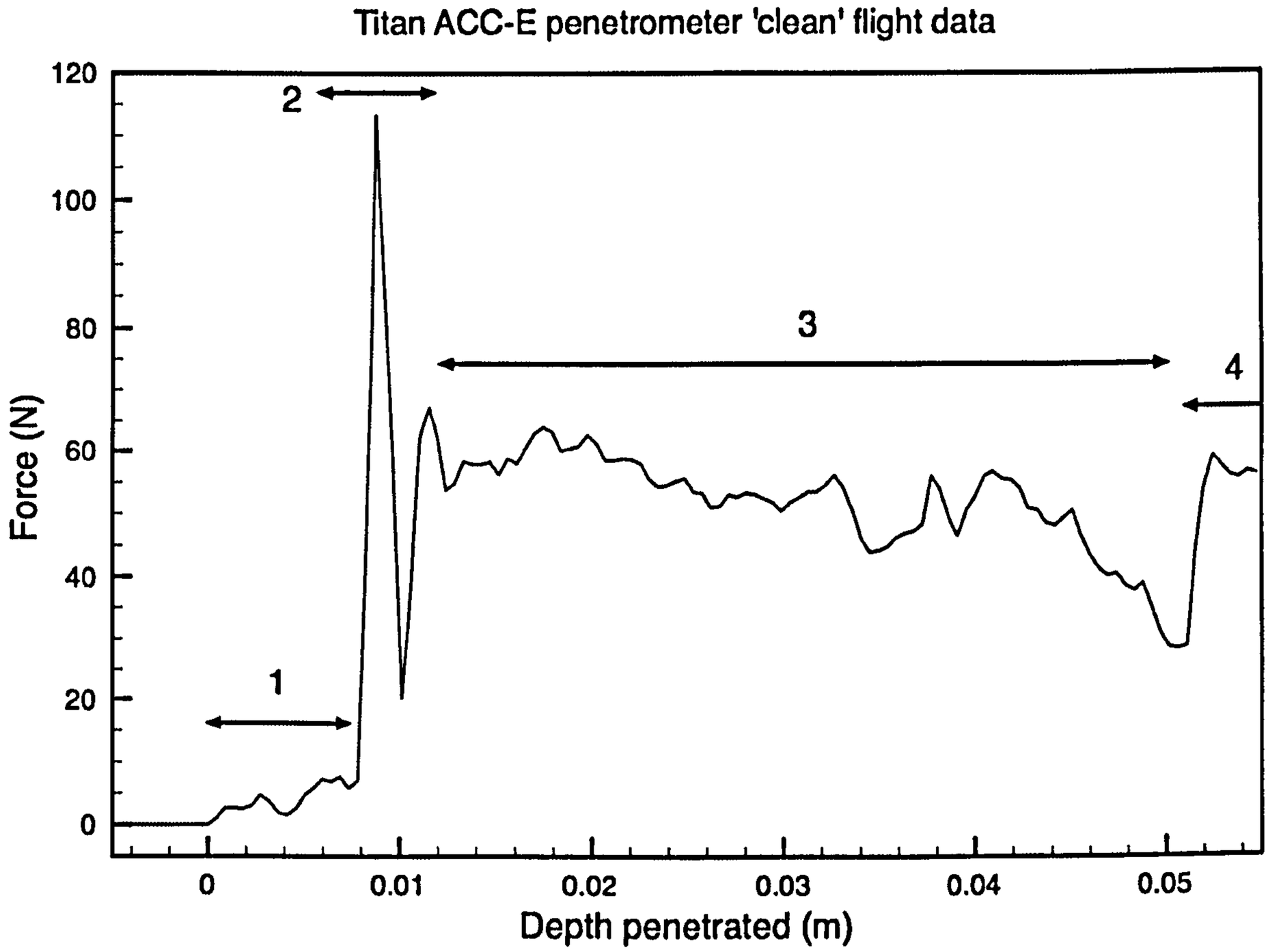

Figure 3.2 The 'clean' part of the ACC-E penetrometery signature returned from the surface of Titan processed into force against depth. The penetration analysis stages are marked.

The successful return of an impact signature constrained the possible material types.

Figure 3.2 shows the penetrometery signature returned by ACC-E from the surface.

For the purposes of analysis it can be considered as four separate stages:

- Stage 1 (1.6 ms duration ≅ 7 mm penetration)

  A weak but rising force. At an impact velocity of 4.6 m s^{-1} this corresponds to a material of thickness 7-8 mm. This could suggest a thin soft material such as a coating of some kind. Another possible cause could be the introduction of the penetrometer's hemispherical tip itself.

- Stage 2 (1 ms duration ≅ 5 mm penetration)

  A sudden rapid 'spike' in resistance lasting for a short duration. This could suggest a thin brittle crust or given the surface image, an impact with a small pebble overlying the surface substrate material.

- Stage 3 (8.3 ms duration ≅ 38 mm penetration)

  This is the longest period of 'clean' penetration. The resistance decreases gradually over the 8.3 ms duration from around 60 N to 30 N. The segment is not completely smooth, indicating that there is some structure present within the material.

- Stage 4

  Impact of the rest of the foredome and end of the 'clean' penetration. The abrupt rise in force signals the arrival of the Electromagnetic Compatibility (EMC) screen of the Surface Science Package.

Stage 1-2 indicates a very weak rising force followed by a sudden spike in resistance of the material. Within the SSP team, it was speculated that this spike might be due to a potential discharge between the probe and the ground although the weak preceding force makes this unlikely. Furthermore, no such discharge was detected by electrical sensors of the Huygens Atmospheric Structure Instrument (HASI) (Fulchignoni *et al.*, 2005). Instead, given the evidence from the Descent Imager/Spectral Radiometer (DISR) images, a pebble impact or possible thin crust (in both cases coated with a very soft layer) seems more likely to be responsible for this signature feature. To examine this possibility, impacts into sugarglass 'crusts' made from caramelised sugar of varying thicknesses and direct and glancing impacts into small pebbles of different sizes were carried out.

Examples of these drops are shown in parts e) and g) of Figure 3.3 and indicate a good agreement with the short duration impulse seen in the probe impact signature.

The underlying substrate material is also intriguing. All drops carried out for the material catalogue prior to the landing had produced signatures where the material resistance either rose or remained constant with increasing penetration depth. The general trend of the substrate material is downward: the material becomes weaker as the penetrometer pushes through it. The variability of the signature clearly indicates small structure in the material leading to the suggestion that this might be consistent with a 'Swiss cheese' type material containing voids (R. Lorenz personal communication). This might be representative of deposits of organic haze filling topographically low areas with porous voids created by liquid methane or ethane that has since evaporated, and is consistent with the absence of specular reflections in recent near-infrared observations near Titan's equatorial regions (West *et al.*, 2005). Specular reflections would imply a very smooth surface indicative of the presence of liquid.

Another possibility, that might explain the reduced mechanical resistance with depth, could be given by the addition of small quantities of liquid methane or ethane contained within a granular surface acting as a lubricant between grains thus reducing resistance. This surface material could be produced by a methane/ethane flow draining away or a lake evaporating, leaving moisture only below the surface. Drops carried out into an analogue of sand wetted with water show this decreasing trend in some cases (Figure 3.3 part f) although the degree of saturation required was not well constrained. Reduced resistance with depth may also be caused by a grain sorting effect or by chemical cementation of grains near the surface.

Due to this hard top surface with soft underlying material, the SSP team's initial reaction to the media on receiving the penetrometery data was to describe the surface as "crème brûlée-like". Figure 3.3 part h) shows an actual laboratory drop into crème brûlée!

Using the catalogue, a qualitative analysis suggested that the surface of Titan had similar strength characteristics to wet sand or clay, and that the substrate surface material was consistent with a granular material (Zarnecki *et al.*, 2005). Following this, the author felt that an improved material catalogue would allow for a more comprehensive analysis of the capabilities of the penetrometer and that to produce this new catalogue would require the development of a new drop rig to overcome the limitations of the original.

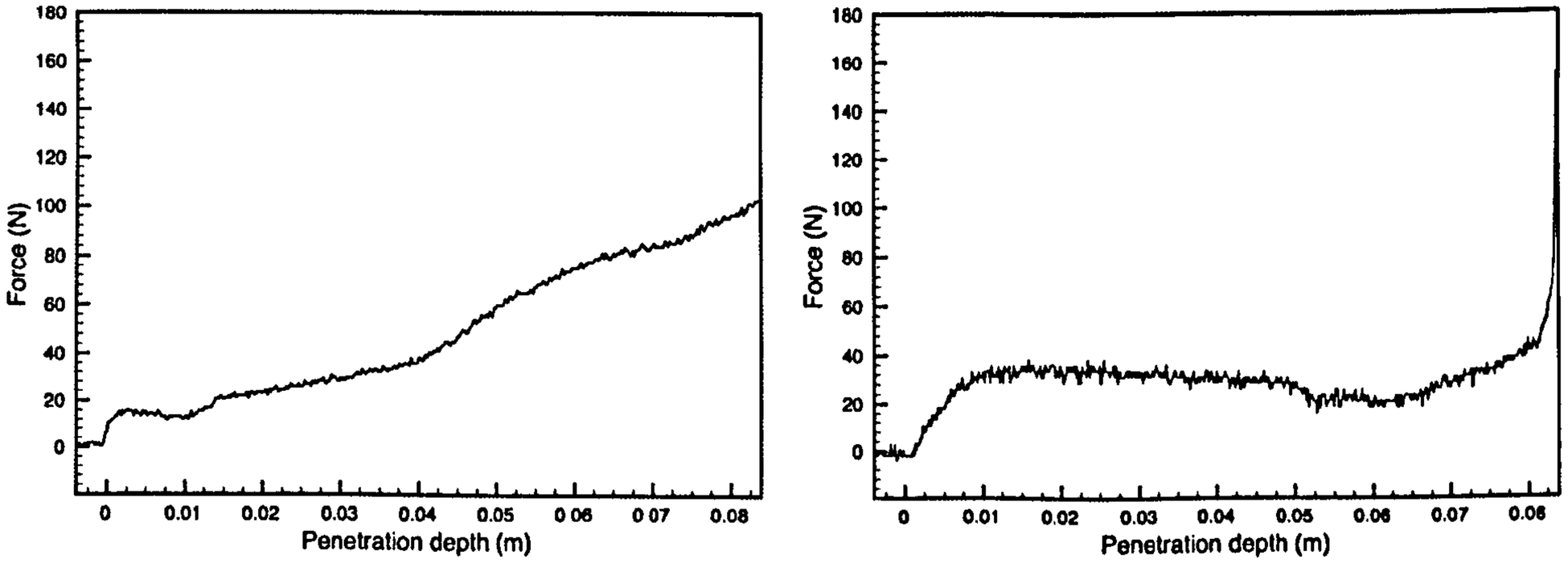

Figure 3.3 Some of the penetrometry signatures from the material catalogue collected using the NEO drop rig in the weeks before and immediately after the landing on 14th January 2005 (*Continued on following page*): (a) Compacted paving sand (b) Molasses (c) Compact modelling clay (d) Coarse gravel (e) Sugar glass crust on top of loose paving sand (f) wet sand (g) pebble on wet sand (h) Crème brûlée. For a full description of the target material choices see text. The signatures were collected at sampling rates between 25-100 kHz and are not corrected for the transfer function of the anti-aliasing filter. Penetration depths are approximate and are estimated based on shaft encoder data where available.

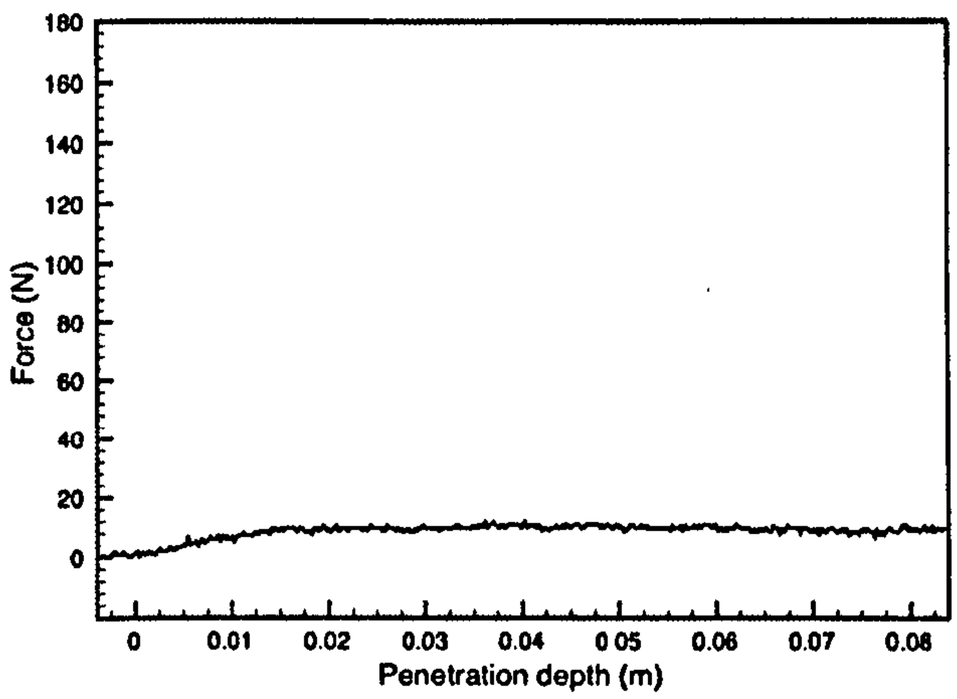
Force (N)
Penetration depth (m)

(c)

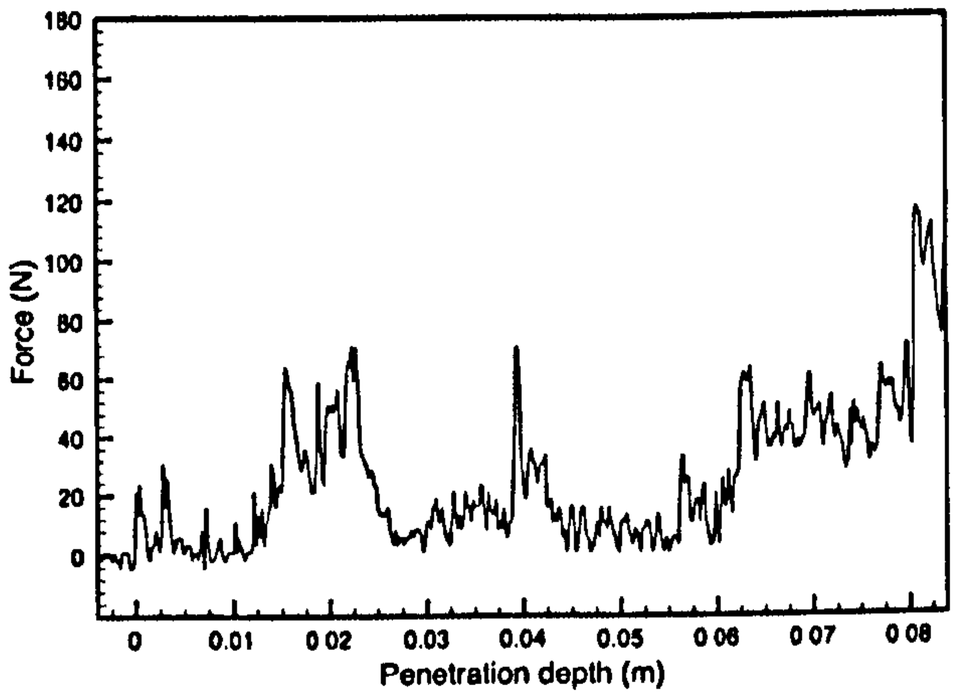
Force (N)
Penetration depth (m)

(d)

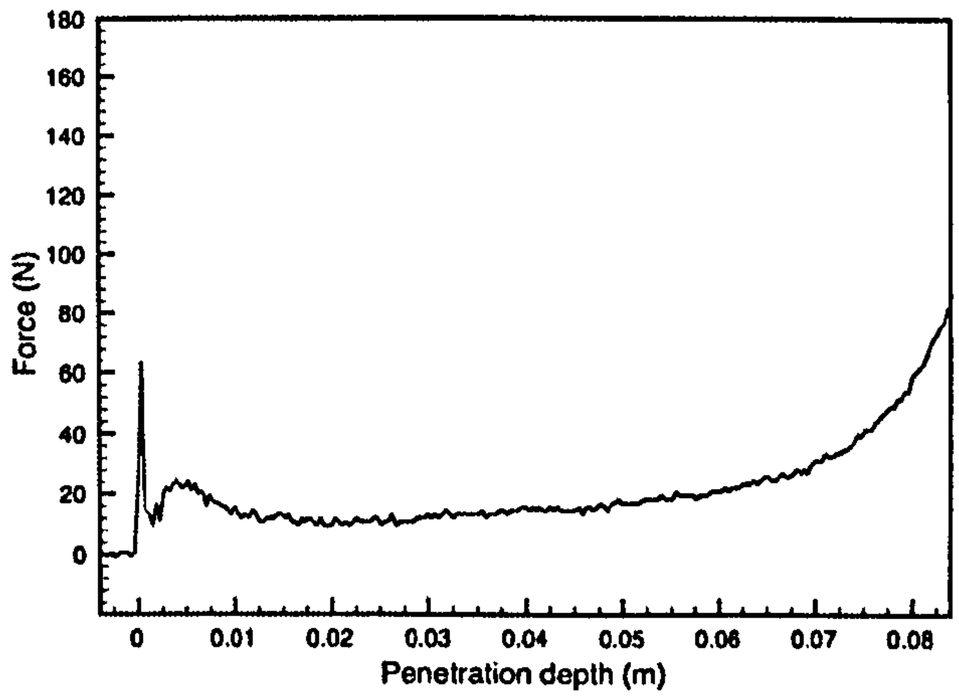
Force (N)
Penetration depth (m)

(e)

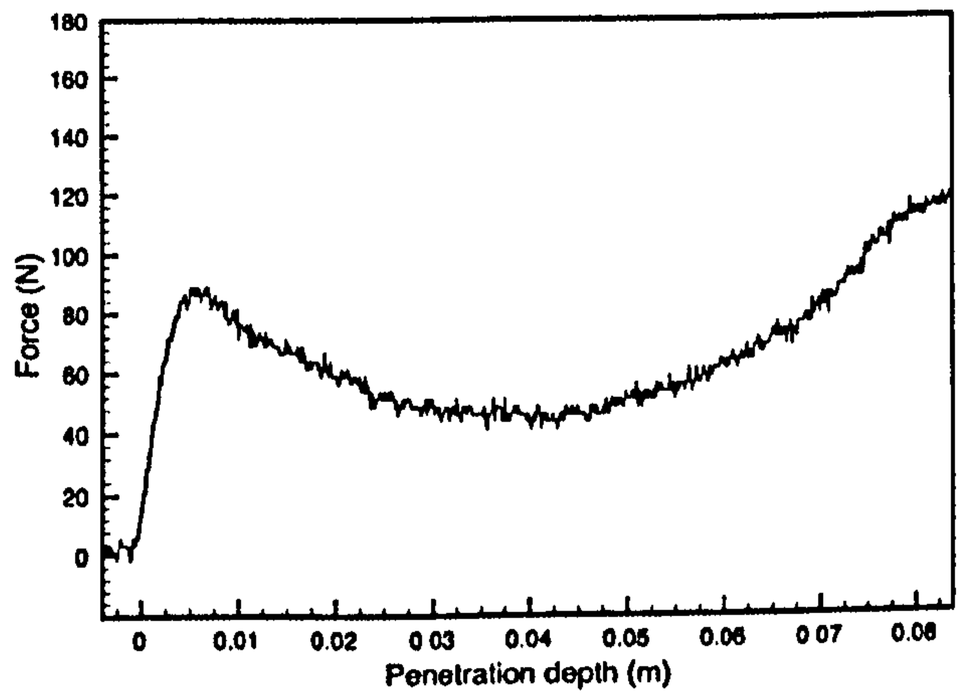
Force (N)
Penetration depth (m)

(f)

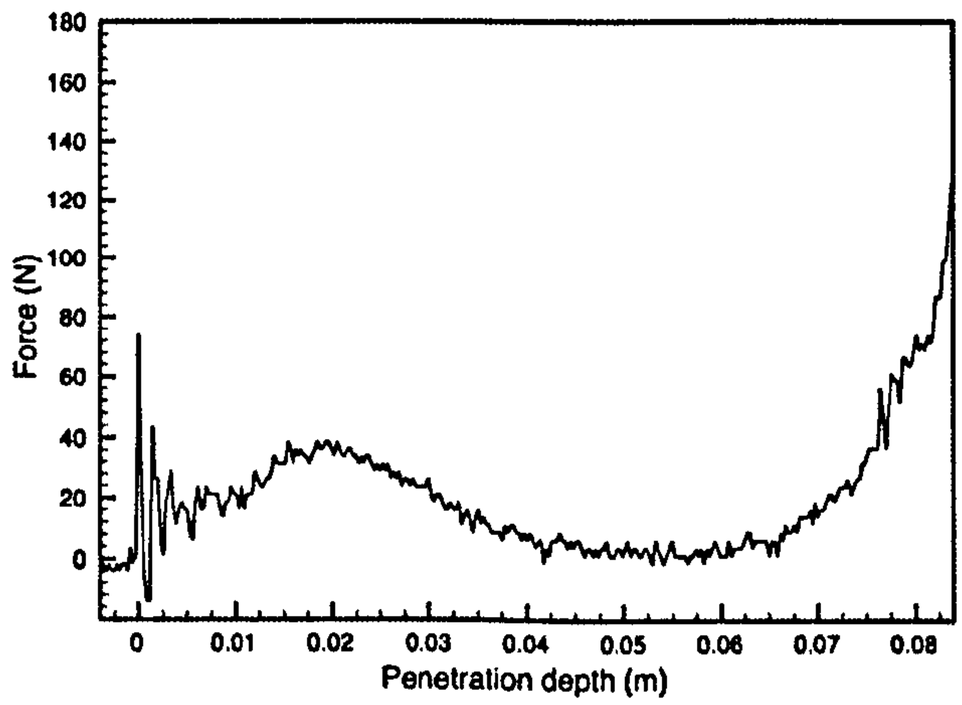
Force (N)
Penetration depth (m)

(g)

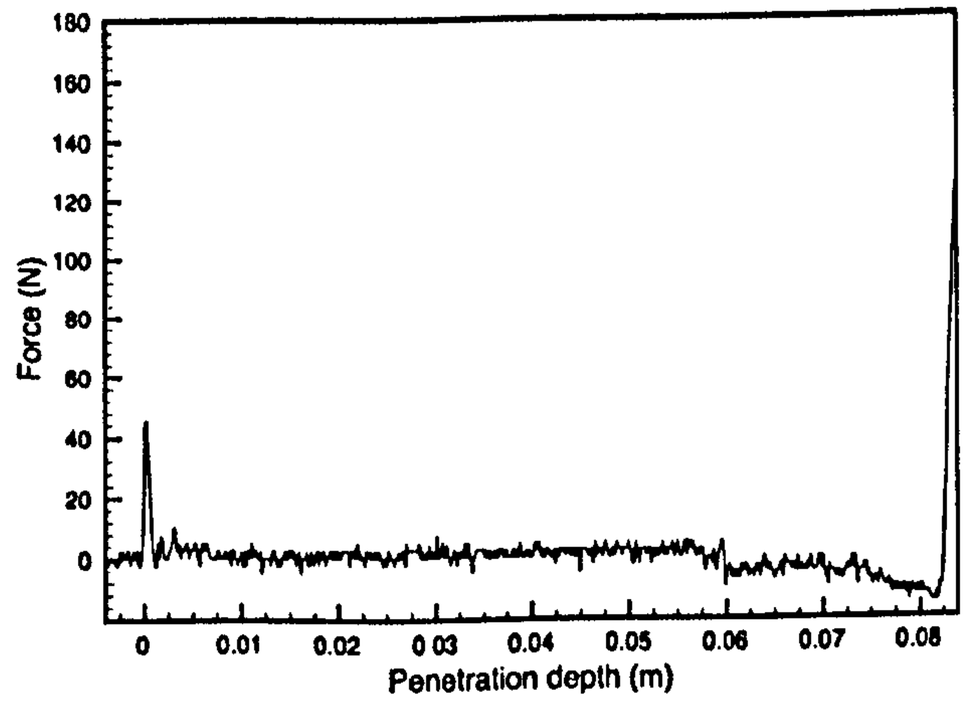
Force (N)
Penetration depth (m)

(h)

3.4 The free fall portable drop rig

3.4.1 Limitations of the original rig

The Huygens probe impacted the surface of Titan at approximately 4.6 m s^{-1}, and to represent this better, the NEO drop rig was modified to increase the speed of subsequent test drops. After removing the balancing weights from the rig design, restrictions still limited the maximum permissible speed to 3.7 m s^{-1}, significantly lower than the impact speed of the probe. The increase in speed placed further strain on the chains supporting the baseplate to which the penetrometer was attached and this, combined with the increased shock of the repeated impacts made the chains stretch. As a result they would sometimes slip off the runners adding mechanical noise to the system. Charge accumulated on the perspex safety glass surrounding the rig was also found to add electrical noise to the system despite careful screening of the charge amplifier circuit. This was confirmed by opening the perspex door, moving it away from the circuit reducing the effect. It was not possible for safety reasons to operate the rig in this configuration, making this noise difficult to reduce.

Later the rig was further modified for single user operation using a pneumatic system that allowed the door locking pins to be withdrawn while also holding the baseplate winding mechanism that controlled the release of the drop. This system proved to be impractical as the winding mechanism could be accidentally released prematurely while trying to operate the pneumatics for the door locks. On one occasion, the pneumatics failed to withdraw fully one of the locking pins such that the baseplate impacted the semi-withdrawn pin requiring extensive repairs that put the rig out of action for a number of days.

3.4.2 Free fall drop rig development

A new drop rig was constructed to overcome the NEO rig limitations. It was designed from the outset to be a lightweight portable unit, allowing it to be used both in the laboratory and for fieldwork, enabling comparative penetrometry of natural terrestrial surfaces. This is shown in Figure 3.4. A free drop principle is used, with the penetrometer attached to a weight held in place by a 12V d.c. electromagnet. By gradually reducing the current applied to the electromagnet, the penetrometer and weight are released without any tilt, vibration or dragging that might be present if dropped manually.

The basic rig construction comprises of a tripod and post of aluminium beams that can be easily dismantled. Rigging cables with tensioners are attached between the legs and post to add structural rigidity and minimise vibration prior to the release of the penetrometer. A short horizontal arm to which the electromagnet is attached, has a spirit level to ensure that the penetrometer is not tilted at an angle when released. Levelling is facilitated by the use of adjustable rubber feet on two of the supporting legs. The arm holding the penetrometer is located in a channel in the post and is completely adjustable over a range of drop heights producing variable impact speeds. The dropping weight consists of a steel cylinder to which an aluminium tail with mirror (discussed later) is attached. The low centre of mass ensures that the penetrometer impacts the target normal to the surface. At the top end of the tail, a shaped steel plug keys the weight into the electromagnet and ensures the correct orientation of the mirror. Initial drop tests showed that the residual magnetism of the electromagnet after switching off was too strong and the penetrometer weight failed to release. To solve this, a thin layer of adhesive aluminium foil was stuck to the steel plug, reducing the effect of the remanent magnetism.

To find the drop height necessary to reach the impact speed of the Huygens probe, an equating of the gravitational potential energy of the penetrometer weight assembly before the drop and its kinetic energy on impact can be used:

$$\frac{1}{2}mv^2 = mgh$$

(Equation 3.2)

This gives an expression relating the drop height to impact velocity,

$$h = \frac{v^2}{2g}$$

(Equation 3.3)

The drag of the penetrometer weight assembly is assumed to be negligible in the above calculation.

The penetrometer drop weight was machined to contain two small 'pockets' one immediately above the penetrometer fixing location and the other at the top of the weight just below the connecting point of the aluminium tail. The intention was to allow the ACC-I accelerometer to be fixed inside one of these pockets and provide an acceleration record. By integrating this record, the velocity and depth penetrated at a given instant could be determined. This was also intended to provide an insight into the response of ACC-I to various test materials which could provide a further constraint of the surface analogue material. Several drops were carried out into various target materials with an Endevco-2271 accelerometer fixed rigidly inside the weight assembly with epoxy resin. The response of the accelerometer was found to be disappointingly insensitive particularly with softer targets and there was a considerable lag between the entry of the penetrometer and the detection of the impact by the accelerometer. The additional cable needed between the falling penetrometer and the electronics box also tended to apply a small torque to the falling assembly so that the impact of the penetrometer normal with the target surface was uncertain.

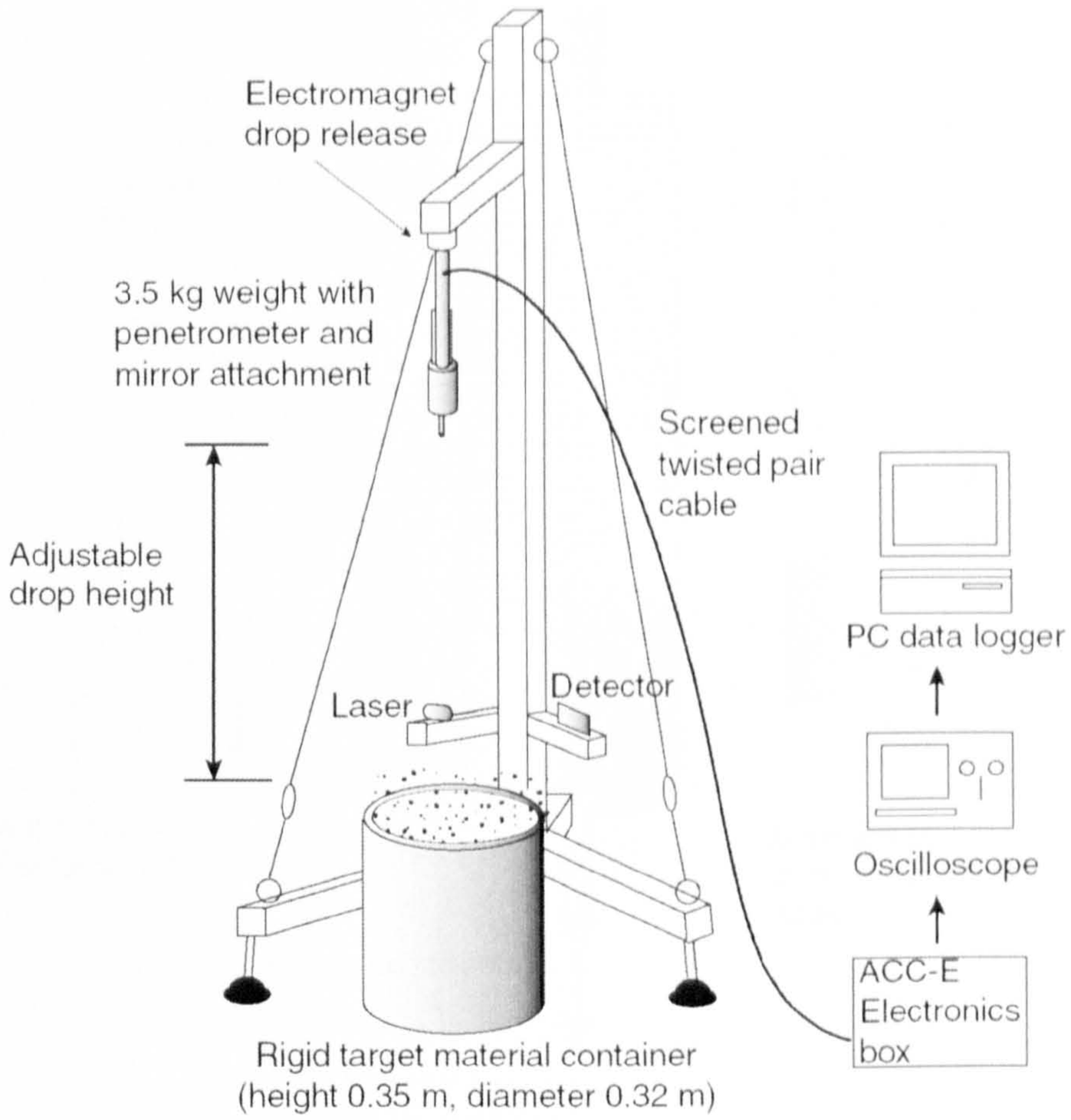

Figure 3.4 Free fall drop rig and data acquisition equipment.

This led to the development of a laser based velocity measurement system to replace the accelerometer which had the advantage of requiring no additional cabling to be attached to the falling penetrometer. Similar systems have been used before with good results (Anderson *et al.*, 1996; Liu and Ahrens, 1999). It consists of a laser beam which reflects off a polished stainless steel mirror onto a detector (Figure 3.5). By machining thin strips into the mirror, a 'barcode' of equally spaced reflective and non-reflective strips was made. As the penetrometer assembly falls past the laser, the beam is reflected into the detector strip or it is dispersed. This results in a series of light pulses (Figure 3.6), allowing the velocity and depth of the penetration to be determined as the penetrometer enters the target material. The detector has three light sensitive photodiode arrays fixed in the same plane as the laser. This arrangement allows slight horizontal rotations in the mirror without affecting the beam detection.

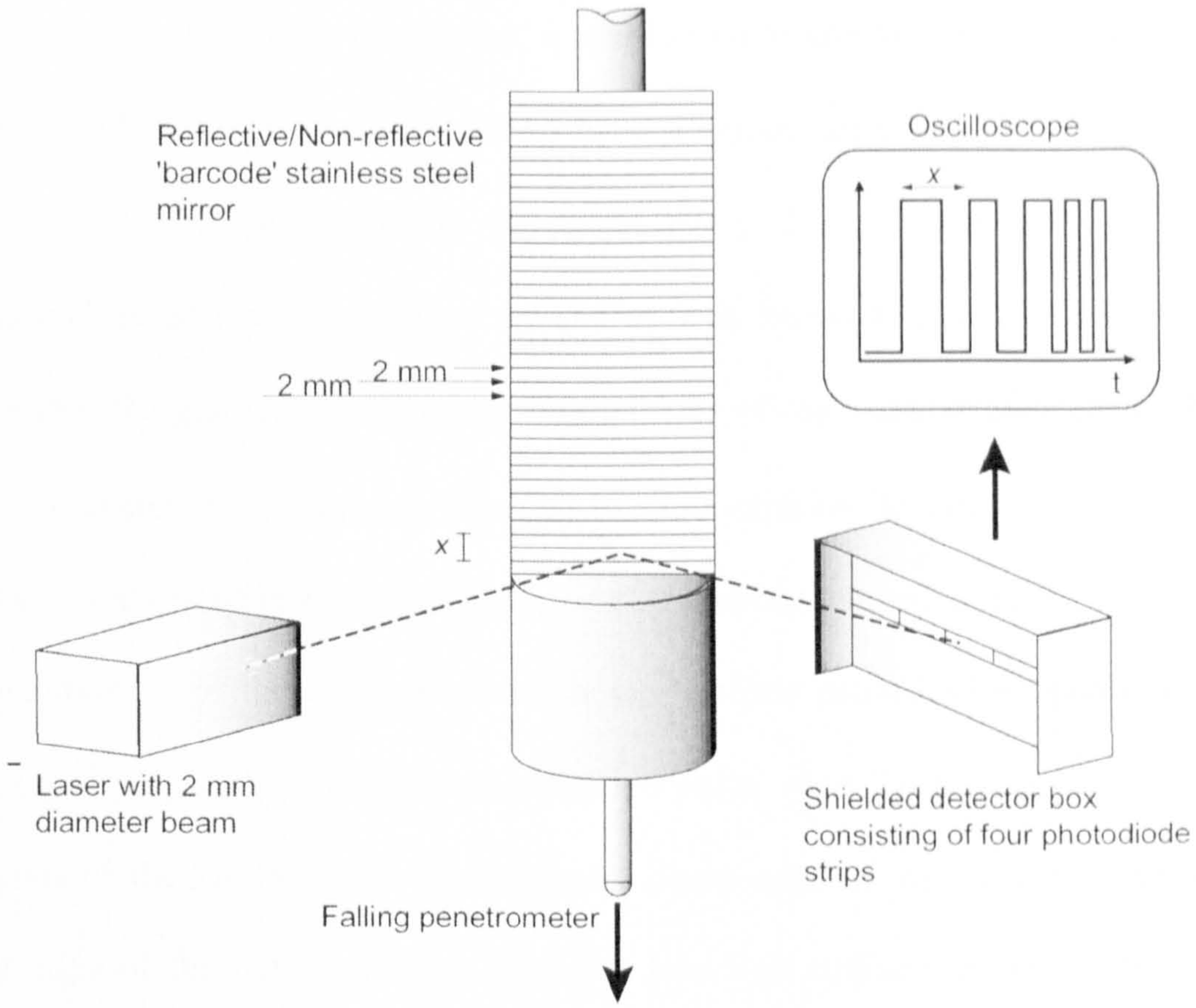

Figure 3.5 Arrangement of the laser system used to measure the penetrometer velocity. A narrow laser beam is reflected off a barcode-striped mirror into a detector box as the penetrometer falls, generating a series of light pulses.

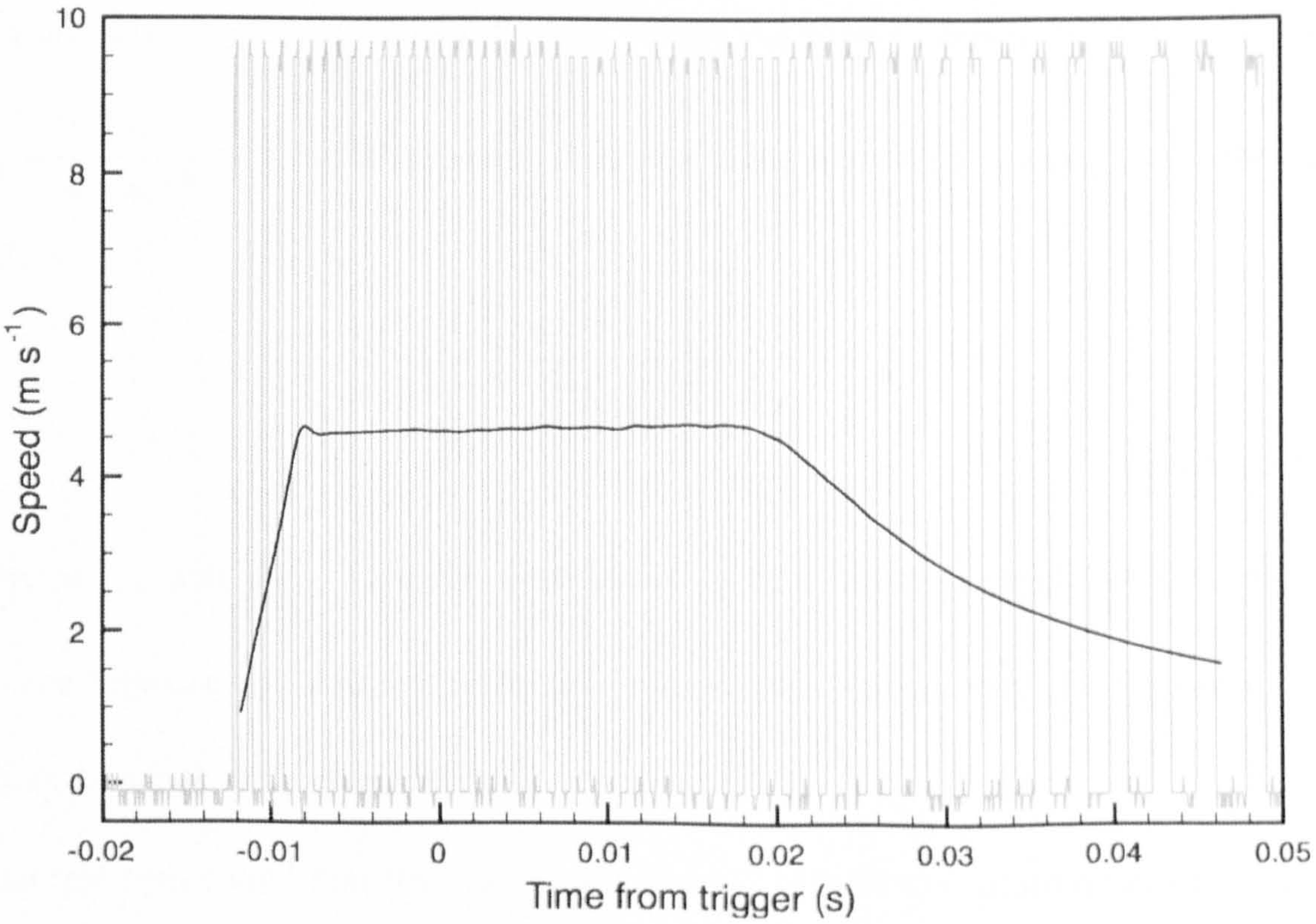

Figure 3.6 Example pulses from laser system and resulting speed measurement.

In order to produce a sharp laser point, a small circular aperture was machined into the laser holder. The mirror was intended to have a narrow strip width of 1 mm allowing regular velocity measurements to be made every 2 mm cycle during the target penetration. Initial tests found that the sensor was insensitive to this small diameter beam width. By gradually increasing the diameter of the circular aperture in the laser holder a diameter of 1.6 mm was found to be the minimum diameter to allow sufficient intensity of light to be reflected off the mirror, triggering the sensor cells.

The manufacture of the grooved stainless steel mirror proved to be problematic; the initial, equally spaced reflective/non-reflective strips were hard to produce due to the limitations of the cutting tool. It could cut a sharp edge on one side but the adjacent leading edge of the next reflective strip was less well defined; however, the distance between the sharp edges was accurately machined to be 4.00±0.02 mm. With an oscilloscope sampling rate of 100 kHz, this gives a combined uncertainty between the start of one bright pulse ('on' state) and the next cycle as $t_{cycle} \pm 0.00001$ seconds. Thus for a nominal impact speed of 4.6 m s^{-1}, where the time to travel the 4 mm distance is $t_{cycle} = \frac{0.004\ m}{4.6\ ms^{-1}}$ or 8.7×10^{-4} seconds, the error in the measured velocity Δv, is then given by:

$$\Delta v = v\sqrt{\left(\frac{\Delta t_{cycle}}{t_{cycle}}\right)^2 + \left(\frac{\Delta x_{cycle}}{x_{cycle}}\right)^2} \qquad \textbf{(Equation 3.4)}$$

where Δt_{cycle} and Δx_{cycle} are the uncertainty in time between bright pulses and in the distance between two adjacent reflective mirror strips respectively. This gives a velocity with an absolute error of ±0.06 m s^{-1}.

Initial test runs found that the laser system would sometimes record an erroneous signal prior to the mirror's arrival at the laser. It was found that natural light from skylights

located some distance away was being detected. Attaching a metal hood to the detector box removed this source. Ideally the signal pulse should be close to a square wave, as this ensures the minimum uncertainty in the timing of each pulse. On some drops, pulses were significantly reduced in height or they were missing altogether. This was traced to differing sensitivities between the photodiode arrays. A light pulse falling on one detector might be correctly detected but a later pulse on an adjacent low sensitivity photovoltaic cell would not. By fitting variable resistors to each detector, the sensitivity of each cell could be adjusted. This was a compromise; reduced resistance increased the sensitivity of the cells but the circuit became slower such that the square pulses became truncated.

3.4.3 Rig electrical noise

Transducer charge amplifier circuits are extremely sensitive to electrical interference particularly between the crystal, which generates the signal charge, and the charge amplifier, which converts this charge into a voltage. Stray electrical noise in the laboratory will therefore affect any measurements made with the penetrometer. In comparison to the probe where the electronics and sensor are connected by a short fixed wiring the laboratory wire is longer as it needs to move as the penetrometer falls. Standard coaxial cable is generally unsuitable for this task as the moving cable flexes generating significant unwanted triboelectric charge that cannot be separated from the signal (see e.g. Kaiser (2007)). A minimal length of screened twisted pair cable was therefore used to help screen the circuit and was routed away from other power cables (Bentley, 1983).

Ideally, when there is no force applied to the tip, such as when the penetrometer is at rest or falling through the air, there is no signal and there should be no detected noise. In practice noise was detected as the penetrometer assembly was falling prior to target impact. Possible noise sources were removed or switched off. Further noise reductions were made by replacing connections with shielded audio jacks; however the noise level was still found to vary between the same experiment carried out on different days. In order to compare these laboratory drops to each other, a measure of the noise present on the signal was required and this was given by examining the standard deviation of the penetrometer signal as it falls immediately prior to impact into a target.

The noise on the flight data is however difficult to quantify. The preimpact signature showed 64 zero-force data points by design (Lorenz *et al.*, 1994) before the low rising force considered to be the start of penetration. However, it is certain that due to the shorter, fixed wiring and better screening noise levels were considerably lower, probably only occupying the first ADC bit level (equivalent to a force of 2 N at Titan surface temperature). Noise is also an important consideration when comparing the laboratory results to the flight signature as it puts an upper limit on the sensitivity of the penetrometer to detect finer granular materials, where care must be taken to study only features that are due to the material and not spurious noise.

3.5 Sensor calibration

The ACC-E penetrometer's piezoelectric crystal transducer generates an electrical charge in response to a force applied to the penetrometer tip. This charge leaks away quickly so it is not possible to calibrate the crystal by applying static loads, a known dynamic force must be used instead (Zarnecki *et al.*, 1997). According to the National Physical Laboratory there are currently no satisfactory standards for the calibration of

dynamic force transducers of this kind (National Physical Laboratory, 2008):

"There are very few sources of traceable dynamic force calibration – and certainly none in the force and frequency ranges measured by the majority of commercially available dynamic force transducers. In the absence of suitable standards and procedures, the statically-derived force transducer sensitivities are generally assumed to be applicable to dynamic force measurements, perhaps after modification to take account of a theoretical model."

The original ACC-E flight model (FM) and flight spare (FS) penetrometers were calibrated using a method developed to apply a known dynamic force to the penetrometer tip (Lorenz *et al.*, 1999). A small pendulum jig was used to hit the fixed sensor tip assembly with impactors made from synthetic rubber for soft impacts and teflon (PTFE) for harder ones. The two impactors of known mass were dropped from different heights onto the tip assembly. From energy considerations the impact velocity could be determined. Assuming a perfectly elastic impact, the resulting force pulse has a roughly sinusoidal shape and can be approximately described by Hertz' law of contact which gives a theoretical expression for a hemisphere hitting a semi-infinite plane (McCarty, 1962). The peak magnitude of this pulse is proportional to $m^{0.6}E^{0.4}V^{1.2}$, where m is the mass of the impactor, E is the Young's modulus of the impactor and V is the impact velocity (SSP, 1995). In order to examine the change in sensitivity of the PZT crystal with temperature, impacts were also carried out after cooling the sensor assembly down using liquid nitrogen. The calculation of the absolute value of the force generated in this way suffered from the uncertainty in the value of the Young's modulus of the impactor. These values were estimated using literature values and by comparing impact profiles of computer simulations with jig impacts. The absolute calibration was believed to be accurate to ~5% (Lorenz, 1994a; Willet, 1994).

The difficulty of accurately determining the Young's modulus of suitable impactors together with the assumption of a perfectly elastic impact led the author to consider other possible methods of calibrating the laboratory penetrometer. This led to a modified calibration method based on one using a mass moving on a frictionless horizontal linear bearing colliding with the force transducer (Fujii, 2006; Fujii and Fujimoto, 1999). The original method uses an optical interferometer to determine accurately the change in momentum of the moving mass in the collision. This change is equal in magnitude to the time integrated impulse acting on the force transducer using the law of conservation of momentum. By replacing the interferometer with a suitable accelerometer, the acceleration and therefore force of the impacting mass of known size could be determined directly.

An air track was constructed using a one metre length of square plastic down pipe drilled with a series of 1 cm separated 0.9 mm diameter holes on two adjacent sides. The impacting trolley was made using a small piece of polished stainless steel bent at right angles to sit on the track. A horizontal table was mounted to the apex of the steel sliding plate to which the accelerometer electronics and different impact materials could be attached. The penetrometer was mounted to one end of the track and positioned so that the impact occurred close to the centre of mass of the trolley ensuring that rotational moments caused by the impact were minimised. An industrial vacuum cleaner was used to provide the air supply that was forced out through the small holes enabling horizontal linear motion of the trolley with minimal friction and controlled 'head on' impacts. The arrangement is shown in Figure 3.7.

An Analog Devices ADXL321 dual-axis accelerometer was used to measure the

acceleration of the trolley on impact. This small, lightweight accelerometer has a full-scale range of ±18g with good sensitivity and adjustable bandwidth and can measure both dynamic accelerations (such as vibration) and static acceleration (gravity).

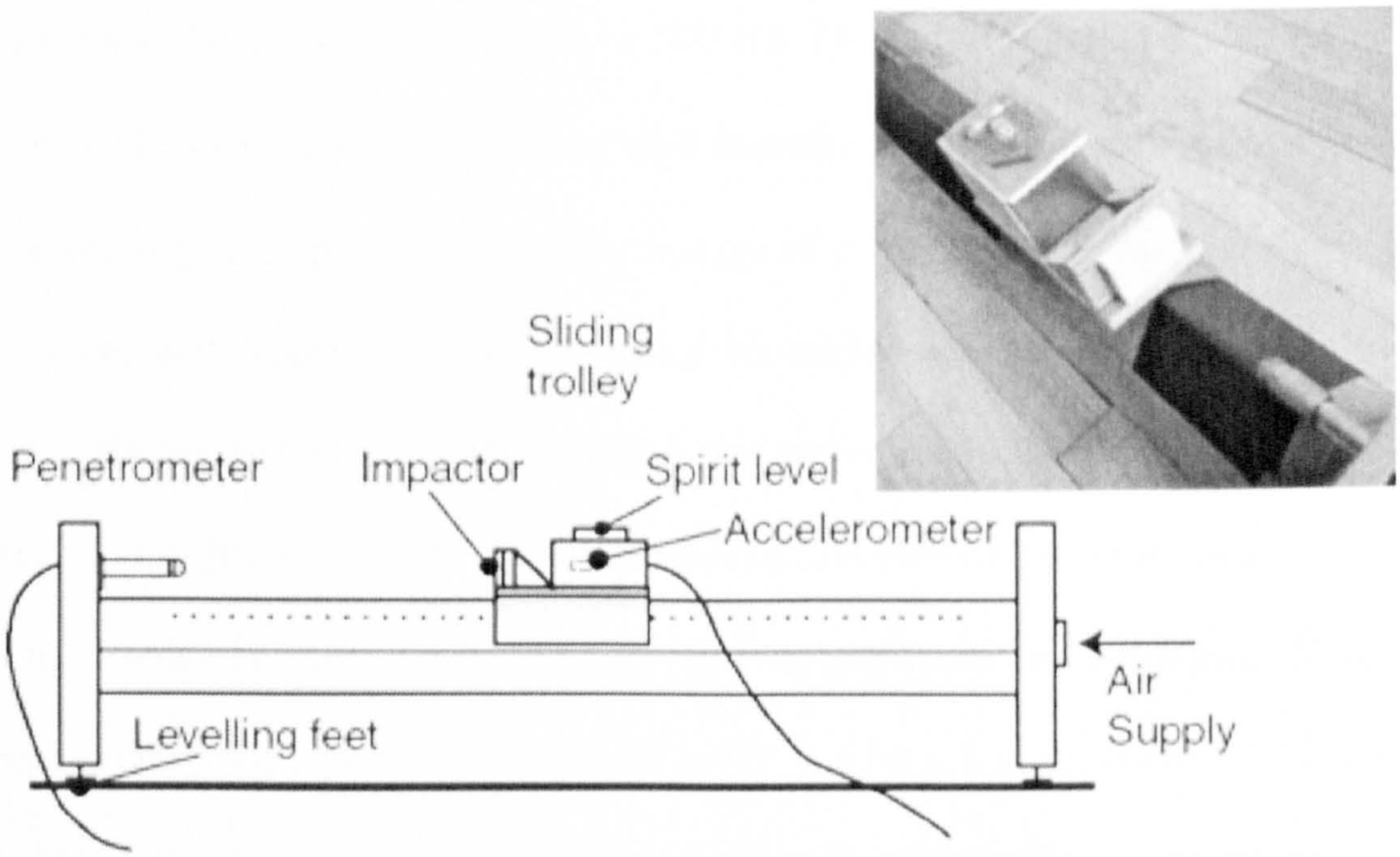

Figure 3.7 Diagram of the air track used to calibrate the penetrometer. The trolley slides horizontally along the levelled air track and impacts the penetrometer tip. The acceleration of the impactor is measured by the accelerometer and used to determine the peak dynamic force experienced by the crystal. Inset: sliding trolley before impact with penetrometer (on lower right).

It consists of a small micromachined structure built on top of a silicon wafer that deflects when experiencing accelerations. A differential capacitor formed between this structure and two fixed plates produces a capacitance proportional to acceleration experienced. The bandwidth of the accelerometer is controlled by a small capacitor on both the X and Y direction output pins. These capacitors determine both the maximum frequency of acceleration/vibration that can be measured and also the measurement resolution of the accelerometer. Due to the extremely small size of the accelerometer package (4 mm x 4 mm) and contacts, a pre-soldered accelerometer breakout board was acquired. This board came with 0.1 μF capacitors setting the bandwidth of the accelerometer to 50 Hz, too slow for the impacts considered. The bandwidth is set by

these capacitors according to the equation:

$$F = 1/(2\pi(32k\Omega) \times C_{(X,Y)}) \qquad \textbf{(Equation 3.5)}$$

The small capacitor on the X-axis circuit was carefully removed and replaced with a 0.01 μF capacitor giving a bandwidth of 500 Hz. The oscilloscope sampling rate of 100 kHz ensured this bandwidth would be well sampled with no aliasing problems. A 9 V battery and regulator provided a supply voltage of 3 V to the chip and the circuit board was rigidly attached to the trolley using mounting spacers (Figure 3.8). Prior to attaching the accelerometer to the trolley it was calibrated to determine the zero g offset and sensitivity. By holding the X-axis horizontal and then orienting it towards and away from the Earth's surface, the 0*g*, 1*g* and -1*g* voltages could be determined. From this, the zero *g* offset voltage was found to be 1.421 V with a 1 *g* sensitivity of 62 mV. The 9-bit ADC resolution of the oscilloscope limits the measurable acceleration to ~1/6*g*. For a sliding ~0.5 kg trolley this would still give a satisfactory dynamic force resolution to the nearest one Newton with a maximum measurable force of ~80 N using the given accelerometer. While this is not the entire range of the penetrometer, it would cover the majority of the well-resolved high gain branch used in laboratory penetrations and the Huygens probe impact on Titan.

The trolley was set in motion by manually pushing it along the air track until the front 'impact face' collided with the penetrometer reversing the trolley's direction of motion. The resulting short impulses from the accelerometer and penetrometer were recorded on different channels of the oscilloscope. The peak acceleration measured corresponds to the maximum force exerted on the trolley by the penetrometer tip (and by Newton's third law of motion, also the largest force exerted by the trolley on the penetrometer tip).

Several impact materials were tested including two hard foams and a soft rubber. These different impact surfaces changed the shape of the voltage impulse produced by the penetrometer. The rubber impactor allowed a wide range of accelerations to be produced with a well defined impact curve and good repeatability and was therefore used for all subsequent measurements. A program was written (cal.m- see appendix A) to find the peak ACC-E and accelerometer voltages and to calculate the force imparted by the trolley using the accelerometer. This was compared to the original SSP 'whole-chain' calibration (i.e. including the filter and amplification stages of the electronics).

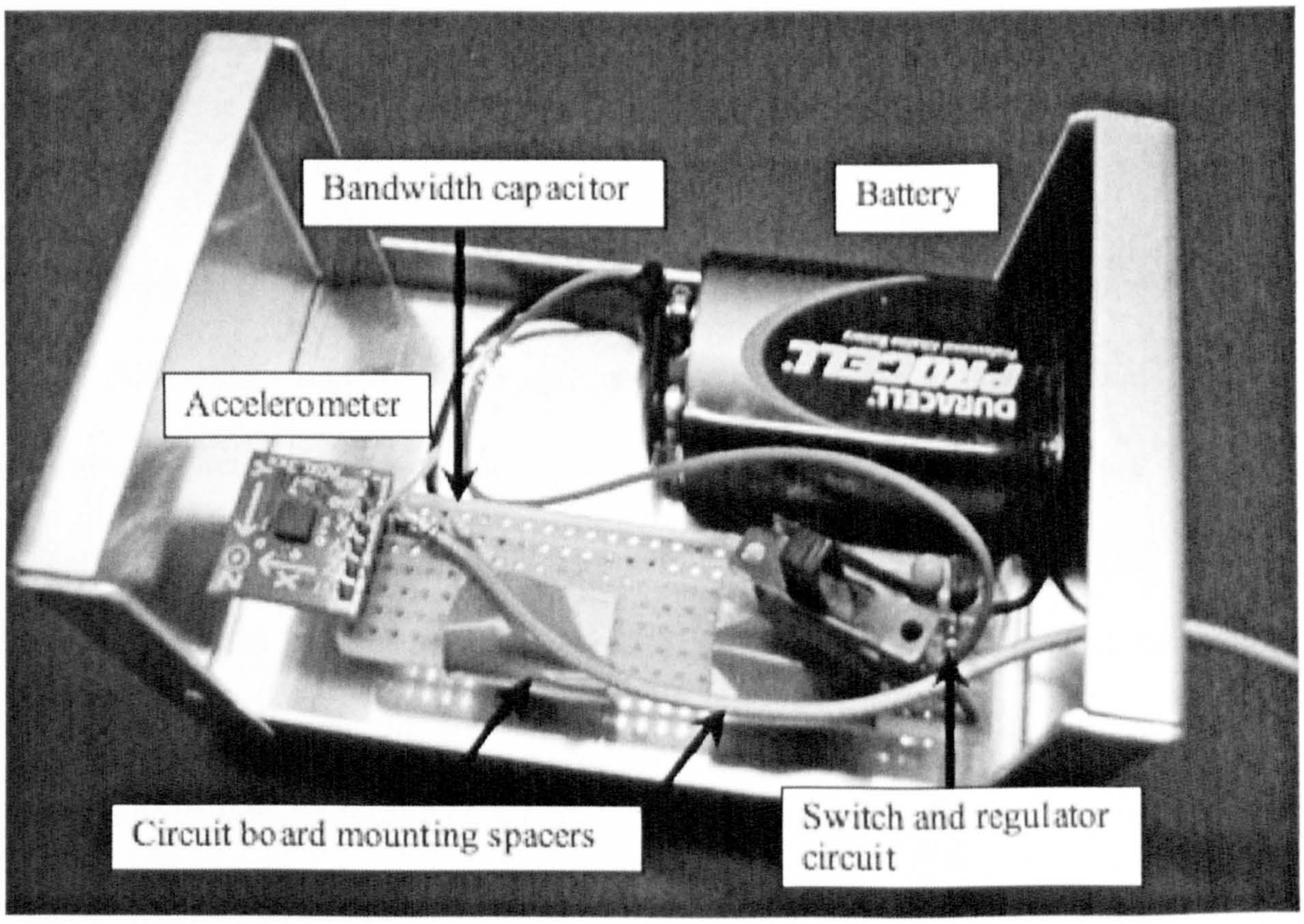

Figure 3.8 Electronics box showing the accelerometer and conditioning electronics.

The initial impact tests with a 0.418 kg trolley also indicated that the track still had significant friction leading to inconsistent results. The vacuum cleaner was replaced with an industrial compressor but even this proved insufficient. By reducing the mass of

the trolley by 105 grams, friction between trolley and track was removed. This however reduced the maximum force that could be measured given the range of the accelerometer. The graph in Figure 3.9 shows the measured voltages produced by a series of impacts of the trolley. This shows that the PZT crystal in the laboratory penetrometer differs from the SSP Flight Spare penetrometer calibration (shown at room temperature and Titan temperature for comparison) although the response in all cases is linear. The difference is most probably due to variations in individual piezoelectric crystals and small differences in the assembly of the penetrometer tip. Examination of data of the responses of the FS and FM[1] PZT crystals indicates a difference of 15-20% in their sensitivities, within the manufacturers specification (SSP, 1995).

This method of calibration has limitations on the range of forces that can be tested, but Figure 3.9 implies that this technique is adequate for the purpose of calibrating the laboratory penetrometer although improvements in the rigidity of the track, a stronger air supply to lift a larger mass and a larger range accelerometer would allow greater dynamic forces to be tested. It is hard to quantify the degree of friction between the track and the trolley as the air escaping from the holes along the track would have different pressures depending on the proximity of the holes to the input air supply.

---

[1] The Flight Spare (FS) penetrometer, an identical replacement penetrometer, was used instead of the Flight Model (FM) penetrometer due to accidental damage on the latter shortly before launch.

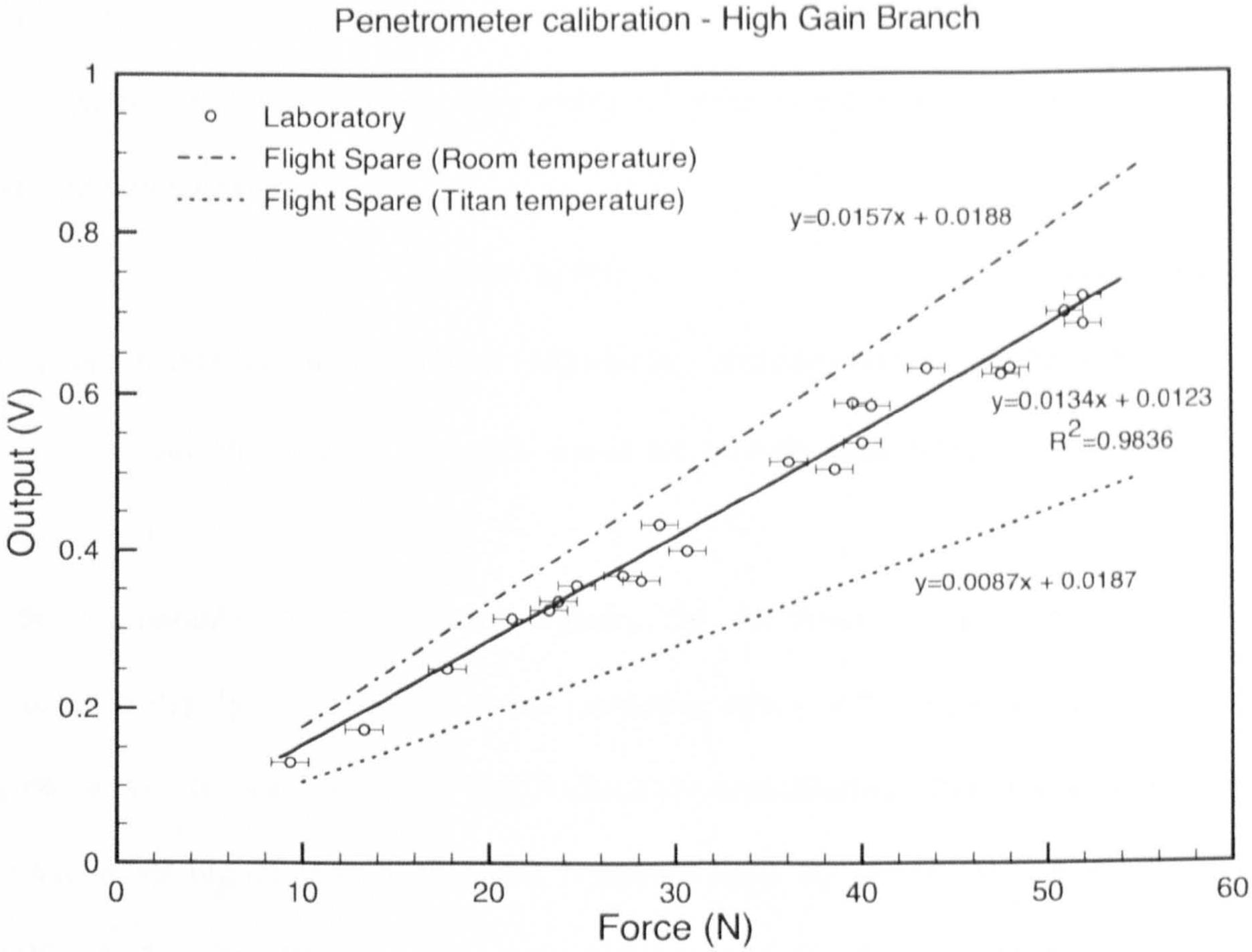

Figure 3.9 Calibration graph for the laboratory penetrometer on the lower section of the High Gain branch of the pseudo logarithmic amplifier. The original FS calibrations carried out by the SSP team are shown for comparison.

3.6 Sampling rates

Sampling rate is an important factor in the design of any dynamic penetrometer. If a sensor is sampled at too low a rate, important information regarding the measurement is lost. In practice, sampling at the Nyquist rate of exactly twice the highest frequency may also be too low and often higher rates are used (Griffen and French, 2004). Oversampling requires increased mass and power resources for processing, storing and transmitting data- both costly commodities in any spacecraft design.

The intention was to examine how the information content of the penetrometry signal varies for different sampling rates. In the laboratory, data were acquired by a Tectronix TDS3014 oscilloscope sampling at 100 kHz, ten times the rate used on the Huygens

probe. These oscilloscope data $x(n)$ can be downsampled by an integer factor, m, in a process called decimation where only every m^{th} point is collected to produce the new downsampled signal $y_m(n)$:

$$y_m(n) = x(mn) \qquad \text{(Equation 3.6)}$$

This process can be done without introducing aliasing errors, as the information contained within the original analogue signal has already been bandlimited (Mitra and Kaiser, 1993).

To be comparable to the onboard signals, the oscilloscope signal needed to be decimated by an integer factor $m = 10$, collecting every 10^{th} sampling point from the original signal. It should be noted that because the anti-aliasing filter sharply attenuates all frequencies higher than 5 kHz (the Nyquist frequency of the ACC-E electronics) sampling higher than 10 kHz will contain no extra 'real' frequency content.

3.7 Data processing and correction

Prior to this analysis, all penetrometry signatures were processed to account for the effects of the anti-aliasing filter. The penetrometer backed by the ~200 kg probe and falling at terminal velocity under parachutes, would have penetrated the surface of Titan at a nearly constant velocity. In the laboratory the penetrometer and mass are falling under gravity such that their velocity is still increasing as the penetrometer enters the target material. Using the laser derived velocity the penetrometry signatures were adjusted to account for the affects of acceleration due to gravity. A program was written using Octave, an open source version of MATLAB, to process the data before analysis. Laboratory data files recorded by the oscilloscope are read in, corrected and new output files are written for each signature. An overview of the data_c.m program flow is shown in Figure 3.10.

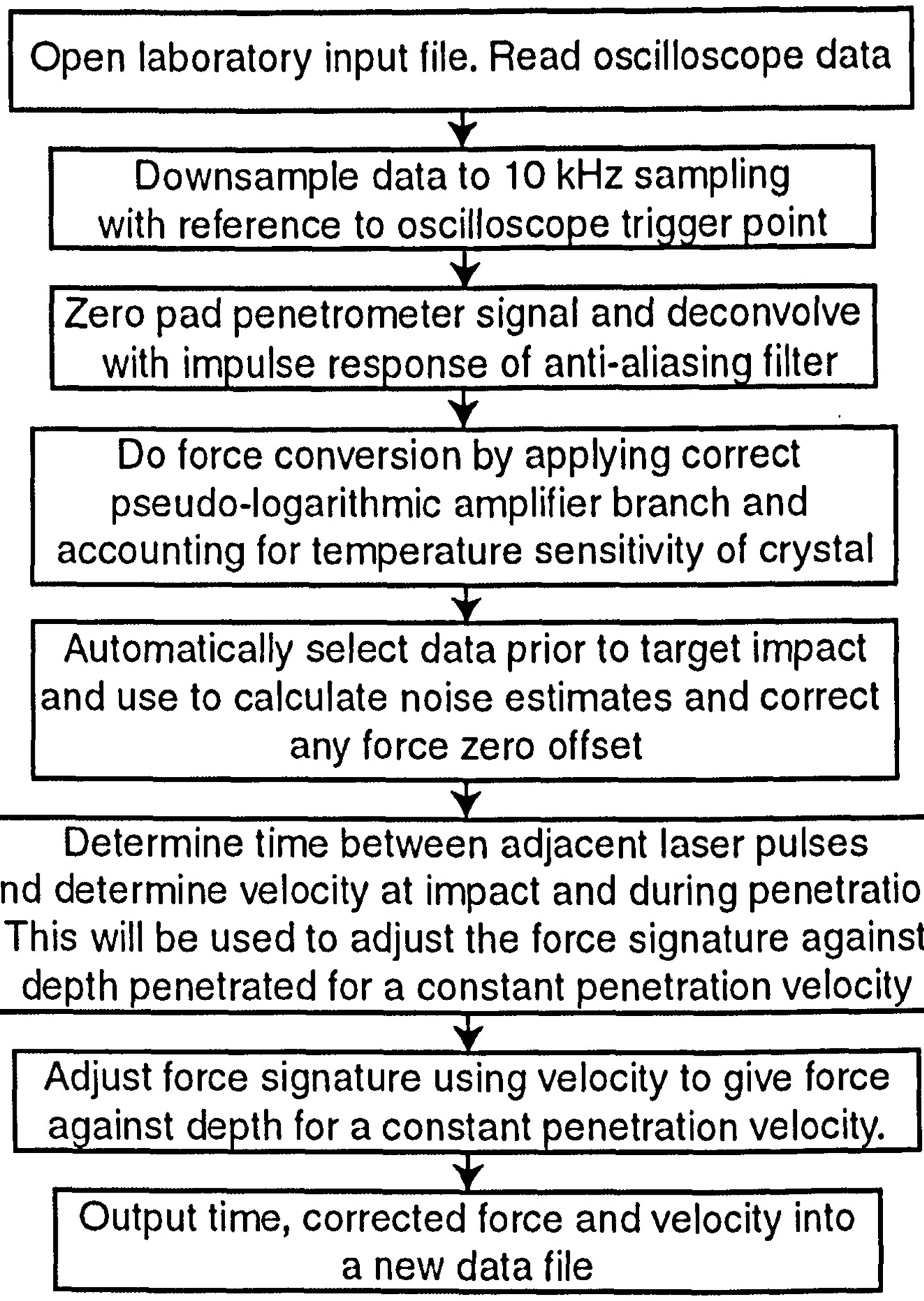

Figure 3.10 Flow diagram of program data_c.m used to process laboratory data.

3.8 Target material characterization

Before valid penetrometry can be carried out, target materials need to be carefully characterized. The following sections describe the methods used.

3.8.1 Grain size analysis

The Udden-Wentworth scale is widely used for grain size classification (Wentworth, 1922). It covers the range from fine clay (0.06 μm) up to boulders of (4096 mm) as shown in Figure 3.11.

	Wentworth class	Diameter (mm)	Phi units
Gravel	Boulder	4096	
		256	-8
	Cobble		
		64	-6
	Pebble		
		4	-2
	Granule		
		2.00	-1
Sand	Very coarse		
		1.00	0
	Coarse		
		0.50	1
	Medium		
		0.25	2
	Fine		
		0.125	3
	Very fine		
		0.0625	4
Silt	Coarse		
		0.031	5
	Medium		
		0.0156	6
	Fine		
		0.0078	7
	Very fine		
		0.0039	8
Mud	Clay		
		0.00006	

Figure 3.11 Udden-Wentworth grain size classification scale (after Wentworth, 1922). Grain diameters are given in millimetres and their equivalent logarithmic phi units, ϕ, commonly used sedimentology. Phi units are related to the Wentworth size scale by the relationship: $\phi=-\log_2 D$ where D is the diameter in millimetres.

Granular materials were characterised for particle diameter by sieving a small representative sample using a nested set of sieves covering the range from the coarsest grains to particles less than 125 μm according to the following procedure (Lambe, 1951). The sample was first dried by baking in an oven overnight and then weighed using an electronic pan balance and this dry sample weight was recorded. The sample was then poured into the top of the sieve stack with a collection pan at the bottom. The sieves were then shaken by hand for a several minutes and the fraction retained in each sieve was weighed, labelled and bagged. Any grains stuck in the sieve were carefully

brushed out and added to the collected fraction. This was repeated for all sieves. The final fraction collected in the bottom pan was all grains finer than 125 μm. The accumulated weights of each fraction were then entered into the grain size and distribution program GRADISTAT (Blott and Pye, 2001) which was used to calculate sample statistics.

3.8.2 Bulk density

The bulk density of the target material, ρ_{bulk}, is the ratio of the total mass, M_{total}, to the total volume, V_{total}, and includes voids between grains if they exist (Craig, 1997):

$$\rho_{bullk} = \frac{M_{total}}{V_{total}} \qquad \textbf{(Equation 3.7)}$$

3.8.3 Particle density

Particle density measures the density of the material from which the grains of the target are composed. In the case of inhomogeneous natural materials such as gravels, it is the average density of the grain material. Particle density is defined as the mass per unit volume of a particle,

$$\rho_{particle} = \frac{M_{particle}}{V_{particle}} \qquad \textbf{(Equation 3.8)}$$

Here the mass can be determined by weighing the material, leaving only the volume of the particles to be determined. The volume of natural materials such as gravel, which are irregular in shape and may contain small pores in the form of fractures, can be determined by measuring the volume of water displaced when the grains are added. This is done using a container of known volume called a pycnometer. In the absence of an available pycnometer, a measuring cylinder with a volume of 100 ml with 1 ml

gradations was used. The empty measuring cylinder was weighed and filled with 50 ml of distilled water. An oven dry sample of the test material was weighed and then placed in the cylinder which was gently agitated by tapping it for a few minutes to minimise the amount of air trapped between the particles. The cylinder was then further filled to the 100 ml mark using a squirt bottle to wash down any sample stuck to the walls. The cylinder was then reweighed and the differences in masses together with the known density of water at room temperature allowed the volume of water and hence the particle volume to be calculated. The solid density was then calculated as:

$$\rho_{solid} = \frac{M_{solid}}{100 - (M_{total} - M_{solid} - M_{cylinder})\rho_{water}} \qquad \textbf{(Equation 3.9)}$$

where M_{total} is the mass of cylinder $(M_{cylinder})$, solid material (M_{solid}) and water up to the 100 ml mark and ρ_{water} is the density of water at room temperature, 0.998 g cm^{-3}. A similar method is described in Lewis (1984).

It should be noted that tiny pockets of air that remain trapped in grain pores affect the accuracy of the volume measurements. These can be reduced by boiling the sample and water before adding further water to make the mixture up to the 100 ml mark; however given the limited accuracy of the available measuring cylinder, this further step is unnecessary for the accuracy required.

3.8.4 Porosity

If the bulk density, ρ, and particle density, $\rho_{particle}$, of a target material are known, it is possible to determine the total pore space contained in the target material:

$$\text{Porosity } (\%) = \left(1 - \frac{\rho}{\rho_{particle}}\right) \qquad \textbf{(Equation 3.10)}$$

3.8.5 Material strength

The strength of a material refers to the limiting stress of the material at failure (the *ultimate stress state*) and affects penetration resistance (Mitchell and Soga, 2005). Stress is related to the applied force acting over a given area,

$$\text{Uniaxial stress, } \sigma = \frac{F}{A} \qquad \textbf{(Equation 3.11)}$$

and is given in pascals (Pa) or newtons per square metre (N m^{-2}). As with strength, it is considered as either compressive, shear or tensile.

Material strength in soils is complex and descriptions are therefore usually empirical. The most commonly used relationship is the Mohr-Coulomb equation that relates the shear stress at soil failure (shear strength), τ, to the normal stress on the failure plane, σ, the angle of internal friction, ϕ, and the cohesion, c (Mitchell and Soga, 2005):

$$\tau = c + \sigma \tan \phi \qquad \textbf{(Equation 3.12)}$$

The cohesion is the component of the shear strength that is independent of friction between particles and, when present, is caused by sticking of the grains. Dry sands and gravels are cohesionless materials where the angle of internal friction alone is the material property that determines failure point. The angle of internal friction (also referred to as the angle of repose) is the maximum angle at which a granular material will form a stable slope, and is dependent on several factors including the shape of the grains (Cho *et al.*, 2006). In practice, materials are often tested in a laboratory using specialised equipment to derive their strength properties. Simpler tests, such as using a pocket penetrometer to measure the unconfined compressive strength of a cohesive soil are not suited to very soft or coarse granular materials. For this reason, an alternative method of determining the approximate material strength was required. This was given by dividing the kinetic energy of a penetrometer on impact by the volume of target

material it subsequently excavates (Garry *et al.*, 1999; Lorenz and Shandera, 2002). This 'effective strength'[2] is dependent on the tip geometry with sharp cone-tipped penetrometers forming a larger cavity than a penetrometer with a hemispherical tip (Garry *et al.*, 1999). As the ACC-E penetrometer is relatively short, the attached structure impacts the surface before the penetrometer comes to rest so that measuring the volume penetrated is not possible. Instead for this work a long threaded brass rod with an ACC-E hemispherical tip attached was dropped from a known height into the target. The effective strength is then described by the following equation:

$$\text{effective strength, } \sigma\,(\text{Pa}) = \frac{m_{rod} g h_{drop}}{zA} \qquad \textbf{(Equation 3.13)}$$

where m_{rod} is the mass of the penetrating rod, h_{drop} is the drop height of the centre of mass of the rod above the target surface, z is the total depth penetrated by the rod and A is the cross-sectional area of the rod. This method has the advantages of the pocket penetrometer; it requires only simple equipment and can easily be used in the field. However, unlike the pocket penetrometer it is suitable for application to most soils, from fine clay to small and medium grained gravels. It is however only an approximate strength indicator as it does not account for how much of the kinetic energy is lost through sound, heating the target material or container wall friction. It must also be noted that a sand target confined to a container in the laboratory may give a higher strength value than equivalent unconfined sand in the field as the material is less easily displaced by the penetrometer.

---

[2] Sometimes referred to as the 'mean deviatoric stress' or 'volumetric strength'- see Garry *et al.* (1999) and Paton (2005)

3.8.6 Grain shape

The shape of individual grains within target materials is an important characteristic that is likely to affect its penetrometry signature. It might also be intuitively expected that rough, angular grains are more able to 'lock' with each other than smooth rounded ones and would therefore offer higher penetration resistance. Grain shape work carried out on sand has demonstrated that decreasing the particle regularity can increase the minimum and maximum void ratios[3] while increasing the roundness property (discussed below), has been shown to decrease the angle of repose which in turn affects the material shear strength according to Equation 3.12 (Cho *et al.*, 2006; Mitchell and Soga, 2005).

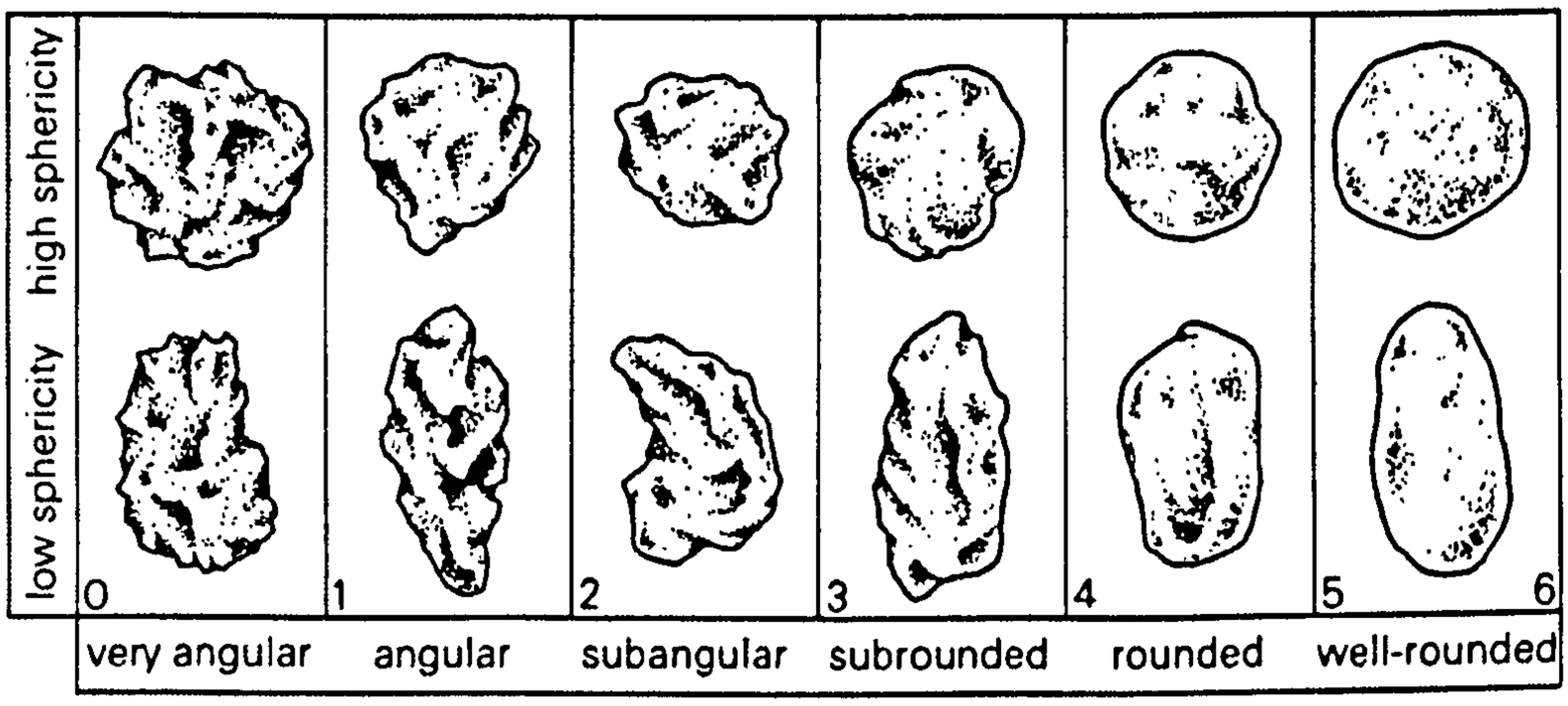

Figure 3.12 Standard grain images for estimating roundness and sphericity shape parameters. From Leeder (1982)

Grain shapes are usually described by two properties: roundness and sphericity. Roundness describes the scale of the large surface features of a grain. It is given by the ratio of the average radius of curvature of the grain corners and edges relative to the radius of the maximum sphere that can be inscribed in the particle (Cho *et al.*, 2006).

---

[3] void ratio e is the ratio of the volume of voids to the volume of solid substance in a material and is related to porosity by $n = \frac{e}{1+e}$, where n is the porosity.

Roundness is determined by the transportation history of the material. Sediments are picked up and abraded by impacts with the ground and each other as they are transported. Sharp, protruding edges are broken off so that the grains become progressively smoother the further they are transported (Nichols, 1998). Sphericity is a measure of how closely a grain approximates to a sphere and indicates the similarity of the particle's three dimensions. Formally it is defined as the ratio of the diameter of a sphere of equal volume to the particle to the diameter of the circumscribing sphere, although several other definitions exist (Mitchell and Soga, 2005). In practice, these parameters can usually be estimated using a standard set of grain images as shown in Figure 3.12.

3.9 Granular target sample preparation

The preparation of repeatable uniform density granular targets is nontrivial. One of the most common granular materials used in penetrometry investigations is sand. While it is a readily available material that can be packed to various densities, it is difficult to reproduce homogenous samples. This affects the resulting penetrometry signature which is greatly dependent on the extent of packing (Lorenz and Ball, 1999). Several methods have been used to try to produce targets with consistent packing densities including: filling the container through a central tube that is drawn upwards (Stone *et al.*, 2004), pluviating the sand or drizzling it through a sieve (Huang and Hsu, 2005; Wang, 1971) and settling by tapping the target container (Velea *et al.*, 2000).

The author experimented with various methods for producing homogenous and repeatable laboratory target samples. Natural granular materials were poured directly into the target container until full and then gently levelled off. This produced an inconsistent density. After discussions with Dr. Gunther Kargl and Alexander Zöhrer at

IWF Graz about the methods they use in quasi-static penetrometry testing, an improved method was adopted. The test sample was prepared by pouring material into the container in layers of equal mass, recording the thickness of each (see Zöhrer (2005)). This method gives an indication of the variation in density of the sample, however the final layer varies in mass for different materials. Producing this final layer of variable thickness to be comparable to the previous equal mass ones was found to be difficult especially when compacting higher density samples. It also meant that the depth of the first layer encountered by the penetrometer was arbitrary. Modifying this method to fill set volumes rather than masses removed this problem with the materials being poured to five marked levels each 70 mm apart.

Shock tamping each layer by dropping a weight from a known height onto a wooden plate was used to prepare consistent denser samples of known bulk density (Figure 3.13). Slight density variations between sample layers are unavoidable, although Figure 3.14 shows the density of cumulative layers for loose and compacted sand and indicates that the variations are small for denser targets as might be expected. The graph also shows the effects of overburden pressure when producing a loose target sample; the weight of each successive layer compacts the sand below it such that the mass of sand required to fill each 70 mm thick layer increases. The effect is less evident in the compacted sand where the sand structure is better able to support the weight of additional layers. Therefore, the production of a uniform loose sand sample is not possible. For loose targets, overburden pressure should be considered; however, as the penetrometer only measures up to 85 mm depth this effect would not be pronounced.

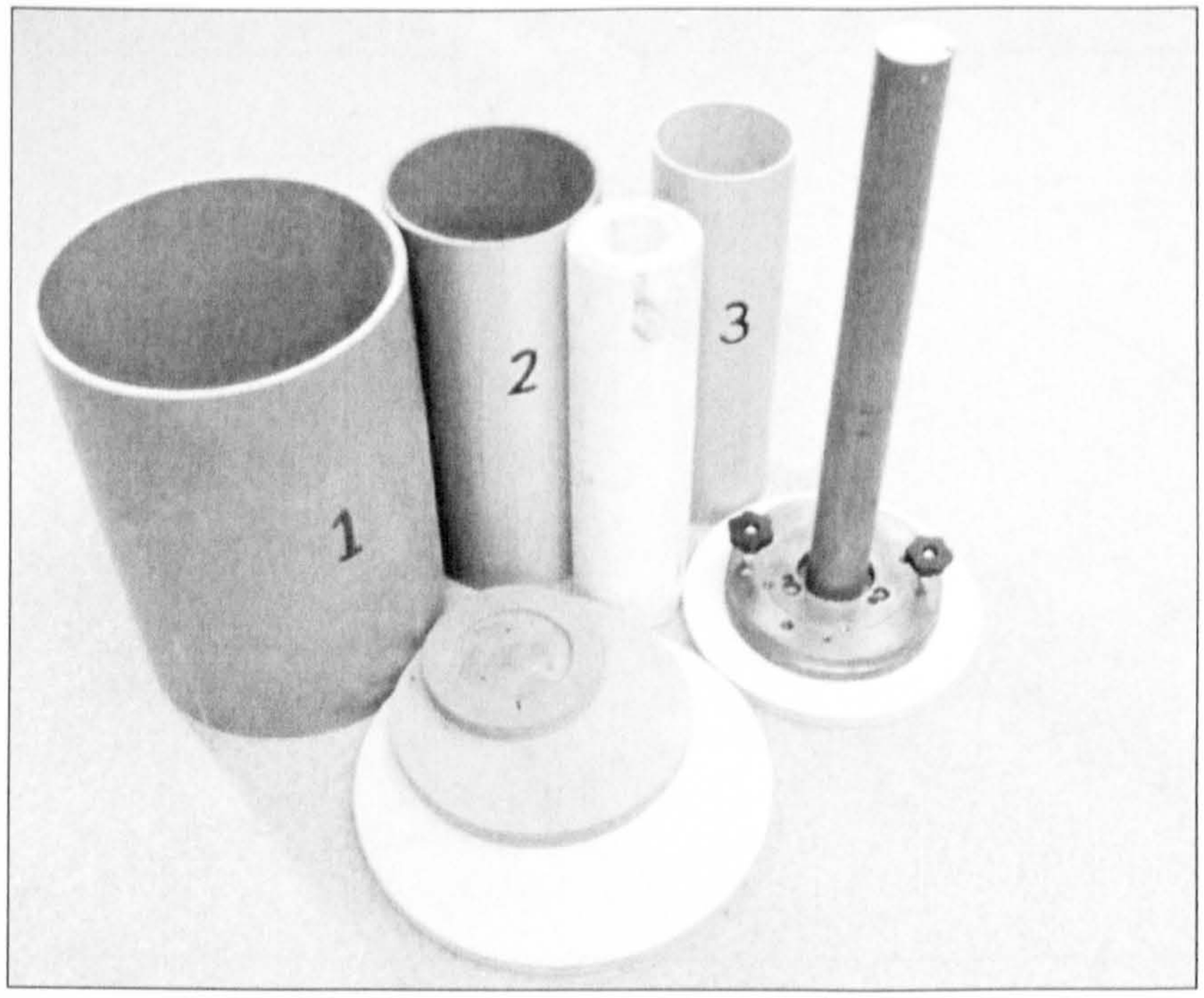

Figure 3.13 Shock tamping device used to increase density of natural granular targets. The weight is dropped from a fixed point on the central tube a set number of times. Image also shows the three smaller containers used to examine the effect of lateral boundaries on the penetrometry signatures (discussed in chapter 4)

Spherical bead targets were used in much of the laboratory work because they represent the simplest grain shape and are considerably easier to prepare due to their consistent packing, and produce a target with a small range of bulk density and porosity. They are cohesionless and also more uniform in their properties unlike grains of natural materials such as gravel and sand that can vary considerably in their density. Targets were prepared by pouring in the beads until the container was filled and then 'skimming' off the topmost beads using a straight rod to level the surface. Unlike natural targets, which required a complete refilling of the target container between impacts, the beads could be simply loosened by stirring and then re-levelled in preparation for a new drop.

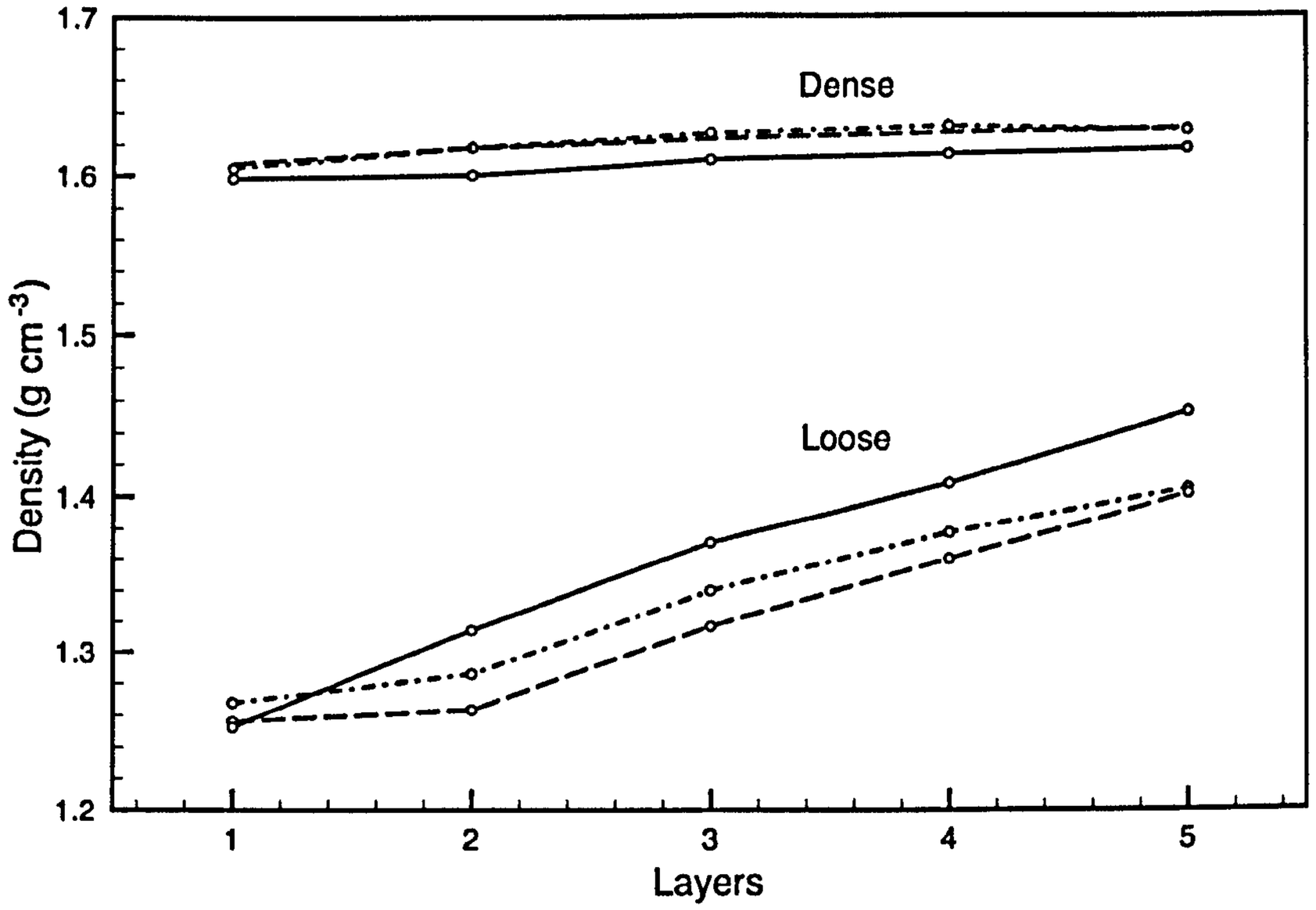

Figure 3.14 Graph of cumulative density for three target samples of loose and dense Leighton Buzzard DA16/30 sand prepared in layers. This is not a true density profile as lower sand layers compact as more sand is added on top. However, the graphs do indicate that although the layered sample preparation method worked well, small density variations are still evident and the preparation of uniform loose targets is significantly affected by overburden pressure.

3.10 Target material parameters

Two different types of sand were used in the laboratory experiments. Leighton Buzzard DA 16/30 is a well-sorted coarse sand and RH T is a much finer sand which is also well-sorted. Both are silicic, Lower Greensands from the Cretaceous period with low iron content and have sub-rounded or sub-angular grains (Figure 3.15). They are locally available from the WBB minerals Ltd. Double Arches quarry in Leighton Buzzard. Their grain size distributions are shown in Figure 3.16. Four gravels were also used in later drop testing. These ranged in grain size between fine gravel to medium gravel as any larger particles could have damaged the penetrometer and would have produced signatures with force content predominantly in the less accurate medium and low gain branches of the electronics.

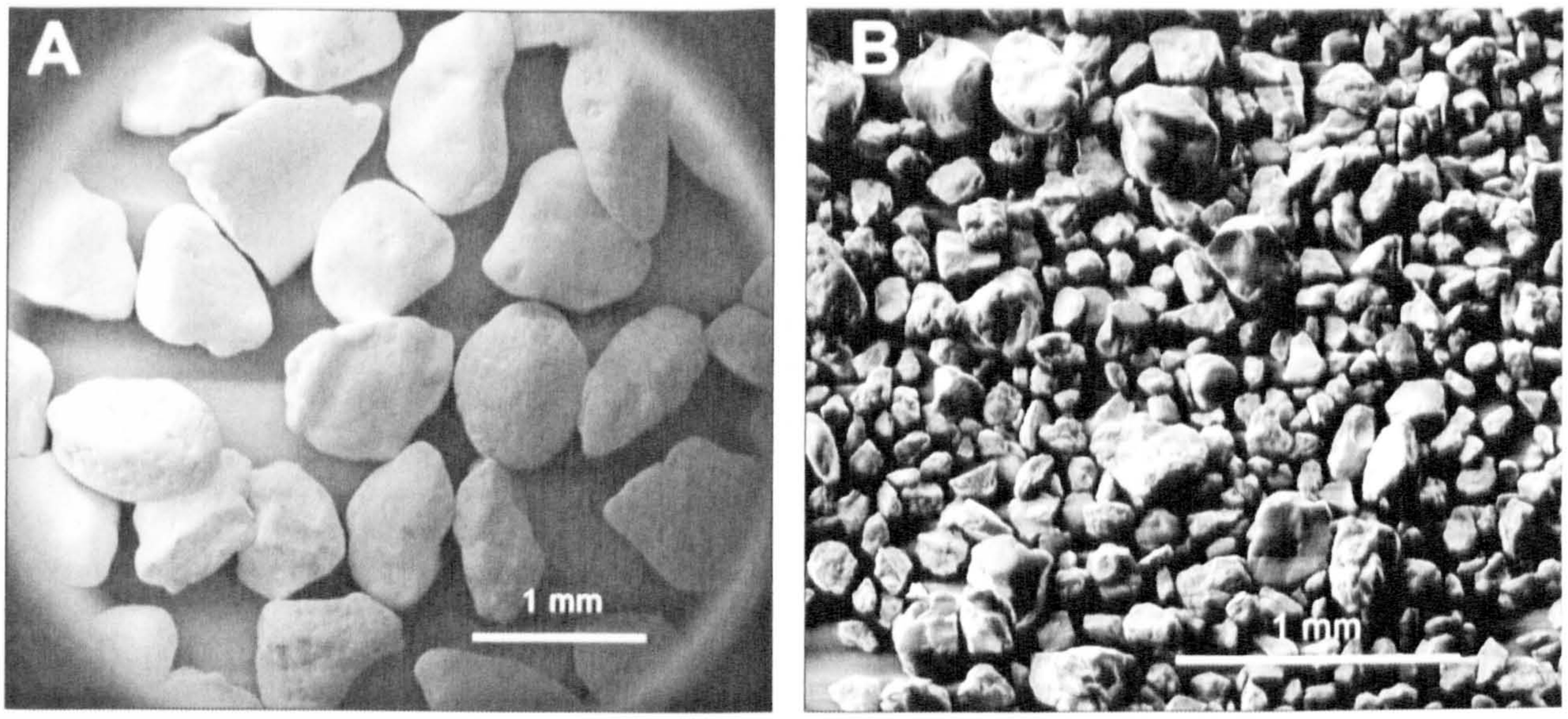

Figure 3.15 Scanning electron micrograph images of (A) Leighton Buzzard DA 16/30 and (B) RH T sand grains. (Images courtesy D. Johnson)

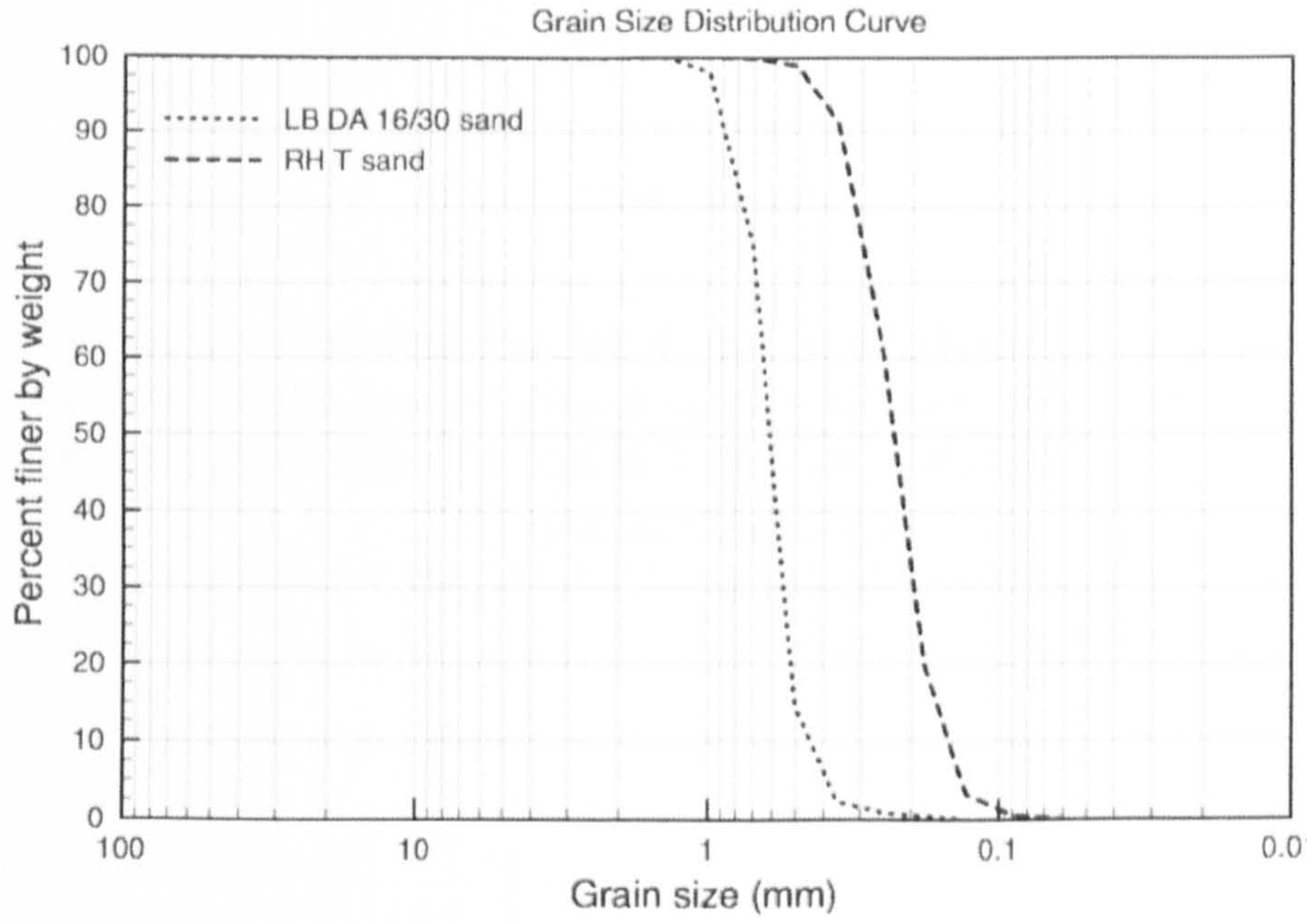

Figure 3.16 Grain size distribution curves for the two test sands used in the laboratory. Percentage finer is the percentage weight of material smaller than the corresponding grain size value at that point on the curve. The steepness of both curves indicates that the sands are well sorted.

Figure 3.17 and Figure 3.18 shows the grain size distributions of the gravels. The curves show that the gravels are either well or very well sorted with most of the grains falling in a narrow size range. Figure 3.19 shows images of the grains of each gravel. The grains vary in their shape and sphericity and how constant these parameters are. For example the largest gravel used, 7 mm mean diameter 'medium gravel', all grains are

well rounded with high and low sphericity. The 5.5 mm mean diameter 'light gravel' in contrast has a mixture of rounded and subrounded grains with some that are even subangular.

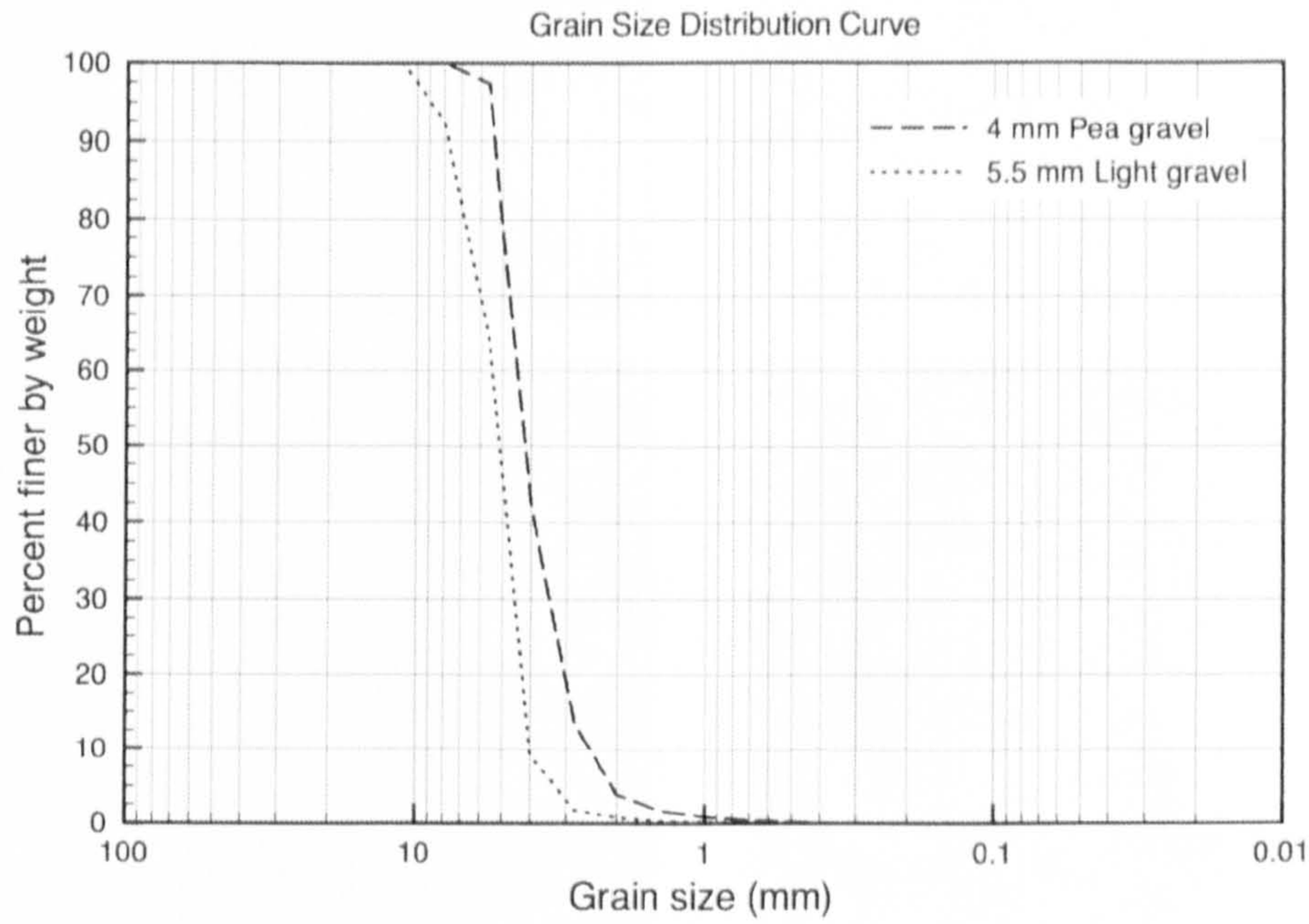

Figure 3.17 Grain size distributions for 4 mm mean diameter 'pea gravel' and 5.5 mm mean diameter 'light gravel'. Steep curves indicate that both gravels are well sorted with the majority of grains within a narrow size range.

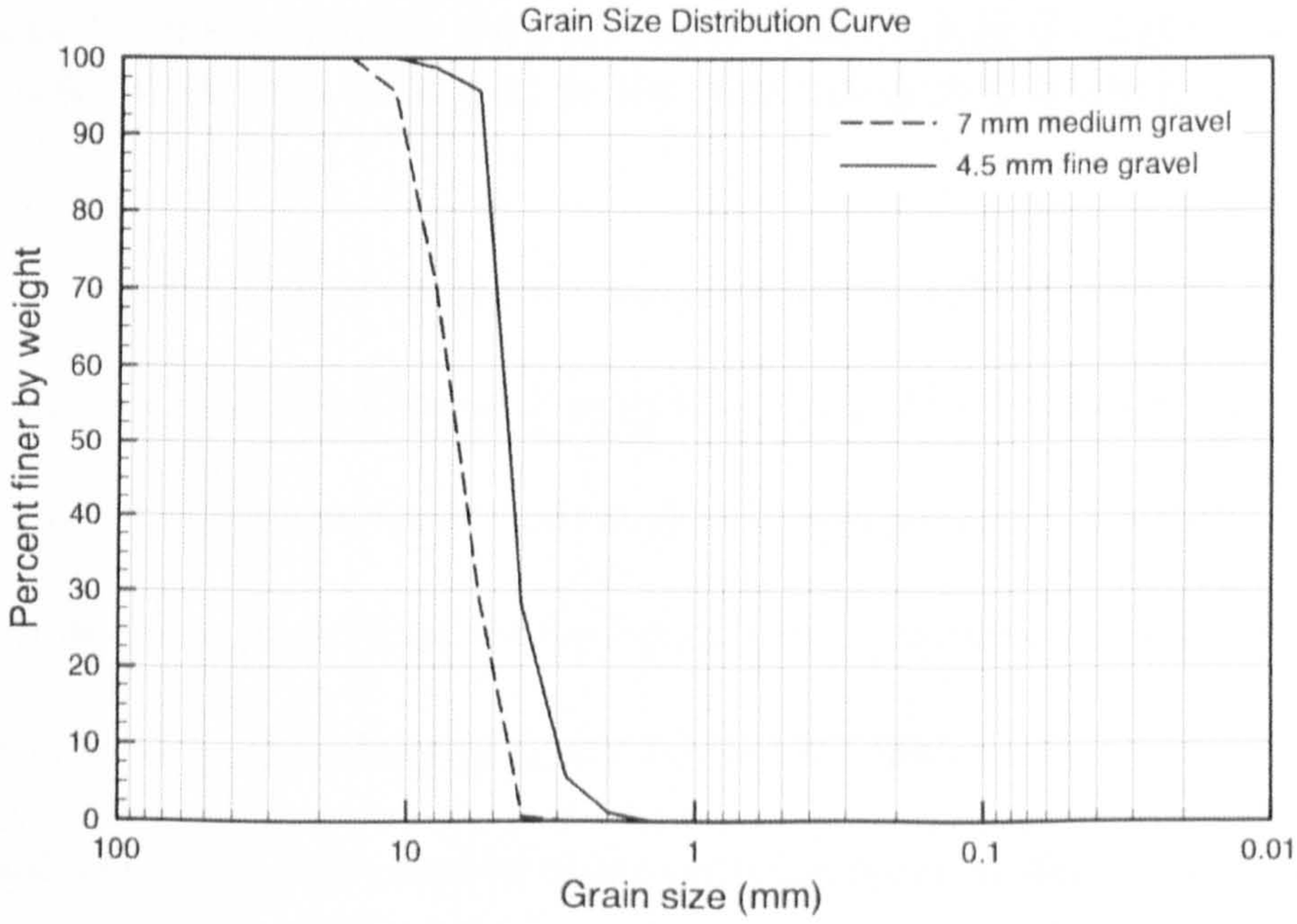

Figure 3.18 Grain size distributions for 4.5 mm mean diameter 'fine gravel' and the largest gravel used, 7 mm mean diameter 'medium gravel'.

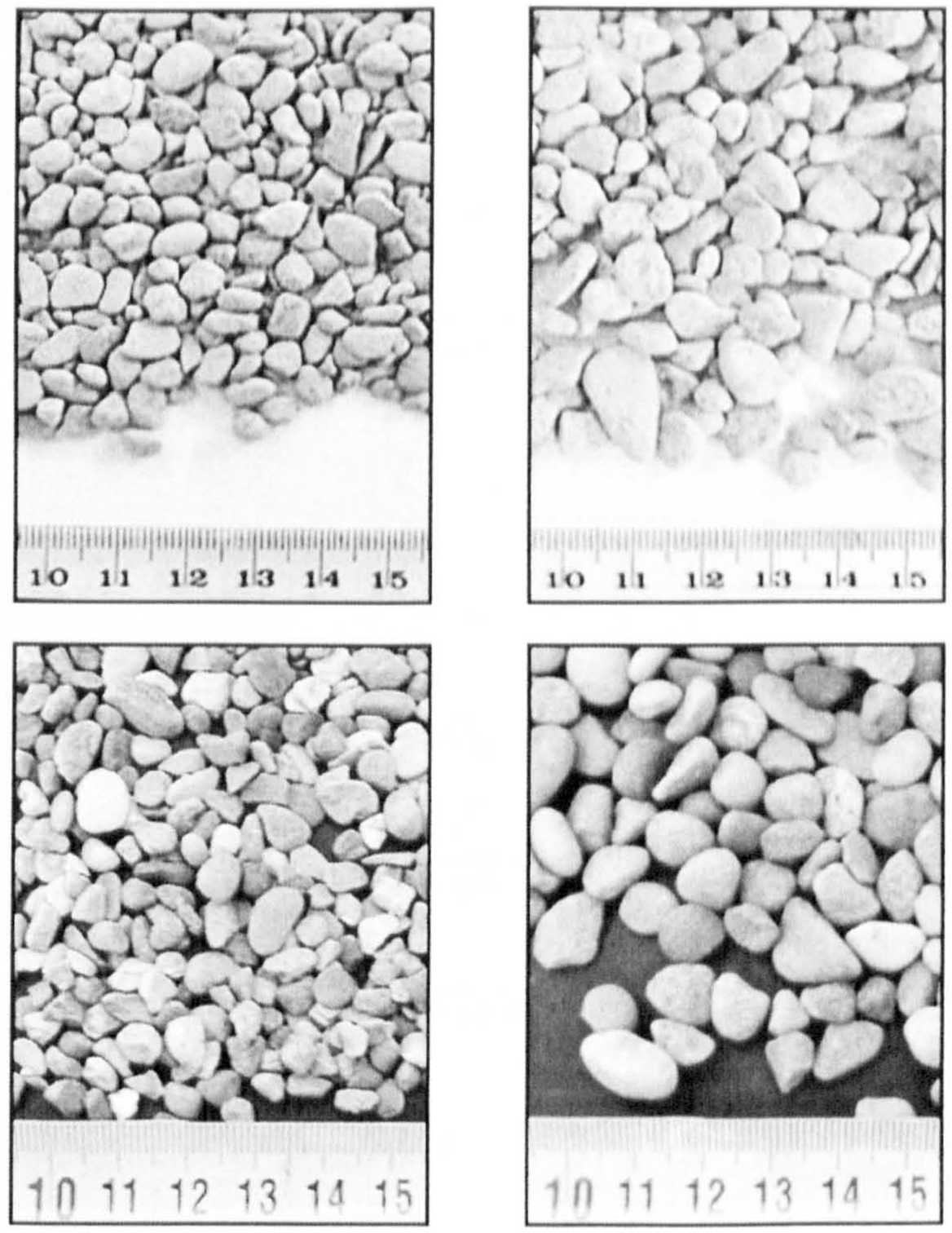

Figure 3.19 Gravels used in experiments (from top left clockwise); 4mm pea gravel, 5.5 mm light gravel, 7 mm medium gravel and 4.5 mm fine gravel. Grains vary in shape from subangular with low sphericity seen in the light gravel through to well-rounded with high sphericity in the medium gravel. Scale is in centimetres.

Four types of glass bead were used with diameters 1,4,6,8 mm manufactured by Sigmund Lindner (SiLi) GmbH and Pumex (UK) Ltd. The beads are all made of soda lime glass and are almost perfectly spherical with similar grain densities. Plastic beads and steel shot were acquired later Grove Beads Ltd. A summary of the bead properties is shown in Table 3.1. The Mohs hardness used in the table, is a measure of the surface (scratch) hardness commonly used to characterize minerals found in the field. It covers the softest material, talc (Mohs hardness 1) to the hardest material, diamond (hardness 10) (Jones, 1987).

Material	Diameter, ∅, (mm)	Effective strength, σ, (kPa)	Bulk density, ρ, ($g\ cm^{-3}$)	Particle Density, $\rho_{particle}$ ($g\ cm^{-3}$)	Porosity, ϕ, (%)	Mohs hardness
1 mm glass beads (Silibeads)	1.00-1.25	130±20	1.49±0.08	2.50	40	6
4 mm glass beads (Silibeads)	3.70-4.30	159±25	1.50±0.08	2.50	39	6
6 mm glass beads (Pumex)	6.0±0.3	192±31	1.50±0.08	2.50	39	6
8 mm glass beads (Pumex)	8.0±0.3	239±39	1.51±0.09	2.50	39	6
6 mm plastic beads (BB pellets)	5.98±0.01	107±17	1.19±0.04	1.80±0.02	34	5*
4 mm plastic beads (Grove)	3.92±0.02	61±10	0.70±0.02	1.01±0.02	31	4*
8 mm plastic beads (Grove)	7.83±0.03	83±14	0.70±0.02	0.96±0.02	27	4*
~6 mm Polystyrene beads (Polybeads)	5.9±0.4	too weak to measure by method	0.18	0.26±0.05	32	1*
2 mm Steel Shot	2.06±0.01	too strong	4.30	7.40	41	7
5 mm Steel Shot	4.99±0.01	too strong	4.30	7.40	41	7

Table 3.1 Material parameters of the spherical granular materials. Effective strength, particle density and porosity values are manufacturers data (without error estimates) or calculated as described in section 3.8.5. Values marked with an asterisk are author's estimates.

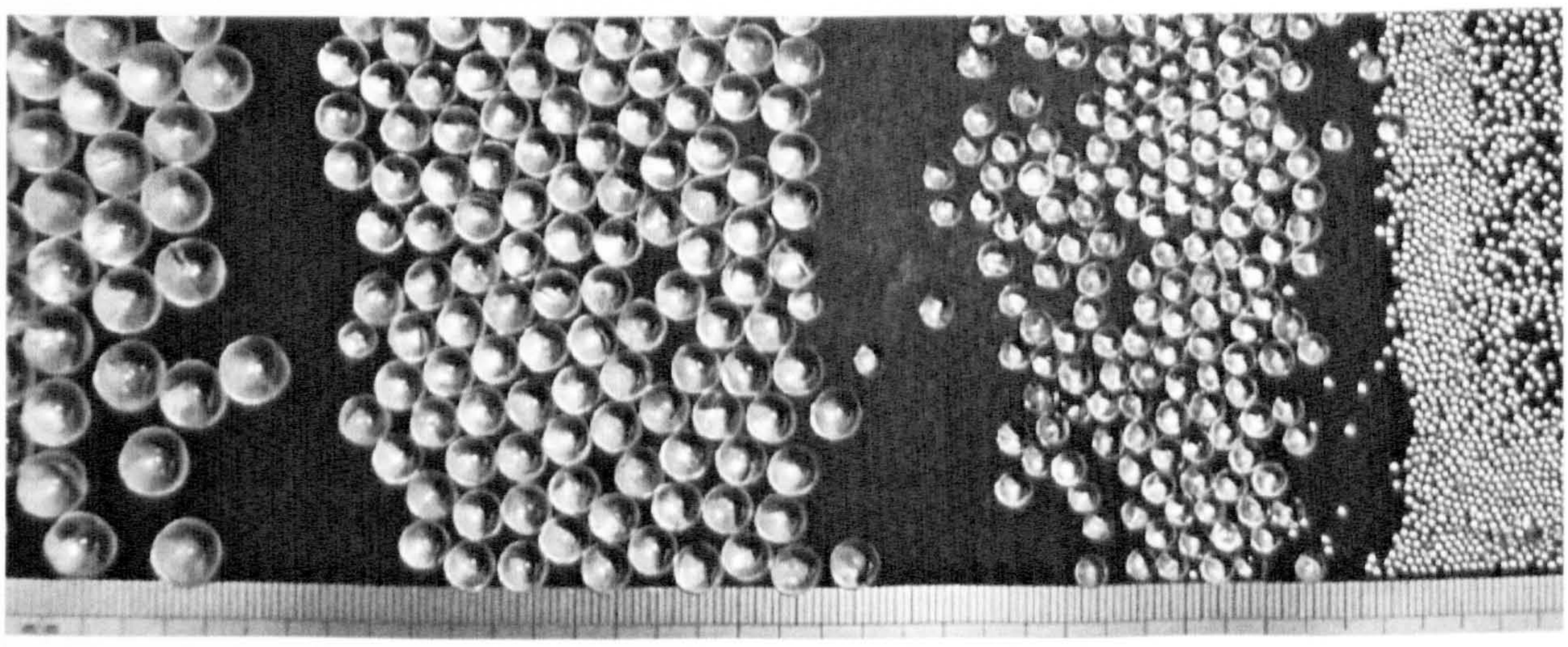

Figure 3.20 The four sizes, 8,6, 4 and 1 mm diameter glass beads used in experiments. The image shows how the spherical beads tend to arrange themselves in a regular fashion. Divisions on the scale are millimetres.

4 Identifying granular target materials

4.1 Descriptive measures to classify penetrometry signatures

Examination of the penetrometry signatures in the material catalogue (section 3.1) shows the variation that can be found between different analogues. It was therefore necessary to define a series of measures both to describe the penetrometry signatures and to allow comparisons to be made between them. The example signature shown in Figure 4.1 gives some of the descriptive measures that were used and Table 4.1 describes them in more detail, giving their variable names within the signature analysis program *penstat.m* (appendix A).

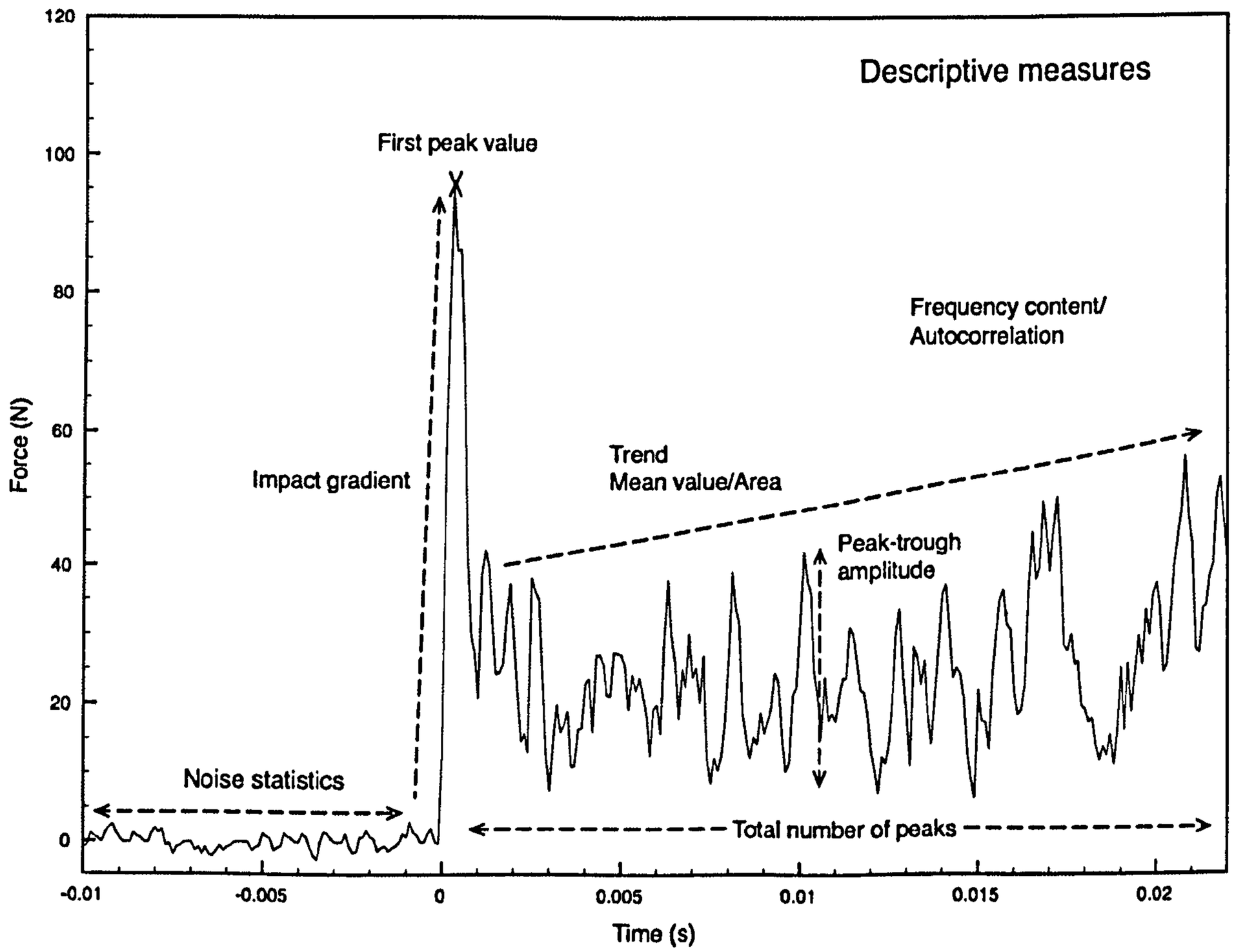

Figure 4.1 A typical ACC-E penetrometry signature with some of the measures marked that can be used to describe the signature.

Signature measures used in *penstat.m* program	Description
no_sig_stdev	Standard deviation of the penetrometry signature prior to impact. Used to determine the noise level present on the signature.
sig_mean	The mean force measured by the penetrometer over the full 'clean' depth penetrated.
sig_stdev	Standard deviation of the signature over the full 'clean' depth penetrated.
tip_mean	Mean force of the 'tip entry' stage (discussed later).
tip_std	Standard deviation of the 'tip entry' stage.
first_grad	Impact gradient (see figure 4.1).
first_max	Magnitude of first force peak after start of penetration.
second_mean	Mean penetration force excluding tip entry stage.
second_stdev	Standard deviation of signature after tip entry stage.
second_grad	Gradient of signature after tip entry stage.
mod_mean	Amplitude mean. Measures the average magnitude between peaks and following troughs in a granular signature.
mod_stdev	Standard deviation of the peak to trough amplitudes. Measures the variability of peaks in a signature.
mod_kurt	The kurtosis of the peak to trough amplitudes. A higher value describes variations that are due to a few large deviations rather than many smaller ones.
mod_skew	Examines whether the distribution of the peak to trough amplitudes are symmetrically distributed or biased more to one side.
spacing_mean	Mean spacing between peaks found using the peak/trough finding algorithm described later.
spacing_stdev	Standard deviation of the spacings between peaks.
spacing_kurt	The same as *mod_kurt* for the distribution of spacings between successive peaks.
spacing_skew	The same as *mod_skew* for the distribution of spacings between successive peaks

Table 4.1 Table of some of the basic measures produced by the analysis program to describe the penetrometry signature. Other measures such as frequency analysis are described separately in later sections.

4.2 Target boundary effects

When carrying out penetrometry in the laboratory, the aim is to produce impact signatures that are representative of similar impacts into a semi-infinite planetary surface. In practice, a laboratory target is necessarily bounded by the rigid sidewalls of the target container and the depth restricted by the container floor. Boundaries may lead to spurious effects on the penetrometer signal caused by the confinement and induce order in the target material near the container wall (Zou and Yu, 1995). This leads to a compromise between as large a target as possible, to minimise these effects, and the

practicality of producing a target that is manageable and not too time consuming to prepare.

Boundary effects are one area of research within Cone Penetration Testing (CPT), with particular attention being given on how to minimise these effects on the measured cone tip resistance (q_c). Experiments use special *cavity-wall chambers* to attempt to simulate an infinite soil mass. These target containers have walls of multiple flexible rubber membranes that are filled with water to adjust their rigidity minimising any boundary effects. A large chamber may have a 1.5 m diameter, approximately 42 times that of the standard cone penetrometer tip (Huang and Hsu, 2005). Despite the use of cavity-wall chambers, boundary effects can still affect CPT measurements and several 'correction factors' have been proposed that take into account the effect of the boundaries (Huang and Hsu, 2005). These effects are also target material dependent. Cone penetration tests into sand carried out by Been et al. (1987) demonstrated that boundary effects are related to the dilatancy of the sand (an increase in porosity caused by shear forces on the sand grains) and may also depend on the mineralogy, fabric and sample preparation. In addition to lateral boundaries the floor of the target container can also affect the recorded signature. In their lower velocity (1.5-9 m s^{-1}) dynamic penetration experiments McCarty and Carden (1962) allowed for a target thickness of at least four times the maximum measured penetration depth into the target, although no physical justification for this figure is given.

Quasi-static penetrometry by Whiteley and Dexter (1982) measured the force required to push a particle of gravel through similar sized aggregate targets while approaching the container bottom, and more conventionally, work by Stone *et al.* (2004) pushing a

flat circular plate into ~1 mm diameter spherical glass beads have both shown that the penetration resistance force on an object increases exponentially as it approaches a rigid bottom boundary. Whiteley and Dexter related this lower boundary effect to the diameter of the aggregate target particles, demonstrating that the effect becomes significant when the boundary distance is 10 particle diameters or less from the penetrometer tip. Both these experiments demonstrate that the effect of boundaries needs to be carefully considered. The effect can be dependent on multiple factors including the sensitivity of a given penetrometer, the target material and its preparation and would ideally be considered for each experimental set-up.

To examine the boundary effects of the target container for faster, dynamic ACC-E penetrometry, two experiments were carried out. The first using different diameter open-bottomed cylindrical containers (shown in Figure 3.11) to examine edge effects and the second using a container with variable depth to examine bottom effects. The purpose of these experiments was not to examine boundary effects *per se*, but to establish that the metal target container intended for subsequent experiments (320 mm internal diameter and 350 mm depth) was of sufficient dimension for them to be negligible. Figure 4.2 shows the two experimental arrangements with the metal target container being the outer one.

The target material used to represent a range of targets was 4 mm glass beads, as they allowed quick, consistent preparation, and also in the case of the bottom effect experiment could produce an impression in the foamglas boundary as the penetrometer approached it. The glass bead properties are given in the table in section 3.6

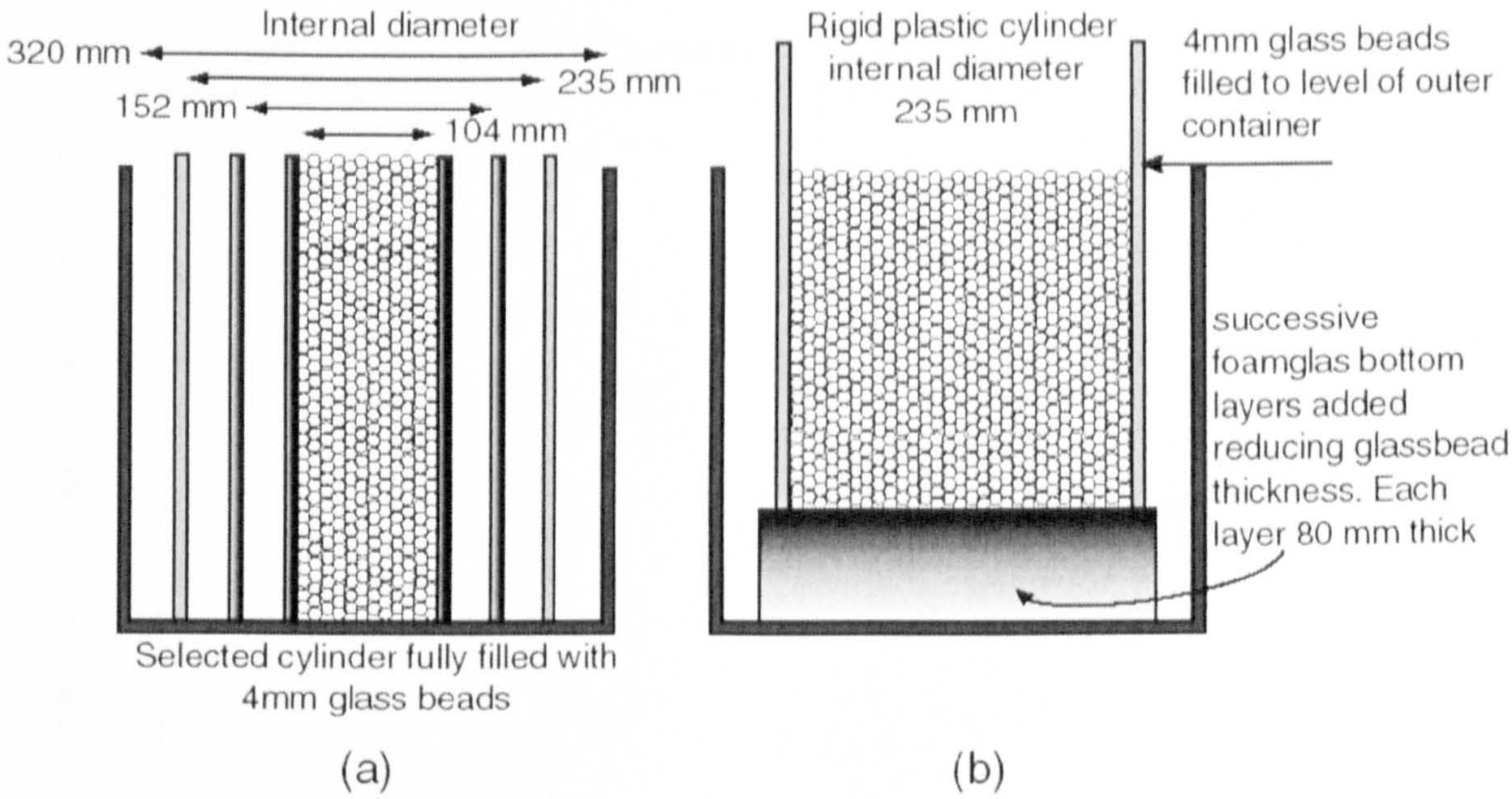

Figure 4.2 (a) Edge effect experiment using different diameter cylinders filled with 4 mm glass beads. (b) Bottom effect experiment using successive layers of foamglas considered a rigid boundary while also preventing damage to the penetrometer should it pass through the target material.

Ten drops, the maximum practicable number, were carried out into three containers with diameters 104, 152, 235 and 320 mm. The penetrometer impacted the target material at 4 m s^{-1} in each case. The data collected were first corrected to account for transfer and calibration as described previously, and the resulting signatures were examined using the analysis program *penstat.m* to obtain the descriptive measures given in section 4.1. Examining these measures showed as expected that the mean force detected by the penetrometer was greater for the drops into the smallest 104 mm diameter target container however the spread of values was quite large. In particular, the first ~8 mm of the penetration or the 'tip entry' stage (see section 4.5.1) varied significantly between drops into the same container. Removing this entry stage and considering only the mean of the remaining signature (described by the measure *second_mean* in the previous section) gave more consistent results. Figure 4.3 shows this second mean value plotted against the size of the target container.

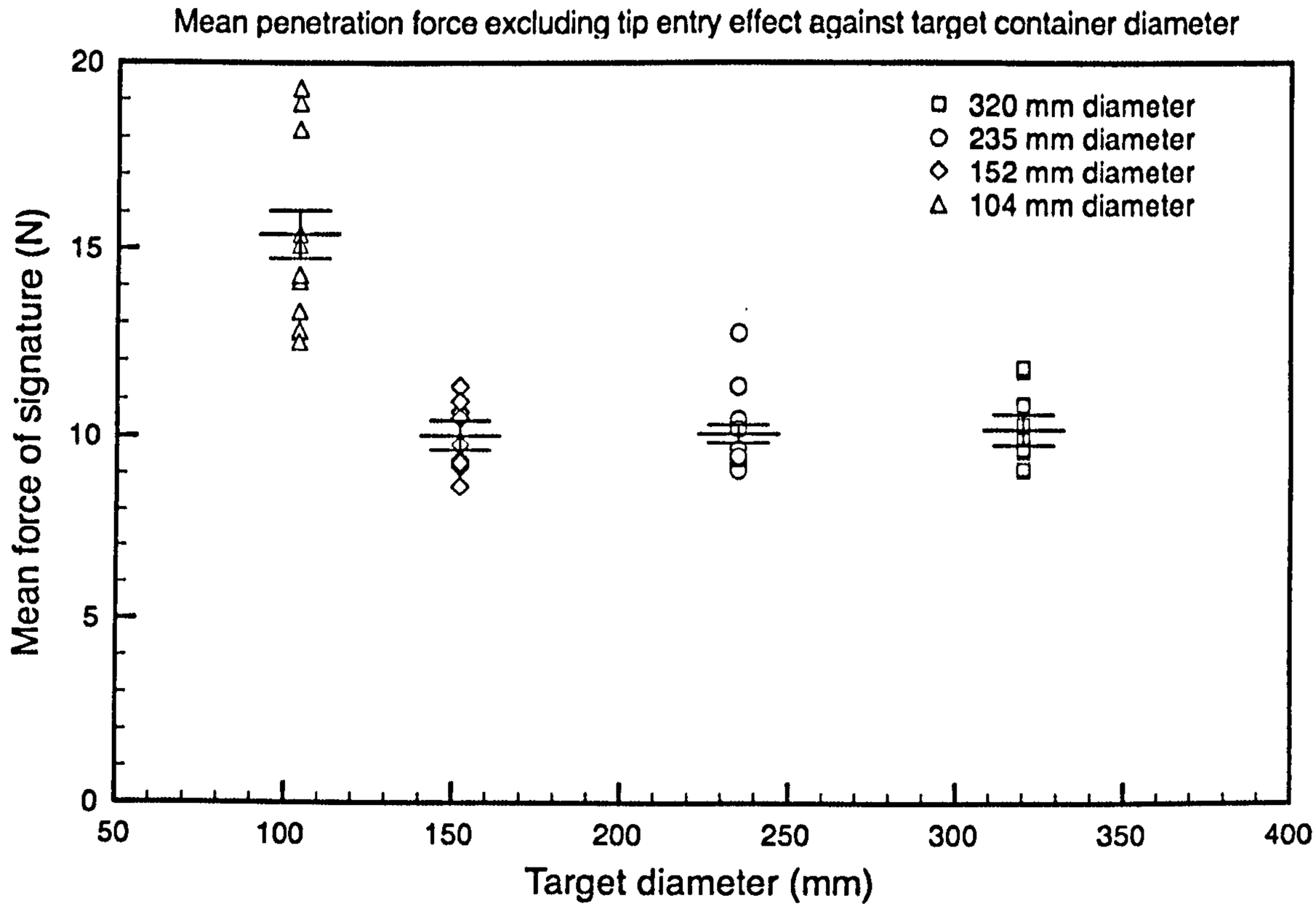

Figure 4.3 Mean penetration force excluding tip entry measured by the ACC-E penetrometer for various diameter target containers. The mean and standard error are plotted for each configuration.

To examine whether the differences between the mean force detected by the penetrometer for the different containers is statistically significant, it is important to first consider the amount of data collected. Given the practicality of a maximum of 10 drops into each container arrangement the data is considered to be of small sample size. Investigating possible differences between *k* independent small sample groups such as these is often done using a one-way analysis of variance (ANOVA) method[1] (Samuels, 1989). The data from each different diameter container (a *group*) are taken as independent random samples from an underlying larger, normally distributed population. The first step in the ANOVA method is to assert a *null hypothesis* that the means of these populations are the same. For the case of the edge effects experiment the

[1] Despite its suggestive name, the ANOVA method compares the means of the data rather than their variances.

null hypothesis is:

$$H_o: \mu_{\text{diameter 104}} = \mu_{\text{diameter 152}} = \mu_{\text{diameter 235}} = \mu_{\text{diameter 320}} \quad \textbf{(Equation 4.1)}$$

where $\mu_{\text{diameter } x}$ is the population mean for drops into the container of diameter x. An alternative *research hypothesis* is also set where some (or all) of the means are not equal. The null hypothesis is tested using the ANOVA calculations and if rejected at the chosen confidence level, implies that not all the means are equal and the research hypothesis is accepted. The ANOVA procedure examines the variation within the collected sample data in two ways: deviation from the group mean (known as *variation within groups*) and deviation between the means of each group (or *variation between groups*). The analysis gives an *F ratio*, a ratio of the variance between the groups compared and the variance within the individual groups. This value then describes the size of the difference between the groups *relative* to the size of variation within each group (Levin and Fox, 1991). A large F ratio will cause the null hypothesis to be rejected in favour of the research hypothesis. The ANOVA analysis of the data was calculated using Excel[2].

These methods require that the input data are normally distributed. While it is reasonable to assume that the mean penetration force for each different target container is normally distributed, a Shapiro-Wilks normality test was used on all data groups to

---

[2] Further details of the ANOVA calculation and the Tukey multiple comparison test can be found in Levin and Fox (1991)

confirm this prior to the calculating the ANOVA[3]. A standard ANOVA results table for the edge effects experiment is shown below.

Edge effects ANOVA summary					
Source of Variation	SS	df	MS	F	P-value
Between Groups	209.57	3	69.86	29.08	9.96E-10
Within Groups	86.47	36	2.40		
Total	296.04	39			

Table 4.2 Summary of ANOVA calculation carried out on the edge effects data. SS is the sum of squares, *df* is the degrees of freedom, MS is the mean square. A detailed explanation of these terms and standard ANOVA method can be found in (Levin and Fox, 1991). The resulting P-value is less than the significance level therefore the null hypothesis stated in equation 4.1 is rejected in favour of the research hypothesis.

The probability value (P-value) is much lower than the significance value i.e. $P < 0.05$ so there is a difference between one or more of the population means and the null hypothesis is rejected. To find *which* of the group means is significantly different a further *multiple comparison test* such as Tukey's HSD (honestly significant difference) test can be carried out. This test compares the difference between any two group means against an 'HSD' value given by (Levin and Fox, 1991):

$$HSD = q\sqrt{\frac{MS_{within}}{N}} \qquad \textbf{(Equation 4.2)}$$

where q is a 'studentised range statistic' for the chosen level of significance (in this case taken as α=0.05) found from tables using the degrees of freedom (*df*) from the mean square within groups of the ANOVA test and the total number of groups k. The variable MS_{within} is the within-groups mean square and N is the number of data points within each

---

[3] The Shapiro-Wilk statistic tests the null hypothesis that the sample is from a normally distributed population. It yields a p-value that causes the null hypothesis to be rejected if it is less than the chosen confidence level α (in this experiment α=0.05). It was calculated using the open source R statistics package.

group. The mean difference between any two groups is considered statistically significant if it exceeds the HSD value calculated. Table 4.3 shows the Tukey test results for the experiment.

Edge effects HSD=1.86	X_{Dia_152}=10.02	X_{Dia_235}=10.09	X_{Dia_320}=10.19	X_{Dia_104}=15.39
X_{Dia_152}	--	0.07 (N)	0.17 (N)	5.361 (Y)
X_{Dia_235}	--	--	0.10 (N)	5.296 (Y)
X_{Dia_320}	--	--	--	5.196 (Y)
X_{Dia_104}	--	--	--	--

Table 4.3 Results of Tukey test carried out on edge effects data. Differences between ordered means are compared to the HSD value given and significance (Y=yes N=no) is given in brackets. The table shows that the smallest 104 mm diameter container had significantly increased force compared to the larger containers (as might be expected from a visual examination of Figure 4.3).

The bottom effects experiment was envisaged to be similar to the Stone *et al.* (2004) quasi-static penetration setup but with the considerably higher 4 m s^{-1} impact speed. This would have created a problem of possible damage to the penetrometer when a rigid bottom boundary is close to the surface and the penetrometer is not completely stopped by the target material. To overcome this, strong type F foamglas was used as the boundary. This material has a high compressive strength and although not completely rigid, for the purposes of this experiment it can be considered a good approximation.

A foamglas boundary allows the penetrometer to record a 'clean' signal as it passes through the glass beads but if necessary impacts the bottom boundary without damage. The results of the edge experiment show that there is no significant difference between the two outer containers. The 235 mm diameter container could therefore be used in the bottom boundary experiment to form the target lateral boundaries. Sitting this slightly smaller container on the foamglas formed a better seal than shaping layers of foamglas to sit inside the round metal target container. It also allowed any foamglas that might be penetrated to be replaced more easily. Using in sequence, up to three 80 mm thick

foamglas layers, 10 drops were carried out into targets of depth 320, 270, 190 and 110 mm respectively. The target surface level was kept constant throughout. The mean penetration force excluding the penetrometer tip entry for impacts into the different depth containers is shown in Figure 4.4.

A similar ANOVA analysis to that used in the edge effects experiment was carried out and the results are shown in Table 4.4 below. The resulting p-value shows that there is a significant difference between means and a Tukey test confirms that the mean penetration force experienced by the smallest 110 mm depth container was significantly higher than for the other three container depths.

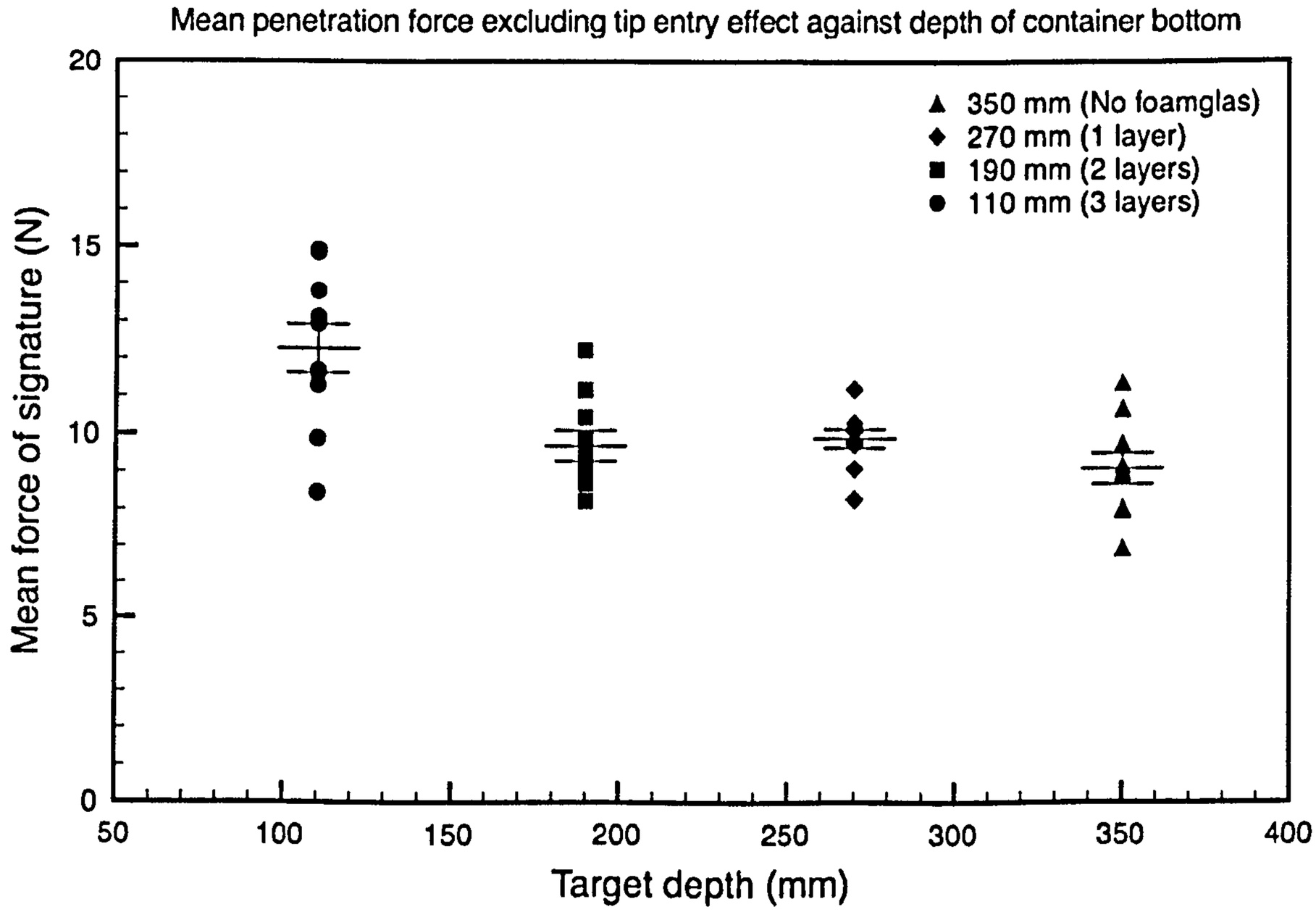

Figure 4.4 Mean penetration force excluding the tip entry for the various bottom boundary depths produced using a sequence of foamglas layers. The mean and standard error are plotted for each configuration. An ANOVA test indicates a significant force increase for the smallest container configuration.

Bottom effects ANOVA summary					
Source of Variation	SS	df	MS	F	P-value
Between Groups	59.01	3	19.67	9.63	8.36E-05
Within Groups	73.57	36	2.04		
Total	132.58	39			

Table 4.4 Summary table of ANOVA calculation for the bottom effects data. The resulting P-value indicates that one or more of the means is significantly different and the null hypothesis should therefore be rejected.

While examining the top layer of foamglas after each drop to see whether it needed replacing, it was found that in the case of a bottom boundary depth of 190 mm although the penetrometer was completely stopped before it hit the bottom boundary, the glass beads immediately below the penetrometer tip were forced into the foamglas boundary. Figure 4.5 shows that the forces on the beads are localised to a small area about twice the penetrometer diameter around the bottom of the tip and the compression is not seen in the deeper targets. The impression is shallow and agrees with the analysis and earlier work that the boundary must be close to the tip before a significant force is measured.

Bottom effects HSD=1.71	X_{350}=9.075	X_{190}=9.689	X_{270}=9.844	X_{110}=12.266
X_{350}	--	0.61 (N)	0.81 (N)	3.19 (Y)
X_{190}	--	--	0.20 (N)	2.59 (Y)
X_{270}	--	--	--	2.38 (Y)
X_{110}	--	--	--	--

Table 4.5 Results of Tukey test carried out on bottom effects data. Positive value differences between ordered means are compared to the HSD value given and significance (Y=yes N=no) is given in brackets. The table shows that the smallest depth container had significantly increased force compared to the other deeper containers.

These two experiment results show that both edge and bottom boundary effects can significantly affect the signature detected by the ACC-E penetrometer. The results of both the ANOVA and subsequent multiple comparison tests give confidence that the data collected using the ACC-E penetrometer into glass beads confined by the large diameter metal container should have only negligible boundary effects and drops into this container should therefore give a good representation of a similar, natural target on

a planetary surface. It would be impractical to examine the possible effects for every material used within the laboratory penetrometry work; however it is reasonable to assume that since no significant effects were seen in containers smaller than the target container, different materials should also be unaffected.

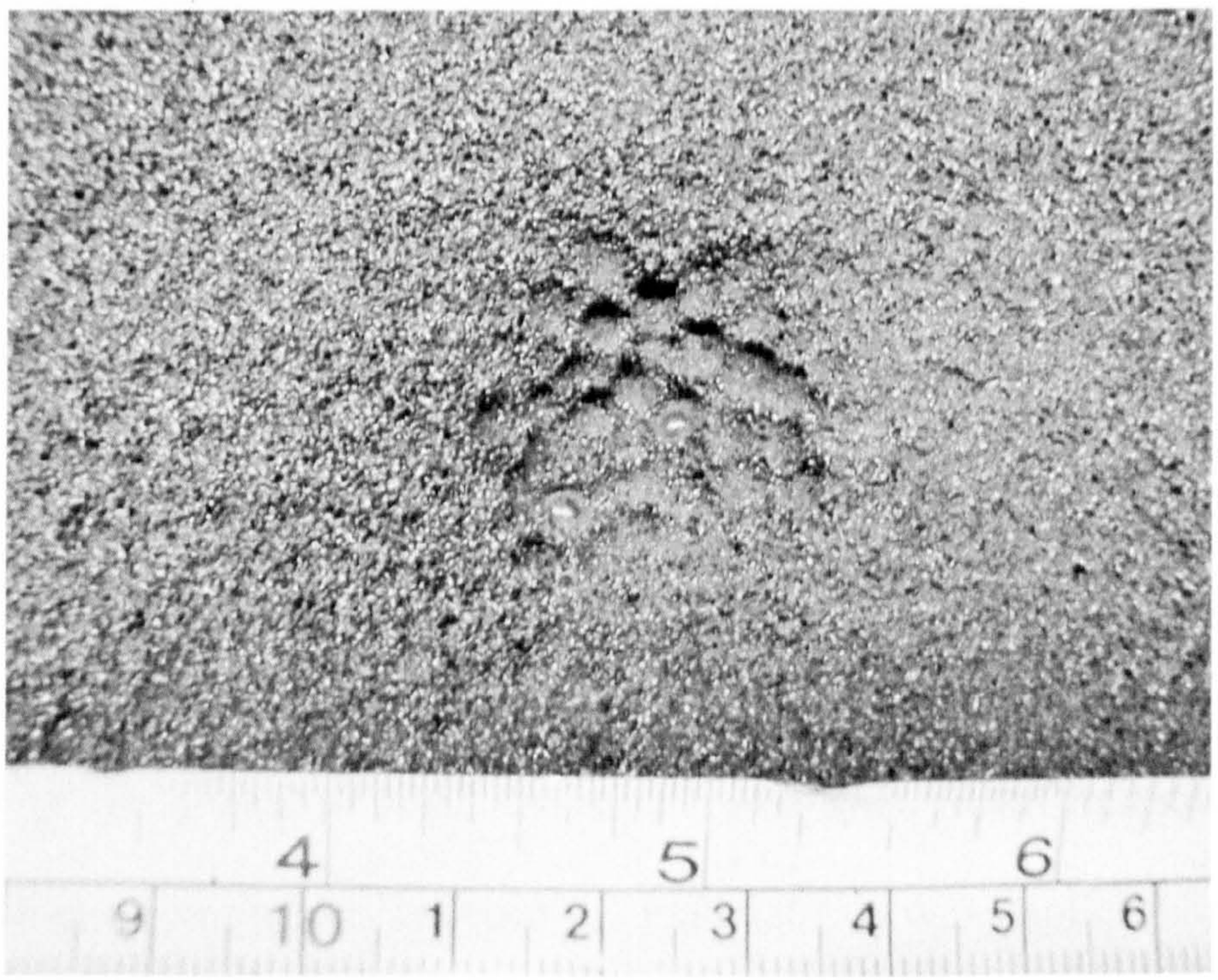

Figure 4.5 Impression left on foamglas bottom boundary by 4 mm glass beads for a target depth of 190 mm (some beads are still embedded). No impressions were seen in deeper targets.

4.3 Velocity dependence of signatures into granular targets

The strong suggestion of Huygens impacting a granular surface focused experiments predominantly on the penetrometer's response to granular targets. By using the NEO drop rig in an unbalanced configuration, the earlier material catalogue entries were limited to a maximum impact velocity of 3.7 m s^{-1}, 19% slower than Huygens. This meant that the penetrometer was still accelerating as it entered the target. The free fall drop rig allows impacts at a range of speeds including that of the Titan probe and using the laser derived penetration speed the signatures can be corrected for acceleration to give the depth penetrated.

To examine how penetrometry signatures change with velocity, a target material of 8 mm glass beads was impacted from six drop heights corresponding to impact velocities of 2, 2.5, 3, 3.5, 4 and 4.6 m s^{-1} (Equation 3.3). The larger beads were chosen to produce signatures with prominent features that would emphasise differences.

Preparation and properties of the targets were as previously described. For each impact velocity, a minimum of five drops were made and the signatures were examined using the descriptive measures given in section 4.1. Figure 4.6 (a) shows, as might be expected, that the mean force measured by the penetrometer rises proportionally with impact speed. The small scatter in the data indicates that the premise of consistent packing of glass beads is correct. The graph does not pass through the origin due to the insensitivity of the crystal to small dynamic loads. This graph indicates that direct granular analogue comparisons between the material catalogue, collected at 3.7 m s^{-1}, and the data returned from the surface of Titan may have underestimated the force by ~25% due to the difference in impact speeds. The second graph in the figure shows how the standard deviation of the force signature varies with the impact velocity. Faster impacts show an increased variability in the signatures possibly due to impacts with individual beads having a greater effect on the tip.

The graph in Figure 4.6 (c) shows an inverse linear relationship between impact velocity and the number of peaks detected. Approximately twice as many peaks are detected for an impact at 2 m s^{-1} compared to impact at 4.6 m s^{-1}. The method used to identify peaks (described in section 4.5.1) removes the effects of noise and, since additional peaks cannot be attributed to ringing of the penetrometer tip, as this effect would be expected to increase with force, they must be considered to be material

information. This would suggest that even with a theoretical ~1 mm depth resolution for a 10 kHz sampled ACC-E impacting a target at ~5 m s^{-1} (shown in chapter 1), there is still information being lost from penetration into 8 mm particles. With the fixed 10 kHz temporal sampling rate of ACC-E, the spatial sampling rate is set by the penetration speed:

$$\text{Spatial sampling rate} = \frac{\text{Temporal sampling rate}}{\text{speed}}$$

(Equation 4.3)

Thus if the temporal sampling rate of ACC-E could be increased or the speed of impact reduced it is probable that more information would be contained within the signatures. For a 2 m s^{-1} impact speed the spatial sampling is increased to 50 cm^{-1} compared to ~22 cm^{-1} at the Huygens impact speed. To achieve this improved spatial sampling at 4.6 m s^{-1} would require an increase in temporal sampling rate to 23 kHz. An experiment to investigate the optimum sampling rate and how it relates signature content for different particle sizes would be useful. The ACC-E electronics set up did not allow this experiment as, although the oscilloscope was able to sample at up to 100 kHz, the anti-aliasing filter attenuated frequencies higher than 5 kHz. The peaks and frequency content of the signatures are examined in more detail in later sections.

Figure 4.6 (Following page) Graphs of (a) the mean signature force, (b) standard deviation of the signature force and (c) number of peaks detected, for penetrometry drops into 8 mm glass beads at different impact velocities.

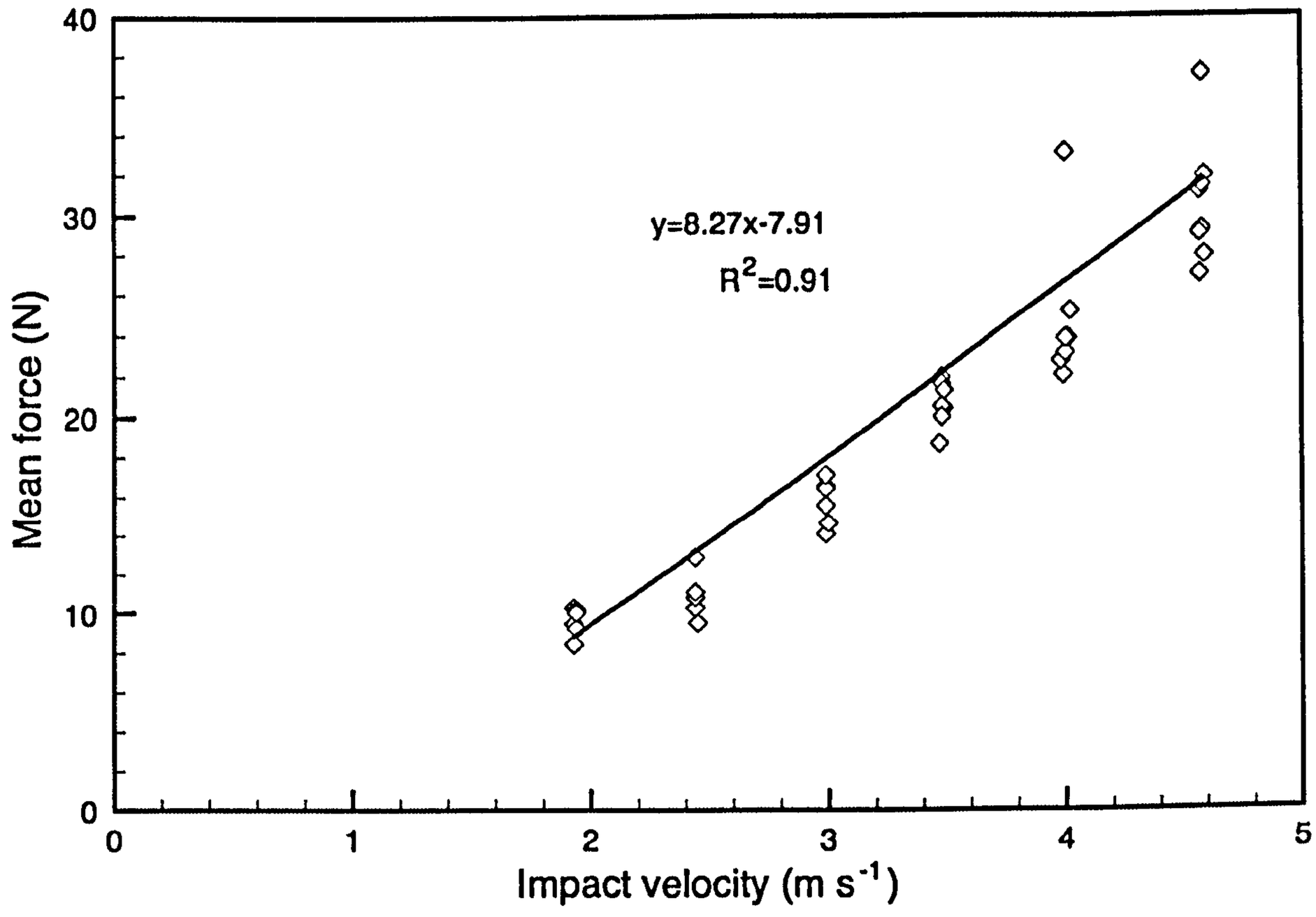
y=8.27x-7.91
R^2=0.91
Mean force (N)
Impact velocity (m s^{-1})
0
10
20
30
0
1
2
3
4
5

(a)

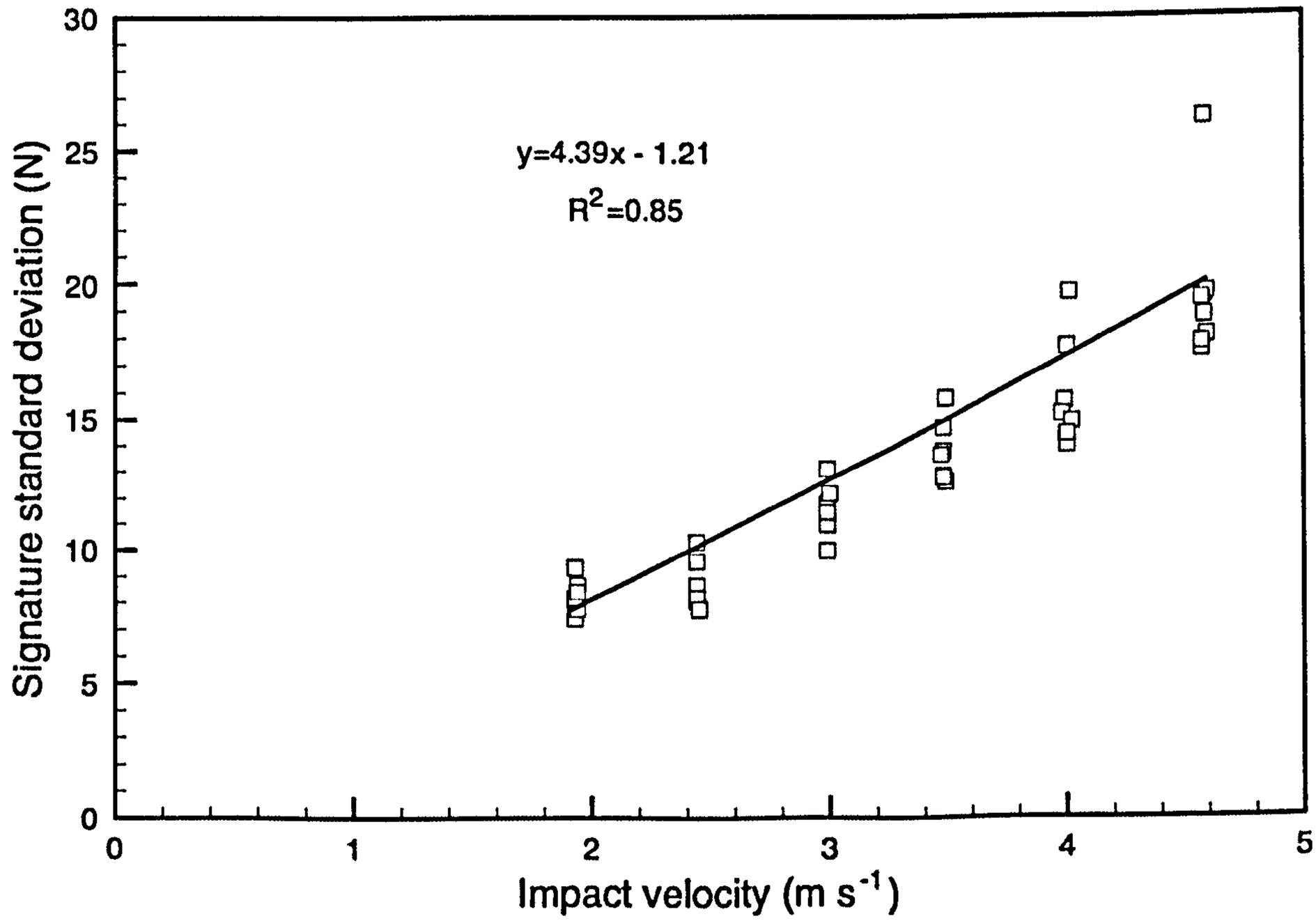
y=4.39x - 1.21
R^2=0.85
Signature standard deviation (N)
Impact velocity (m s^{-1})
0
5
10
15
20
25
30
0
1
2
3
4
5

(b)

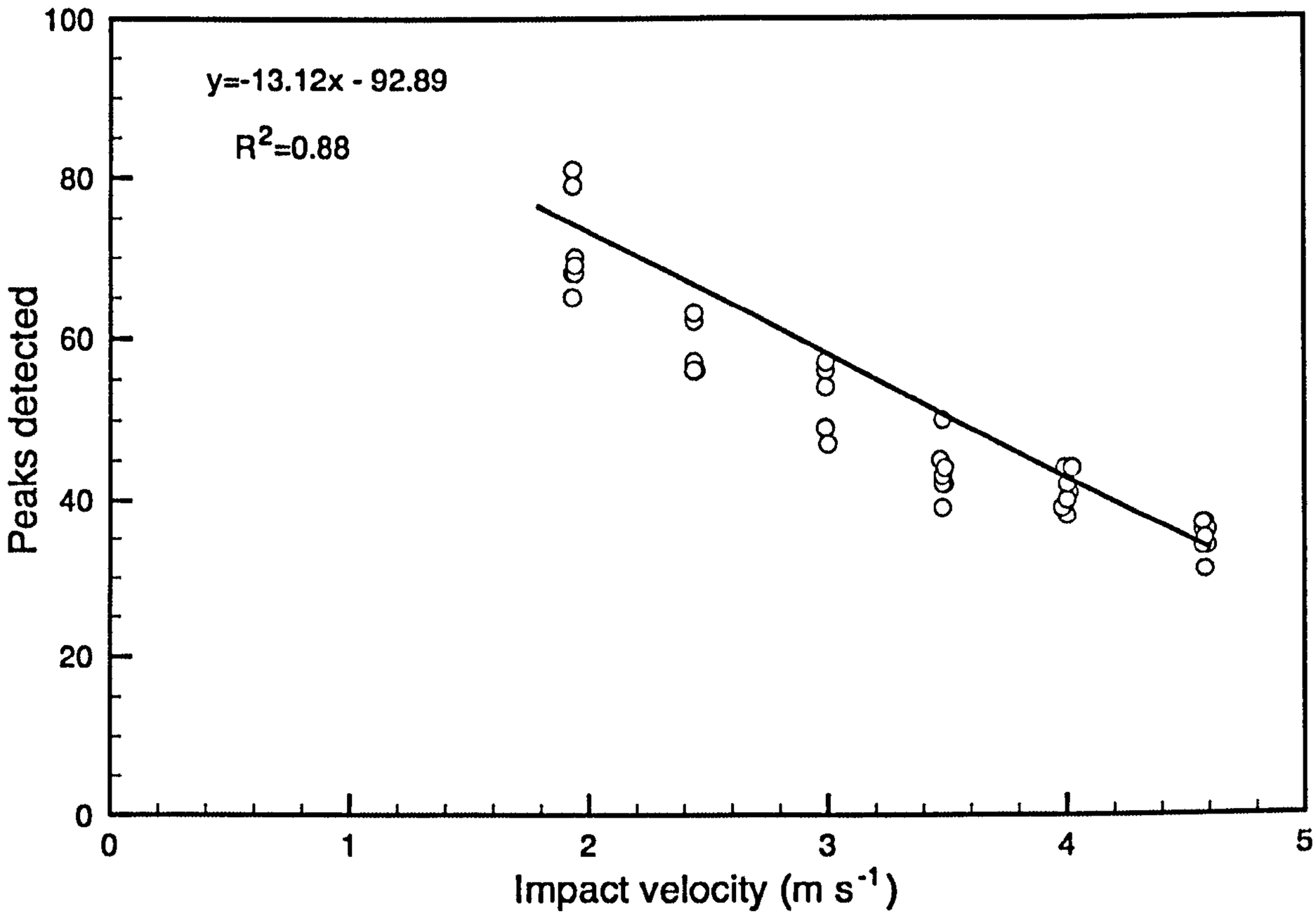

(c)

4.4 Sediment texture and environmental interpretation

Terrestrial regolith contains structure produced by the action of environmental processes of weathering, erosion and deposition. Weathering is the in-situ breakdown of rocks and soils by mechanical and chemical processes (Mitchell and Soga, 2005). On Earth, this material is transported and further disintegrated through the action of wind, water or ice in a process called erosion. Eventually this material is set down as a sedimentary deposit.

The *sediment texture* describes the size, morphology and distribution of the grains in the deposit and also the fabric of the sediment. These properties are important to describe a material and can be useful in interpreting the mechanisms and environments of deposition (Tucker, 2001). Wind erosion of rock for example can transport small

fragments over significant distances producing Aeolian deposits such as sand dunes. These typically consist of poorly stratified, low-density deposits of well rounded and sorted sand grains with the degree of rounding affected by the distance the material is carried by the wind (Ahlenbrandt, 1979; Legget and Hatheway, 1988). Water can also erode and transport material of different sizes. In a river, coarser *bedload* material is transported along the riverbed by bouncing, rolling and saltating while finer *suspended load* material travels with the fluid at the same velocity. These finer grains are more readily transported and will tend to travel further from the source than the coarser material before being deposited. This means that nearer the sediment source the surface of the bed will consist of poorly sorted predominantly larger grained material while further downstream the sorting would be improved and the coarser material would no longer be present (Dyer, 1986). The deposition of material in rivers and streams according to grain size contrasts with for example, *till* material deposited by a glacier. As the ice can transport a large range of different sized material from fine dust up to large boulders at the same rate this results in unsorted deposits (Mitchell and Soga, 2005). The capacity of the ACC-E penetrometer to determine textural properties as well as bulk properties is of interest as when combined with other information, it may help to infer the environmental processes acting at the landing site.

4.5 Identifying material grain size

The potential for determining the grain sizes present in a surface material is one of the most interesting and much discussed aspects of penetrometry (Kargl *et al.*, 1999). Several experiments have indicated that penetrometry signatures can distinguish coarser granular materials from finer or more homogeneous materials such as clay (e.g. (Lorenz *et al.*, 1994)) although the extent to which this is possible is not known; does the

penetrometer respond the size of the grains, their masses or both? If both the grain size and mass could be independently determined this would allow an estimate of the grain density to be made which would constrain the type of material from which the grains are made. Earlier experiments using a 2× scaled version of the ACC-E penetrometer dropped into gravels and sands suggested that the typical amplitude of the spikes in the signature related to the size of the particles (Bailey, 1997). Other work supports the earlier hypothesis that the amplitude of these spikes might relate to the mass of the particles, rather than their radius which instead is correlated to the spacing between peaks although no controlled study was carried out (Lorenz, 1994a; Lorenz *et al.*, 1999). Particle size detection must also be related to penetrometer sampling rate and this implies that there is an optimum sampling rate that allows detection of most grains without unnecessarily increasing the data storage and transmission requirements of the sensor. The size and geometry of the penetrometer tip may also affect detection: a large penetrometer will be unlikely to be able to resolve individual particles of a fine granular material.

The ability of penetrometer to determine some of this information from granular materials is still under investigation. Slow dynamic penetration has been used to attempt to derive the size of soil particles for the purposes of characterising the tillage of a field- an important measure of the quality of the field as a seedbed (Olson, 1992). This investigation consisted of drawing a mini-penetrometer with a diameter of 5 mm horizontally through a range of different aggregates at a speeds varying between 0.1 and 0.8 m s^{-1}. This penetrometer measured the forces on the tip using a steel blade spring instrumented with strain-gauges and was capable of measuring forces up to 5 N before the spring would yield to avoid damage to the sensors. The resulting signal was sampled

at 100 Hz with 12-bit resolution over an effective measuring distance of 1.65 m. The small diameter of the probe was chosen to be approximately the same as the size of the particles encountered, the idea being that the penetrometer tip should be better able to detect the force arising from the individual grains and that the force contribution from an individual grain would disappear after the tip had passed by. An analysis of the frequency content of the penetrometry signatures from laboratory experiments into medium sand through to 16 mm diameter gravel, Ohlson (1992) concluded that the spectral analysis of the force signatures did not offer information on the specific particle sizes contained in the material. He did however find that it was possible to derive a more general parameter based on the increase in force signal power at low frequencies for the larger grained materials. This correlated well for laboratory tests when aggregate sizes were within a relatively narrow range; however fitting the model to field test data was less successful (Ohlson, 1992).

More recently, Kargl *et al.* (2005) have examined frequency content of quasi-static penetrometry signatures to reconstruct grain size distributions for Martian soil analogues with promising results. The limitations imposed by the length and sampling rate of the ACC-E penetrometer together with the higher impact speed may restrict the information that can be derived from the penetrometry signature. Nevertheless, this information is of interest to the Huygens penetrometry investigation of Titan due to strong indications of a sedimentary granular environment at the landing site (Tomasko *et al.*, 2005).

4.5.1 Grain size and mass

Four sizes of glass beads were used to fill the target container respectively and drops

were carried out into each with an impact speed of 4.6 m s^{-1}. Data from these drops were read into the data_c.m program and processed as described in section 3.3.2. The resulting signatures were then depth adjusted using laser derived penetration speed data to account for the penetrometer change in speed within the target. Examination of the penetrometry signatures for the different glass bead sizes showed that a 'tip entry effect' seen in earlier experiments was evident. In comparison with the remaining signature, large forces were observed within the first 8-10 mm of target penetration (Figure 4.7). This corresponds approximately to the length of the ACC-E hemispherical tip as it enters the target surface.

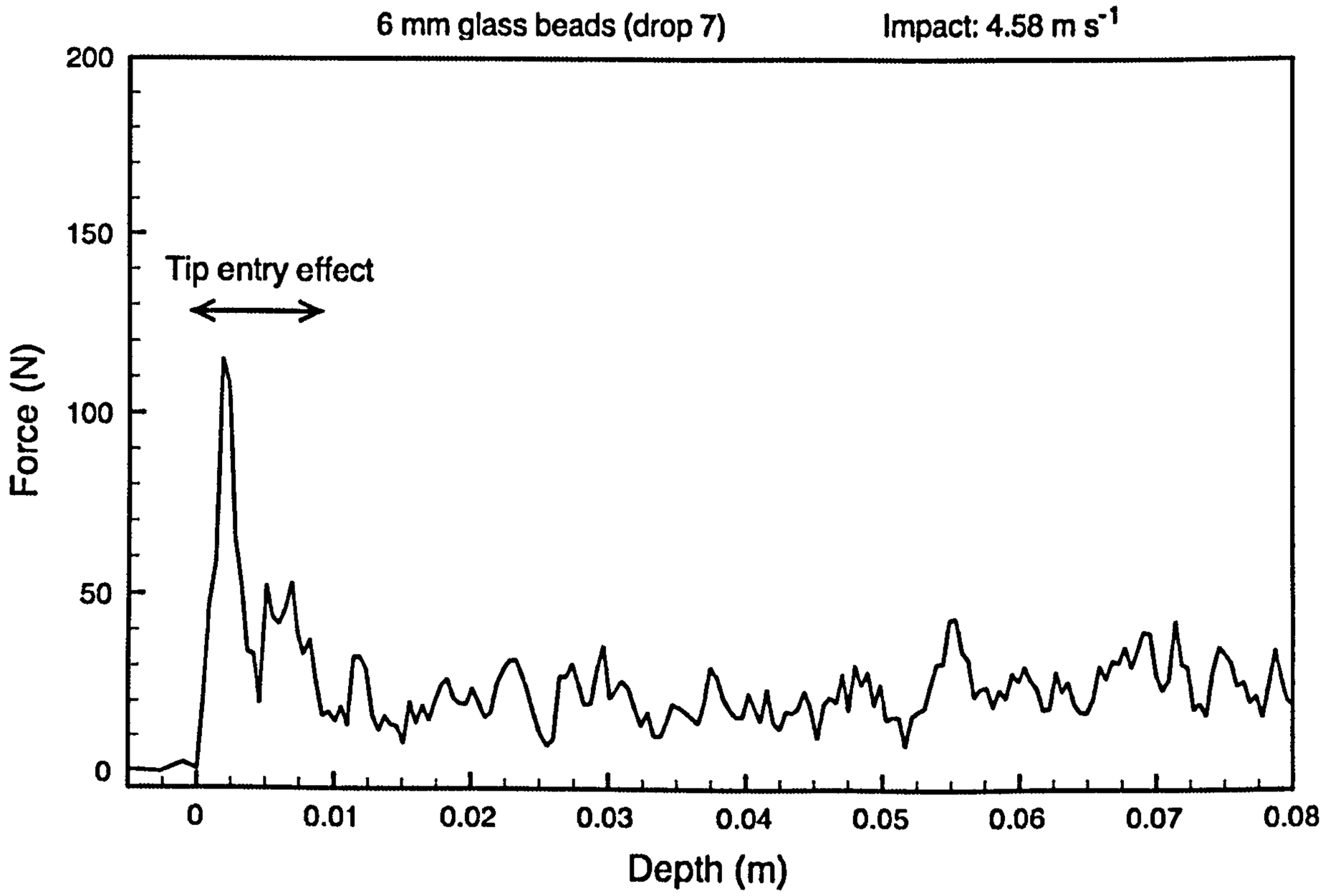

Figure 4.7 Drop into 6 mm glass beads with impact velocity of 4.6 m s^{-1} showing a pronounced 'tip entry effect' discussed in the text.

This effect varied between drops into the same sized glass beads; however closer investigation showed that, in general, it was proportionately greater for larger beads when the force is compared to the rest of the signature (Figure 4.8). Furthermore, the variability in the mean force increased with increasing bead size. The difference

between the mean force during and after the tip entry stage is small when the bead diameters are small compared to the size of the penetrometer tip. This is probably due to the arrangement of the beads and where the impacts occur.

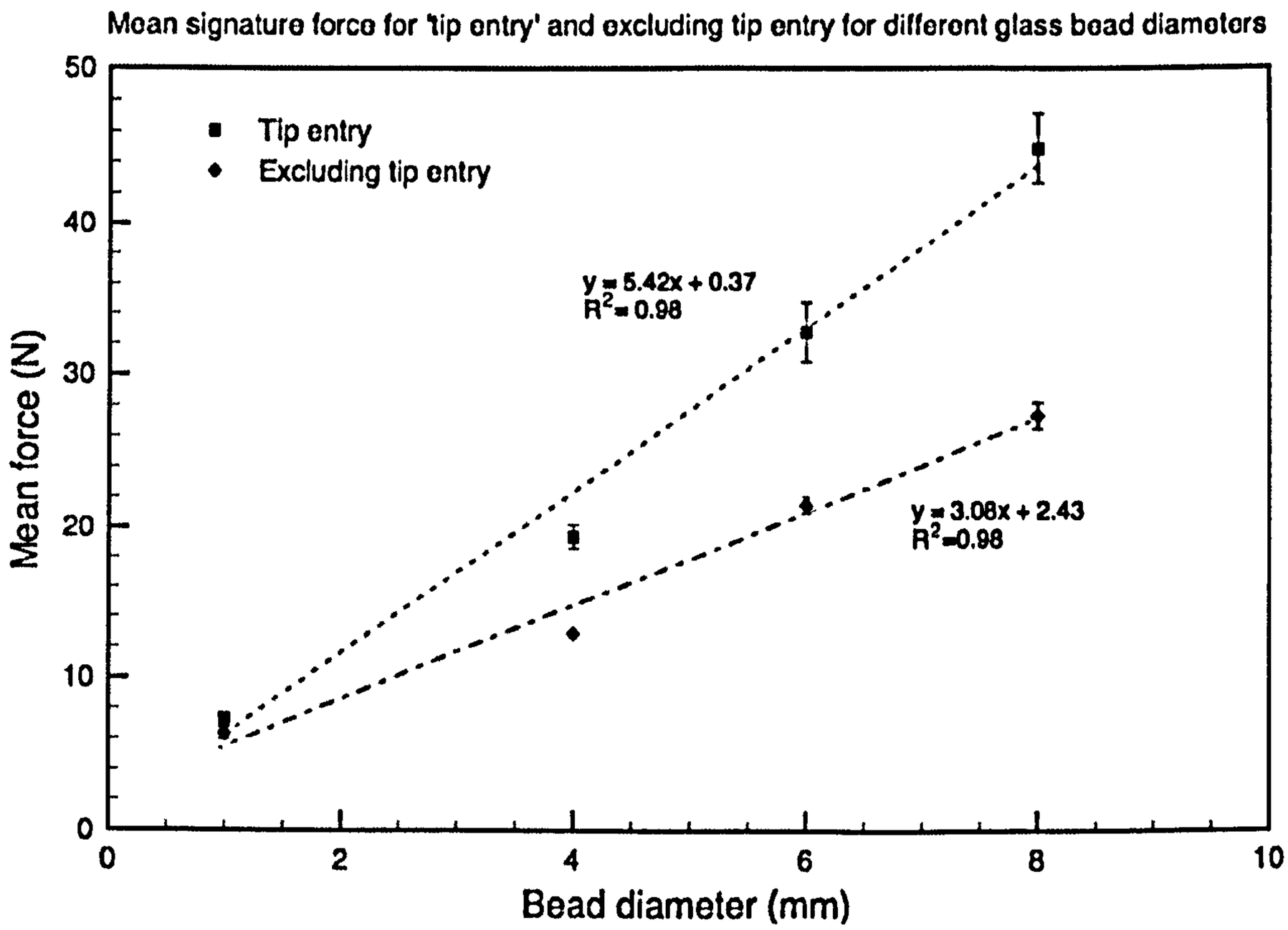

Figure 4.8 Graph of the standard deviation of penetration force for 'tip entry' compared to excluding it. Four different sizes of glass bead at 4.6 m s^{-1} impact speed were used with a total of 28 drops represented. Standard errors are plotted for each point.

One possible explanation is given by comparison of the size of the penetrometer tip to the target beads. Figure 4.9 shows the hemispherical tip immediately prior to impacting into targets of large and small beads. It can be seen that the beads which are considerably smaller than the tip consistently form a more level surface with approximately the same number of beads impacting the penetrometer tip each time. The larger penetrometer tip 'sees' the material as more of a continuum with each small bead having proportionately less effect on the tip. However, large beads whose size is comparable to the tip form an uneven target surface with variations in both the number and position of the beads impacted. After entry the tip is completely surrounded and

therefore gives a more uniform response. It has also been shown to vary due to hemispherical geometry (Paton, 2005) and these factors could explain the changes in tip effect between similar drops into larger beads.

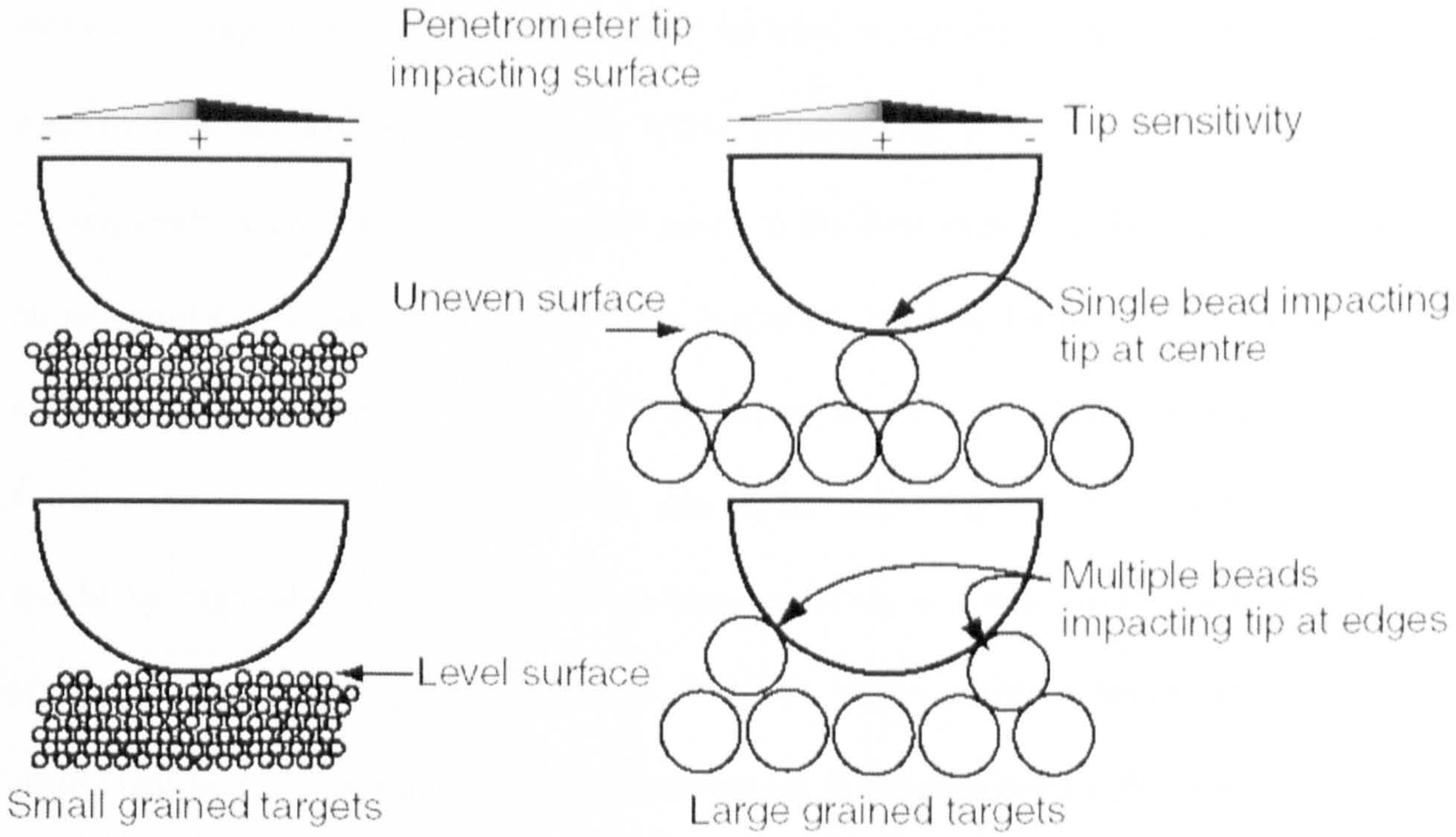

Figure 4.9 Explanation of tip entry effect for large and small beads. The small beads form a level surface relative to the penetrometer tip with individual spheres having less influence on the tip force. In contrast, very variable numbers impact the tip for successive drops into large beads and this combined with the difference in sensitivity of the tip for different impact points leads to large variations in the force felt as the tip impacts the target.

A characteristic of these granular signatures is their 'spiky' appearance. Using the glass bead data, the analysis program *penstat.m* was used to identify significant peaks and troughs in the granular signature. It first ensures that the data is stationary i.e. that no trend is included. A method commonly used in time series analysis to ensure stationarity is to difference the data (Diggle, 1990):

$$Dy_t = y_t - y_{t-1} \qquad \textbf{(Equation 4.4)}$$

where Dy_t is the first difference data generated from the original series y_t. With data that have higher orders of trend it is necessary to difference the data repeatedly to remove them (Gottman, 1981). Penetrometry signatures often contain various orders of trend so

it was difficult to verify when trends had been completely removed. A better approach for removing trend was to subtract a moving average from the data leaving only the peak/trough fluctuations. By examining several signatures, an optimum length for the moving average was found. For a 10 kHz sampled signature, a 9-point moving average was best at identifying the trends while minimising peak removal. The program subsequently searches from the impact point to the first trough in the data. To mitigate noise spikes, all consecutive rises are summed until a falling value or series of consecutive falling values is found. If the sum of the rises is greater than a threshold of 4 times the standard deviation of the preimpact noise signal (i.e. peak to trough this would be equivalent to the 95% confidence level) it is considered *significant* and the point is marked as a peak *candidate*. For this value to be accepted as a peak, an equivalent significant fall or sum of consecutive falls must follow this candidate point. A similar method is used to find the trough candidates after a significant fall or sum of falls. These are confirmed as troughs if they are followed by a significant rise. The method is illustrated in Figure 4.10 and has proved robust for the penetrometry data. The stored peaks and troughs were then used to examine the peak to trough variations and the spacing between adjacent peaks. Using this algorithm and removing the 'tip effect' from the glass bead signatures, a graph of the mean magnitude of the remaining peak/trough amplitudes for the different glass bead diameters was plotted (Figure 4.11).

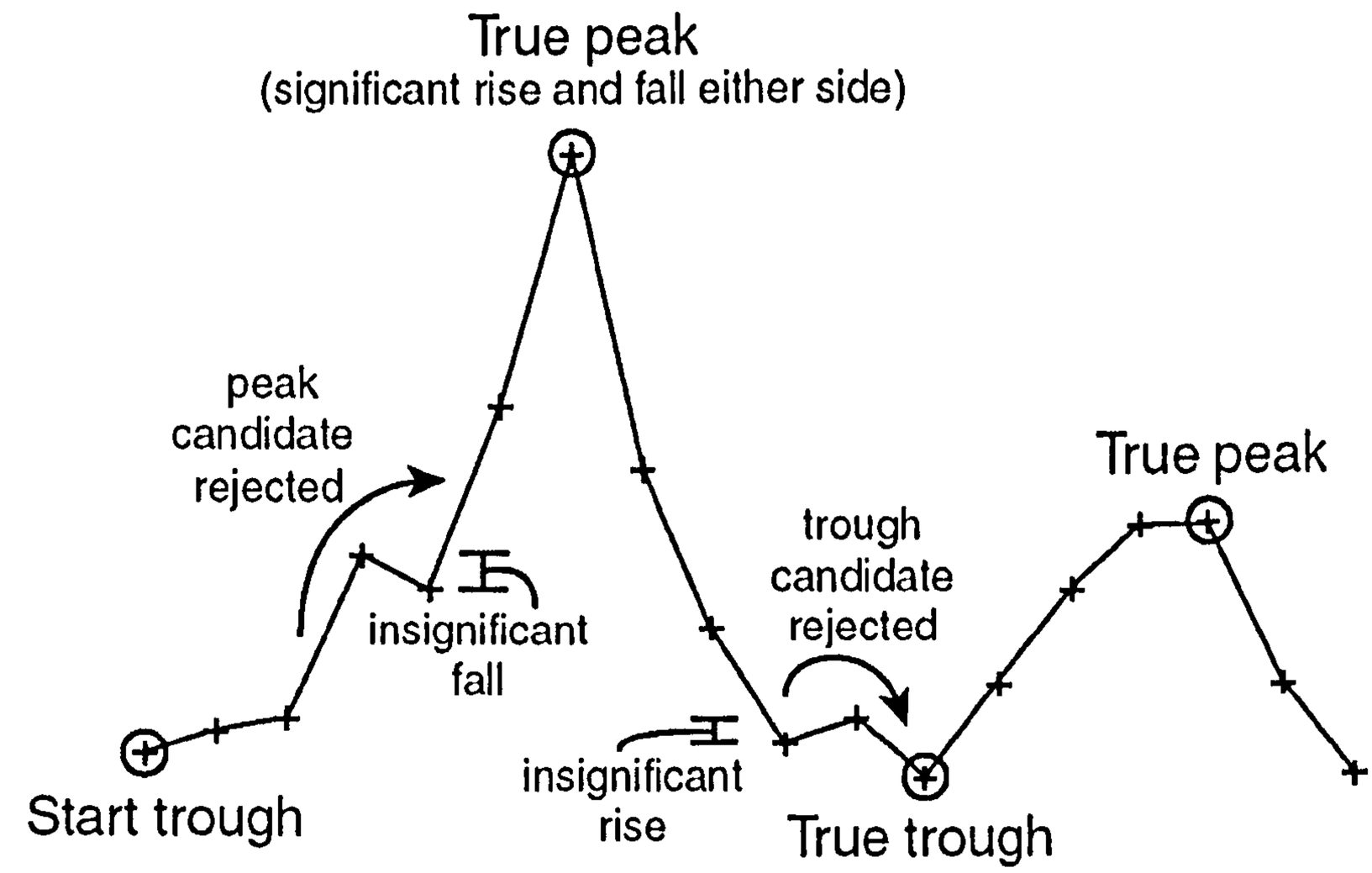

Figure 4.10 Illustration of the operation of the peak and trough finding algorithm. From a defined start trough at the beginning of the penetration, the program searches along for candidate peaks and troughs. For these to be accepted as a true peak or trough the data either side must show both a significant rise and fall. The significance is based on the standard deviation of the preimpact noise as the penetrometer falls prior to impact with the target surface.

This shows that the peak amplitudes are linearly related to bead size although in the case of the 1 mm beads the number of significant peaks detected was small due to peaks approaching the magnitude of the laboratory noise. As the beads are all made of glass of the same density this experiment does not distinguish between the size of the beads and their masses. To examine this issue further, 4 and 8 mm diameter spherical beads made of plastic were sourced from the wholesaler Grove Beads UK Ltd. and BB pellets used for air pistol ammunition were sourced as 6 mm plastic beads. These pellets are made of slightly denser plastic but are perfectly spherical within tight tolerances. Dense spherical steel shot of 2 and 5 mm diameter was also available in the laboratory in small quantities (Properties are given in chapter 3).

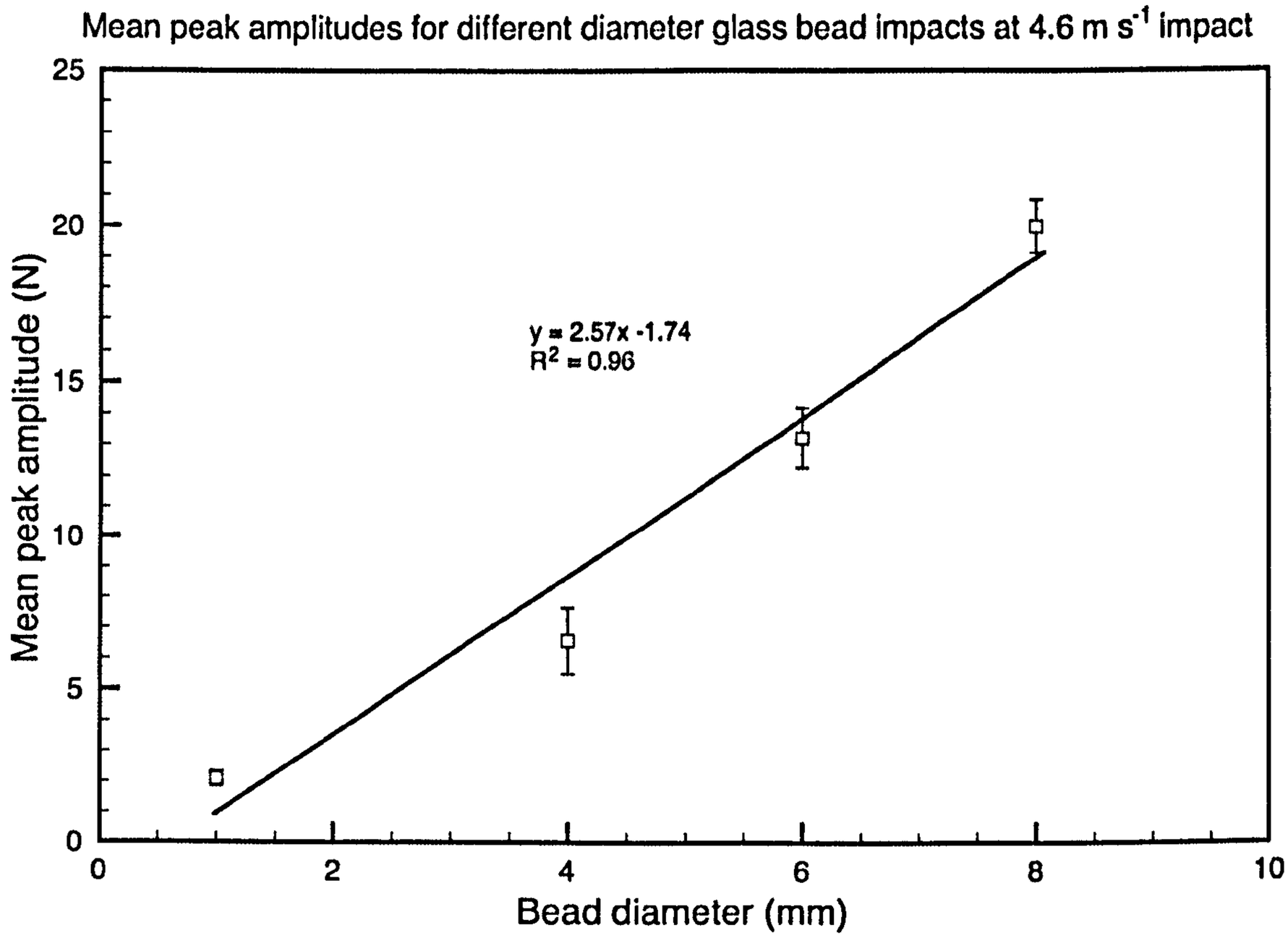

Figure 4.11 Graph of mean amplitudes of the significant peak-trough transitions against glass bead particle diameter for 28 drops at 4.6 m s^{-1} impact speed.

Unfortunately the steel shot and larger plastic beads proved difficult to source or were prohibitively expensive to buy in the quantities required to fill the target container and this placed limits on the experiment. To overcome this, all beads were poured into a smaller open bottomed cylinder (~130 mm diameter, 150 mm depth) and surrounded by loose sand (Figure 4.12). The cylinder was then removed leaving a cylindrical volume of the beads loosely confined by a sand boundary. Although these dimensions were close to the limit for which boundary effects were not seen (section 4.2), this was not ideal and for this reason drops into the glass beads with sand surround were also repeated to ensure comparability between the different materials. Drops at 4.6 m s^{-1} were made into these materials to compare the equal sized beads with different masses. After each drop, the beads were refilled and a plumb line was used to ensure that the penetrometer impacted the centre of the cylindrical volume.

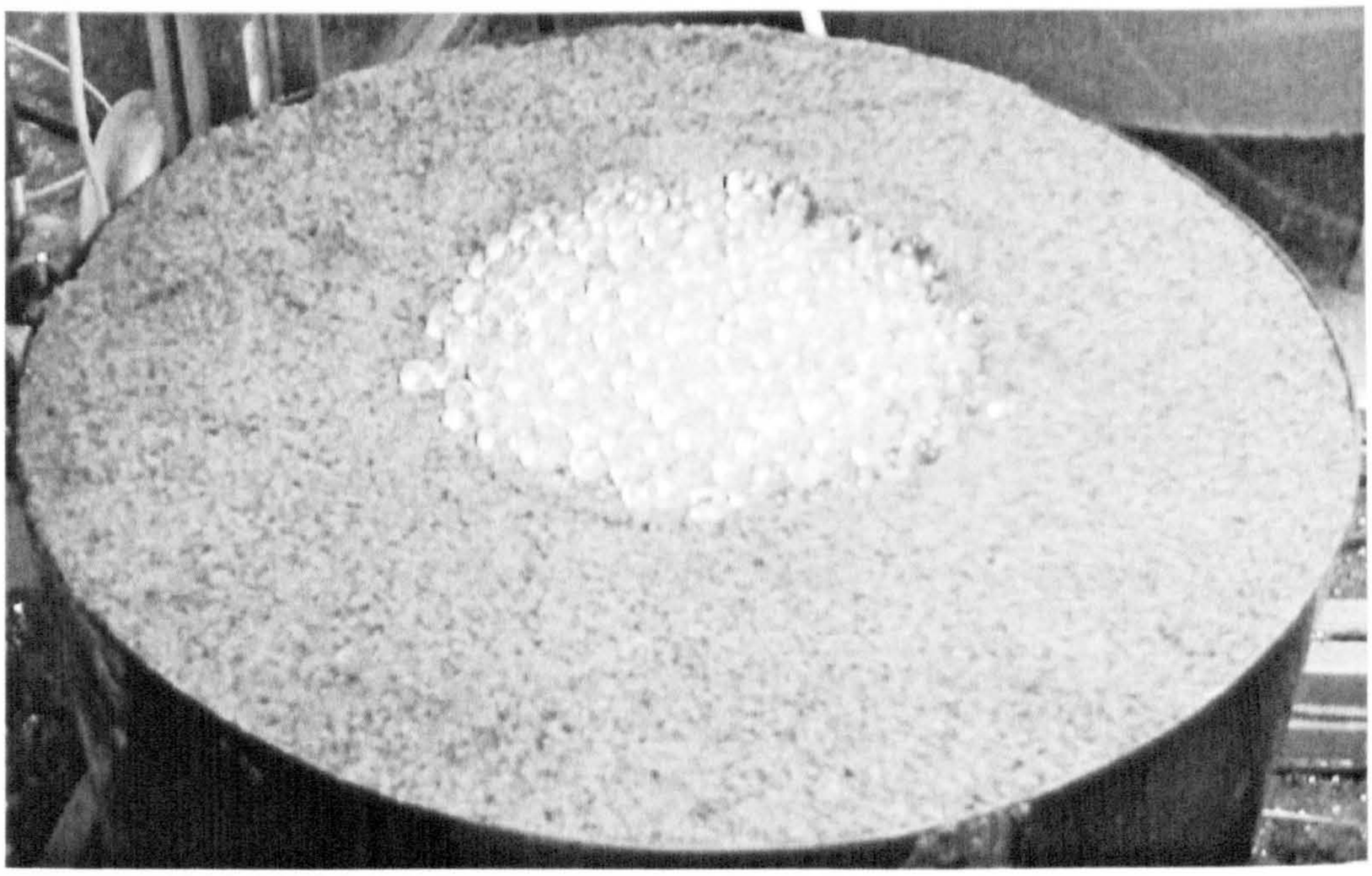

Figure 4.12 Sand surrounding a cylindrical volume of 8 mm glass beads. Due to the limited quantities of plastic and steel beads available all materials were surrounded by sand to make drops comparable. A cylinder filled with the various beads was surrounded by loose poured sand and removed prior to the test drop.

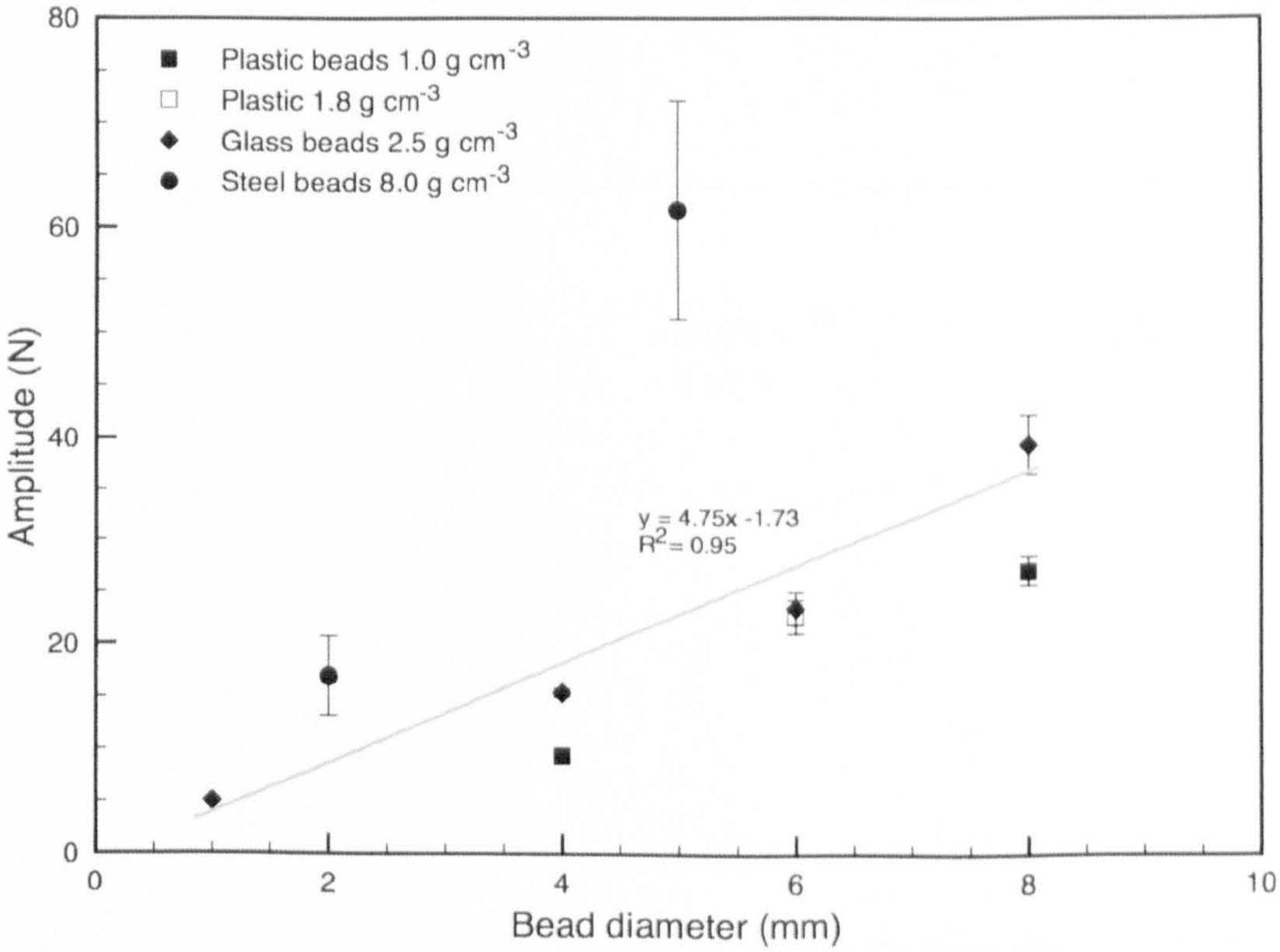

Figure 4.13 Mean peak amplitude for 39 drops into different density spherical beads. 1mm glass beads have been included although detected peak statistics were poor.

In order to reduce the effect of anomalous results caused by random errors such as a change in the electrical noise level within the laboratory, drops were repeated on each material several times. One such effect, observed on drops into 6 mm plastic beads, showed an increase in the force level immediately prior to impact of the penetrometer tip (Figure 4.15). This was due to triboelectric charging of the beads as they were poured into the target container. A grounded probe was pushed into samples before subsequent drops were performed and the metal target container was grounded. These measures removed the effect. The results for the different density bead materials are shown in Figure 4.13. The graph shows how the magnitude of the peak-trough amplitude against bead size for different density materials and shows that mass is a factor determining these peak heights. Figure 4.14 shows the same peak-trough amplitudes against the bead mass. The steel shot has been excluded from this graph because numerous peaks entered the medium gain branch of the pseudo-logarithmic amplifier.

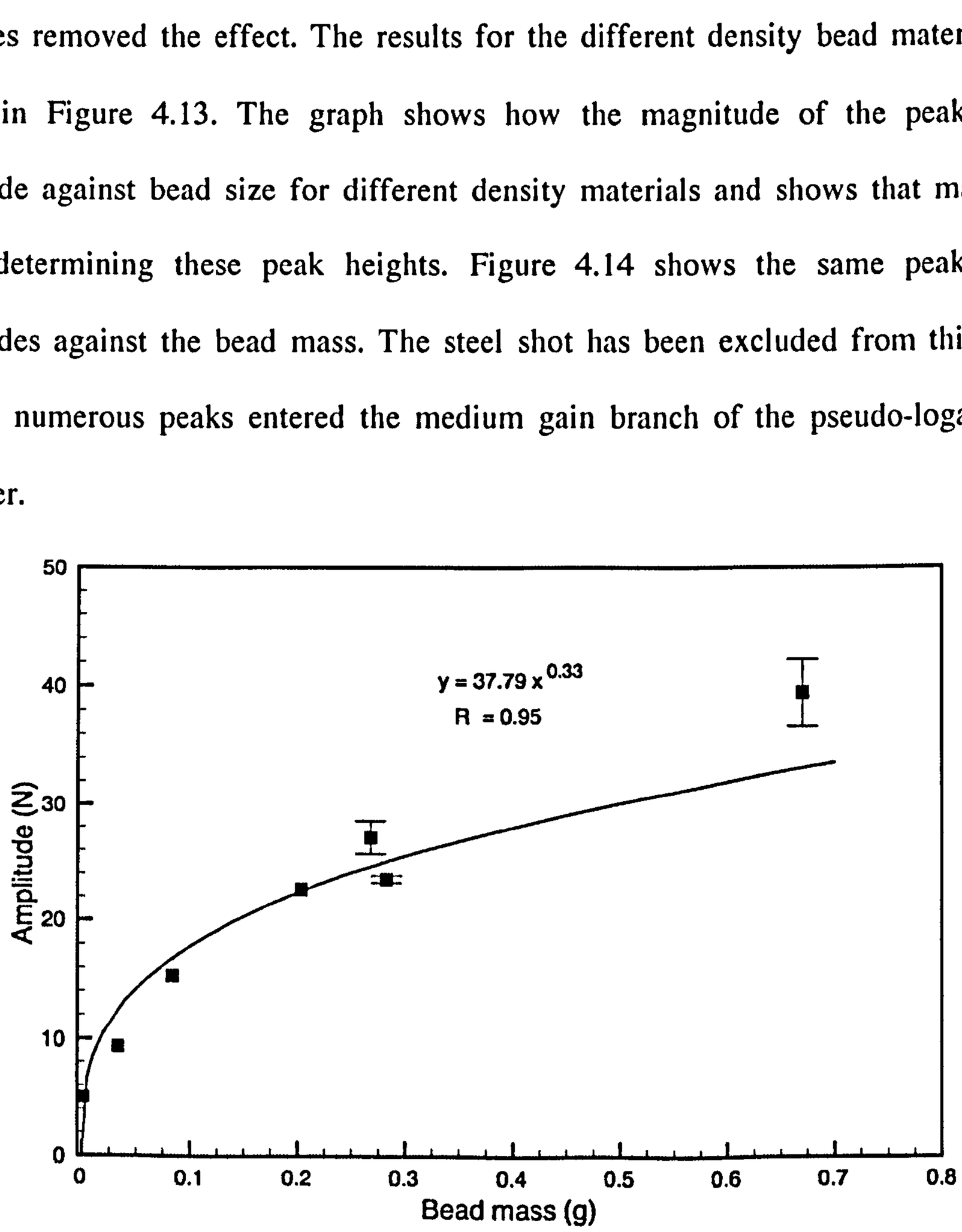

Figure 4.14 Mean peak to trough amplitudes against bead mass for the plastic and glass bead targets. Standard errors are marked.

The graph shows a good empirical relationship between bead mass and mean peak-trough amplitude for bead targets:

$$\text{Peak to trough amplitude} = 37.79M^{0.33} \qquad \text{(Equation 4.5)}$$

A further test of this result was to create a target consisting of large grained but low mass particles. Polystyrene beads ranging from 5.5-6 mm in diameter are cheap and readily available in large quantities. The target container was one third filled with compacted sand to act as a buffer. The remaining space was filled with the beads. Several drops were carried out and in each case the penetrometer failed to trigger until it had passed through the polystyrene beads and had impacted the sand below even though the oscilloscope was set to the minimum possible trigger level. This supported the suggestion that the mass, not the size of the grains is responsible for the spikiness seen in the signatures.

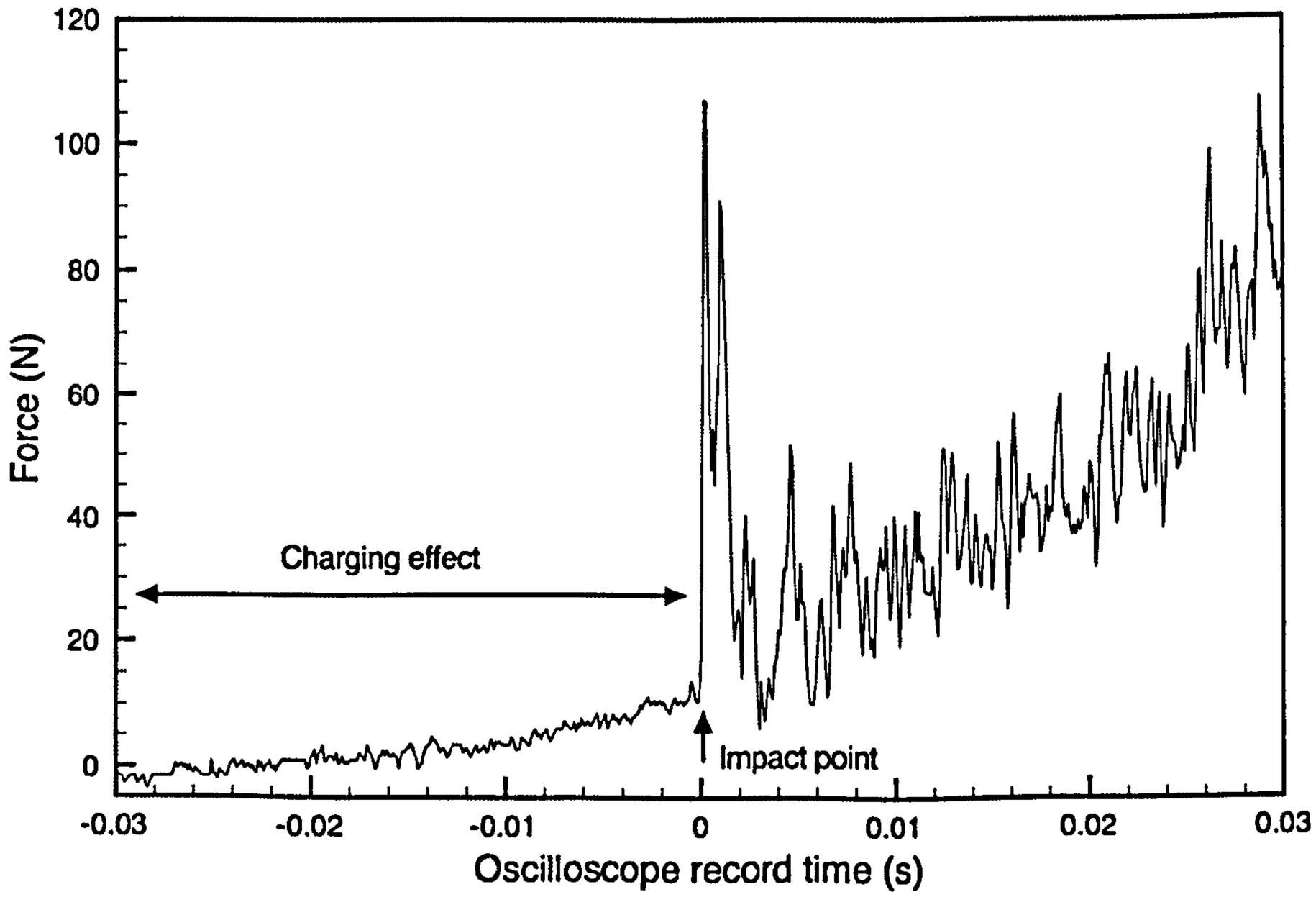

Figure 4.15 Effects of triboelectric charging of plastic beads on the sensitive charge amplifier circuit used in the ACC-E penetrometer. This effect was minimised by inserting a grounded probe in the target prior to the drop.

4.5.2 Frequency and time series analysis

Signals are either deterministic, where future values can be determined from past values using a mathematical expression, or stochastic/random that cannot be described by a mathematical rule. The penetration signals returned by ACC-E are at least partly stochastic or random due to the electrical noise present in them. Each penetrometry signature is a group of observations, of force in this case, made sequentially through time known as a *time series* (Chatfield, 2004). Analysis of these series can be carried out in the time or frequency domain and this is one of the most widely used methods of examining stochastic signals.

The previous section examined how the amplitude of the peaks seen in a signature relates to the small-scale grain structure of the material. It is also of interest to investigate how these peaks are related in time (and equivalently, depth). The signatures were first investigated in the time domain by examining their autocorrelation and then in the frequency domain using the related power spectral density function.

The autocorrelation function measures the dependence of the signal at a given time to the same signal at some later time. Data are autocorrelated if later observations have some predictability based on examining earlier values (Gottman, 1981). A signal from a material sample with a similar grain size throughout might be expected to have repetitions along its length. This would show positive autocorrelation.

The autocorrelation function was applied to the signatures for the various glass and plastic bead sizes after first correcting for stationarity using a 9-point moving average. Correlograms (Figure 4.16) are plots of the autocorrelation coefficients against different time delays or *lags*, and indicate whether any of the lags are significant. No consistent significant lags were identified for all drops of the same bead size.

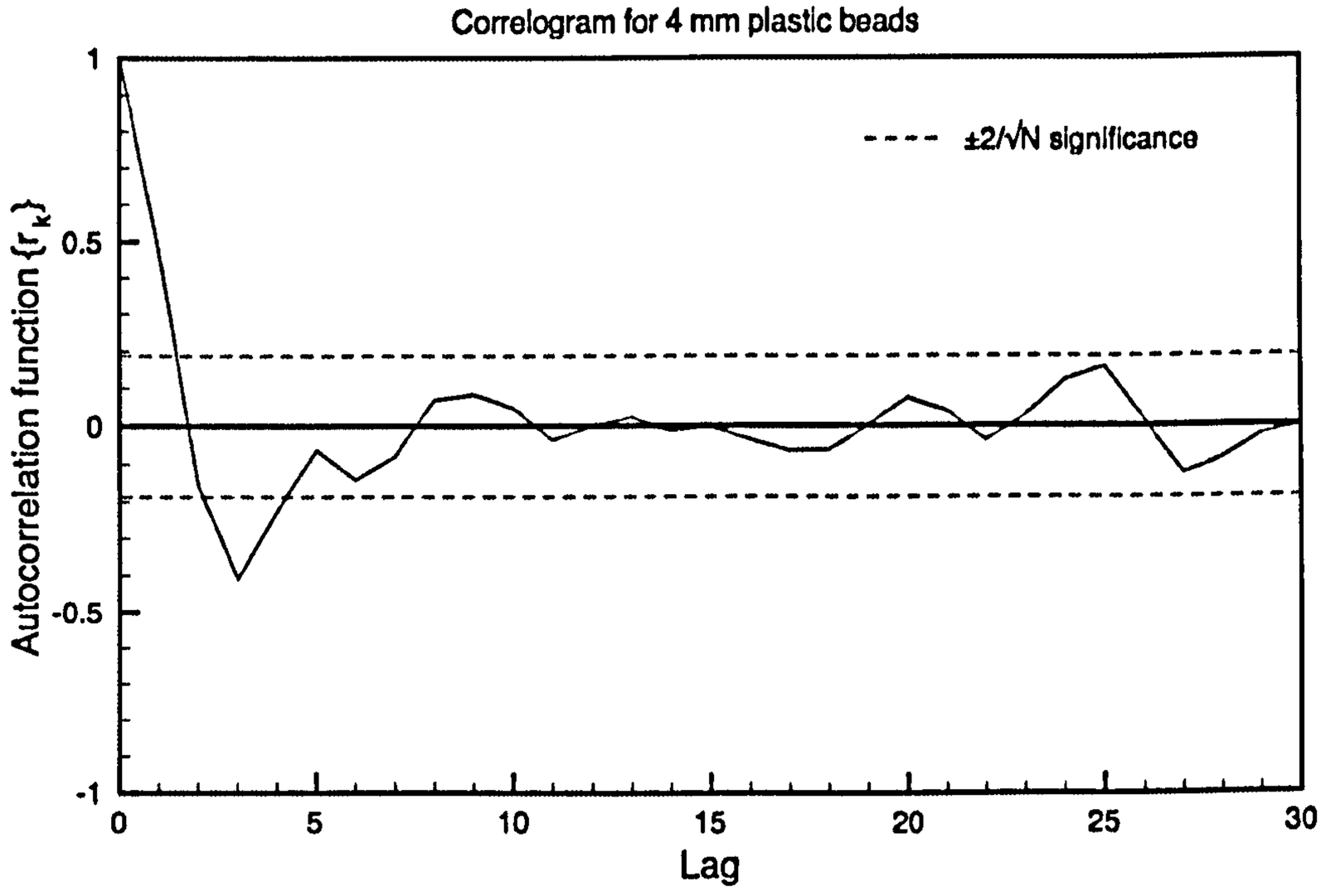

Figure 4.16 Example correlogram for 4 mm plastic beads. No positive autocorrelation is seen above the significance level marked.

Recent quasi-static work by Kargl (2005) suggests that the frequency content of a signature may enable small-scale material structure size to be found, while other workers suggest it may allow other material parameters such as density to be determined (Butterfield and Mahmoud, 1989). To examine the faster, dynamic ACC-E penetration data for frequency content, a program freq.m was written.

The power spectral density (PSD) characterises which frequencies contain the power of a signal, or equivalently, the frequencies that contribute to the variance of the time series (Chatfield, 2004). It is defined as the power per frequency interval:

$$PSD = \frac{|X_n|^2}{f} \qquad \textbf{(Equation 4.6)}$$

where X_n is the signal's Fourier transform and f is the frequency. The method used estimates the PSD by calculating the square modulus of the Discrete Fourier Transform (DFT) of the signal using the Fast Fourier Transform (FFT) algorithm. First, as with the time domain analysis, any offset or trend is removed to produce a stationary time series.

Trends are variations longer than the signature length and would not be resolved properly resulting in the distortion of the low-frequency end of the estimated spectrum (Eriksson, 2000). The result is a *periodogram* showing the power spectral density that has a frequency range and resolution defined by the sampling frequency and total number of samples (Brooke and Wynne, 1988):

$$\text{frequency resolution } (\Delta f) = \frac{1}{\text{period of window } (T)} \text{Hz} \qquad \textbf{(Equation 4.7)}$$

where in the case of the simple periodogram the period of the window covers the complete length of the finite signal. In terms of the sampling frequency, f_s, and total number of samples, N, this can be rewritten using $f_s=N/T$ as:

$$\Delta f = \frac{f_s}{N} \qquad \textbf{(Equation 4.8)}$$

and the positive half of the frequency range is given by:

$$f_+ = \frac{\Delta f . N}{2} = \frac{f_s}{2} \qquad \textbf{(Equation 4.9)}$$

As the discrete Fourier transform approximates the finite penetrometer signal by an infinite Fourier series, this periodogram would suffer from *spectral leakage* where some of the power of the signal at a given frequency spreads into adjacent frequencies. It is caused by the finite penetrometer signal that is sharply truncated at both ends not being periodic. The DFT assumes that this input signal is one complete period of an infinite waveform. This assumption is rarely true and the sharp discontinuity of the signal at the ends causes the leakage. By multiplying the data with a special window function that smoothly decays at the signal boundaries, this effect is reduced. The PSD of the resulting *modified periodogram* is then normalised to account for the attenuating effect of the ends of the windowing function.

The resolution condition (Equation 4.7) effectively limits the ability to determine

accurately individual frequency components within the short ~20 ms ACC-E penetrometry signature. A recommended minimum of between 100 and 200 samples is required for a reasonable estimate of the spectrum as with smaller N values only larger peaks can be found (Chatfield, 2004). For the ACC-E penetrometer length of ~8 cm impacting at 4.6 m s^{-1}, N=174 samples and this is on the limits of applicability of spectral analysis with the best resolution of 58 Hz. Despite this limitation, it is still possible to examine the overall frequency structure of the signature up to the Nyquist limit set by the 10 kHz sampling rate. The FFT algorithm requires the input data to be a factor of two in length. Where this is not the case the signal is padded by adding zeros. The resulting spectrum is smoothed but does not increase its resolution and the additional signal length must be accounted for in the normalisation since the added zeros do not contribute to the power of the signal.

Using a single time record in the above method is at best a reasonable estimate of the true spectrum. To improve the estimate, the spectral components from several time records can be averaged together to produce an ensemble average (Brooke and Wynne, 1988). This is the basis of the Welch method which divides the signal into windowed records and computes the squared magnitude of the DFT of each one separately. The resulting periodograms are then averaged. This reduces spectral leakage and improves the spectral estimate but reduces frequency resolution due to the shorter signal time interval and results in the loss of signal power at the tapered ends of the window. By first overlapping the windows, this power loss and also the effect on frequency resolution is reduced. Thus there is a trade off in the Welch method between spectral resolution and statistical stability. In all analysis, a 'standard' overlap of 50% was used. In order to examine the noise for a given signature, the preimpact signal was used to

calculate a spectrum. No frequency content was seen except for a peak occurring around 50 Hz caused by the mains hum. By detrending the data using a moving average before examining frequency content, this mains noise was removed. The periodograms for each of the signatures into the 4 different glass beads were then calculated using the Welch method and seven repeated drops of each were then averaged together. The results are shown in Figure 4.17. It can be immediately seen that despite the relatively poor resolution of each periodogram the overall shape and power distinguishes the different sized beads. The signatures from the 8,6 and 4 mm beads have the majority of their spectral power located between ~1-2 kHz with the 8 mm beads dominating over all frequencies but notably also between 4-5 kHz. As might be expected, the spectrum for the 1 mm beads is flat with no noticeable frequency content. It also appears that the 8 and 6 mm glass bead may share similar bands of frequency content although resolution is limited.

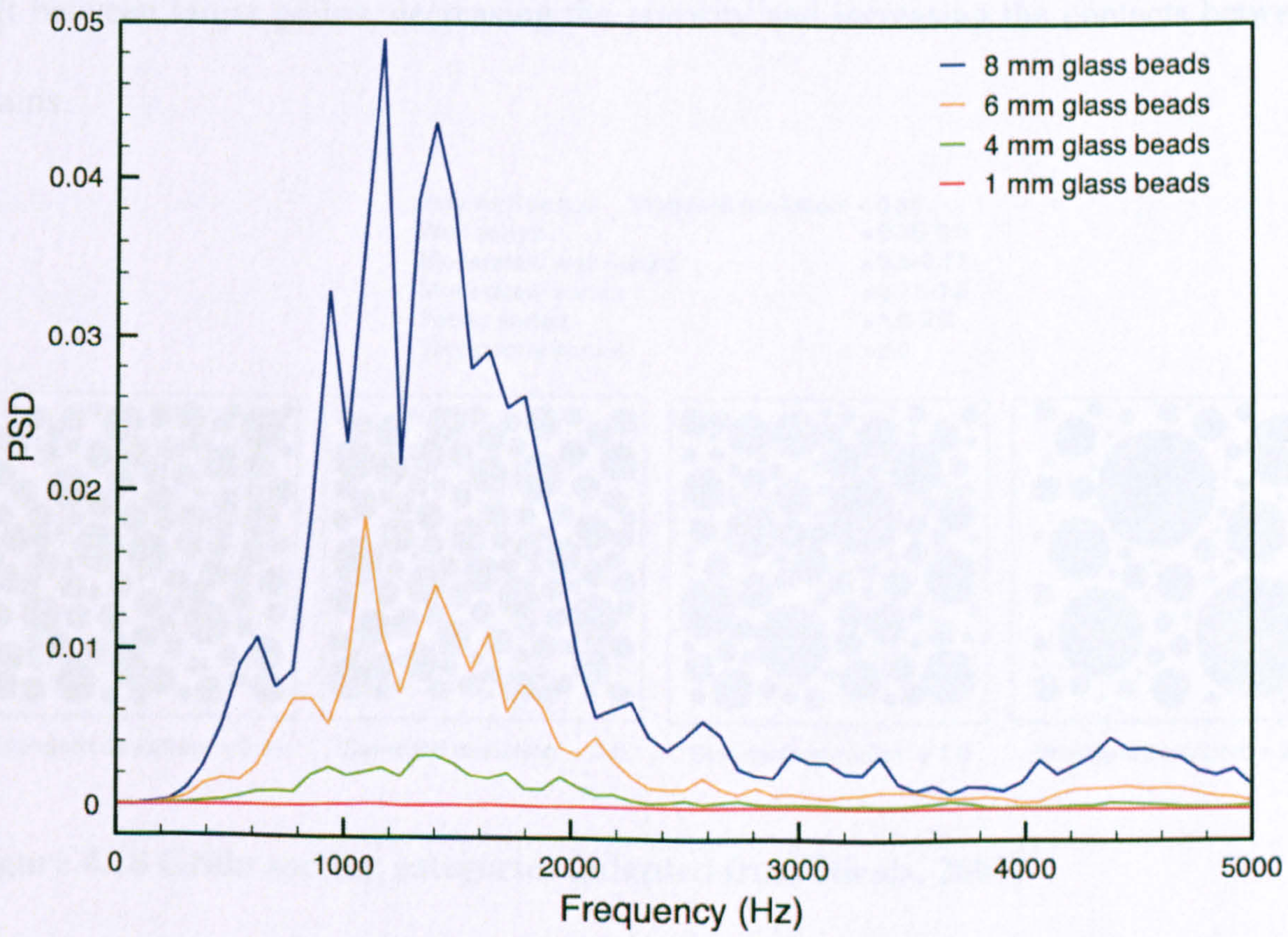

Figure 4.17 Modified periodograms for the 4 sizes of glass beads. No low frequency content is seen as the input data were first detrended by a 9-point moving average.

4.6 Layering and sorting

4.6.1 Sorting

The term *sorting* is a description of the range of the grain sizes present in a sedimentary material. A sedimentary material can vary between *well-sorted*, where the grains present have a narrow size range typically falling into one class of the Udden-Wentworth scale, through to a *poorly-sorted* deposit containing a wide range of sizes. The degree of sorting is determined in part by transportation, with increasing distance and agitation progressively dividing the sediment (Nichols, 2001). A sample sieve analysis allows the material to be categorised into one of the sorting classes shown in Figure 4.18 given by the standard deviation of the grain size distribution data.

The sorting of the grains is one factor likely to affect the resistance of the material with poorly sorted granular material containing smaller grains that are able to fill in the voids left between larger grains, decreasing the porosity and increasing the contacts between grains.

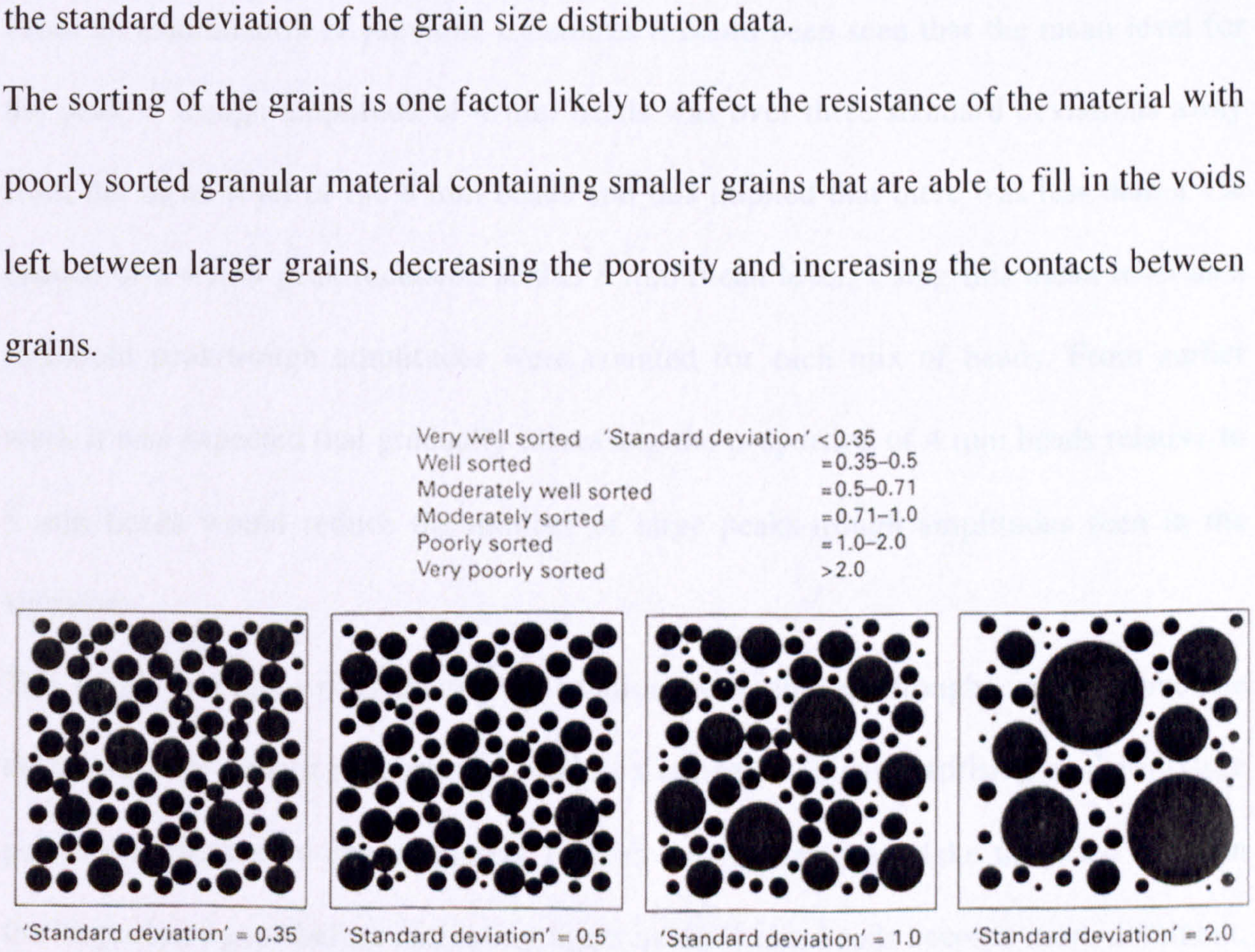

Figure 4.18 Grain sorting categories (adapted from Nicols, 2001)

An experiment was carried out to look at how changing the sorting by varying the proportions of two glass bead sizes relative to each other might be identified in the

penetrometry signature. Smaller 1 mm beads were first considered; however they quickly fell through the gaps leaving the top of the target virtually devoid of them. For this reason the two bead sizes chosen were 4 mm and 8 mm. The beads were mixed by mass in proportions of 8mm/4mm as: 100/0, 75/25, 50/50, 25/75 and 0/100 and a minimum of 5 drops were carried out into each mix at 4.6 m s^{-1}. The bulk density and porosity of each mix is given in Table 4.6.

Bead mix % (8 mm/4 mm)	100/0	75/25	50/50	25/75	0/100
Approximate Bulk density, ρ, (g cm^{-3})	1.50	1.60	1.61	1.55	1.50
Porosity, ϕ, (%)	39	36	35	38	39

Table 4.6 Bulk density and porosity of the various glass bead mixtures.

From an examination of previous signatures it could been seen that the mean level for the peak to trough amplitude of 4 mm beads was over three standard deviations away from the mean level of the 8 mm beads and this implied that there was less than a 1% chance of a 4 mm peak incursion at this 8 mm mean level. Using this mean level as a threshold peak/trough amplitudes were counted for each mix of beads. From earlier work it was expected that gradually increasing the proportion of 4 mm beads relative to 8 mm beads would reduce the number of large peaks-trough amplitudes seen in the signature.

The graph in Figure 4.19 shows the relation between peak/trough counts above the threshold level against proportional bead mix is linear. This is surprising as the mixture porosity decreases by approximately 12% as the smaller beads take up space between the larger bead gaps before increasing again as the 4 mm beads become more dominant. This suggests that the peak to trough amplitudes are not affected by porosity but only by particle mass.

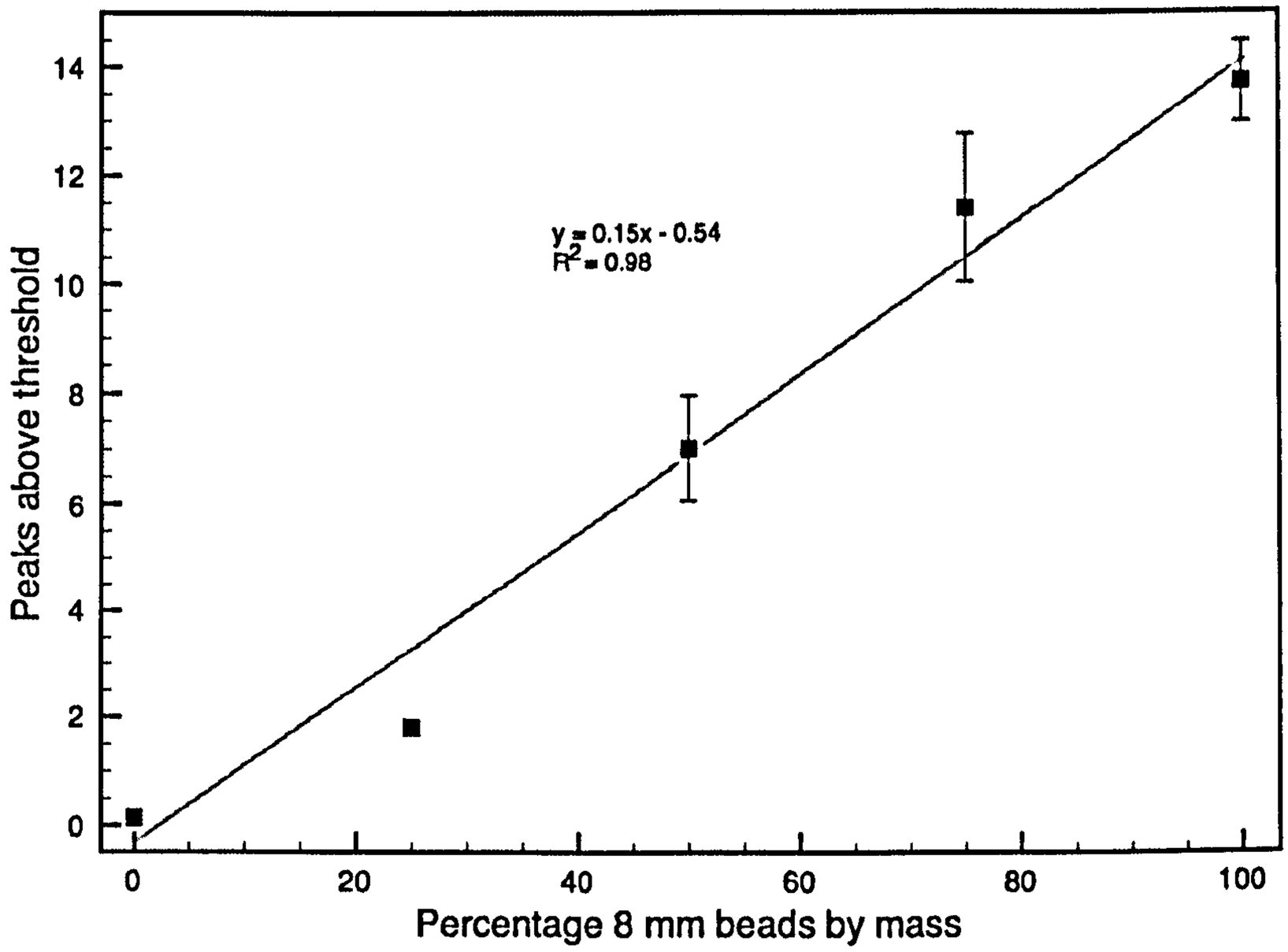

Figure 4.19 Number of peak amplitudes detected above a threshold set by the mean of the 8 mm beads.

4.6.2 Graded Bedding

Fluvial deposition of granular materials can lead to characteristic size sorting of grains with depth. This effect, known as graded bedding, is due to changes in the flow velocity of the transporting liquid (Nichols, 1998). Terrestrially both *normally graded* beds that exhibit grain size coarsening with depth and *reverse or inverse graded* beds where material becomes finer with depth have been observed (see Figure 4.20). Normal grading, terrestrially the most common type, is typically the result of a decrease in the flow velocity of the transporting liquid (Tucker, 2001). As the energy of the flow decreases, the coarsest (generally heaviest) particles are not able to be carried further and are deposited. As the flow continues to decrease in velocity, increasingly finer material is set down. Reverse or inverse grading is less common and is caused by gradually increasing flow strength. This is seen for example in the thin layers (*Laminae*) deposited on beaches by the swash-backwash (Tucker, 2001).

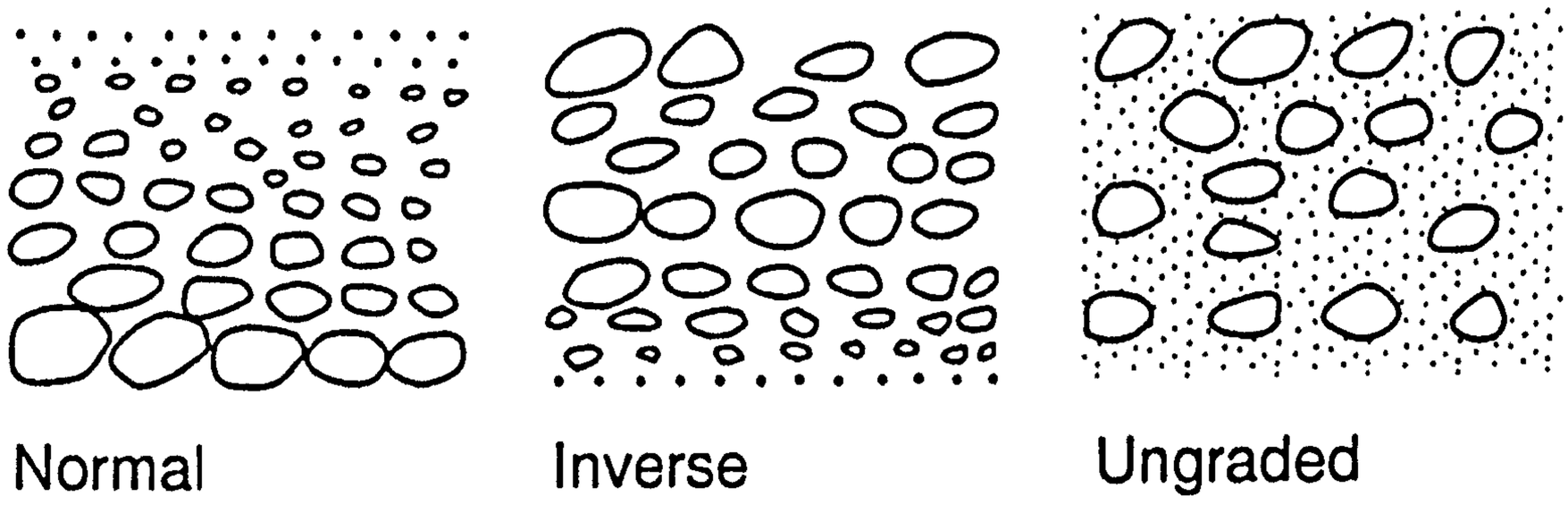

Figure 4.20 Graded beds exhibit a particle size that either increases (Normal) or decreases (Inverse) with depth. (From Tucker, 2001)

Investigations of gravel bed streams on Earth have found that these different grain stratification regimes are often associated with the flow characteristics of a stream. Perennial streams are commonly found in humid areas where thunderstorms of low or medium intensity occur regularly. The constant flow of water in these streams tends to remove the finer grained material leaving a coarser surface layer. This contrasts with the opposite grading found in ephemeral streams. This type of stream occurs in arid areas where infrequent, torrential rainstorms occur (Almedeij and Diplas, 2003). The geological interpretation of this type of structure is a topic of active research and beyond the scope of the work presented here, however the ability of a penetrometer to detect this structure is of interest as supportive evidence for interpretation.

To investigate grading, drops at 4.6 m s^{-1} were made into arranged layers of the four available glass bead sizes. These ~20 mm surface layers were prepared in increasing or decreasing bead size to represent a normally or inverse graded material. Thin paper disks were placed between each layer to keep the different bead sizes separate. To represent an ungraded target, the four sizes of bead were mixed in equal proportions. The periodograms for targets of a single bead size (section 4.5.2) demonstrated that frequency content can be used to distinguish different glass bead size and therefore to

examine material grading, the change in this frequency content over time was considered. This was done by producing spectrograms, made by dividing the signal into overlapping slices, determining their spectra and plotting them against time.

The possibility of determining the time at which certain frequencies occur does have restrictions. There is a compromise in this time-frequency analysis between the resolution of frequency content and locating the time where that content occurs. Equation 4.5 defined the frequency resolution of a periodogram i.e. considering the complete length of the signal. For a signal of N points in length sampled at a rate f_s, the resolution has been shown to be $\Delta f = \frac{f_s}{N}$ when considering the complete signal. The time resolution is equal to the number of samples in the signal divided by the sampling rate:

$$\Delta t = \frac{N}{f_s} \qquad \textbf{(Equation 4.10)}$$

This shows that better resolution in frequency must necessarily result in poorer time resolution and vice-versa (see e.g. (Eriksson, 2000)). Therefore, when examining how the frequency content of the short ACC-E signal varies during penetration it is only possible to look at how the overall spectrogram changes.

The first spectrogram (Figure 4.21) shows the importance of removing a trend before examining frequency content. Along the bottom of the spectrogram, a high power band of low frequencies pervades across all times, making any other frequency content hard to discern. After removal (Figure 4.22) clear structure can be seen despite the poor frequency resolution (the colour map now has greater contrast). In this drop the penetrometer entered a positively graded target; at first, very little spectral power is seen at any frequencies with the exception of that caused by the tip effect.

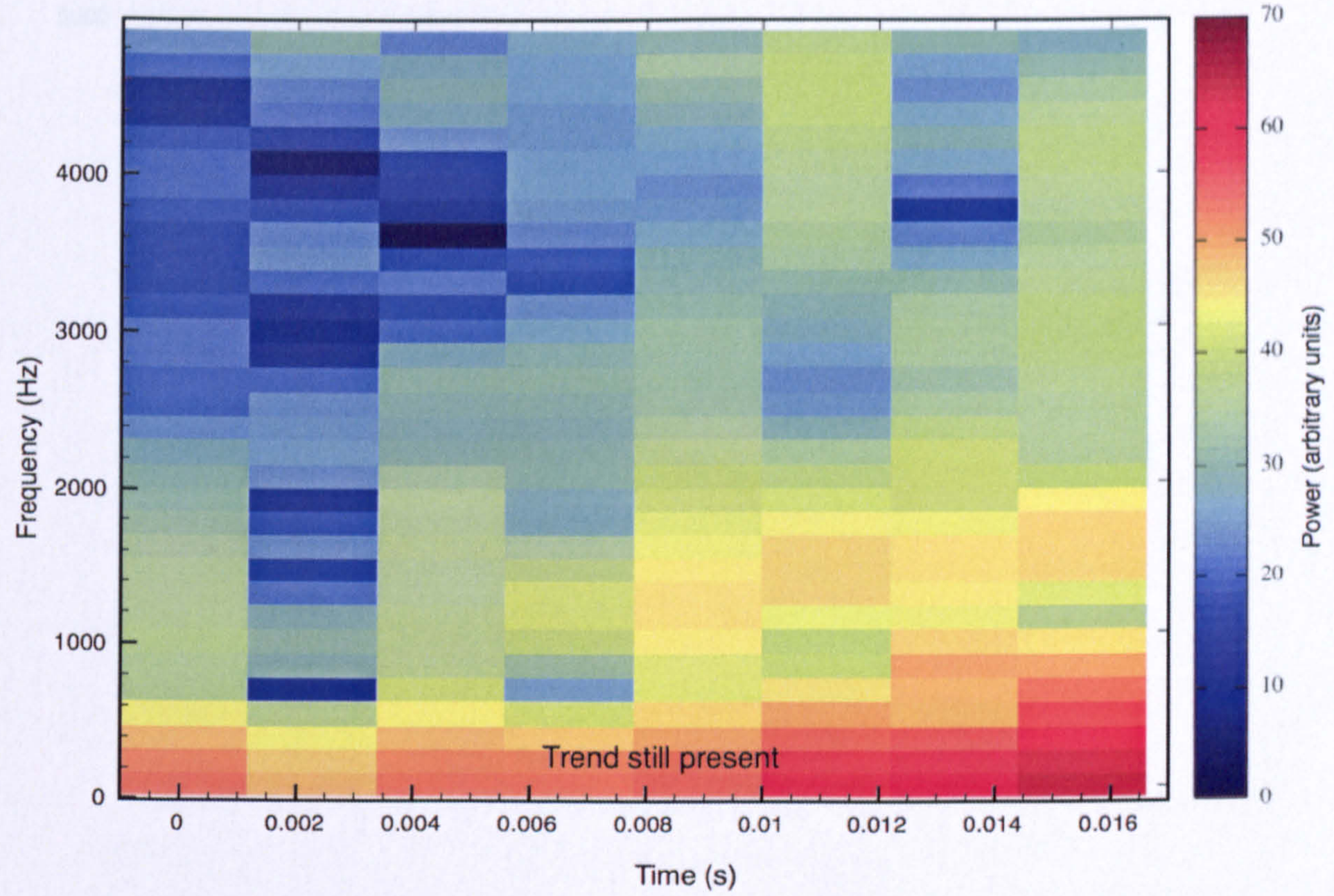

Figure 4.21 Spectrogram for positively graded glass beads where low frequency trends have not yet been removed. The large power in these frequencies swamps detail over the colour map range.

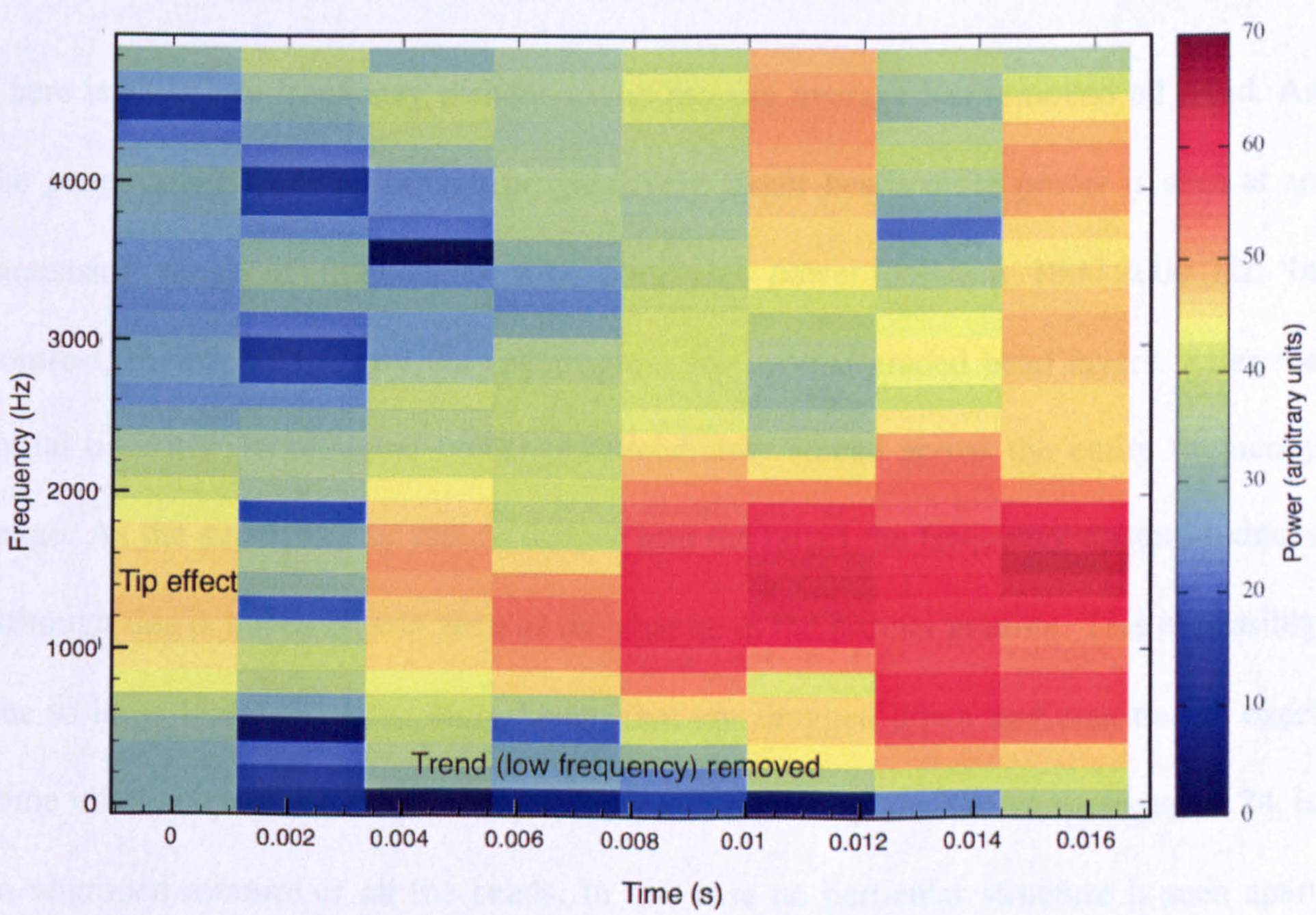

Figure 4.22 Normal graded glass bead target after low frequency trend removal. An initial tip entry effect can be seen at the beginning of the spectrogram

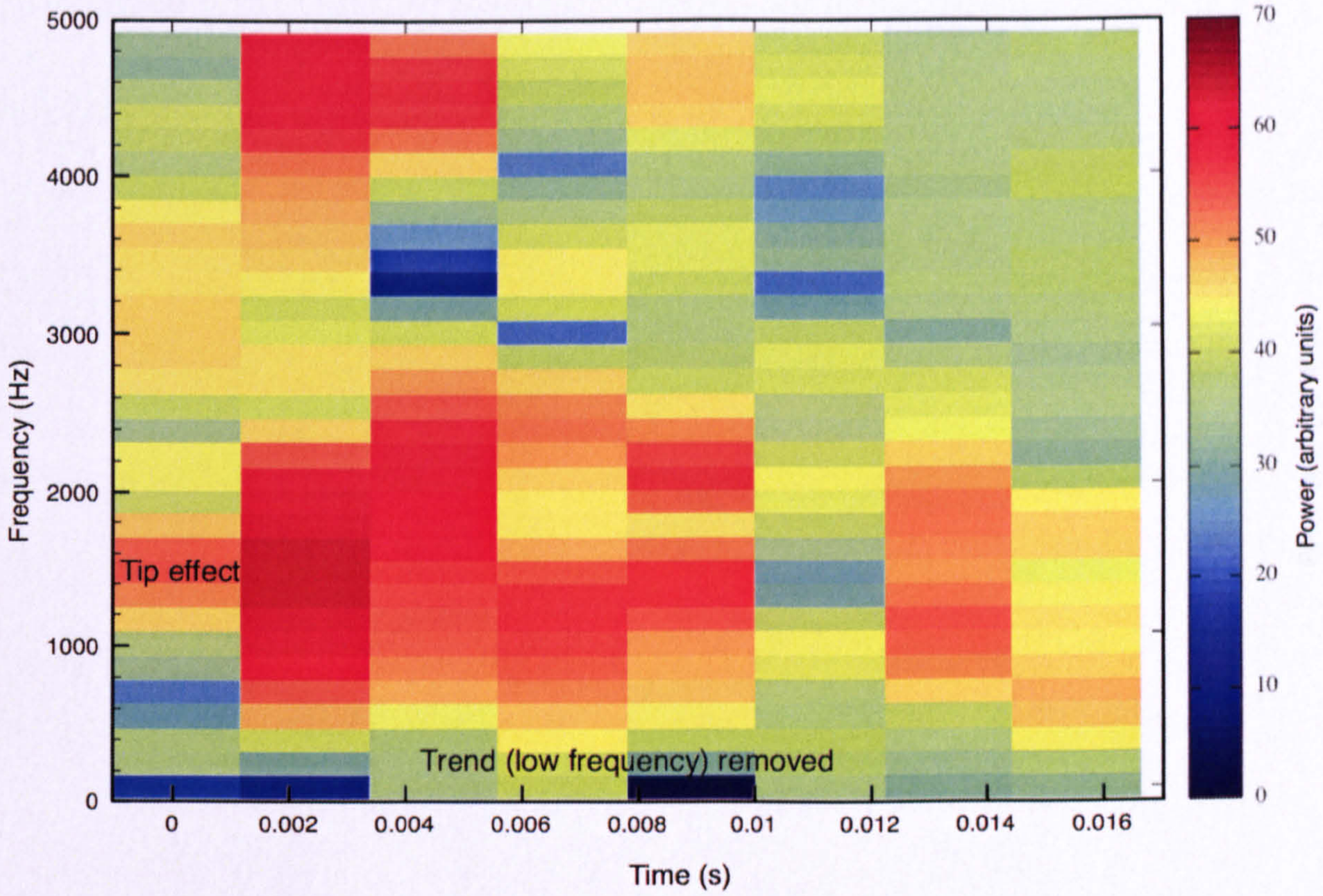

Figure 4.23 Inverse graded bead target. Frequency content is gradually lost with depth penetrated.

There is little low frequency content as the moving average has removed all trend. As the penetrometer moves through progressively larger beads more power is seen at an increasing range of frequencies with particular power between 1000-2000 Hz. In contrast, Figure 4.23 shows the spectrogram for inverse graded bead layers. After the initial tip entry, large signal power is immediately spread across the entire frequency range. As the penetrometer moves deeper into the target the frequency content reduces although this is not as clearly seen as the change in the normal grading. This is possibly due to large beads from the early layers that are dragged down and continue to exert some influence on the penetrometer tip. The final spectrogram, shown in Figure 4.24, is an ungraded mixture of all the beads. In this case no particular structure is seen apart from most of the power being contained in frequencies between 800-2000 Hz.

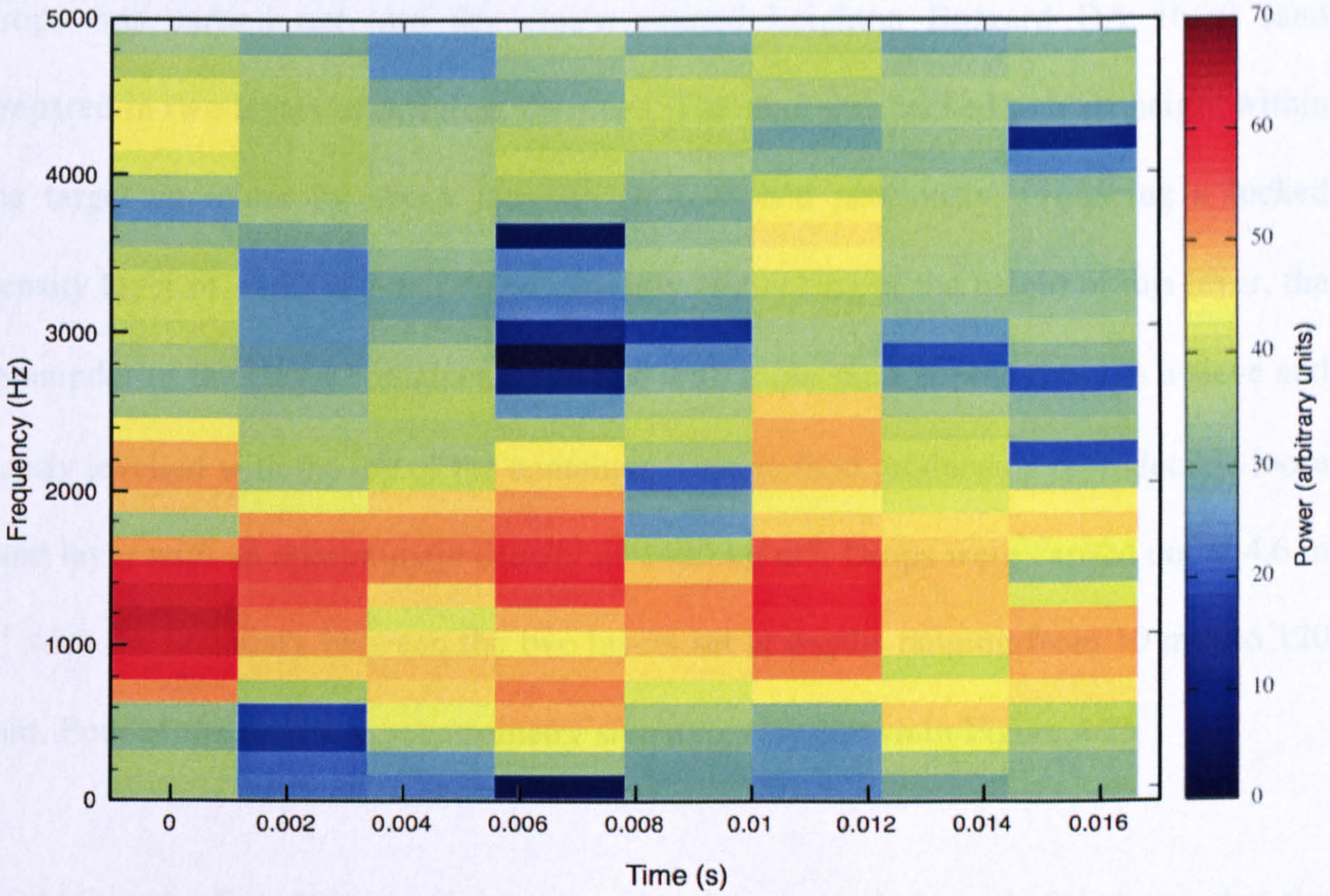

Figure 4.24 An evenly mixed ungraded target. No particular structure is seen.

The artificial targets used in this experiment consist of only four, well-separated grain sizes that have layer thicknesses carefully chosen to suit the penetrometer. On Earth, such beds would usually contain many grain sizes that vary smoothly in size with depth and therefore the targets in this experiment can only be simple representations of graded beds. Nevertheless, the spectra shown above demonstrate that distinguishing between the different types of grading is possible providing the changes in grain size are reasonably large within the depth penetrated.

4.6.3 Layering

In nature, layering can be produced by different materials overlying each other, sorting of a single material according to its grain size and also by variations of density within a single material. To investigate the response of the ACC-E penetrometer to layered targets and how well it could locate and distinguish these types of layers, a series of

drops was carried out into dry coarse-grained Leighton Buzzard DA 16/30 sand prepared in two layers of different densities. The sand was packed to a set height within the target container by shock tamping as described previously, producing a locked density layer of ~1600 kg m^{-3}. After carefully rechecking of the height of this layer, the remainder of the target container was filled with loose sand poured through a sieve and gently levelled with the top of the container. This method produced a reproducible loose sand layer with an approximate density of 1400 kg m^{-3}. Drops were carried out at 4.6 m s^{-1} with the boundary between the two layers set at depths ranging from 10 mm to 120 mm. Four of the resulting penetrometry signatures are shown in Figure 4.25.

Excluding the first 10 mm of tip entry, the signatures a), b) and c) indicate that the density boundary has no immediate effect with little change in force until the penetrometer approaches the denser layer. Within 1-1.5 cm of this boundary the force begins to rise steadily by ~20 N as seen clearly in b) and c). This shows that the density boundary influences the force detected a short distance before it is actually reached by the tip. In Figure 4.25 a) when the boundary is at 90 mm, the limits of the penetrometer where the small base plate has already impacted, it can be seen that the rise is not completed before the weight impacts. When the loose sand layer is only 10 mm thick, any rise is totally masked by the tip entry characteristic although the subsequent signature is constantly at 40 N (Figure 4.25 d). The drops involving thicker layers of loose sand also show a slightly increasing resistance with depth before the onset of the dense layer is detected. This is in contrast to the force experienced as the tip passes through the dense layer and is probably due to slightly increasing density caused by the weight of the overlying material known as *overburden pressure.*

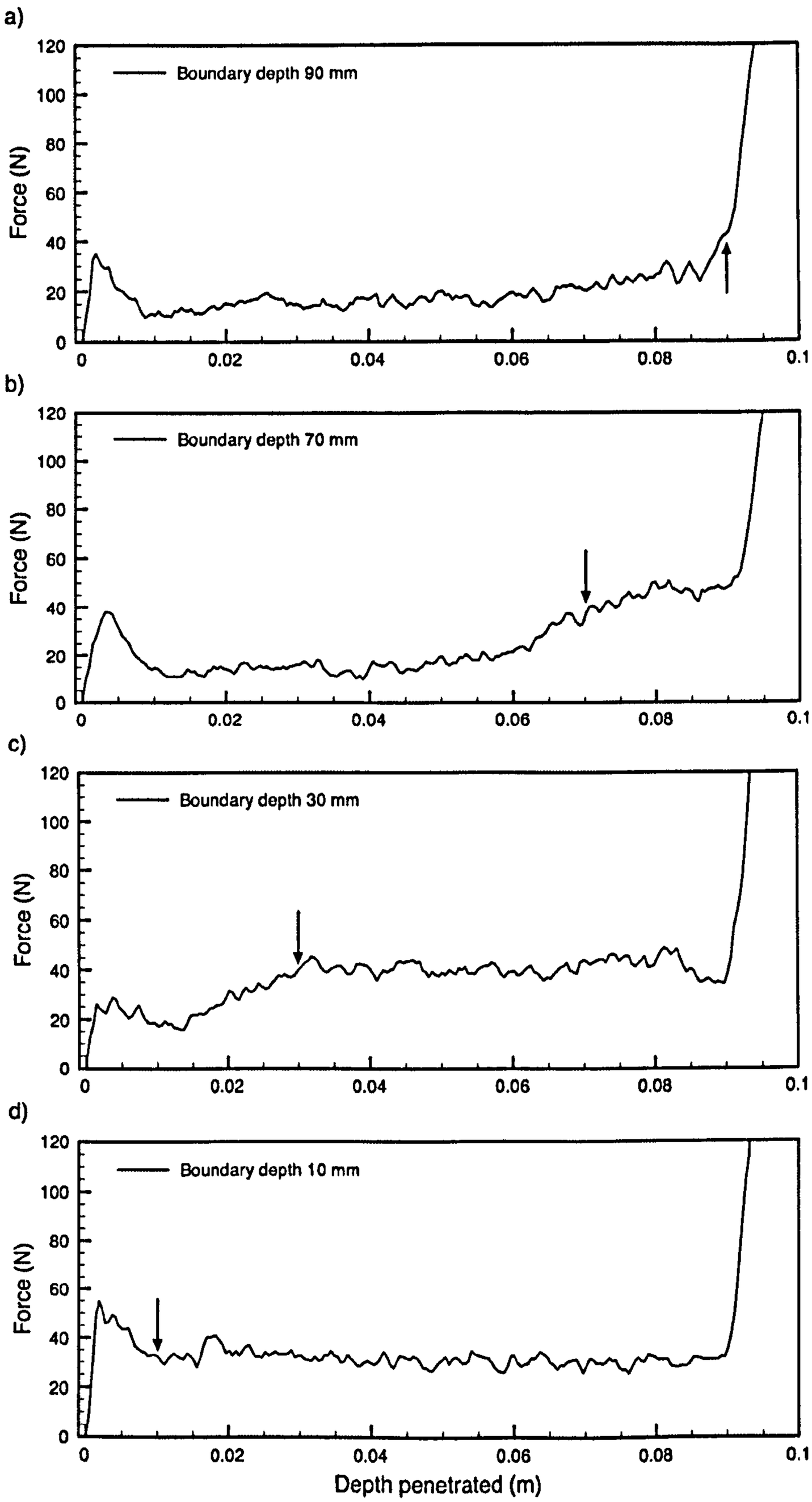

Figure 4.25 Penetrometry signatures into layers of different thickness loose LB DA 16/30 sand overlying the same sand packed dense. Arrows indicate the density boundary.

4.7 Tip flow visualisation

The PSSRI department's acquisition of an ultra high-speed camera (1,000,000 frames per second) provided a fortuitous opportunity to visualise how the tip shape affects the entry stage and subsequent penetration. During the training period, a slower (~1,000 frames per second) camera was also demonstrated and this proved more suited to low speed impacts as it has a higher resolution and frame area. It also did not suffer from the 8-frame capture limitation of the faster camera and made triggering and capture of an event easier. Following a brief demonstration, Mr Brian Speyer of DRS Technologies Ltd. kindly offered one day of penetrometry imaging using this camera.

The demonstration session was restricted to imaging the impact of the penetrometer with the surface material. To allow the subsurface penetration effects to be examined a "Quarter space" technique was employed (Schultz *et al.*, 2005). Used in impact crater studies, this technique involves carefully aiming the projectile (penetrator) at a target placed directly adjacent to a Perspex sheet and filming the impact normal to this window. An open-top, clear 10 mm thick Perspex box of dimensions 400×300×400 mm was constructed in which the sand target would be prepared. Dropping so near to the edge of the box required a substitute penetrator to avoid possible damage to the laboratory ACC-E. This penetrator consisted of a steel tube weighted at the front by a small piece of threaded brass rod which ensured that it would fall straight down and also allowed the easy attachment of the ACC-E collar and tip.

To examine the effect of tip geometry two additional tip shapes were manufactured that could be easily attached: a flat face cylinder and a 30° opening angle cone. The arrangement is shown in Figure 4.26.

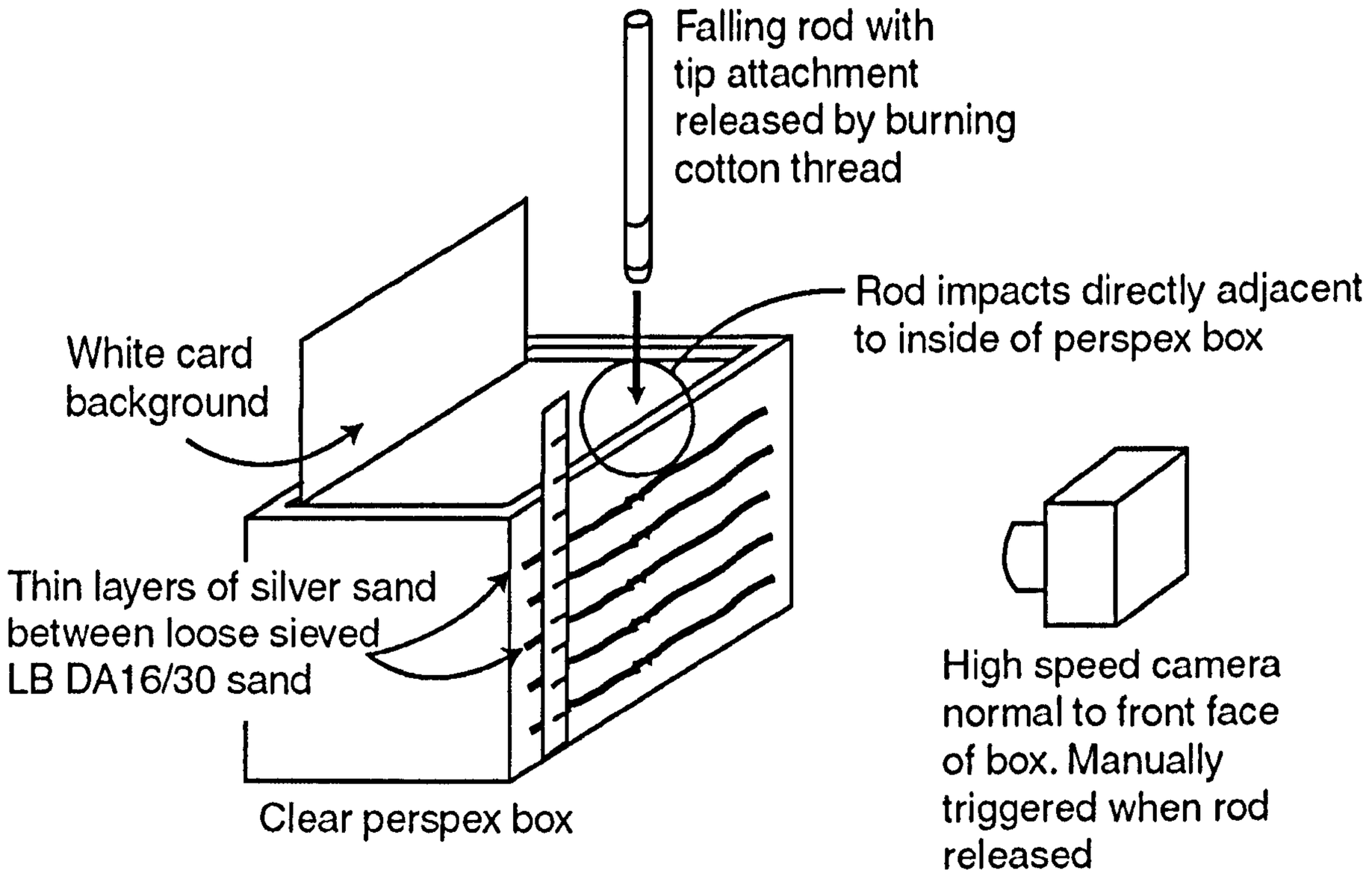

Figure 4.26 Quarter space experimental setup showing how subsurface penetration flow was visualised using interdispersed silver sand layers next to a Perspex window.

To aid the visualisation of the flow, loosely sieved Leighton Buzzard DA 16/30 sand was interdispersed with thin layers of the same sand stained with food colouring. Unfortunately, on camera, the contrast between the sand colours was poor. By replacing the coloured sand with thin layers of silver sand next to the Perspex facing the camera, closer thinner layers were possible with greatly improved contrast.

For each drop, the rod was attached to a ceiling crossbeam using a piece of cotton thread. By burning the thread with a lighter, the rod was smoothly released without vibration. Due to the accuracy required to impact directly next to the Perspex face, test drops were carried out gradually bringing the impact point of the rod closer to the side of the box. This was one of the biggest challenges with the technique because the rod starts to tip slightly away from the face of the box as it penetrates deeper and looses energy making the overall motion harder to see. A heavier mass penetrator or greater

impact velocity would have improved this. The resulting images were combined to create a movie of the penetration process. Figure 4.27 and Figure 4.28 show sequences of the still frames taken from the impact of the hemisphere, flat-face and conical tips.

The sequences show that the majority of the sand deformation occurs within ~8 mm or one radius of the edge of the penetrometer tip. Immediately after the tip contacts the sand, slight downward motion can be seen up to 4 layers away (~40 mm). Sand heave is seen at the surface before material is ejected outwards. The motion of an individual grain below and slightly to the side of the impact point is tracked in the first sequence. The grain is at first pushed down and slightly outwards, then, as the penetrometer tip nears, it is pushed hard outwards and upwards before being dragged down with the shaft of the penetrometer. This downward dragging motion may provide a mechanism by which particles that have hit the very front of the penetrometer tip are able to interact with the tip again. Unfortunately this is not seen in the hemispherical drop as the penetrometer fell away from the Perspex face too quickly. It would be useful in future to film an instrumented penetrometer tip with carefully prepared fine sand containing a series of carefully placed large ~4 mm beads at different depths and correlate the peaks seen in the signature with the film.

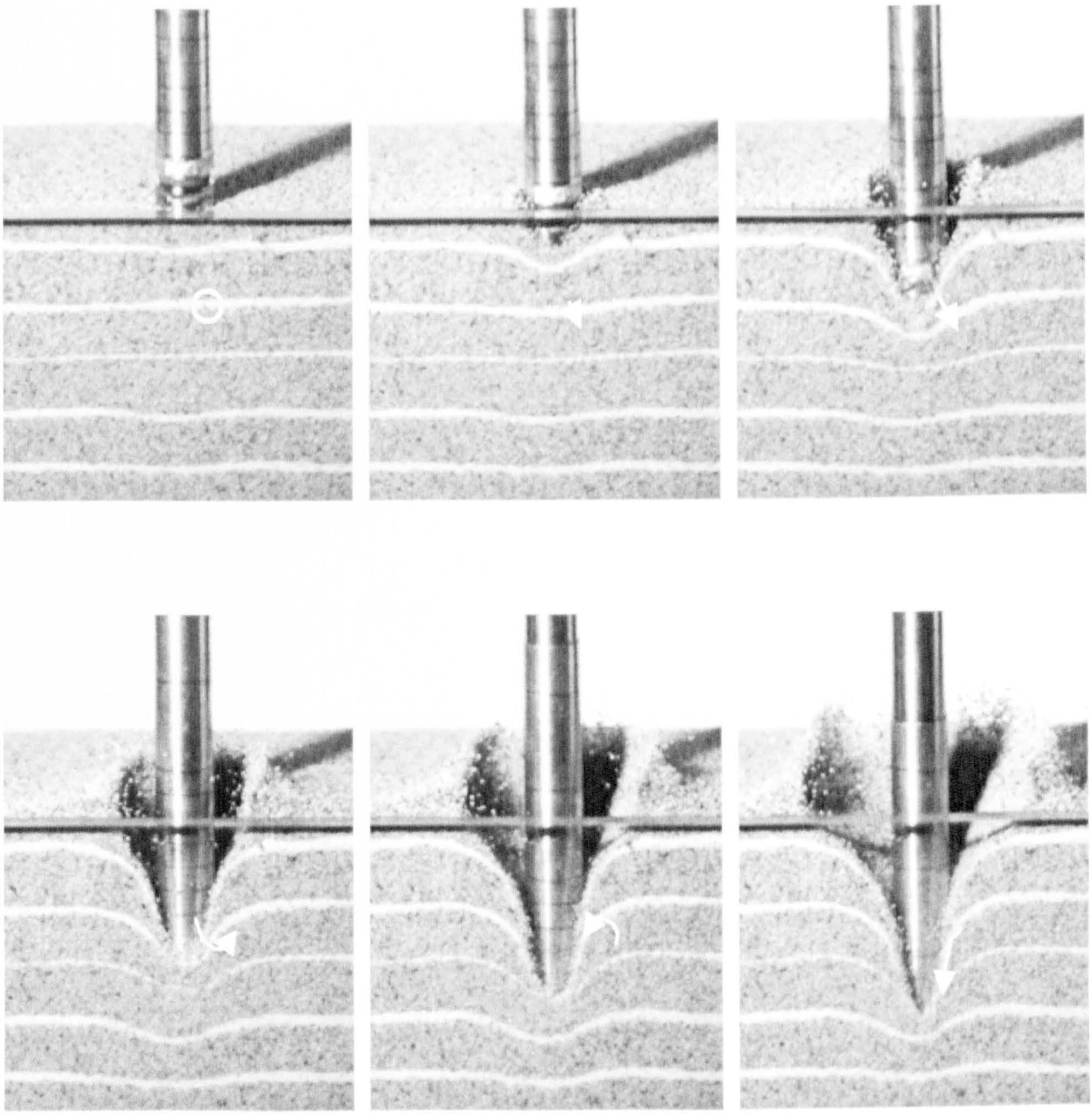

Figure 4.27 High speed video sequence of a flat faced penetrator tip impacting sand at ~4.6 m s^{-1} using the "Quarter space" technique. The first eight markers on the rod are at a spacing of 6 mm. An individual grain motion is tracked- see text. (Image frames 11,12,15,19,25,34)

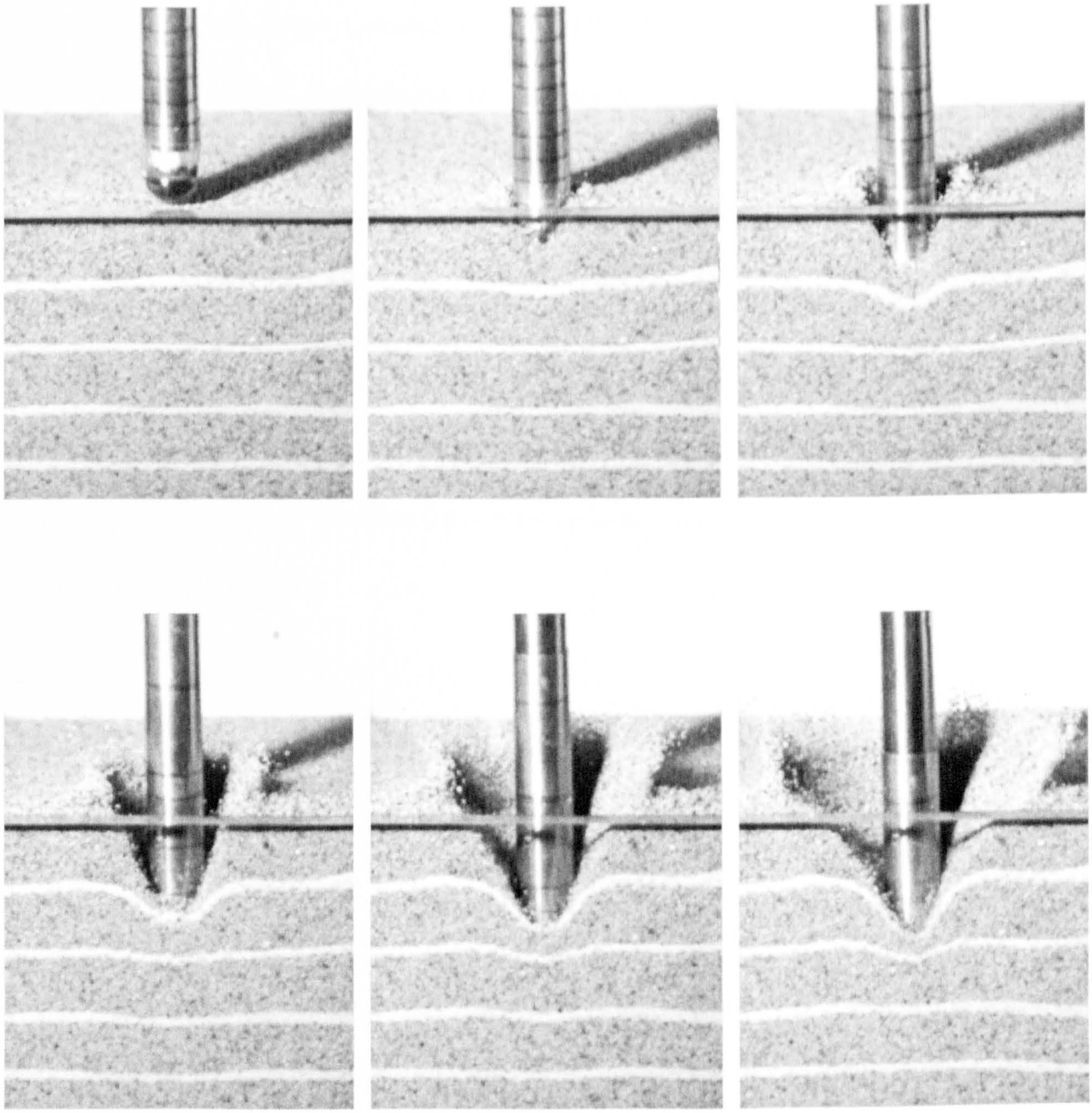

Figure 4.28 Hemispherical tip impacting layered sand at ~4.6 m s^{-1}. Silver sand layers spaced at ~15 mm intervals form deformation contour lines.

4.8 Summary and Conclusions

The aim of this chapter was to examine the penetrometry signatures quantitatively using a range of descriptive statistical measures. Some of the measures described at the start of this chapter proved useful for analysing the impact signature of the target while others were discarded. Before useful penetrometry signatures that provide consistent results can be collected it is necessary to consider the influence of boundary effects caused by the target container. In nature target materials are usually unconfined and so

to represent this, the target container must be sufficiently large, but remain practical, so that any effect of the confinement of the target is negligible. A full treatment of boundary effects in penetrometry is an advanced research topic; however for the purposes of this investigation, it was only necessary to find a container size that minimised sufficiently these effects. Experimental work carried out with containers of various sizes and depths found that a target container of diameter 152 cm and depth 190 cm was of adequate dimensions. This was when the diameter of the target was over 10 times the penetrometer's diameter. In practice a larger container was used with diameter 320 cm and depth 350 cm.

An experiment examining the effect of velocity on the signatures found that an increased number of peaks were detected at slower impact velocities and this suggests that the 10 kHz sampling rate of the ACC-E may be too low. Further sampling rate experiments were planned however due to the limits of the ACC-E electronics anti-aliasing filter, which attenuates frequencies above 5 kHz, this was not possible. Using a peak and trough finding algorithm that accounts for noise, a relationship between peak/trough amplitude and spherical bead size was explored and then using beads of different density an empirical relationship between these amplitudes and bead mass has been suggested.

While time domain analysis proved unproductive, frequency analysis highlighted differences in the frequency content of drops into four different diameters of glass beads but due to the short duration of the data, resolution was poor.

Several experiments were also carried out using man-made targets to look at granular material structure including sorting, layering and grading. Some success was had in

identifying these structures. Finally, preliminary high-speed camera work was carried out using a quarter space technique to explore target material flow around various standard shapes of penetrometer tip.

5 Field testing

5.1 Introduction

The artificial laboratory penetrometry targets discussed in previous chapters were useful for examining the response of the penetrometer to a range of targets in a carefully controlled way. However, these targets are unlikely to be representative of natural targets created by the action of wind and liquid flow. For this reason, an important part of the free fall drop rig design was that it should be portable to allow drops to be made into natural field targets.

The rig design allowed easy assembly, ready for operation in 25 minutes and yet in its disassembled state was compact enough to fit in the back of a car to be transported between field sites (Figure 5.1). A further requirement was the ability to record the penetrometry and impact speed signatures, and although the oscilloscope used in the laboratory was able to write to floppy disks, it required AC power. Two 12 Volt batteries with a capacity of 12 ampere hours were used to supply the required power: one battery was used with an inverter to supply AC power to the oscilloscope while the other supplied DC power to the ACC-E electronics, release electromagnet and laser speed sensor. This battery size was chosen as although heavy, was compact enough to carry to the drop location and provide sufficient power for nearly two hours. The two batteries also ensured that the AC inverter could be kept separate from the sensitive ACC-E electronics and allowed the batteries to be swapped if required since the ACC-E electronics and release electromagnet required very little power. Separate electronics boxes were made up to regulate the power supplied to the electronics and sensor. The arrangement is shown in Figure 5.2.

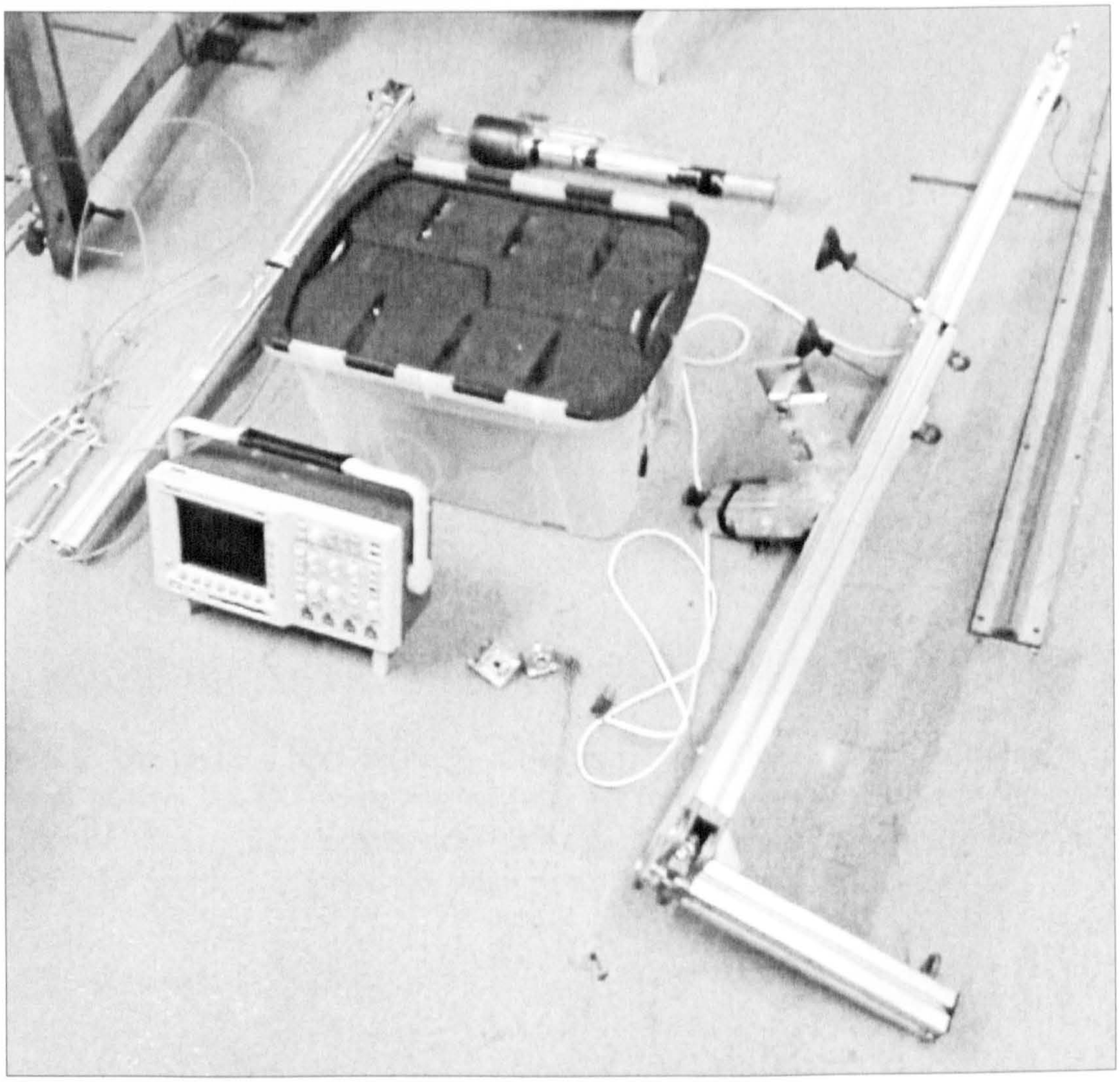

Figure 5.1 Drop rig shown disassembled prior to transport. The bottom of the main post (shown on the right) has the longest length (140 cm) when split from the electromagnet. Rigging wires and tensioners can be seen on the left that add to the structural rigidity without greatly increasing weight. The ACC-E penetrometer and falling weight can be seen in background.

At two locations, the rig was set up with the laser speed sensor; however due to sensor alignment issues on sloping ground and excessive natural light encroachment on the sensor, the speed sensor system did not function properly and instead impact velocity was assumed from the drop height above the ground. This demonstrated the difficulty in making a reliable laser speed detection system for outdoor use that could be dismantled, reassembled and realigned quickly.

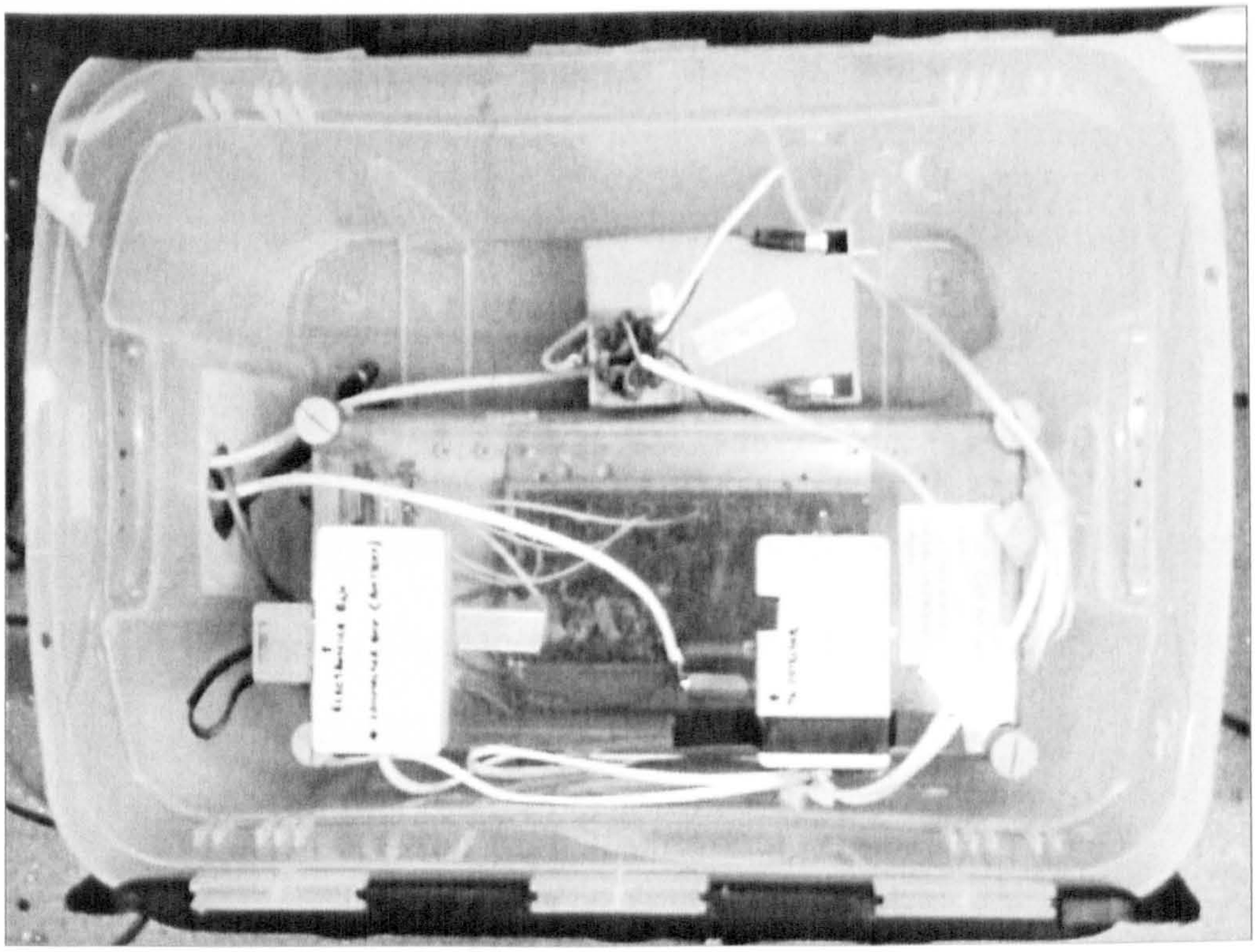

Figure 5.2 Electronics and battery container box. The battery supplies power to the clear plastic ACC-E electronics box, electromagnet and laser detector. The small white boxes are power regulators. A separate container was used to transport the oscilloscope and inverter powered by a separate battery.

5.2 Chesil Beach, Dorset, England (50° 37' N 02° 33' W)

Chesil beach in Dorset is a good example of a beach that exhibits grain sorting along its length (long-shore sorting) (Komar, 1998). It is a predominantly shingle beach extending ~28 miles from Bridport in the west to the Isle of Portland in the east. The mainly flint and chert grains present as well sorted and rounded fine gravel at the western end of the beach at West Bay, and become progressively coarser until they are cobble sized at the eastern end of the beach at the Isle of Portland. The geological processes that caused the variations are still uncertain although it is thought that variations in wave energy along the beach might sort the material by its ability to transport it (Carr *et al.*, 1970; Komar, 1998). The varying grain sizes provide a good environment to test the ACC-E penetrometers' ability to investigate a natural sedimentary texture.

Four sites were chosen along the western end of Chesil Beach (Figure 5.3). The start of the beach at West Bay (A), the National Trust beach at Burton Bradstock (B) some 2 miles to the east, and the beaches at West Bexington (C) and Abbotsbury (D), 4 and 6 miles respectively east of Burton Bradstock. These sites were chosen for three main reasons; the material at each site exhibits noticeably different grain sizes but without being too coarse so as to present the risk of mechanically damaging the penetrometer. The sites are also reasonably close together and offered easy access by car such that the equipment did not need to be carried for long distances.

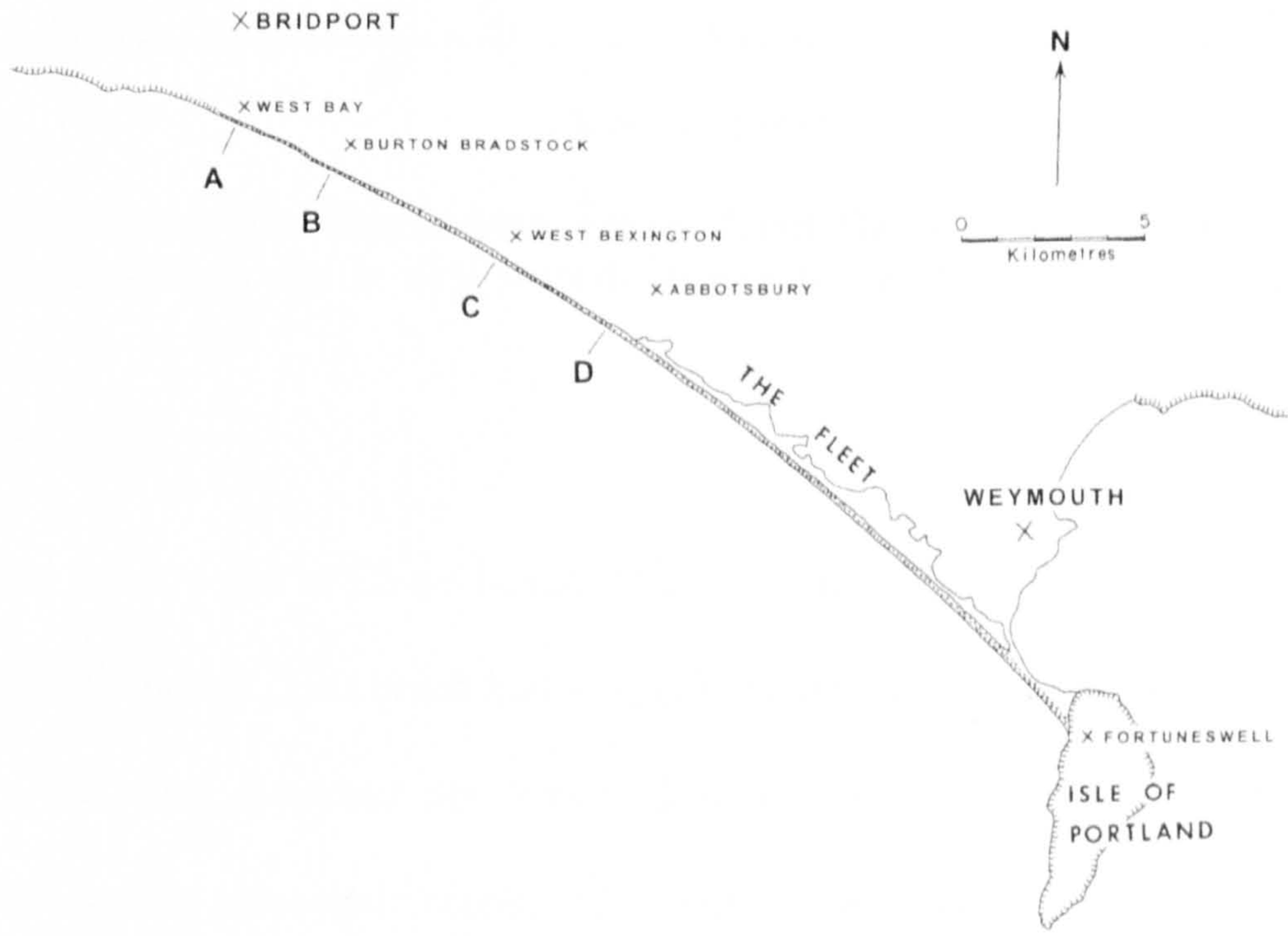

Figure 5.3 Map of Chesil Beach showing the four test sites (marked A, B, C & D) at the western (finer grained) end of the beach. Adapted from Komar, (Komar, 1998).

Figure 5.4 shows the grain size distributions from samples at the four locations (materials were returned after sieving to the sites). The steepness of the curves show that the coarsest material at Abbotsbury followed by that at West Bexington is very well sorted. Finer material at Burton Bradstock and West Bay is slightly less well-sorted exhibiting larger tails in the distributions.

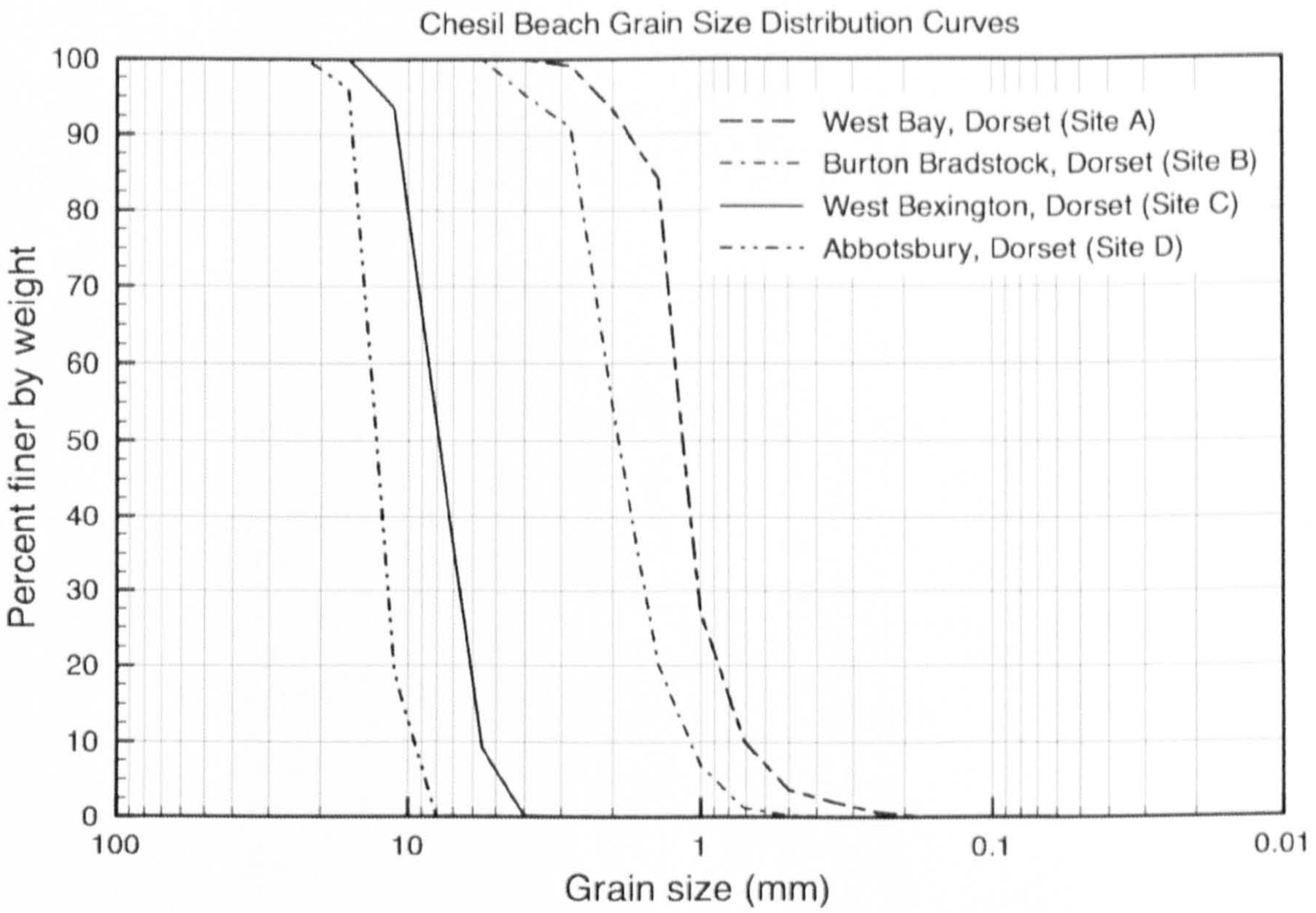

Figure 5.4 Grain size distribution curves from the four sites on Chesil beach. Material from each site is well sorted, increasing in size along the length of the beach.

5.2.1 West Bay

This is the western end of Chesil beach. The easily accessible public beach has a gentle slope down to the sea. This beach had a significant amount of pedestrian traffic and was therefore the most disturbed site tested. However, a short distance along the beach small, undisturbed areas were found. The sand was slightly damp and cohesive due to rain earlier that morning although the surface was drying quickly due to strong sunshine (Figure 5.5). Two types of texture were observed at this site; generally fine grains (Figure 5.6) with no change in structural arrangement with depth, and further up the beach, wave action had caused a ~1 cm thick slightly coarser layer of material to be deposited on the top (Figure 5.7). Four drops were carried out at this site, two into the area with the layering effect (site A1) and two nearer the sea where no layering had been observed (Site A2).

Figure 5.5 The drop rig seen at West Bay, the start of Chesil Beach. Despite heavy pedestrian traffic, small areas of the beach were undisturbed and could be used. Evidence of cross-shore grain sorting was seen between regions in the foreground and background of this picture and this was reflected in the penetrometry signatures. The ground was damp due to light rain earlier that morning.

All signatures showed a gradual increase in mechanical resistance with depth although the average resistance was ~10-15 N higher at site A1. Furthermore, although no surface layer was seen in the A1 signatures, the mean height of peak to trough forces was 3-4 N higher than the two drops at A2. This suggests that this material was actually slightly coarser in general, not just at the surface. Unfortunately no separate sample was taken to verify this. Signatures at an impact speed of 4.6 m s^{-1} from the two sites A1 and A2 are shown in Figure 5.8.

Figure 5.6 Image of surface grains at West Bay. The grains are quite well sorted and predominantly well rounded, although occasional sub angular pieces can be observed.

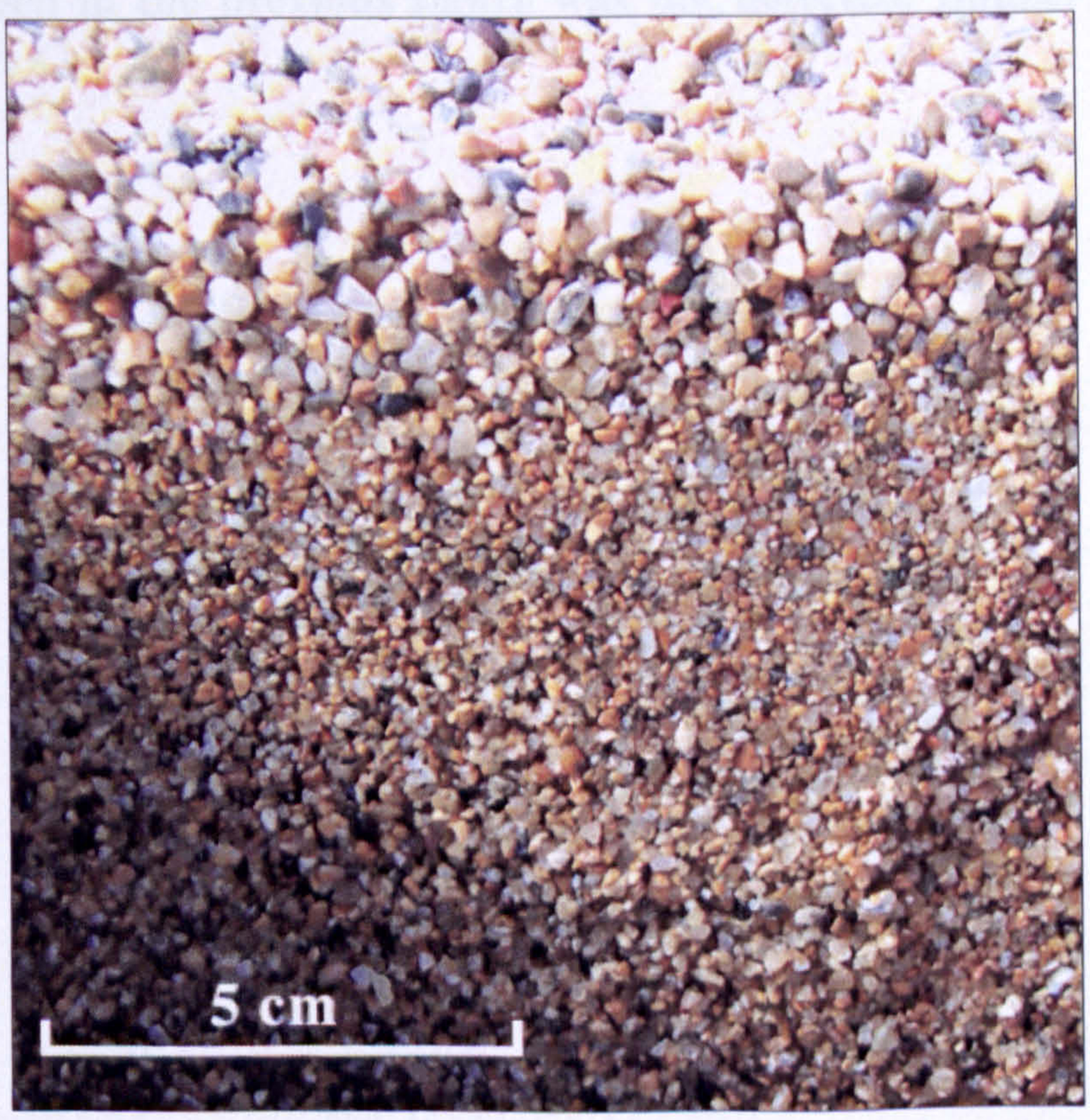

Figure 5.7 Cross section showing coarser grains forming a layer approximately 1 cm thick on top of finer material near the top of West Bay beach.

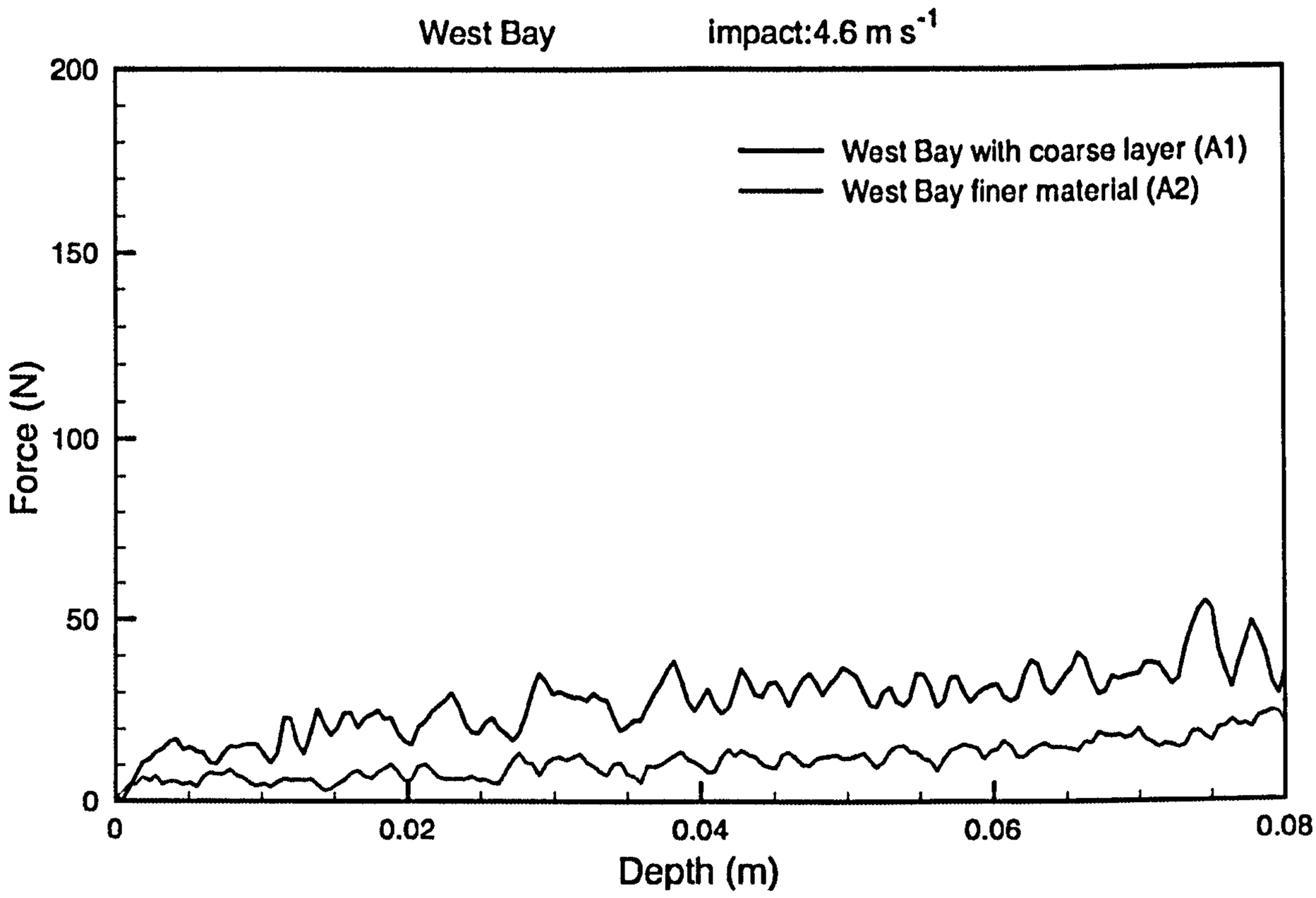

Figure 5.8 Penetrometry signatures from the two areas of West Bay beach. These signatures indicate that the material from the top of the beach is, in general, coarser grained and more resistant than that nearer the sea. The influence of a coarse layer seen in the previous figure was not detected. Impact speed in both cases was 4.6 m s^{-1}.

5.2.2 Burton Bradstock

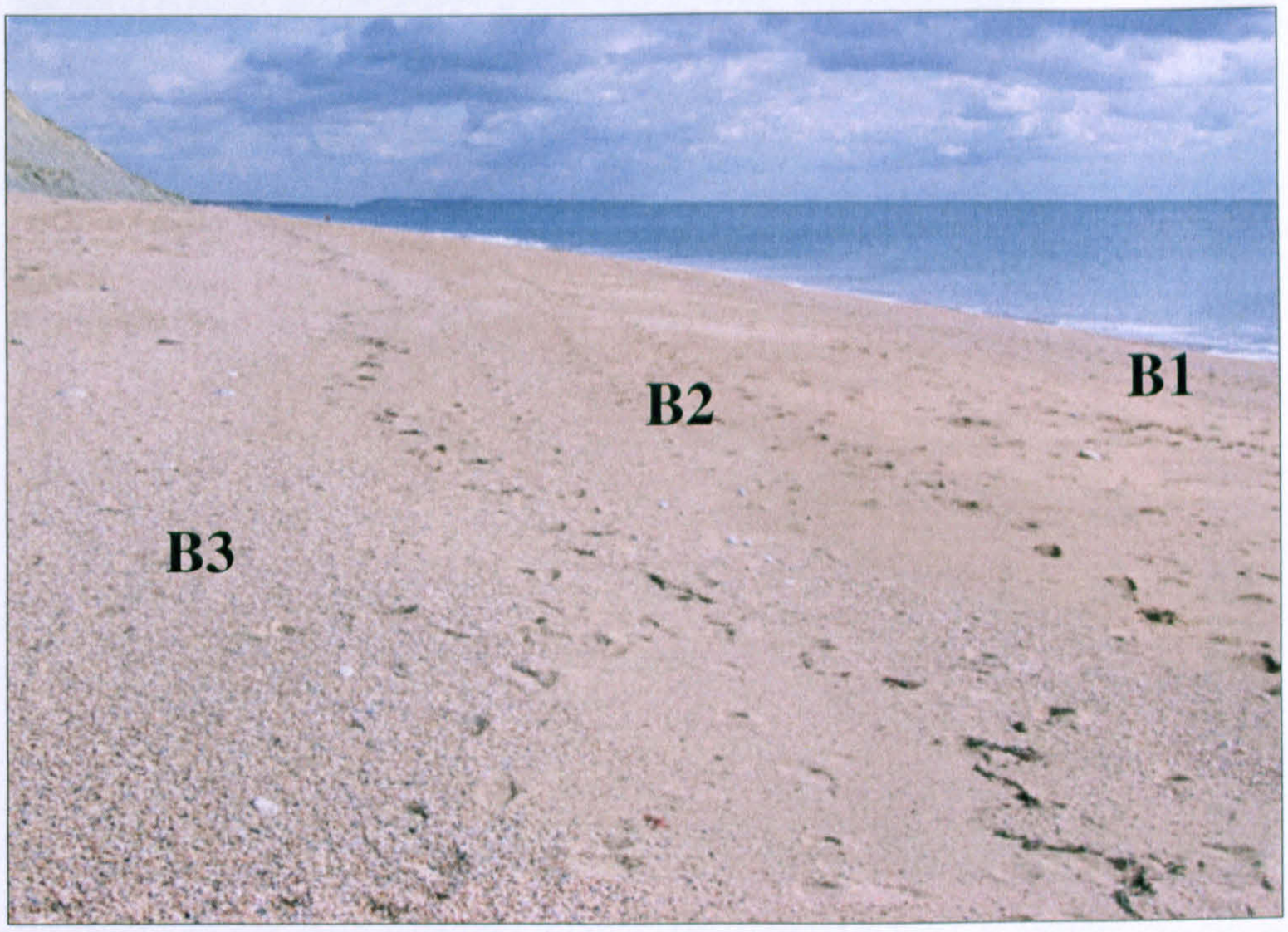

Figure 5.9 Beach at Burton Bradstock looking east towards Portland. Wave action has produced cross-shore sorting with coarser material being deposited on the higher ground seen on the left side of the picture.

The National Trust beach at Burton Bradstock proved to be one of the most diverse sites on Chesil beach as it exhibited several different material arrangements within small depths. This site was more remote than the West Bay site and was therefore considerably less disturbed. Figure 5.9 shows a view of the beach towards Portland. The action of cross-shore sorting processes can clearly be seen; coarse-grained material to the left of the image and finer material on the right.

Starting at the lower section of beach near the sea, Figure 5.10 shows surface grains typical of this beach. The penetrometer signature from a drop here (site B1 in Figure 5.11) shows a gradual clay-like rise with no tip-entry peak typical of laboratory drops into dry sand. However the relatively high mean resistance (~60 N), is consistent with similar laboratory drops into cohesive wet sand of grain size ~500 μm.

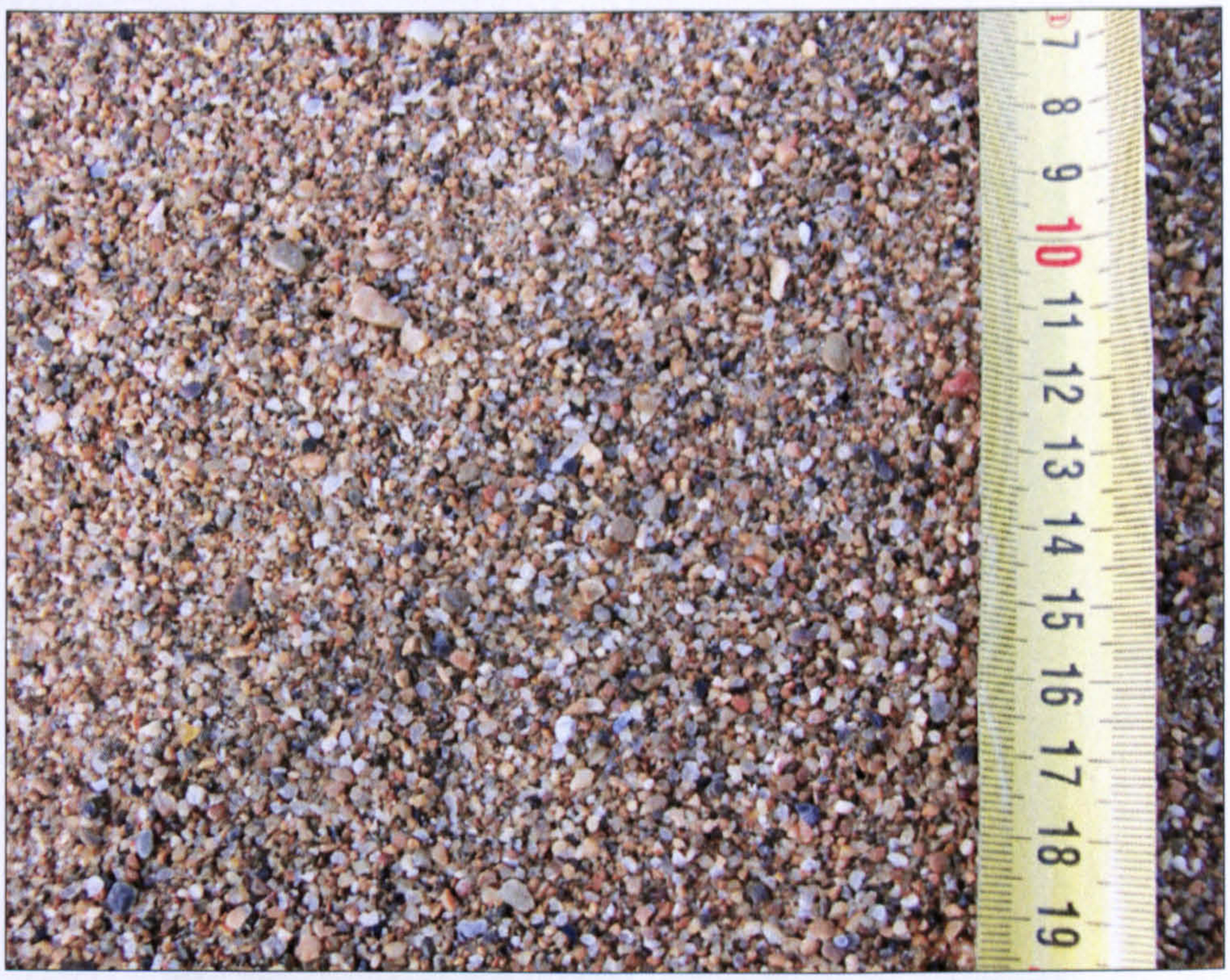

Figure 5.10 Typical grains on the foreshore of the Burton Bradstock site, B1.

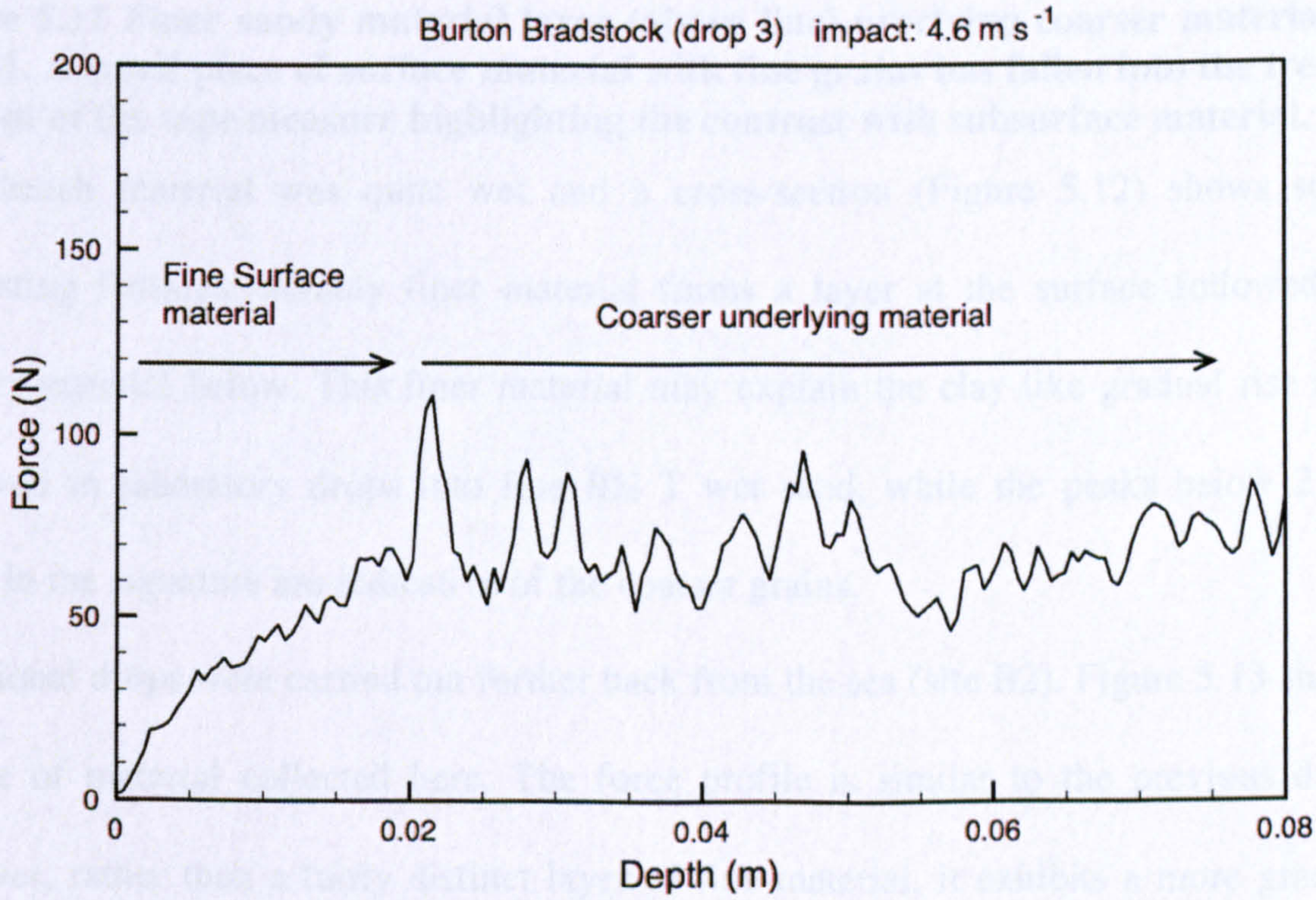

Figure 5.11 Site B1: a damp, cohesive finer material layer gives a smooth, gradual clay-like rise devoid of tip-entry peak. Coarser material below this layer gives rise to a clearly demarcated fluctuating signature below 2 cm.

Figure 5.12 Finer sandy material layer (above line) overlying coarser material at site B1. A small piece of surface material with fine grains has fallen into the trench in front of the tape measure highlighting the contrast with subsurface material.

This beach material was quite wet and a cross-section (Figure 5.12) shows some interesting features; notably finer material forms a layer at the surface followed by coarser material below. This finer material may explain the clay-like gradual rise also observed in laboratory drops into fine RH T wet sand, while the peaks below 2 cm depth in the signature are indicative of the coarser grains.

Additional drops were carried out further back from the sea (site B2). Figure 5.13 shows a slice of material collected here. The force profile is similar to the previous drop; however, rather than a fairly distinct layer of fine material, it exhibits a more gradual change from fine material to coarse, an example of normal grading. A spectrogram of a drop here is shown in Figure 5.14. This clearly shows the increasing frequency content and increased power of the signal as the penetrometer tip impacts progressively larger material grains.

Figure 5.13 A section through beach sand at site B2. Grains exhibit normal bedding caused by action of waves with finer material at the surface.

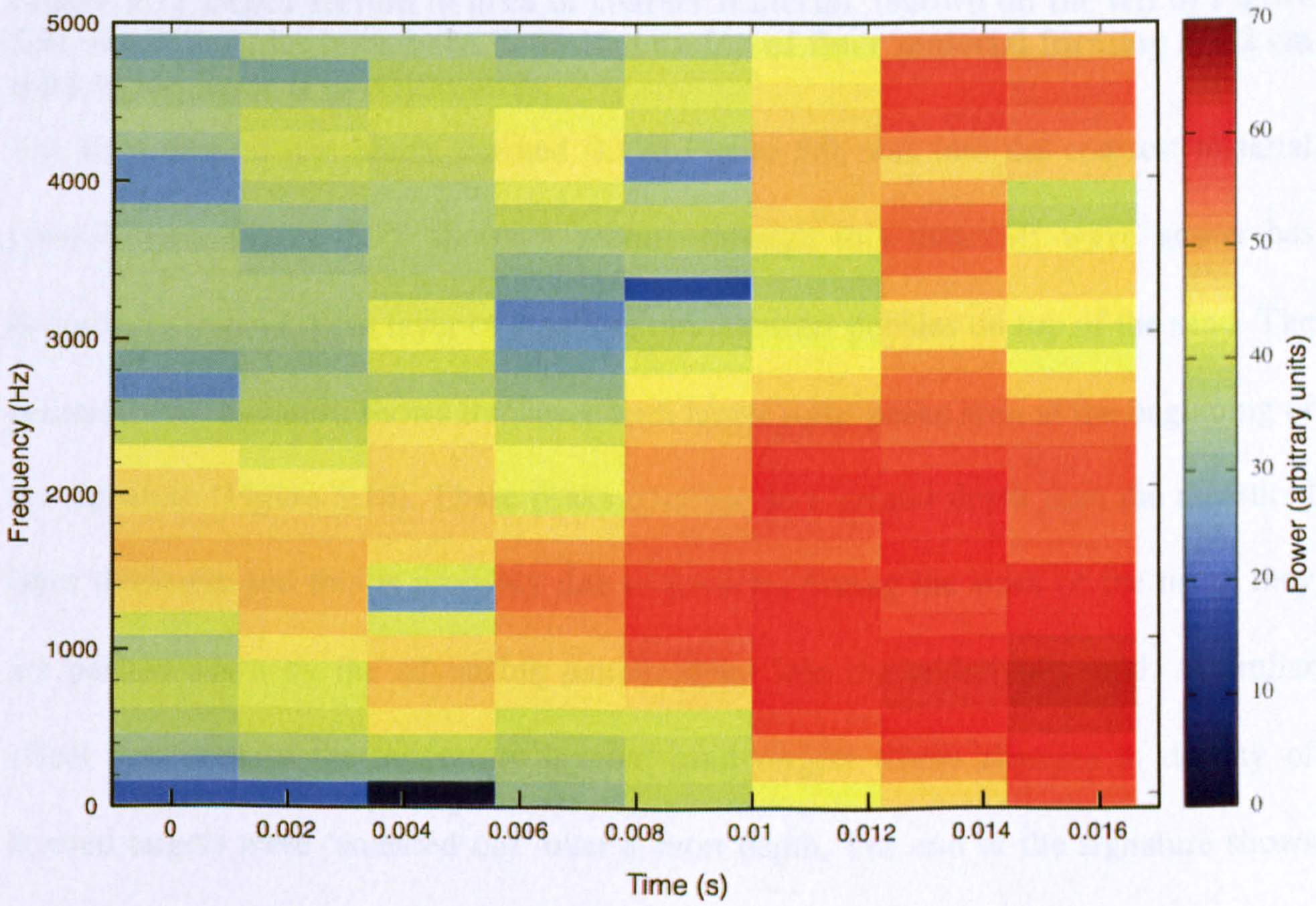

Figure 5.14 Spectrogram of a penetrometer drop into normally graded material near to the sample shown in the previous figure. Power scale units are arbitrary.

Figure 5.15 Depth section in area of coarser material (shown on the left of Figure 5.9). Small pebbles have been deposited on top of finer material forming a 1-2 cm thick layer. Scale is in centimetres.

The final drop at this beach, marked B3 in Figure 5.9, was into the coarsest material present here. Figure 5.15 shows a section through this material; wave action has deposited a thin ~1.5 cm layer of small ~1 cm diameter pebbles on top of the sand. The penetrometer signature shows this layer with larger force peaks seen at the beginning of the signature (Figure 5.16). These peaks continue to a greater depth than the measured layer thickness and this is probably due to particles hitting the sides of the tip as they are pushed down by the advancing penetrometer into the underlying sand. A similar effect was seen in the laboratory layered sand targets where changes in density of layered targets were 'smeared out' over a short depth. The end of the signature shows quite a sharp rise in force that may be due to an increase in moisture content observed, adding cohesion to the sand or, it could be due to compaction of this material.

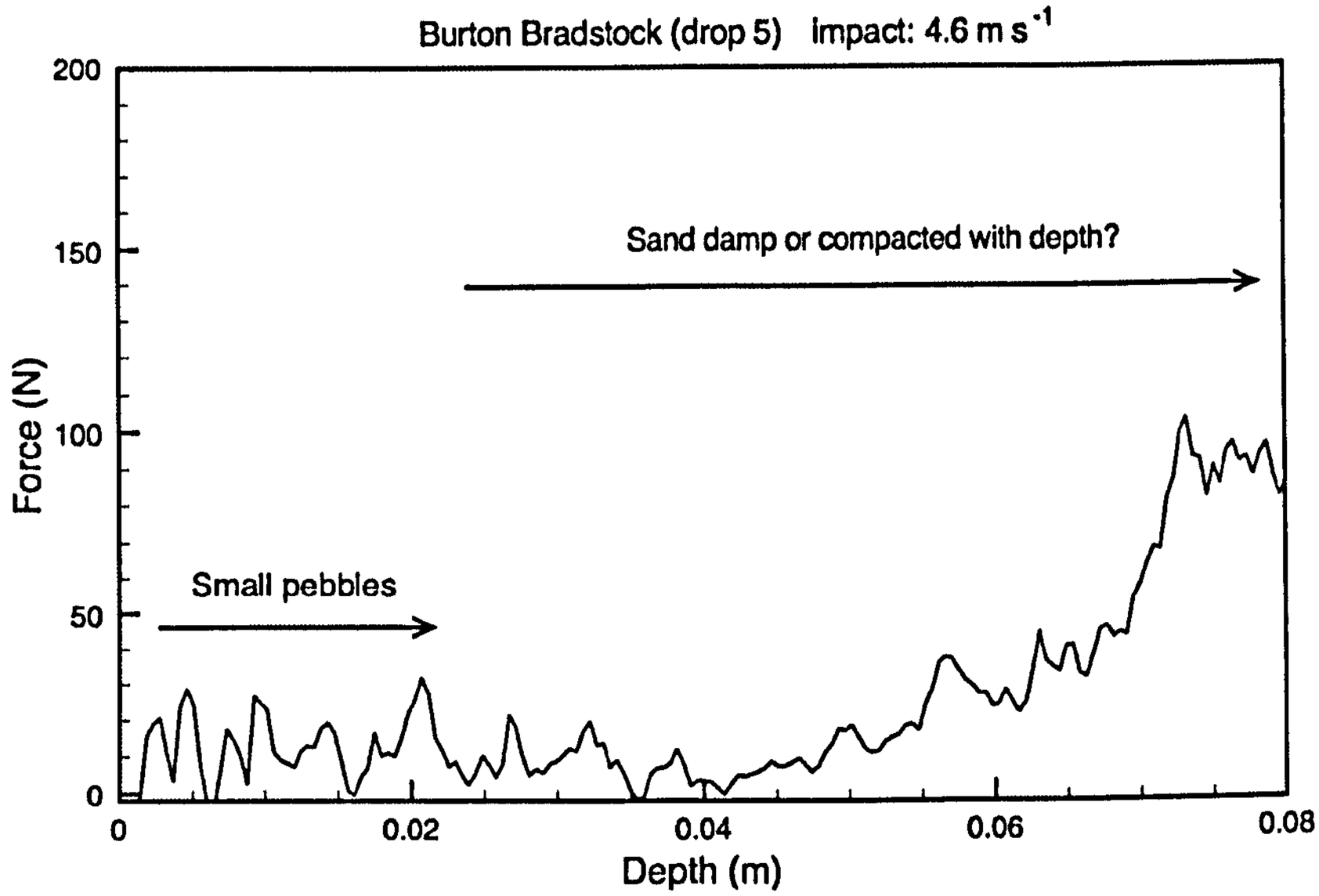

Figure 5.16 Layer of small ~1 cm pebbles overlying sand material on upper reaches of Burton Bradstock beach, site B3.

A comparison of the relative levels of mean force between the signatures at the lower beach levels (B1) and further up the beach (B3) is striking. The force levels of the signatures produced by drier material further up the beach are considerably lower than those of the finer grained material near the sea. This is due to the lower cohesion caused by the absence of moisture sticking grains together.

5.2.3 West Bexington and Abbotsbury

The beaches of West Bexington and Abbotsbury (sites C and D) are similar in their shape with much steeper slopes from the sea to their ridges than the other two sites. For this reason, drops were carried out on the flatter berms (horizontal portion at the rear of a beach formed by deposition of sediments by waves). Figure 5.17 shows the flatter berm at Abbotsbury with small surface undulations typical of both sites. Figure 5.20 and Figure 5.21 show their respective penetrometry signatures. The peak forces seen are considerable higher than those at previous sites and would occasionally enter a different gain branch of the pseudo-logarithmic amplifier. Both signatures are similar in character however, and no clear order was detected. Figure 5.18 and Figure 5.19 show typical pebble size and shape from the two beaches.

Figure 5.17 Abbotsbury (site D). Due to the very steep foreshore region it was not possible to set the rig up near the sea and drops were therefore carried out on the flat berm region shown.

Figure 5.18 Well sorted and rounded pebbles on the beach at West Bexington, site C. Scale is in centimetres.

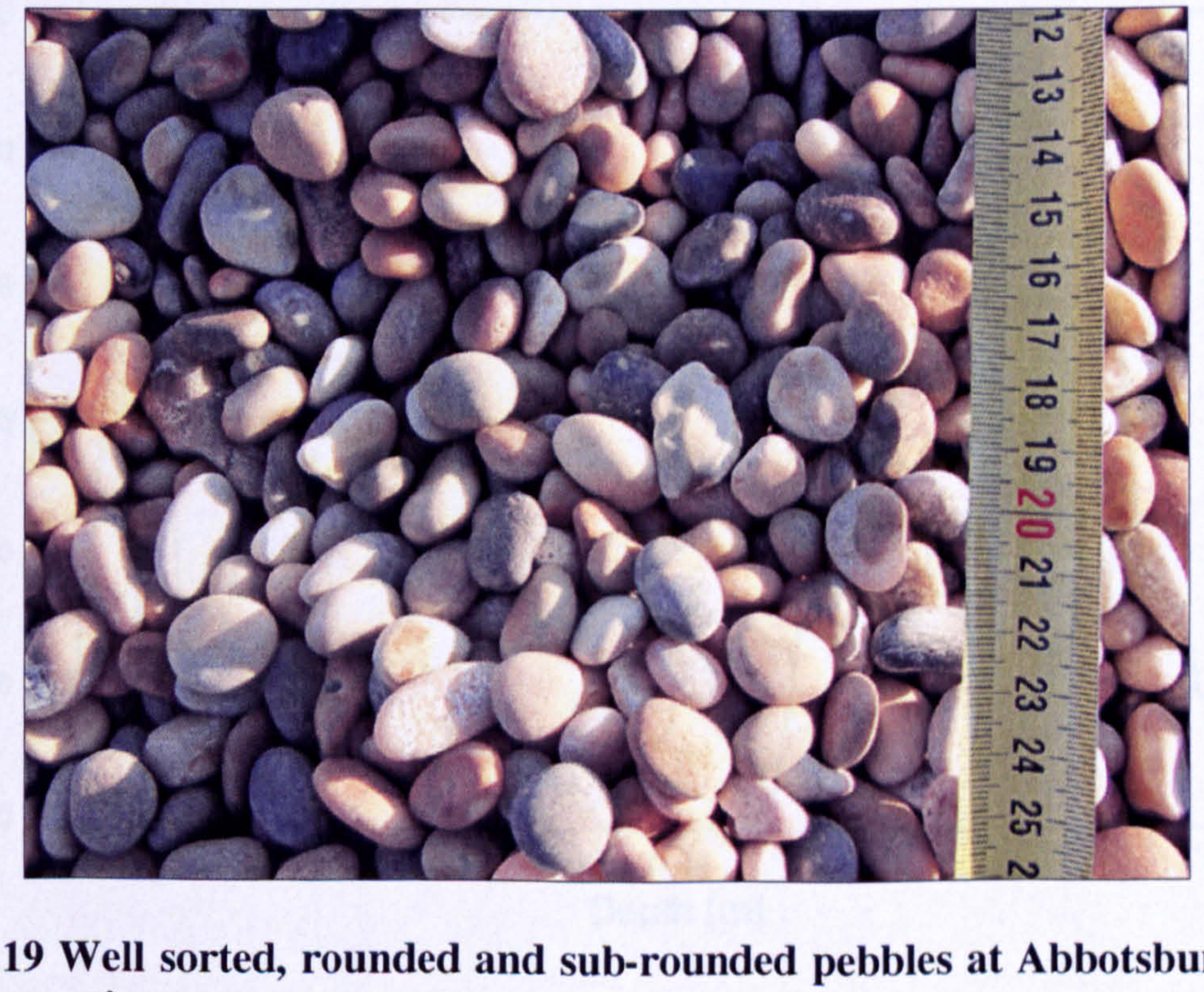

Figure 5.19 Well sorted, rounded and sub-rounded pebbles at Abbotsbury, site D. Scale is in centimetres.

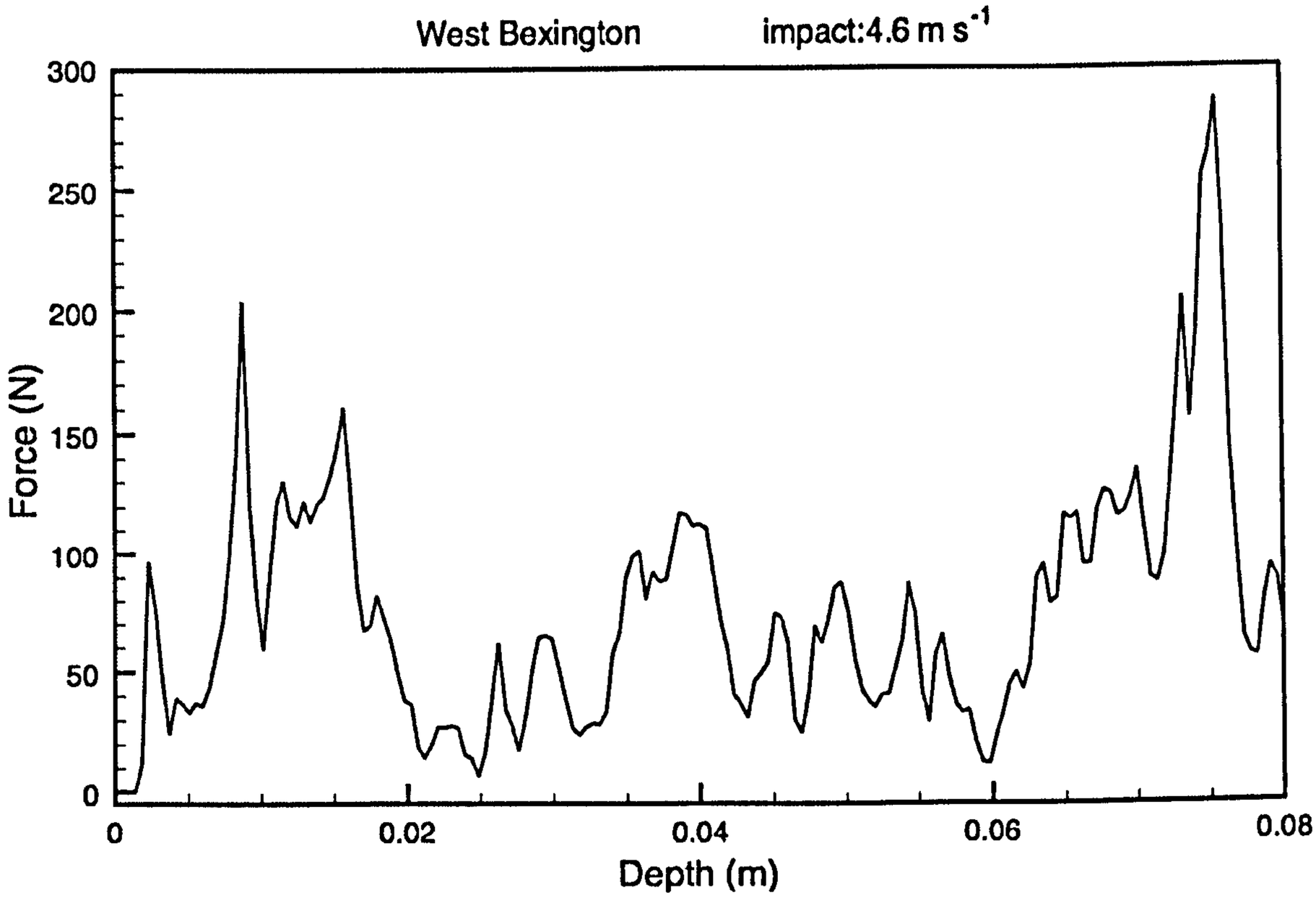

Figure 5.20 ACC-E signature of pebbles at West Bexington, site C. Note the extended range of the force axis.

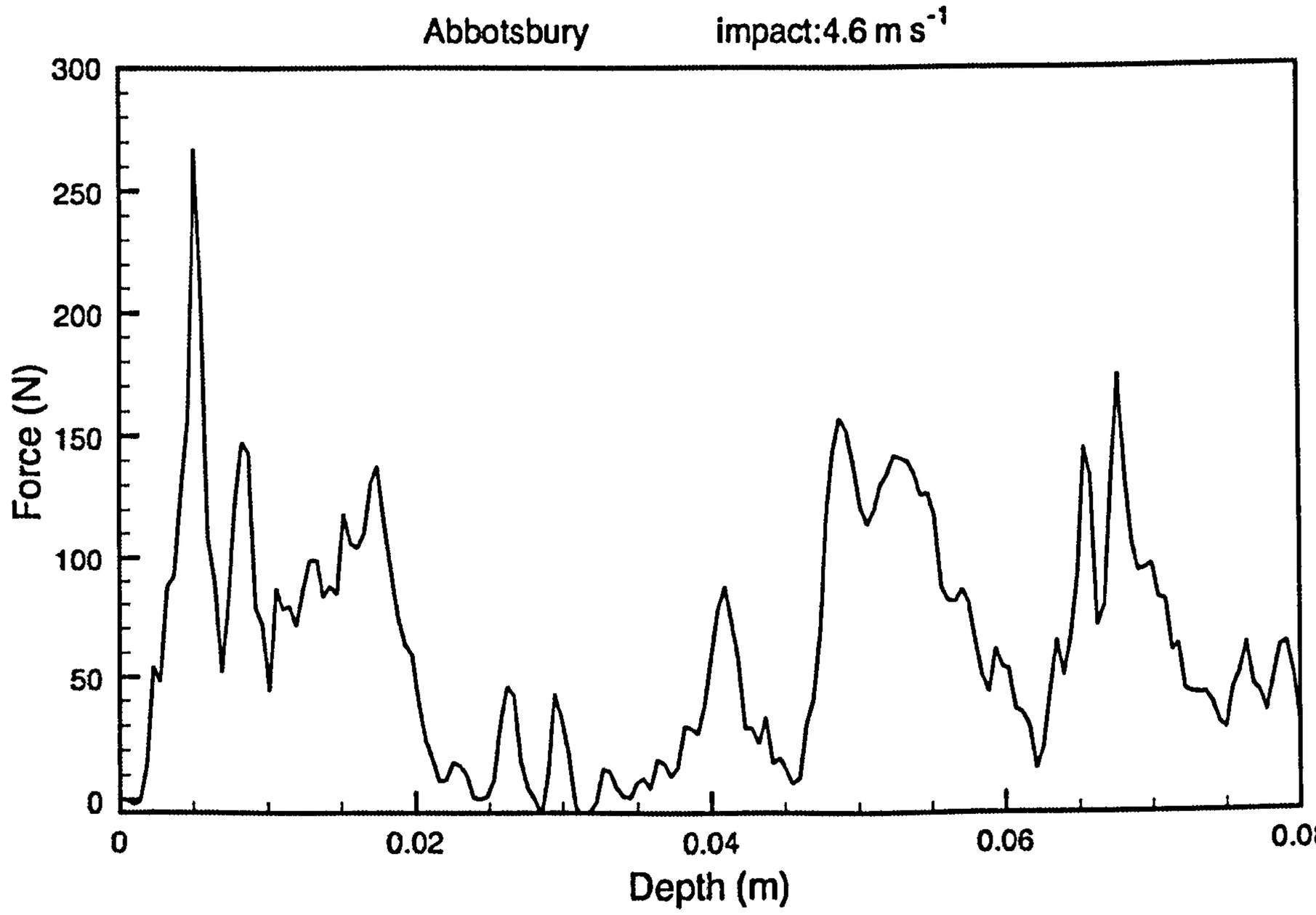

Figure 5.21 Penetrometry signature from Abbotsbury, site D, the coarsest grained site examined on Chesil Beach. Note the extended range of the force axis.

Site	Mean particle diameter from sieve analysis (mm)	Drop number. Mean peak to trough height (N)		Estimated particle diameter using mean value of all peak to trough transitions, (mm)
A: West Bay	1.2	1	10.67, coarser material	2
		2	5.88, finer material	
		3	7.62, finer material	
		4	9.50, coarser material	
		Mean:	**8.42**	
B: Burton Bradstock	2.1	1	17.79, graded grains	4
		2	16.47, graded grains	
		3	16.90, fine layer at top	
		4	16.22	
		5	14.66, coarser top layer	
		Mean:	**16.41**	
C: West Bexington	8.2	1	28.16	8
		2	47.49, Excluded- pen. tipping	
		3	34.07	
		Mean:	**31.12**	
D: Abbotsbury	13	1	31.87	7
		2	23.65	
		3	30.97	
		Mean	**28.83**	

Table 5.1 Mean grain size at the four Chesil beach test sites from sieve analysis compared to grain size estimates using mean peak-to-trough transitions from their penetrometry signatures.

Considering the sediments at the four beach sites to consist of idealised spherical grains, it is interesting to estimate a grain size based on the earlier laboratory work into spherical beads. Taking the magnitude of the mean peak to trough forces of the penetrometry signatures for each site and using the empirical relationship found in Chapter 4 allows an estimate of the mean particle mass, M, that produce these peaks.

$$\text{mean peak to trough force} = 37.79M^{0.33} \qquad \textbf{(Equation 5.1)}$$

As Chesil beach is known to consist of predominantly flint and chert, an average grain density of 2.6 g cm^{-3} was assumed. Using the definition of density and substituting in for a spherical volume gives $\rho = \frac{3M}{4\pi r_{particle}^3}$, where M is the particle mass, V is volume

and $r_{particle}$ is the particle radius. Rearranging this gives a relationship between particle diameter and particle mass for a given grain density:

$$d_{particle} = 2\left(\frac{3M}{4\pi\rho}\right)^{\frac{1}{3}} \qquad \textbf{(Equation 5.2)}$$

where ρ is the grain density of the material being considered. Table 5.1 shows the results of using this equation together with the particle mass determined from the empirical relationship, to estimate the diameters of the particles at the four sites. The estimates show reasonable agreement with the mean particle size gained from sieve analysis for smaller particles; however, at the last site the estimate is poor, in part because the peak forces entered the medium gain branch of the pseudo logarithmic amplifier where errors are enhanced.

5.3 Studland Bay, Dorset (50° 38' N 01° 57' W)

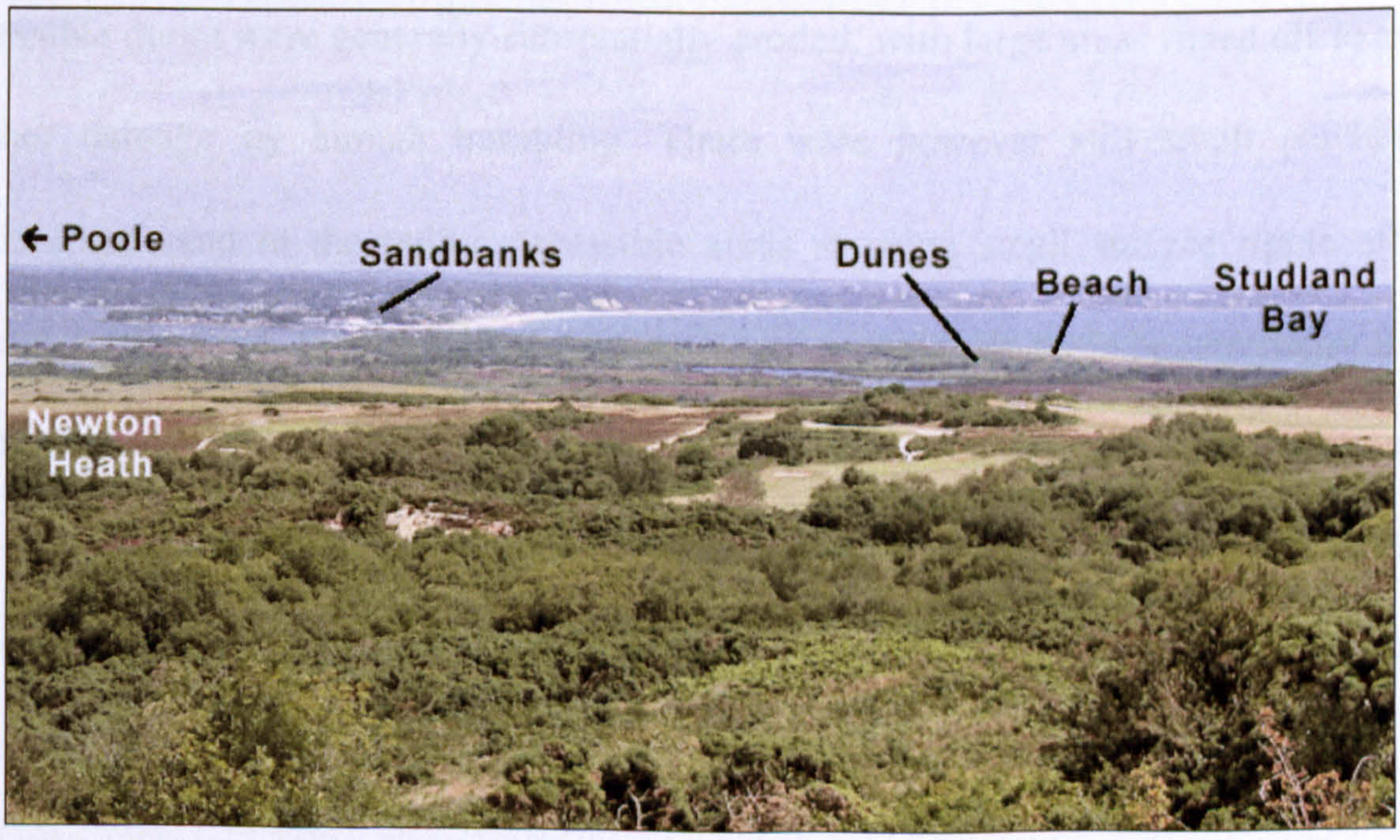

Figure 5.22 Overview of the Studland Bay area near Poole, Dorset.

To contrast with the penetrometry drops into the sorted pebbles and coarse sands of Chesil Beach produced by the wave action of the sea, a location was sought where granular material texture was produced by aeolian (wind) processes. The National Trust beach at Studland Bay near Poole is about 25 miles east of Chesil beach. It is well known for its coastal dunes held together by networks of Heather and Marram grasses. These dunes have built up from fine wind-blown sand in the last 400 years (Wilson, 1960). The beach also consists of the same fine sand with no coarse gravel or pebble content due to the bay being sheltered from prevailing south-westerly winds (and hence waves with sufficient energy to carry larger material) by the protruding Foreland peninsula (Figure 5.22) (West, 2007).

5.3.1 Sand dunes

Due to the weight of the rig, penetrometer and accompanying electronics, the areas of the dune that were accessible for penetrometry testing were limited. Unfortunately the accessible dunes were generally substantially eroded, with large areas roped off to avoid further damage by human trampling. There were however still small patches of undisturbed sand in the public accessible areas showing small surface ripple effects caused by the wind. Figure 5.23 shows the location used with three penetrometry drops being carried out as far from vegetation as possible. The sand in this area is extremely fine with similar colour and grain size characteristics to the RHT sand used in laboratory testing. The grains were dry with no evidence of any cementing or clumping together. The signature from one of the drops is shown in Figure 5.24.

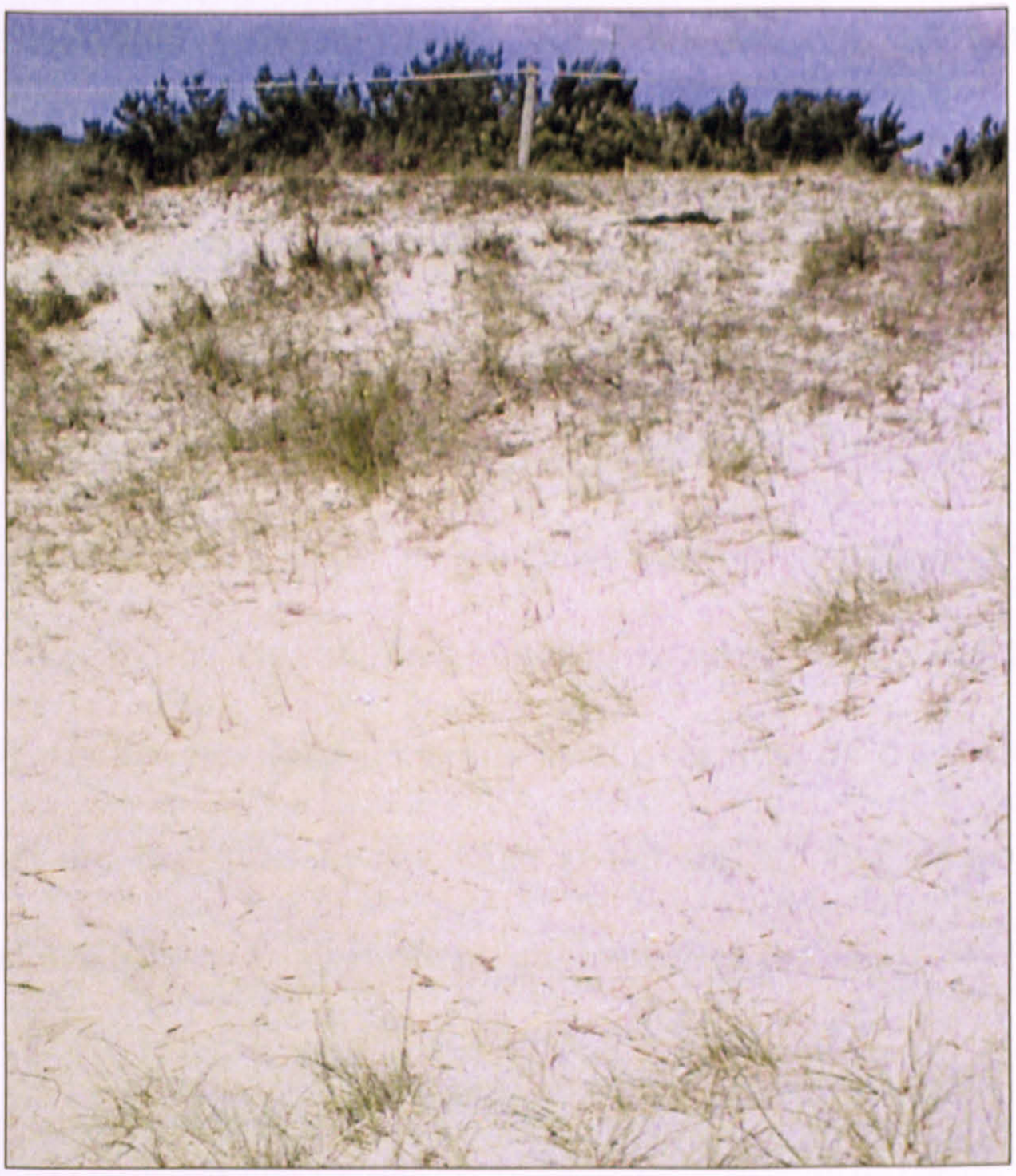

Figure 5.23 Dune at Studland Bay, Dorset. Large parts of the dunes were roped off and therefore not accessible due to trampling preservation measures.

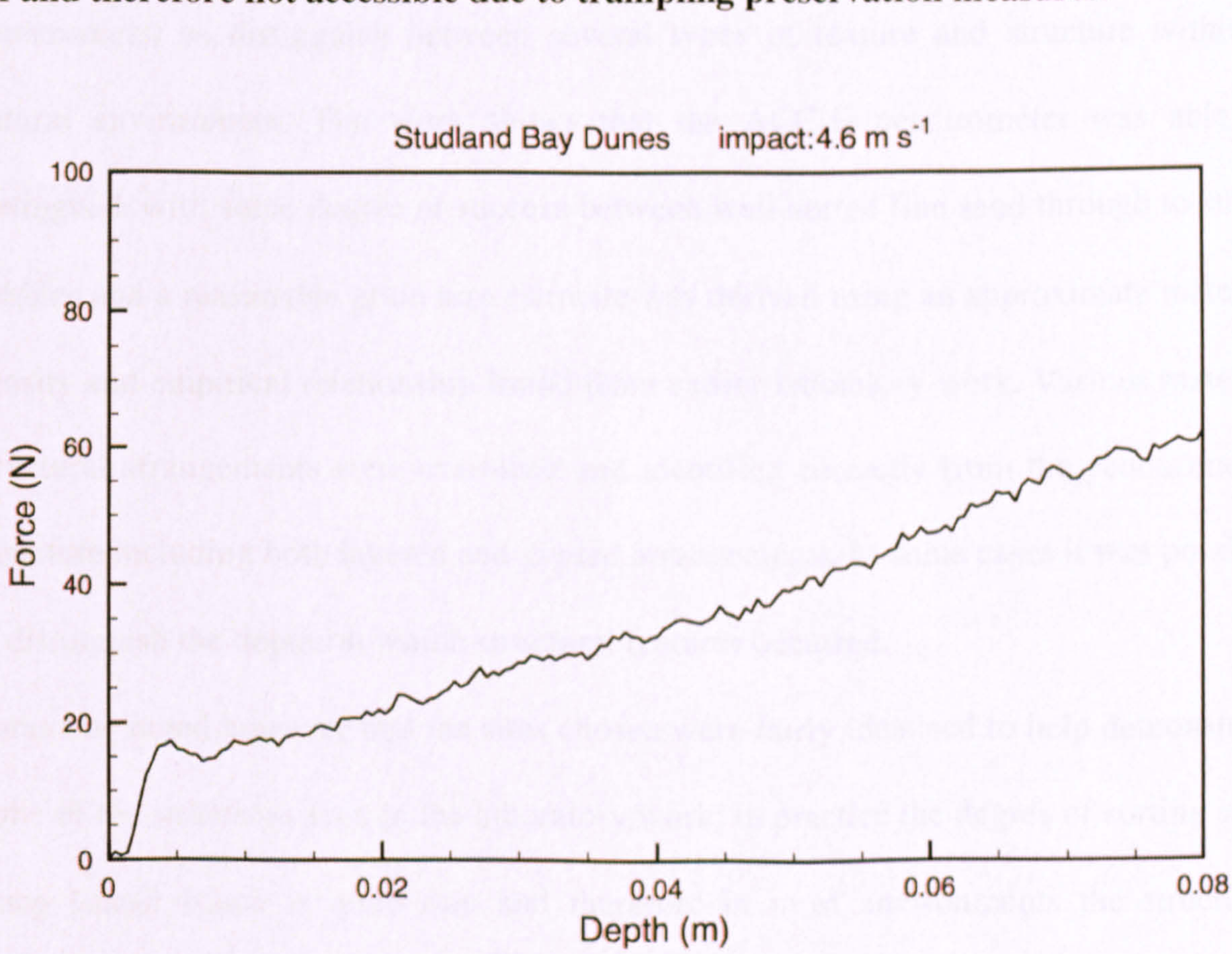

Figure 5.24 Signature from a drop into dune sand at Studland Bay, Dorset.

Comparing this signature to the laboratory drops into the two test sands loosely and densely packed (Figures 7.11 and 7.12), similarities can be seen with the finer RH T sand penetrometry signature. In particular there is only a small tip-entry peak unlike the pronounced peak seen in the loose and dense LB sands. The resistance at the start of this signature is similar to the loose RH T sand- around 20 N. This was expected as the wind blown sand deposits are likely to be loose; however, surprisingly, the resistance rises rapidly so that by the end of penetration, it is similar to compacted RH T sand. This is probably due to consolidation of the sand over time by overburden pressure as more sand layers are deposited by the wind at the surface and also by the action of precipitation and drainage causing further compression of the sand.

5.4 Summary and Conclusion

The fieldwork presented in this chapter has demonstrated the ability of the ACC-E penetrometer to distinguish between several types of texture and structure within a natural environment. The work shows that the ACC-E penetrometer was able to distinguish with some degree of success between well-sorted fine sand through to small pebbles and a reasonable grain size estimate was derived using an approximate material density and empirical relationship found from earlier laboratory work. Various material structural arrangements were examined and identified correctly from the penetrometry signature including both layered and graded arrangements. In some cases it was possible to distinguish the depths at which structural features occurred.

It must be noted however that the sites chosen were fairly idealised to help demonstrate some of the structures seen in the laboratory work; in practice the degree of sorting seen along Chesil beach is quite rare and therefore in most environments the structural features would be less easily identified. A number of improvements could have been

made to the experimental set-up. Despite being designed to be portable, carrying and setting up the rig was quite labour intensive and time consuming. Some of the equipment weight, such as the lead acid batteries, was unavoidable however the rig structure was probably somewhat too cumbersome. Another factor that could be improved is the adjustability of the rig supports to better accommodate sloping surfaces. These improvements might have allowed more sites to be explored notwithstanding the heavy dependence on suitable weather.

6 Penetrometry modelling

6.1 Introduction

Modelling the penetration process is a way of predicting the interaction between penetrator and target material. It can also allow target material properties to be inferred and may be useful to help understand the underlying physical processes. In general, penetrometry models can be divided into two classes; those that treat the material as a continuum, using only target bulk properties, and discrete particle models where the material is considered as a collection of individual interacting particles. The latter is a relatively new area of research requiring extensive computational power.

Models can vary in complexity from simple, purely empirical fits to data through to the most advanced two and three-dimensional finite element models (FEM) often used for predictive purposes. An FEM model was investigated using Century Dynamics Autodyn application which was ultimately unsuccessful due to the difficulty in obtaining material data and, more fundamentally, the slow velocities employed in the problem which lead to unavoidably large calculation errors. Another type of model is the idealized physical model that considers the combined effect of the various forces thought to act on the penetrator. These models are much simpler than the finite element approach and are therefore more appropriate to the interpretation of planetary penetrometery data (Kömle *et al.*, 2001). An adaptation of a model of this type is considered in the following section.

Many models have been developed to describe the penetration process (e.g. Farrel *et al.* (1966), Boguslavskii *et al.* (1996), Forrestal *et al.* (2007)), however their usefulness when applied to 'real' situations is limited by their requirements for multiple target

material parameters to be known *a priori*. These parameters can often only be determined by comprehensive testing of soil samples using specialist equipment which is not possible in the case of planetary penetrometry where the target is remote. In terrestrial investigations, where samples of the material can be taken, the parameters derived from laboratory tests are inevitably from disturbed samples that may not necessarily represent the *in-situ* material state (Craig, 1997). Terrestrial penetrometry models have been developed that require few input parameters which can usually be estimated or measured in the field (see e.g. Whalley (2006)). Similarly, a model for extraterrestrial targets must have few unknown inputs relating to the target material. These free variables can then be adjusted alongside the known parameters relating to the penetrator geometry or dynamics (e.g. mass and diameter of penetrator, impact speed etc.) by forward modelling until the closest fitting match is found to the measured deceleration history and penetration depth. Too many free inputs would not constrain the target material resulting in numerous solutions.

6.2 A physical penetration model

Penetration equations normally described the deceleration experienced by the penetrating body after impact and are based on Newton's Second Law of Motion and can be expressed in the form (Fuchs, 1963):

$$-M\frac{dv}{dt} = R(v) \qquad \textbf{(Equation 6.1)}$$

where M and v are the mass and velocity of the penetrator respectively and t is the time; $R(v)$ is the resisting force as a function of the penetrator velocity which can be considered as the combined result of up to three velocity components as described by a generalised penetration equation (Allen, 1957; Fuchs, 1963),

$$-\frac{dv}{dt} = av^2 + bv + c \qquad \textbf{(Equation 6.2)}$$

Several analytical penetration equations have been derived from this basic equation using some or all of its velocity terms. The three terms with coefficients, a, b and c are associated with the dynamic, dissipative and static components of the resisitive force respectively; for sub-sonic impacts into granular targets the second term, representing losses due to viscosity and wave generation, is negligible (Boguslavskii *et al.*, 1996; Jaeger and Nagel, 1992). The penetrometery models described in this section are of this type, and build on one formulated by Anderson *et al.* (1996) and subsequently used for investigations of the effect of ambient pressure on slow penetrometry (Garry *et al.*, 1999), and the ~50 m s^{-1} test shots of the harpoon anchor of the Rosetta cometary lander (Kömle *et al.*, 2001; Kömle *et al.*, 1997).

A projectile, such as a free falling penetrometer, will come to rest when its inertia has been totally dissipated by the interaction with the target material. It looses its kinetic energy in the target material by several methods including generating stress waves and sound waves, transferring momentum to the target material (in sand for example the grains are accelerated from rest on contact with the penetrometer tip), crushing the target material e.g. breaking up (comminution) of the material grains, and overcoming the bearing strength; these last three factors are considered the most significant in low velocity impacts (Wang, 1971).

Anderson's model considers the dynamic component of the resistive force (the term proportional to v^2) to be due to failed target material behaving analogously to a fluid that imparts a drag-like force to the penetrometer over the contact or 'wetted' surface between them. In fluid mechanics, the drag force that resists the motion of a body

through a fluid is caused by two stresses; a pressure stress that acts normal to the surface and a tangential stress due to the fluid's viscosity and the variation of flow velocity near the surface (Granger, 1995). The drag is often expressed in terms of a dimensionless drag coefficient that has a magnitude determined primarily by the shape of the body moving through the fluid. The Anderson model replaces this drag coefficient with an analogous stress concentration factor C_d. The model uses a limited number of input parameters most of which can be measured without requiring special soil testing equipment that was not readily available. Such an approach is useful when considering materials where very little information is known. It has been adapted to consider the hemispherical geometry of the ACC-E tip and fitted to the laboratory data collected at an impact speed of 3.2 m s^{-1} and extended to consider impacts into layered targets.

Anderson *et al.* (1996) consider the penetration after initial contact (after a finite amplitude elastic wave has been imparted), described by Newton's second law with the decelerating force F acting on penetrometer:

$$\frac{d\vec{p}}{dt} = -\vec{F} \qquad \textbf{(Equation 6.3)}$$

where p is the momentum of the penetrometer and therefore can be written,

$$|p| = mu = m\frac{dx}{dt} \qquad \textbf{(Equation 6.4)}$$

Here, m is the mass of penetrometer and x is the depth of the leading edge of the tip. Writing the equation of motion in terms of the momentum, p, can then allow for the mass of the penetrometer to vary (if for example, compacted material collects in front of the penetrometer tip, effectively becoming part of the mass of the penetrometer).

From equation 6.3,

$$-F = m\frac{du}{dt} + u\frac{dm}{dt} \qquad \textbf{(Equation 6.5)}$$

Therefore,

$$-\frac{du}{dt} = -\frac{d^2x}{dt^2} = \frac{F + u\,dm/dt}{m} \qquad \textbf{(Equation 6.6)}$$

Where the mass is considered to be constant (no material build up in front of the penetrometer). The decelerating force is then considered to consist of two orthogonal components; a normal component, F_n, and a component tangential to the surface of the penetrometer, F_t. These forces can then be divided into components normal (F_n) and tangential (F_t) to the penetrometer surface that act parallel to the direction of motion, decelerating the penetrometer:

$$F_n = \iint_{S_w} (C_d P_d + \sigma_d)\cos\theta ds$$

(Equation 6.7)

$$F_t = \iint_{S_w} (C_d P_d + \sigma_d)\mu_f \sin\theta ds$$

The terms in brackets are stress terms that act where the surface of the penetrometer is in contact with the target material, or the 'wetted' surface S_w as described by Anderson *et al.* (1996). This 'wetted' surface concept accounts for the tip shape of the penetrometer and grows larger as the penetration depth increases. The factor μ_f is the coefficient of dynamic friction of the failed material against the penetrometer surface and σ_d is the maximum normal stress the material can support before failing in compression, known as the effective bearing strength. For conical tips such as those considered by Anderson and Kömle, the angle made between the penetrometer surface and the direction of motion, θ, is constant on entering the target surface and is related to the half opening angle of the cone, θ', by $\theta = \frac{\pi}{2} - \theta'$. However, in the case of the

hemispherical ACC-E tip, the angle θ varies with depth as the penetrometer tip enters the target (see Figure 6.1). This tip entry is the first stage of penetration after which the contact angle reaches a constant value once the tip is fully embedded.

Examining the stress terms, the $C_d P_d$ term results from the transfer of momentum from the penetrometer to the surrounding target material. C_d is a stress concentration factor analogous to a drag coefficient in a fluid. Interestingly, Anderson took C_d to have a typical value of 2, whereas Kömle *et al.* (1997) found that they could not fit their data unless higher values (ten times the Anderson value) were used for this parameter. They suggest that the analogy of dynamic resistance force with the equivalent hydrodynamic drag force has its limits, with lower values of C_d possibly only being applicable to much harder and more cohesive target materials used in the Anderson *et al.* (1996) experiments. Furthermore, they cite the reported experimental results of Allen *et al.* (1957) which suggest that penetration into sand targets at slower velocities may result in a strong increase in the value of C_d. The dynamic pressure, P_d, is given by the expression analogous to drag in a fluid:

$$P_d = \frac{1}{2}\rho_0 V^2 \cos^2\theta$$

(Equation 6.8)

where V is the velocity and ρ_0 is the bulk density of the target material. With low velocity impacts ($<<$ 100 m s^{-1}) the deceleration force provided by the dynamic pressure is small so that the main deceleration force is provided by the material bearing strength, σ_d (Anderson *et al.*, 1996). Combining the two components of equation 6.7 gives the total force on the penetrometer:

$$-F = -M\frac{dV}{dt} = \iint_{S_w} (\frac{1}{2}C_d\rho_0 u^2 \cos^2\theta + \sigma_d)(\cos\theta + \mu_f \sin\theta)ds$$

(Equation 6.9)

In addition to the stress terms above, when applying this approach to the Rosetta anchor, Kömle *et al.* (2001) considered further force terms that they regarded to be of clear or plausible physical origin, producing a similar equation with three additional terms added:

$$-F = \iint_{S_w} \left[(\frac{1}{2} C_d \rho_0 u^2 \sin^2\theta' + \sigma_d + \rho g N_q z)(\sin\theta' + \mu_f \cos\theta') + k_v V \cos^2\theta' \right] ds - Mg$$

(Equation 6.10)

The first of these, $\rho g N_q z$, considers 'overburden pressure' that is, the weight per unit volume of the overlying material which increases with depth z. Here Nq is a bearing capacity factor depending on the angle of internal friction only (see Craig (1997)). Due to the short length (and hence penetration depth) of the ACC-E penetrometer, contributions due to this term are negligible. The second added term, $k_v V \cos^2\theta'$, is termed a 'viscosity' or 'damping' term, which keeps with the fluid analogy and is added to account for some viscous flow of material around the penetrometer. The authors discuss the disagreement over the physical validity of this extra force term and suggest that it may simply be used to improve the model fit. The final added term, due to the weight of the projectile, is significant in the laboratory environment and needs to be considered. Note that equation 6.10 also differs from the more general expression in equation 6.9 by using the constant cone half opening angle θ', described previously instead of a varying surface contact angle since this was derived for Rosetta, which has a conical tip.

In the case of the ACC-E penetrometer initial tip entry stage, the contact area over which the decelerating forces act is described by the area of a 'cap' that increases with depth (Figure 6.1).

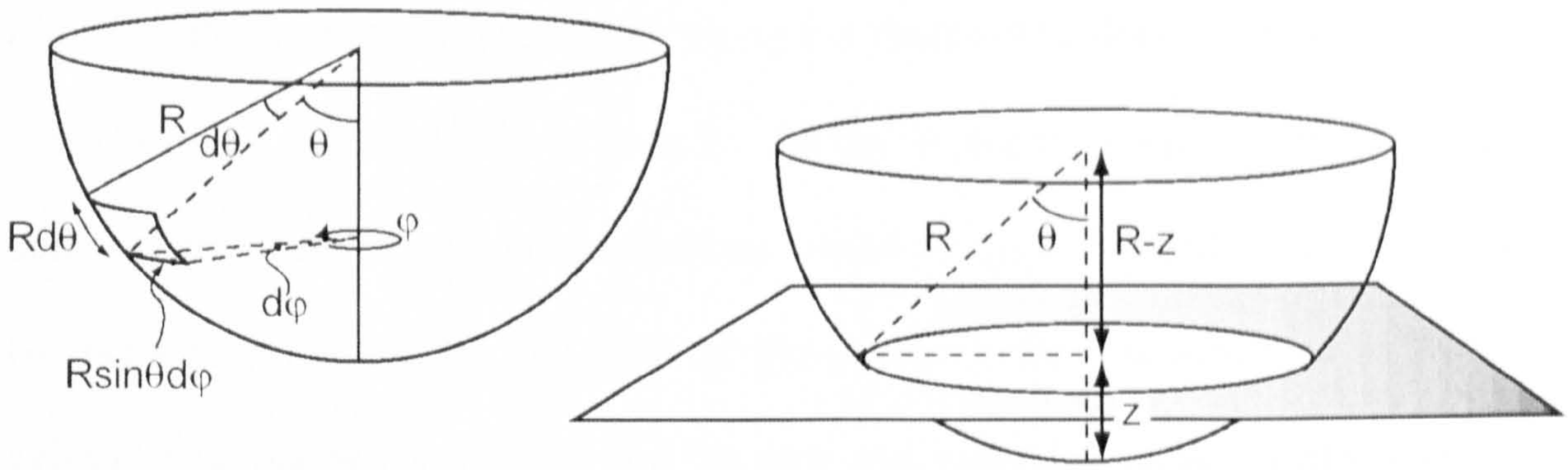

Figure 6.1 Diagram showing spherical coordinate based calculation of surface area wetted for a given depth of penetration, *z*.

Integrating twice over the varying contact angle θ, and azimuthal angle φ in spherical coordinates gives:

$$S_w(\theta,\varphi) = \int_0^{\theta}\int_0^{\varphi=2\pi} R^2 \sin\theta d\varphi d\theta$$

(Equation 6.11)

where R is the radius of the hemisphere. For a given depth this surface area is dependent only on the contact angle:

$$S_w(\theta) = 2\pi R^2 \int_0^{\theta} \sin\theta d\theta$$

(Equation 6.12)

Combining equation 6.12 above with equation 6.9 including the weight of the penetrometer and rearranging gives an expression for the deceleration of the penetrometer during the initial tip contact stage of the penetration:

$$-\frac{dv}{dt} = \frac{2\pi R^2}{M}\int_0^{\theta}(\frac{1}{2}C_d\rho v^2\cos^2\theta + \sigma_d)(\cos\theta\sin\theta + \mu_f\sin^2\theta)d\theta - g$$

(Equation 6.13)

From Figure 6.1 the relationship between the contact angle and depth penetrated can be seen to be:

$$\theta = \cos^{-1}\left(\frac{R-z}{R}\right)$$

(Equation 6.14)

Once the tip has fully penetrated, new terms can be added to consider the effects of the shaft. The force measured by the penetrometer crystal is only that acting on the tip;

however, the frictional forces acting along the shaft act to slow the penetrometer down which in turn affects the force seen by the tip. In the first version of the model, the author allowed decelerating contributions caused by the collar and shank of the shaft to be included as an option. The shaft of the penetrometer was modelled as two joined cylinders of diameters 14 mm and 10 mm and related lengths 23 mm and 50 mm respectively. For a penetrometer entering the target normally, the surface of the shaft is aligned with the direction of the penetrometer and therefore only the force components tangential to the surface are considered to act:

$$F_t = \iint_{S_w} (\frac{1}{2} C_d \rho_0 v^2 \cos^2\theta + \sigma_d) \mu_f \sin\theta ds$$

(Equation 6.15)

In this case, $\theta = \frac{\pi}{2}$. Using cylindrical coordinates, the deceleration is given by:

$$-\frac{dv}{dt} = \frac{2\pi R_{cyl}}{M} \int_{h1}^{h2} \sigma_d \mu_f dh$$

(Equation 6.16)

Here the limits h_1 and h_2 define the start and finishing depth of a shaft cylinder of radius R_{cyl} embedded in the target material.

The model assumes that the penetrometer is a rigid non-deformable body that impacts a horizontal target surface normally. In the first instance, the target is assumed to be homogenous. The simulation starts at time $t = 0$ and runs as follows: initial conditions that consider the penetrometer to be immediately above the target surface with no penetrated depth ($z = 0$) and an initial velocity $u_0 = 3.2$ m s^{-1} are set together with one known target material parameter, the bulk density.

Three values are set for the first simulation run for the free parameters C_d, μ_f and σ_d and a finite difference scheme is then applied to find the new depth penetrated after one time step, Δt:

$$z_{i+1} = z_i + u_i \Delta t \qquad \textbf{(Equation 6.17)}$$

This new depth is then used to find the area wetted by the tip, as described earlier, and the shaft (which until the tip is fully embedded will be zero). Using this area, the force on the tip and the acceleration of the penetrometer can be calculated which in turn can be used to calculate a new velocity for use in the next time step cycle.

The simulation for any combination of the free parameters (C_d, μ_f, σ_d), ends when the velocity reaches zero and this represents a stationary penetrometer. Comparison with the depth reached by the laboratory penetrometer acts to constrain the model depth and gives the best value of σ_d for a given combination of C_d and μ_f. As the model does not account for the effect of the impact of the weight structure to which the penetrometer is attached, the depth constraint required that the laboratory penetrometer stop before the weight structure impacted. This, together with the need for a well-characterised target material, led to the choice of foamglas as a target and also a necessary reduction in impact velocity from that used in previous experiments.

For each simulation run with a different combination of C_d, μ_f and σ_d, the model program includes a least squares fitting routine to compare how well the calculated tip force fits the measured data. Table 6.1 gives the input and fitted parameters used in the model and laboratory target material parmeters.

Model parameter	Input value
Mass of penetrometer, M	3.245 kg
Radius of penetrometer, R	7 mm
Final depth of penetration	58 mm (T4), 37 mm (F)
Bulk density	See below
Initial velocity	3.2 m s^{-1}
Stress concentration factor, C_d	fitted
Coefficient of dynamic friction between penetrometer and target	fitted
Target material effective bearing capacity	fitted

	Foamglas T4 (soft)	Foamglas F (hard)
Bulk density (kg m^{-3})	120	165
Porosity (%)	95	93
Nominal crushing strength (MPa)	0.85	1.70
'effective strength' (MPa)	1.10	1.40

Table 6.1 Model parameters and target material properties. Foamglas data with exception of effective strength are from Kömle *et al.* (2001).

6.3 Results

Simulations were run for blocks of the two types of foamglas. The range of values considered for the three fitted parameters C_d, μ_f and σ_d are shown in Table 6.2. An example of the model output for a drop into the softer T4 type foamglas is shown in Figure 6.2. The evolution of four physical quantities: depth penetrated, force measured by the tip, velocity and kinetic energy of the penetrometer are shown with time. Laboratory data from a 3.2 m s^{-1} drop to which the model was fitted are overlaid for comparison. The graphs show a good least squares match to both the laboratory force data and also fit the penetrometer velocity as measured by the laser system reasonably well; however quite a wide range of σ_d values were able to produce reasonable results. Furthermore, this strength term was generally higher than the measured value given in Table 6.1 varying between 0.8-1.6 MPa.

	Parameter range		
Fitting parameter	Lower limit	Upper limit	step size
C_d	2	26	6
σ_d (MPa)	0.6	2	0.1
μ_f	0.0	0.1	0.05

Table 6.2 Fitting parameter range used for most simulations.

This is reasonable given the uncertainties in the force calibration and quoted variations in strength of up to 30% both in and between different blocks of foamglas as measured by Kömle *et al.* (2001). The stress concentration factor C_d was found to have minimal effect on the model output over the range considered. This might be expected, as the density of foamglas and impact velocity are small, making the effect of this drag term minimal. It can be seen in the speed graph that the laser system was only able to detect the speed down to approximately 1.5 m s^{-1} before the pulses were lost. This loss is probably due to the vibration on impact deflecting the laser beam or disturbed foamglas dust obscuring the detector. However the model fits the earlier deceleration gradient up to this point.

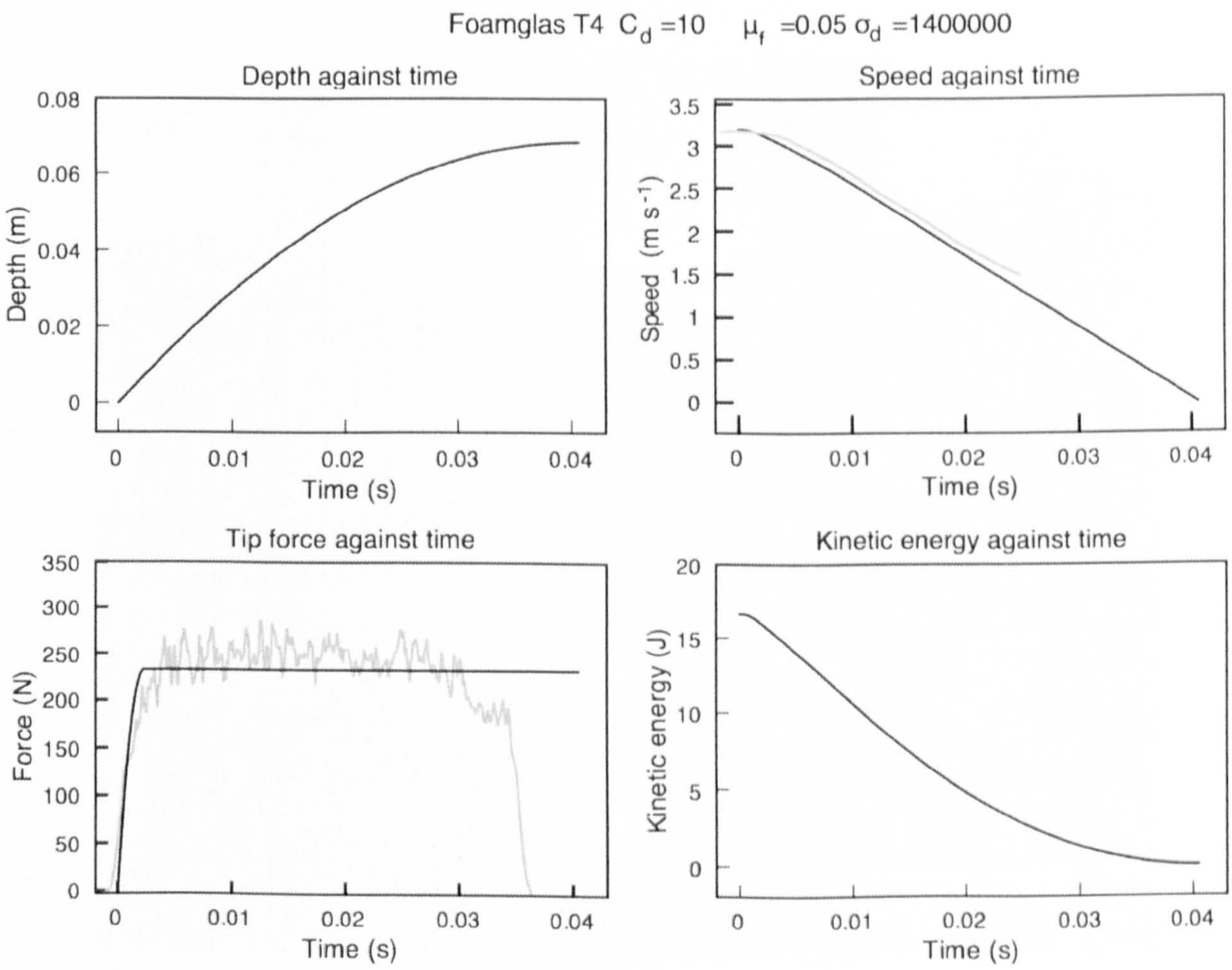

Figure 6.2 Example output from the hemi.m model impact simulation into type T4 foamglas. The model time histories are shown in black with the laboratory measured tip force and speed as measured by the laser system shown in grey.

It was found however that the best fits of the model generally overshoot the actual measured final penetration depth of 61 mm. This is at present not fully understood, as an extrapolation of the laboratory laser velocity data would seem to agree with the final penetration depth. The model also fails to reduce the tip force before the simulation stops as seen in the laboratory signature. This fact was first pointed out by Garry et al. (1999) and suggests that the model strength term is oversimplified.

However one factor that needs to be considered is the build up of failed material in front of the hemispherical tip. This has been clearly observed in foamglas penetration by Lorenz and Shandera (Lorenz and Shandera, 2002) and also by the author in the course of these experiments (Figure 6.3).

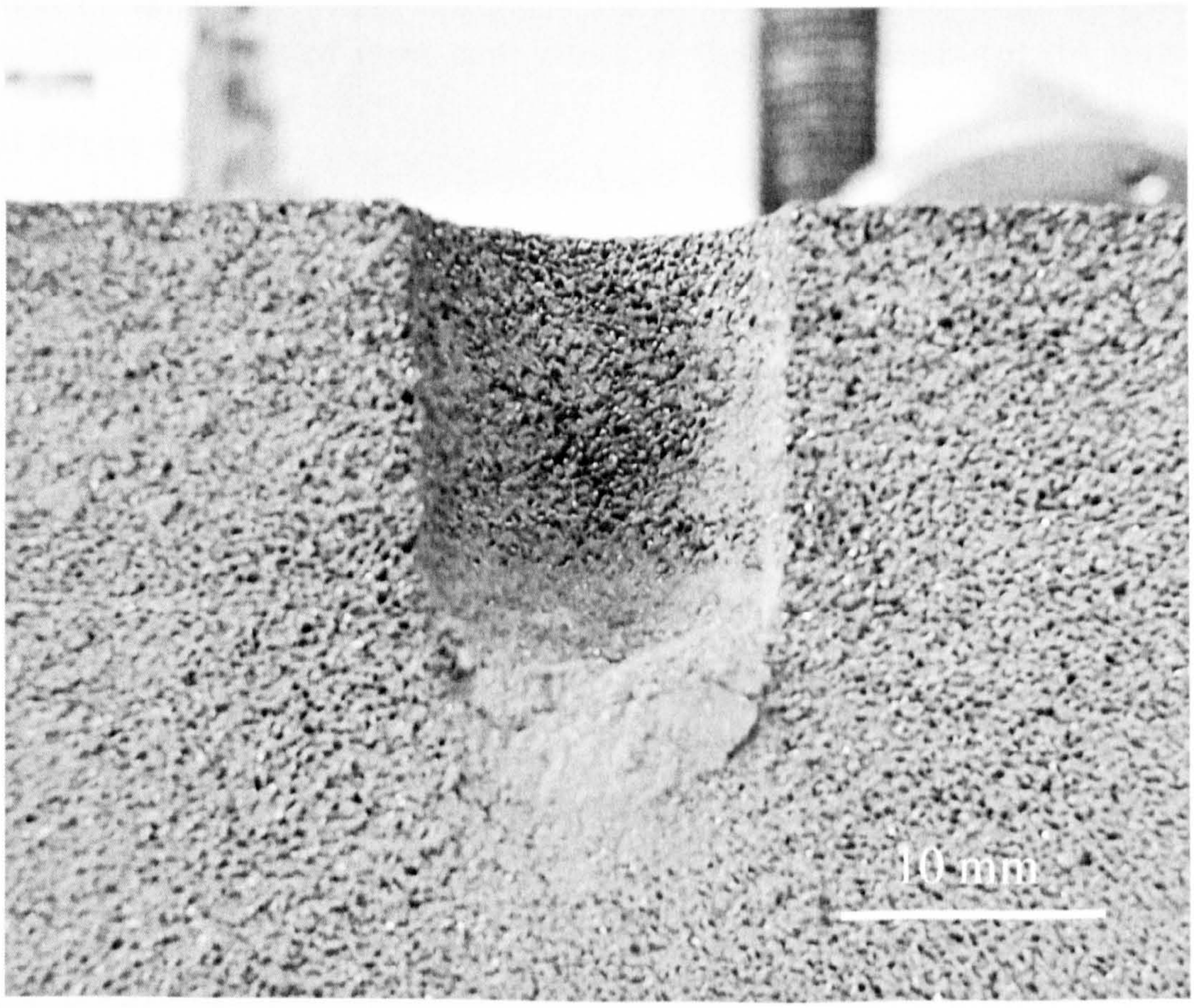

Figure 6.3 Example of failed material build up in front of penetrometer tip in type T4 foamglas.

6.4 Model for layered targets

A new program hemi2.m (Appendix A) was written for layered targets where the density and position of each material layer is known *a priori*. The program works by setting the initial velocity, v=3.2 m s^{-1}, at zero depth and time and assigns starting values to the three fitting parameters, C_d, μ_f and σ_d as in the previous model. It then runs multiple penetration simulations for the first target layer with different fitting parameter values, stopping in each case once the tip reaches the depth of the next layer. The best fit for this layer is then chosen by comparison with the laboratory data using a least squares fit and these parameter values are recorded. As the tip or shaft traverses into the subsequent boundary layer, these best fit parameters are used to calculate the deceleration due to the parts of the tip and shaft still in the previous layer together with the deceleration calculated from new values of these parameters for the layer being entered (Figure 6.4).

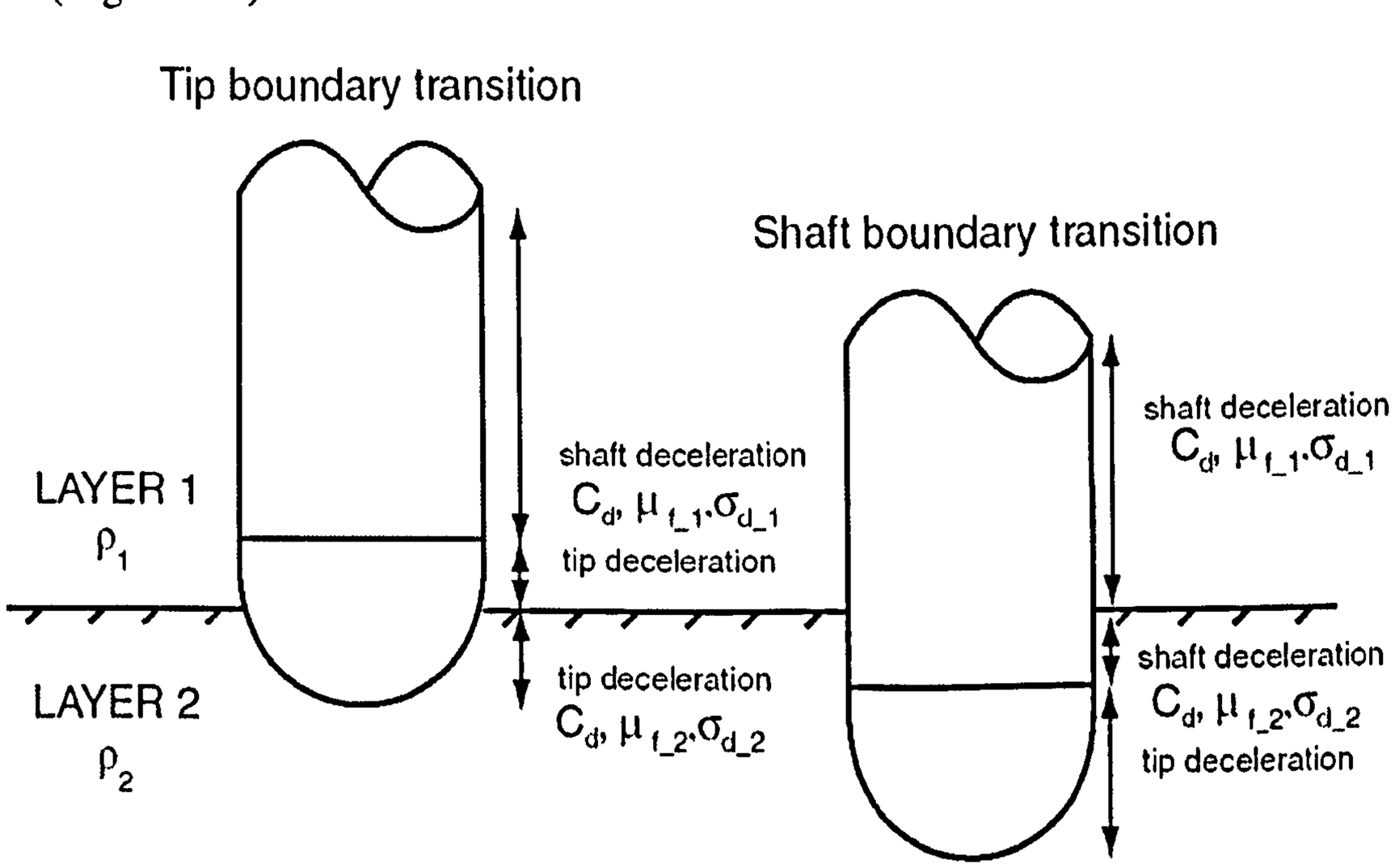

Figure 6.4 Tip and shaft boundary transitions and the fitting parameters used for calculating tip and shaft decelerations in each case.

The new layer parameters are also varied until a best fit has been achieved for the current layer. This process of best fitting parameters for each layer is repeated until the velocity has dropped to zero, equivalent to the penetrometer having stopped. A closest

match to the laboratory measure depth is then used to determine which of these complete target simulations was best. Figure 6.6 shows a simplified overview of the model. The assumptions made in this model are the same as previously with the added condition that the thickness of any layer must be greater than 7 mm, to avoid the possibility of the hemispherical tip transiting two layers at once.

A simulation into a softer 11 mm thick layer of T4 type foamglas overlying hard F type is shown in Figure 6.5. A small increase can be seen from the onset of the F type layer in the rate at which the penetrometer decelerates and loses kinetic energy.

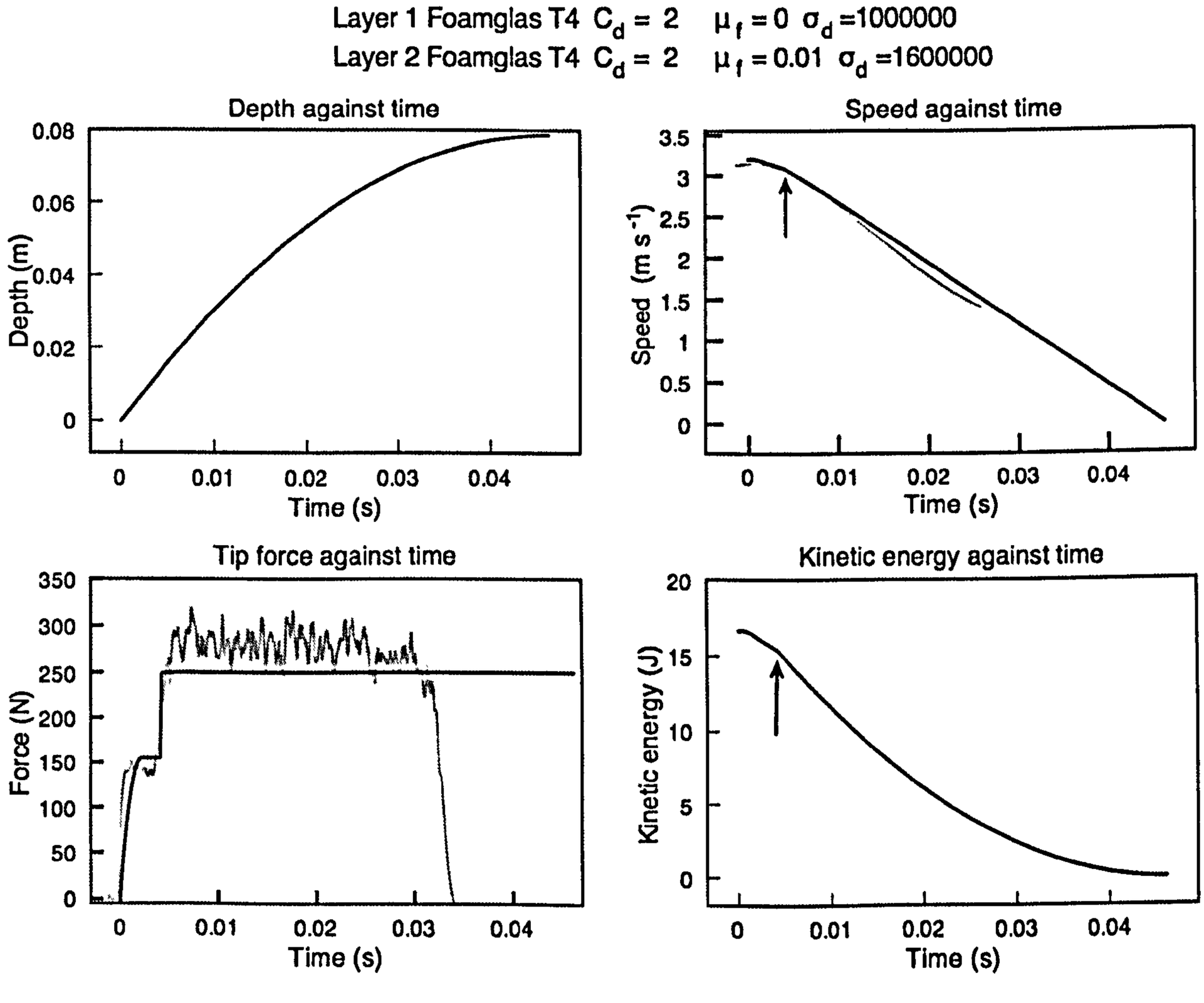

Figure 6.5 Example output from the layer program hemi2.m into a 11 mm thick T4 foamglas layer overlying hard F type material. The arrows highlight the start of a small increase in the rate the penetrometer decelerates and kinetic energy is lost due to entering the harder material. Black lines are model data; grey lines are laboratory-measured data.

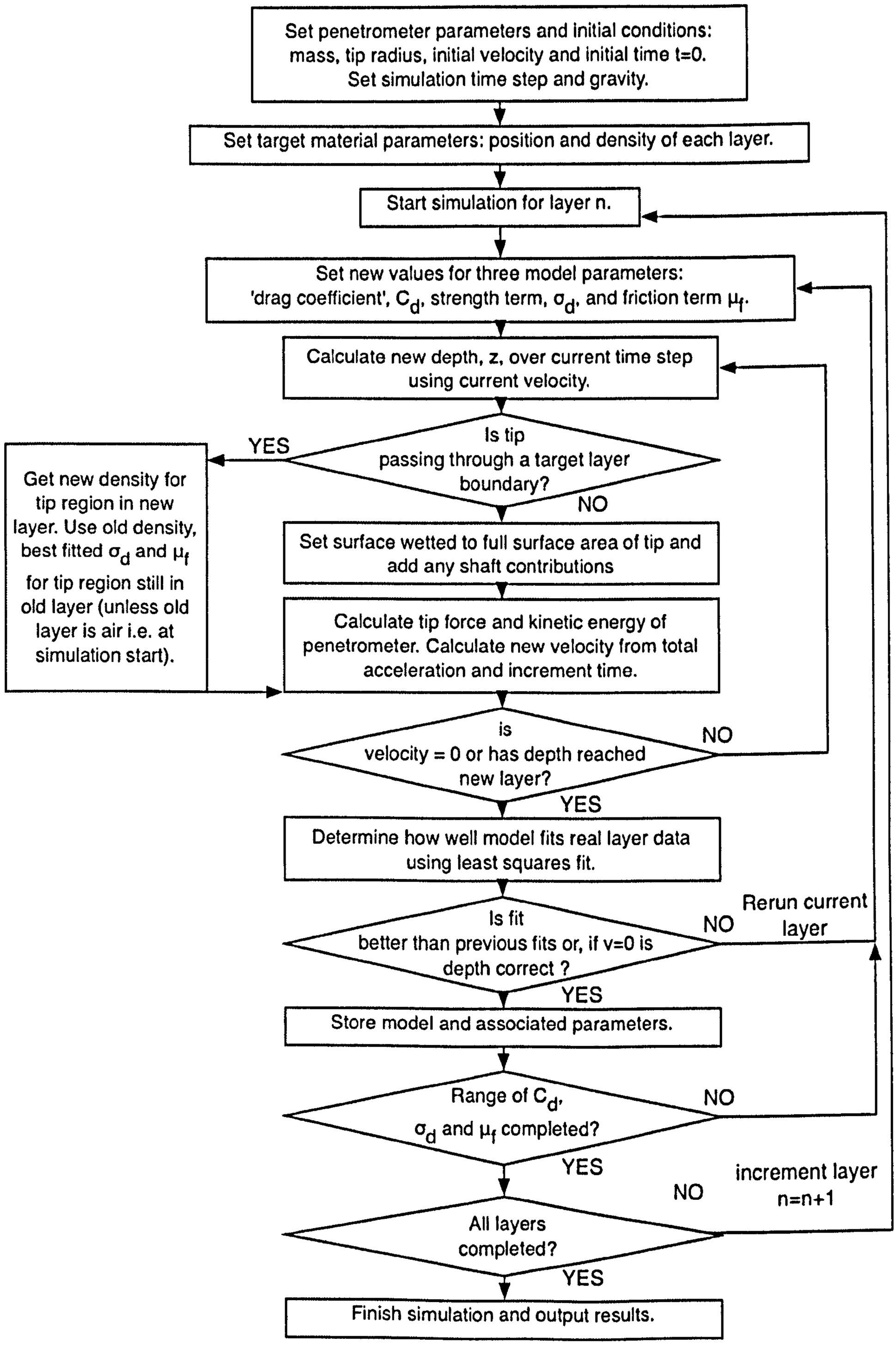

Figure 6.6 Flow diagram of layered target penetration model, hemi2.m.

6.5 Summary and conclusion

Several laboratory drops into two types of foamglas target have been simulated using a model based on previous work by other researchers. This model has been adapted to suit the tip and shaft geometry of the ACC-E penetrometer used and then extended to include layered targets of known bulk density and depth. The aim of this work was to examine how a physical penetrometry model with few input parameters might be able to provide an estimate of target material strength. Both versions of the model gave reasonable results; however model strength estimates were higher than their expected values. This can be attributed to uncertainties in calibration at the higher tip force levels and variations in the target material.

More work is needed to understand the parameter C_d and its limitations when applied to different targets. The simulations showed this parameter had little effect in the foamglas target material. Unfortunately due to the necessity of the maximum depth penetrated as a model constraint, the possible material targets that could be considered were limited with the need for the penetrometer to stop before the attached weight structure impacted the surface. Future work must use a longer penetrometer or one where the entire mass is contained within the shaft diameter. This would allow softer granular materials such as sand and more cohesive ones such as chalk powder to be examined although one can imagine that this work has already been done in a military setting.

In the simulations presented, the value of μ_f was found to be critical, with the best data fits being obtained only for values of μ_f less than 0.1. Comparison of these results with those found by Garry *et al.* (1999) using a larger 3 cm diameter hemispherical penetrometer impacting sand and flintag targets at slightly slower speed of 2.7 m s^{-1},

found that much higher values of μ_f = 0.4-1.0 were required for good fits. The values found in this experiment are however plausible given that there would be less infilling by failed foamglas material and, in contrast to their penetrometer, the ACC-E shaft has a reduced shank diameter for most of its length lessening the effect of shaft friction. An improvement to the model would be to allow for the build up of material in front of the tip effectively extending its length.

7 Analysis of the Titan penetrometry signature

7.1 Introduction

This chapter examines in more detail the penetrometer signature returned from the surface of Titan in the context of the understanding gained from laboratory and field work presented earlier. The Titan signature is considered as before, in stages. Several specific experiments have been carried out to explore different aspects of the signature and in the last section the author presents an interpretation of the signature and discusses how this might fit within the context of other recent work.

7.2 First stage

The design of the penetrometer's circular buffer allowed the capture of a small signal prior to the threshold trigger force of 5 N being reached. This initial rising force consists of 16 samples with a low average force of ~4 N (section 3.1.2) and hints at a possible soft coating on the surface. As these samples only correspond to a depth of 7 mm at 4.6 m s^{-1}, it was speculated that this rise could be attributed to the hemispherical geometry of the tip. However, this seems unlikely as no similar rise is observed in any of the material catalogue work or in subsequent work carried out by the author at the Titan impact speed. Furthermore if this low rise were exclusively a geometrical effect, it would not explain the sharply delineated increase in force seen immediately after 7 mm. Materials including molasses, fine chalk powder and snow were examined as possible analogues for this 'coating'. Figure 7.1 shows the signature of a drop into loosely packed snow with the Titan signature overlaid for comparison. Although this analogue has a higher average resistance of ~10 N compared to Titan it was the closest match to the low rising force (arrowed) seen in the Titan signature and shows that the

penetrometer could have encountered a material coating similar in mechanical properties to terrestrial snow. In very weak signals like this, noise must be carefully considered and the results interpreted with caution. The lowest noise achievable in the laboratory was 0.04 V, equivalent to ~2 N at room temperature and, as discussed, the noise on the Titan signal would almost certainly have been lower than this due to shorter wiring runs and high quality components (i.e. at the 1-bit level of 0.0176 V). The average of this low rising signal is therefore above the noise threshold.

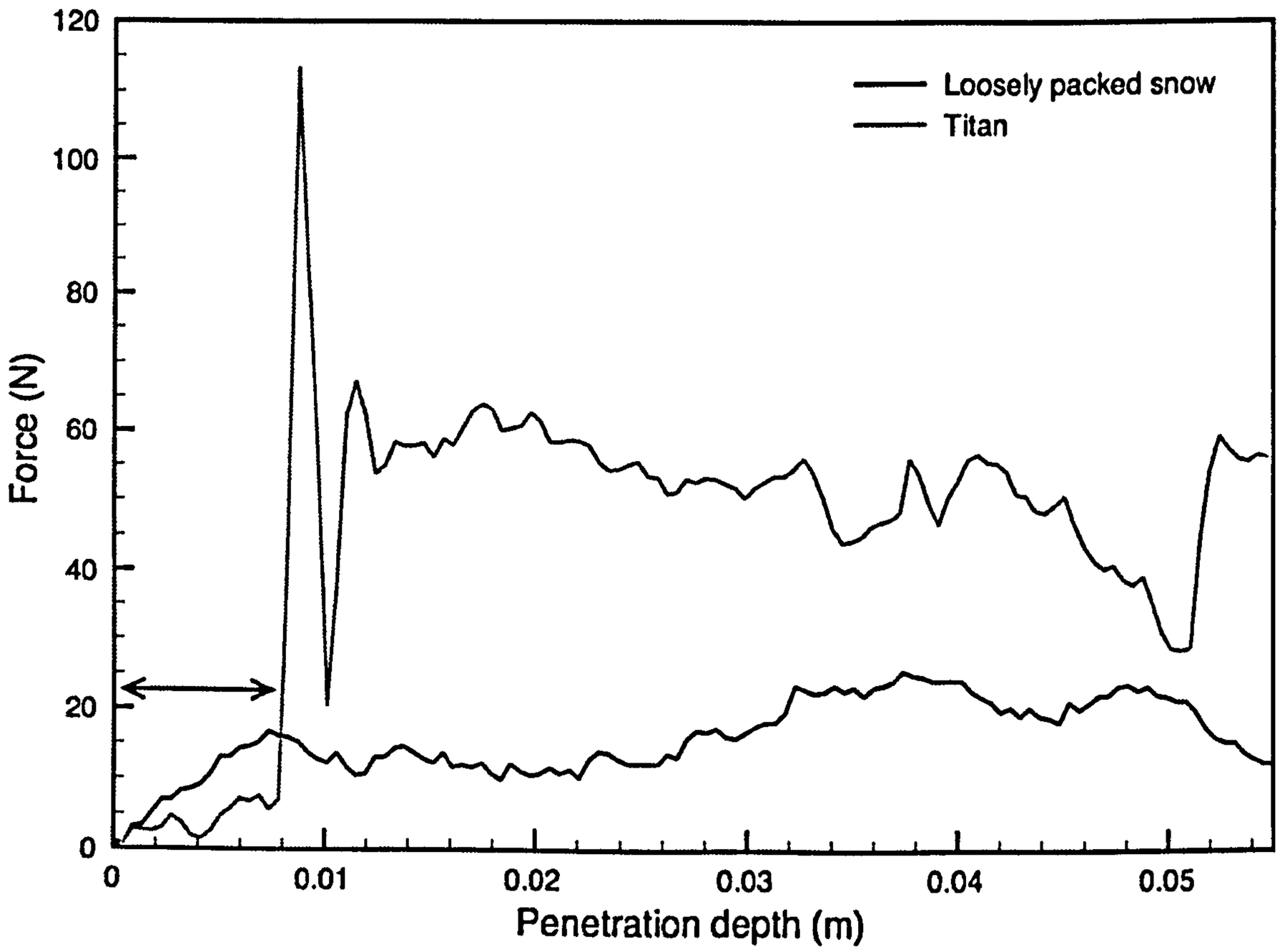

Figure 7.1 Signature of a drop into loosely packed snow at Huygens impact speed. The signature from the probe (grey) has been plotted for comparison to the entry force (arrowed). The snow signature indicates the variation in density with depth of the material caused by packing it, albeit carefully, into the target container.

7.3 Second stage

The laboratory results presented in chapter 4 showed that the peaks seen in the penetrometry signatures are related to the masses of the beads impacted. As discussed, the 'tip entry effect' can produce large variations in the initial impact force and it was

suggested that this could be caused by the number of particles impacting simultaneously and where on the tip these impacts occur. The Titan material catalogue work, supported by DISR surface images, had suggested an impact onto a surface pebble. On Titan, evidence suggests that these pebbles may be composed of water ice, presumably hardened considerably by the low surface temperatures (Keller *et al.*, 2008; Soderblom *et al.*, 2007; Tomasko *et al.*, 2005). To examine further this possibility and produce a closer signature match, ice pebbles of different masses were made by freezing water down to liquid nitrogen temperature (at -196°C or 77 K close to the temperature of Titan's surface). Small balloons were filled with water and weighed before being immersed from a thread into a dewar of liquid nitrogen (Figure 7.2). After several minutes the expanded frozen ice pebbles were removed and carefully placed on a sand surface at the centre of the target container directly below where the falling penetrometer would impact.

Drops at 4.6 m s^{-1} were carried out with pebbles ranging in mass from ~2 to 85 g (with equivalent diameters between ~15 and 50 mm assuming spherical particles) and the heights of the resulting impact peaks recorded. Table 7.1 gives the mass of the pebble and the resulting peak impact force. This shows that, despite the small number of pebbles tested, the peak impact force is in general larger for impacts into more massive pebbles in agreement with the earlier bead work. Exceptions are seen; the drop into 4 g and 19 g pebbles both have lower peaks than might be expected. This is possibly due to variations in the pebble shape or small weaknesses in its surface caused by the sudden change in temperature between the dewar and the sand surface. These weaknesses might account for the state of the pebbles after impact; some were crushed while others were neatly split in half (Figure 7.3). Another, perhaps less likely possibility may be some

irregularity in the underlying sand surface. A more controlled experiment would require a constant temperature cooled chamber.

Figure 7.2 Preparation of a water ice pebble with the help of Dr. Tim Ringrose. A water filled balloon is suspended with thread into a dewar of liquid nitrogen and allowed to cool for several minutes.

Pebble mass (g)	TITAN	54	22	20	19	14.5	13	11	8	4	2	2
Approximate diameter (mm) (if considered spherical)	--	48	36	34	34	31	30	28	25	20	16	16
Signature peak height (N)	114	339	216	360	107.	434	303	300	228	59	101	91

Table 7.1 Impact peaks recorded from 11 successful direct impacts (one drop failed to trigger the oscilloscope and another did not impact directly) with water ice pebbles of various masses on loose sand.

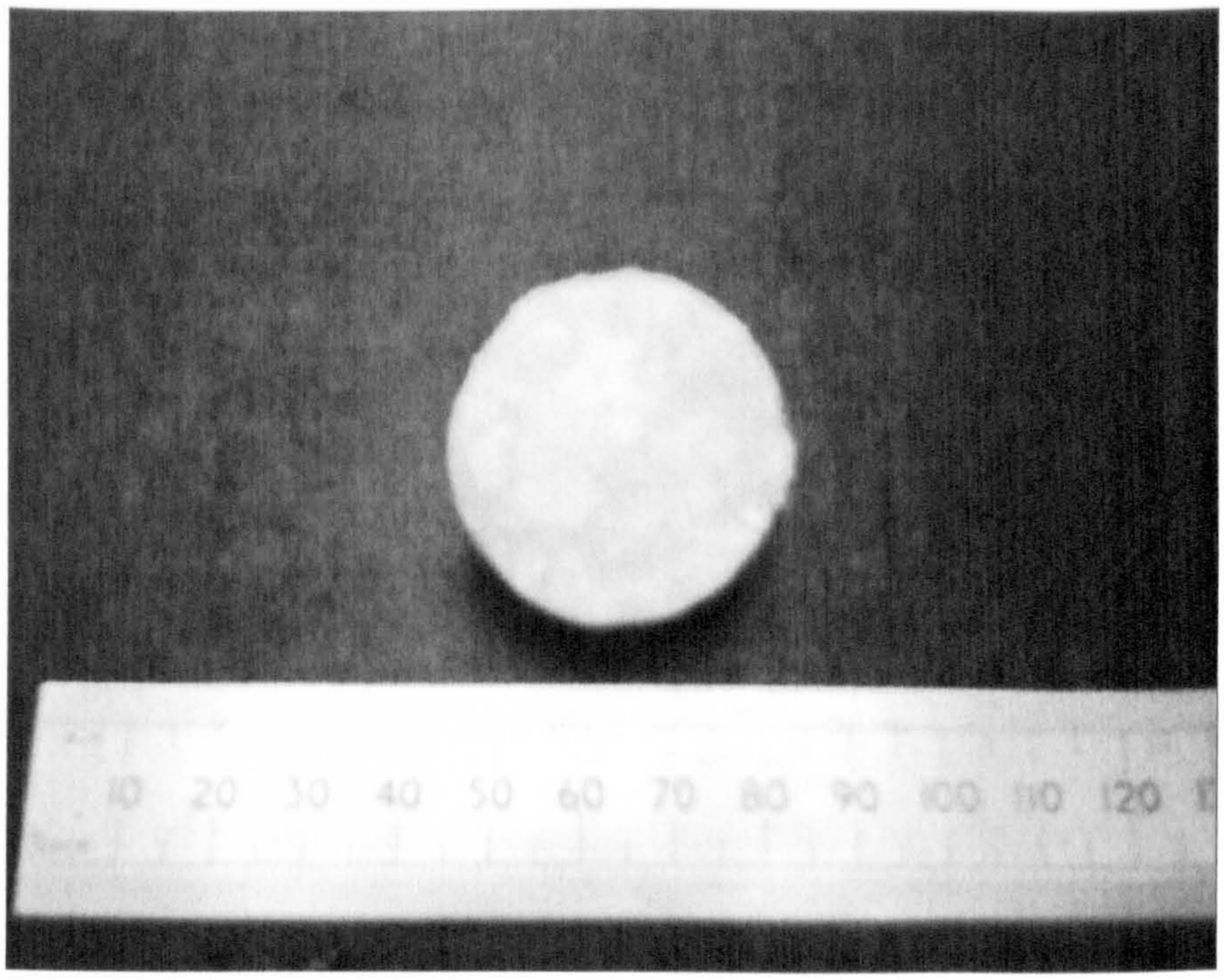

Figure 7.3 Ice pebble after impact. Some pebbles were crushed during impact and others split possibly due to weaknesses caused by temperature changes.

The table also shows that the smallest 2g pebbles (approximately 16 mm in diameter) produced a similar peak magnitude force to that seen in the Titan signature. This suggests that on Titan the penetrometer may have hit a single pebble smaller than those imaged by the DISR cameras. This however does not exclude the possibility of the 'tip entry' effect where several even smaller substrate grains could impact the penetrometer tip at the same time to produce the necessary impact peak.

To examine the surface the penetrometer may have hit, a model of the penetrometer impact was created using the two DISR 'rock count' data sets derived from the Side Looking Imager (SLI) (the upper panel in figure 2.3)[1]. The DISR team visually

---

[1] The 'rock count' the DISR team derived from the Medium Resolution Imager (MRI) was not used as the author considered it to be incomplete due to the image overexposure by the Surface Science Lamp (SSL). Note that the American term 'rock' can signify a stone of any size.

identified 'rocks' greater than 1.63 cm diameter in the SLI image from a distance of 48 cm from the probe to 103 cm and 227 cm respectively. This allowed them to compare the distributions of rocks seen in the foreground with those further afield (Keller *et al.*, 2008; Tomasko *et al.*, 2005). Similarly, the penetrometer impact model uses these rock counts separately and assumes that either could be representative of the unseen surface under the probe. The model provides a probabilistic estimate of whether the penetrometer hit a surface rock and its likely size. It creates a square surface of the same area as that considered by the rock counts data and randomly places the particles on it in accordance with the DISR derived distribution. The size of the model surface was calculated using the current estimate for the height of the SLI camera above the surface of 48 cm, the known field of view of the camera of 25.6° and the 'rock count' distances from the probe (Karkoschka *et al.*, 2007). The program then simulates a random penetrometer impact and records whether a rock was hit and if so, its size. By repeating this surface impact many times using a Monte Carlo method, a probabilistic estimate of the surface impacted can be found.

The program, rockhit.m (appendix A), starts by generating a list of particles with diameters given by the DISR rock distribution data. As the rock distribution data are binned diameter values, the program particle diameters are randomly generated within the given bin range. For simplicity the particles are assumed to be circular.

Each particle in the list is then randomly placed on the surface by generating candidate x and y coordinates for the particle centre. These are accepted subject to two conditions; the placed particle edges must be totally contained within the boundaries of the surface, and, if particles have already been placed on the surface, the currently placed particle is allowed to touch their edges but not overlap. This last condition is achieved by

calculating a *touching distance* determined by the particles' radii and a *particle distance* between particle centres using Pythagoras' theorem with the particle centres coordinates as shown in Figure 7.4.

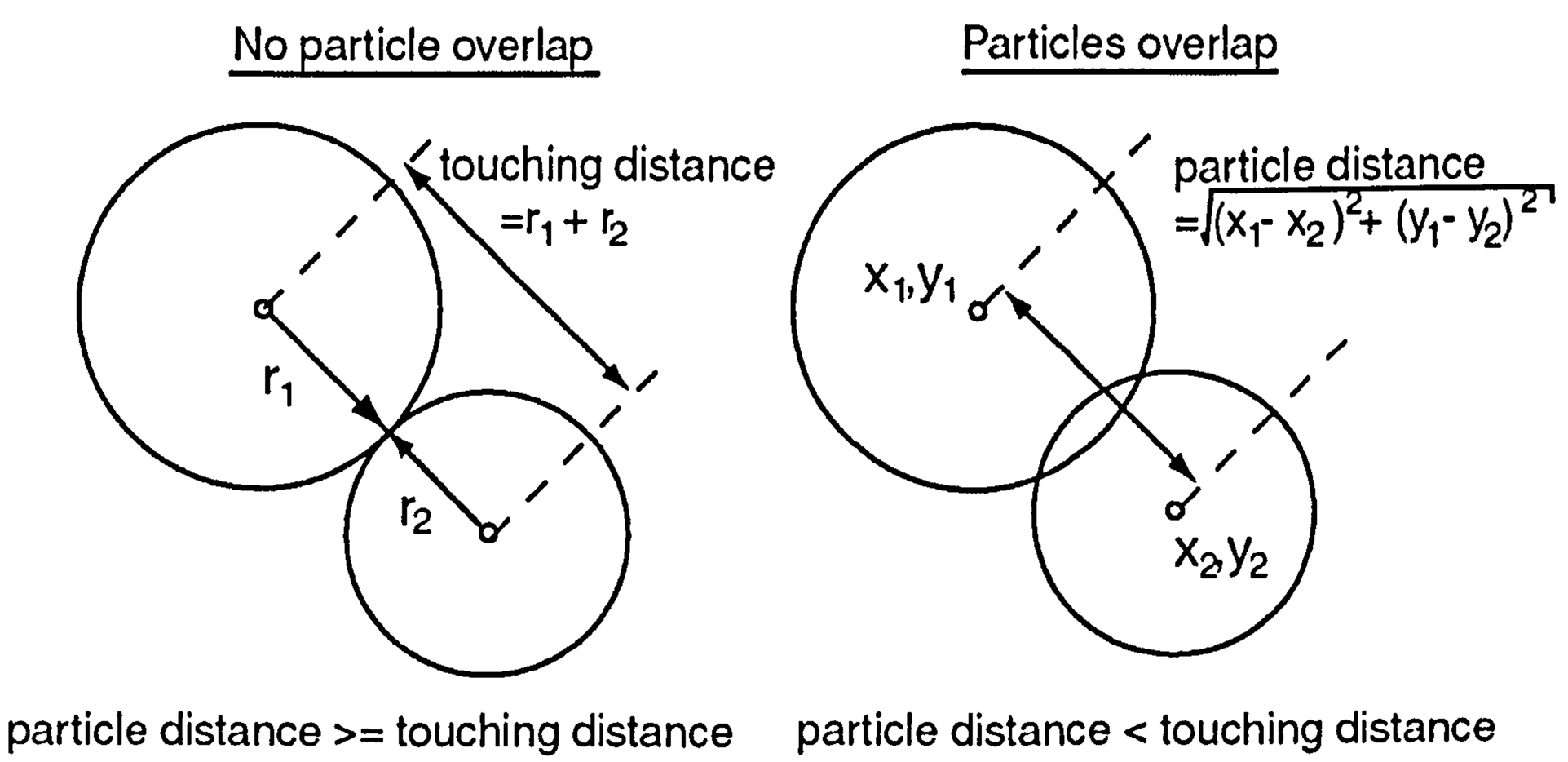

Figure 7.4 Measures used to determine if particles are overlapping when placing them on the simulated surface and also used to determine if the penetrometer impacted a given rock.

If the difference between the particle distance and the touching distance is less than zero, the particles are overlapping and new coordinates are chosen for the particle currently being placed. The positions of the centres of the successfully placed particles are then recorded together with their diameters. A simulated penetrometer is then 'dropped' randomly on the surface and a similar method to that described above is used to determine if a collision with a particle occurred and its size recorded. The penetrometer may occasionally impact two touching particles at once. In this case the diameter of the larger particle is noted as in a real situation the penetrometer would likely impact the larger particle first as it would probably rise off the ground further. Figure 7.5 shows graphic output (used for testing purposes) of one such simulation.

To gain stable estimates, the simulation was then run 100000 times for each of the SLI rock data with distances 103 cm and 227 cm from the probe. The results from both are given in Table 7.2.

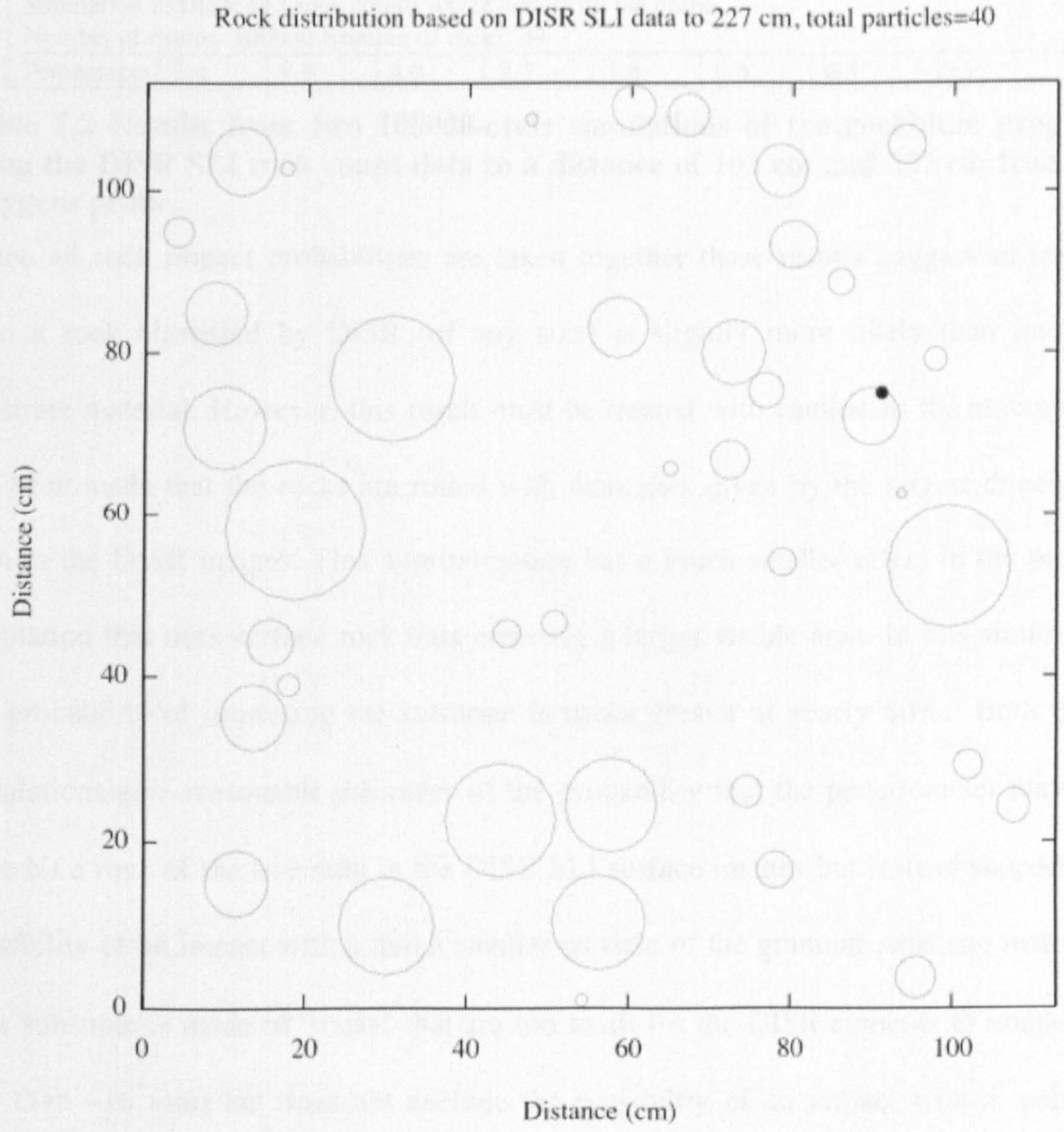

Figure 7.5 Graphical test output from the rockhit.m program of a simulated impact of the penetrometer. On this occasion the penetrometer (filled circle) has impacted the edge of a medium sized rock.

The table shows that when considering the near field rock counts data to distance of 103 cm from the probe, the single category most likely impacted is the substrate material ~45% with the next closest category being medium rocks (size between 9.65 and 15.70 cm) at 34%.

Simulation 1: DISR SLI rock counts 48-103 cm from the probe Number of cycles: 100000 Number of rocks: 14								
Rock bin diameters, *x* (cm)	15.70≤ *x* <20.09	9.65≤ *x* <15.70	6.83≤ x <9.65	4.83≤ x <6.83	3.42≤ x <4.83	2.42≤ x <3.42	1.63≤ x <2.42	Substrate
Percentage	12.9	34.0	3.1	1.7	2.0	0.6	0.9	44.8
Simulation 2: DISR SLI rock counts 48-227 cm from the probe Number of cycles: 100000 Number of rocks: 44								
Percentage	2.4	8.9	4.0	2.3	1.6	0.6	0.3	79.9

Table 7.2 Results from two 100000-cycle simulations of the rockhit.m program using the DISR SLI rock count data to a distance of 103 cm and 227 cm from the Huygens probe.

When all rock impact probabilities are taken together these results suggest an impact onto a rock classified by DISR (of any size) is slightly more likely than into the substrate material. However, this result must be treated with caution as the assumption has been made that the rocks are round with diameters given by the largest dimension seen in the DISR images. This approximation has a much smaller effect in the second simulation that uses surface rock data covering a larger visible area. In this simulation the probability of impacting the substrate is much greater at nearly 80%. Both these simulations give reasonable estimates of the probability that the penetrometer may not have hit a rock of the size seen in the DISR SLI surface images but instead support the possibility of an impact with a much smaller particle of the granular substrate material. This substrate is made of 'rocks' that are too small for the DISR cameras to image (i.e less than ~16 mm) but does not exclude the possibility of an impact with a 'pebble-sized' particle as defined by the Udden-Wentworth scale. This suggestion that the penetrometer only impacted the substrate is supported by the ACC-I accelerometer. When the penetrometer and accelerometer data are overlaid a small rise is seen in the ACC-I data prior to the penetrometer impact (Figure 7.6). The two sensors are sampled at different rates and there are small uncertainties in the timings; however this signal implies the probe foredome must have hit a rock first to register this signal (Zarnecki *et al.*, 2005).

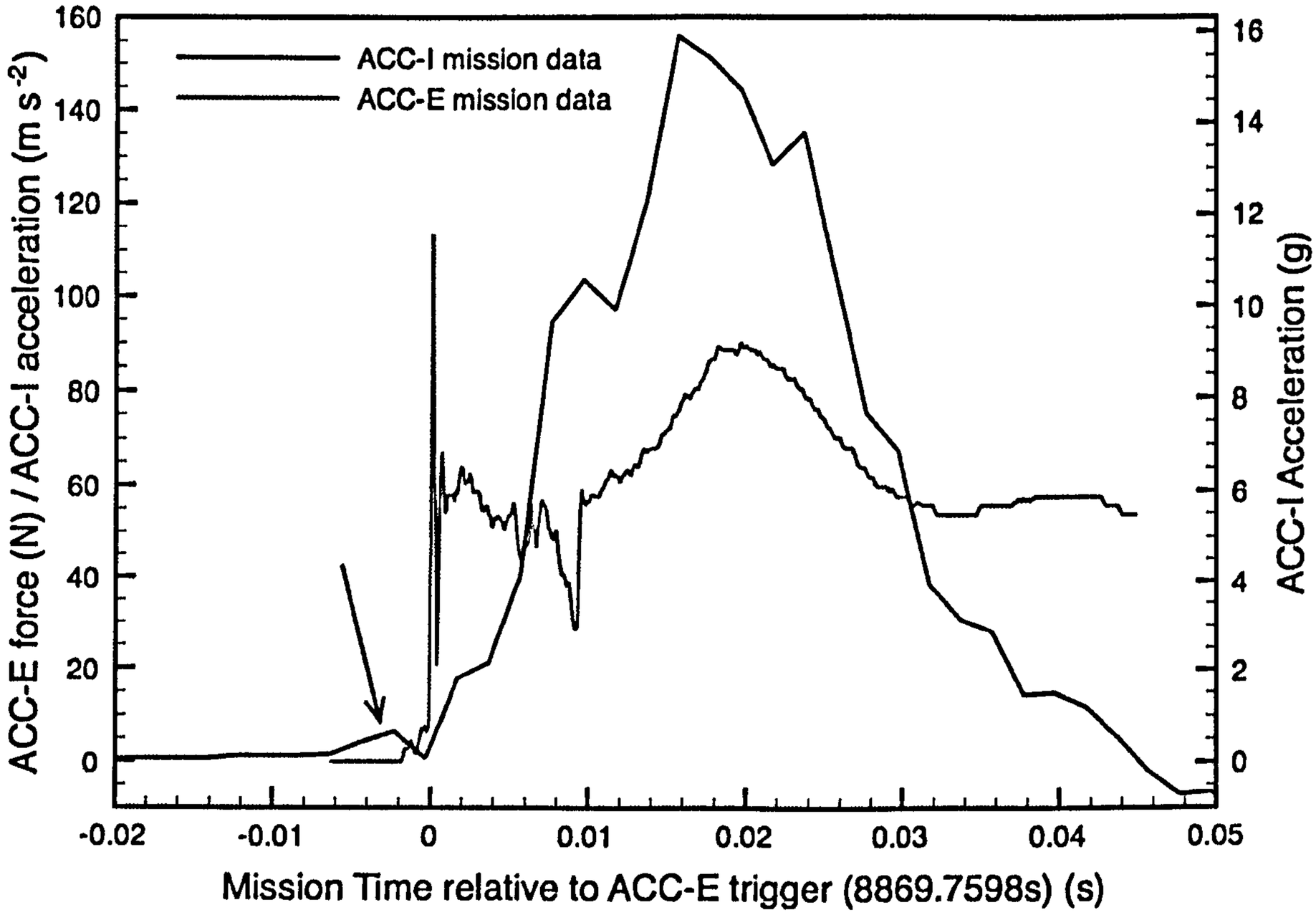

Figure 7.6 ACC-E penetrometer and ACC-I accelerometer data plotted relative to the ACC-E hardware trigger occurring at Mission Time of 8869.7598 s. Arrow marks a small precursor peak of approximately 0.6 g in magnitude that could signal the foredome impacting an ice rock before the penetrometer impacts the substrate material. Plot adapted from M. Leese (personal communication).

7.4 Third stage

The third stage of the Titan penetration signature is the longest, lasting 8.3 ms and is unusual due to a significant downward trend; resistance usually increases as the target material becomes compacted in front of the advancing penetrometer. Attempts to reproduce this downward trend using targets with voids made by pushing various sizes of metal rods into a clay block were only partially successful in modifying the flat clay penetrometry signature to a slightly downward-sloped one. As the downward gradient of the Titan signature is significantly greater than any seen in the clay with voids, this would appear to be an unlikely analogue. The significance of this slope is discussed later in this chapter after considering one further analogue.

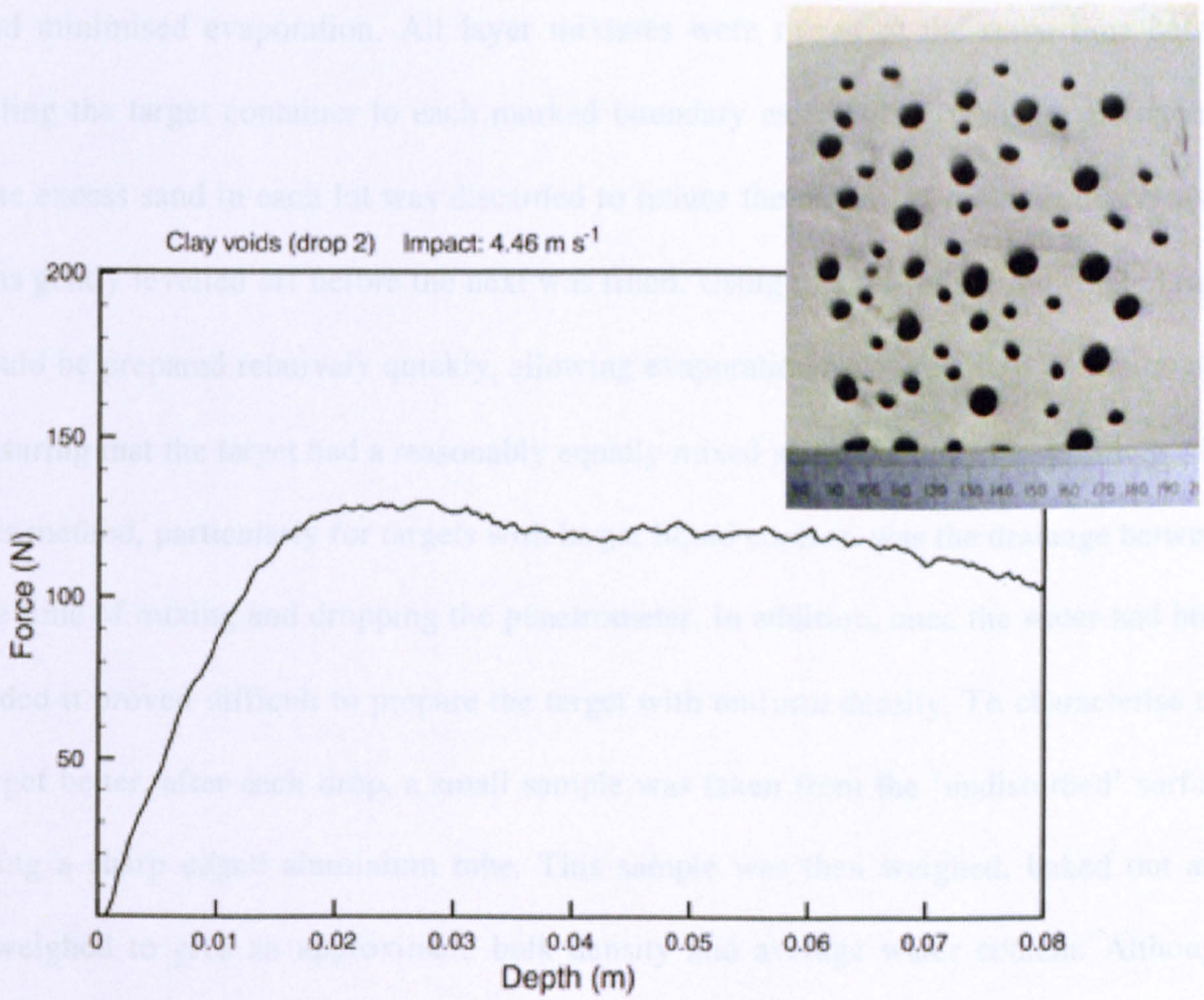

Figure 7.7 Penetrometry signature for a compacted clay void target (shown in inset). The signature after tip entry is generally flat or slightly downward but not as significantly as seen in the Huygens signature as discussed later.

The work for the material catalogue (section 3.1) contained a few drops into wetted granular sand targets. Although these drops into paving sand did not have well-characterised moisture content, with no measure of the amount or distribution of water in the sand, they did seem to show the unusual feature of decreasing material resistance with depth, similar to that seen in the Huygens signature. This behaviour made revisiting this analogue worthwhile.

As a first attempt to examine the effects of liquid content in sand, targets were prepared in layers by mixing 10 kg lots of sand with a set proportion of water by weight using a spiral paint mixer. This allowed quick and thorough mixing of the water into the sand

and minimised evaporation. All layer mixtures were mixed at the same time before filling the target container to each marked boundary as for the dry sand experiments. The excess sand in each lot was discarded to reduce the effects of drainage. Each layer was gently levelled off before the next was filled. Using this procedure the whole target could be prepared relatively quickly, allowing evaporation to be kept to a minimum and ensuring that the target had a reasonably equally mixed water content. The problem with this method, particularly for targets with larger liquid content, was the drainage between the time of mixing and dropping the penetrometer. In addition, once the water had been added it proved difficult to prepare the target with uniform density. To characterise the target better, after each drop, a small sample was taken from the 'undisturbed' surface using a sharp edged aluminium tube. This sample was then weighed, baked out and reweighed to give an approximate bulk density and average water content. Although this improved the method, it was still not suitable for targets with higher water content where taking a sample became difficult. Furthermore, sampling did not overcome variations in the target density and might not be representative of the liquid arrangement seen by the ACC-E, since the penetration process itself was likely to cause moisture changes within the pores by dilatancy. These problems led to a reassessment of how to prepare targets that are well characterised and best represent a wet granular material seen in nature.

7.4.1 Measuring moisture and preparing targets

Current research examining the effect of water on penetration resistance in soils in the field has focused on the development of penetrometers that are combined with special Time Domain Reflectometry (TDR) probes that measure the soil water content *in situ* as they penetrate the soil (see for example Vaz *et al.*(2001) and Cassel *et al.*(2007)). These

penetrometers have the advantage of accurately measuring water content but without causing additional disturbance to soil before the penetrometer enters. Clearly, it would be difficult to add retrospectively this capability directly to the laboratory ACC-E penetrometer. However it was still desirable to be able to measure the water content of the material targets directly with minimal disturbance immediately prior to the impact of the penetrometer.

There are various methods of measuring soil water content in field soils and these were investigated. Two devices commonly used are tensiometers and theta probes. Both had been used by researchers in another university department at The Open University and were therefore available on-site. The Delta-T ML2x theta probe (Delta-T, 1999; Gaskin and Miller, 1996; Yang and Davidson-Arnott, 2005) (Figure 7.8) was chosen as it can measure water content quickly and directly, causes minimal target disturbance, and does not remain in the target during impact. The probe has four thin rods of 3 mm diameter that are inserted 60 mm into the target causing minimal disturbance to the material that will be in contact with the penetrometer. It measures the local volumetric water moisture content, θ_v, which is the ratio of the volume of water to the total volume of the sample contained within a cylindrical volume by the four probe rods:

$$\theta_v = \frac{\text{Volume of water}}{\text{Total volume of sample}} \qquad \textbf{(Equation 7.1)}$$

This is a usually expressed as either a percentage or a ratio with 0.0 m^3m^{-3} being a sample containing no water and 1.0 m^3m^{-3} the measurement for pure water (i.e. no soil). The operating principles of the probe are described in section 7.4.2.

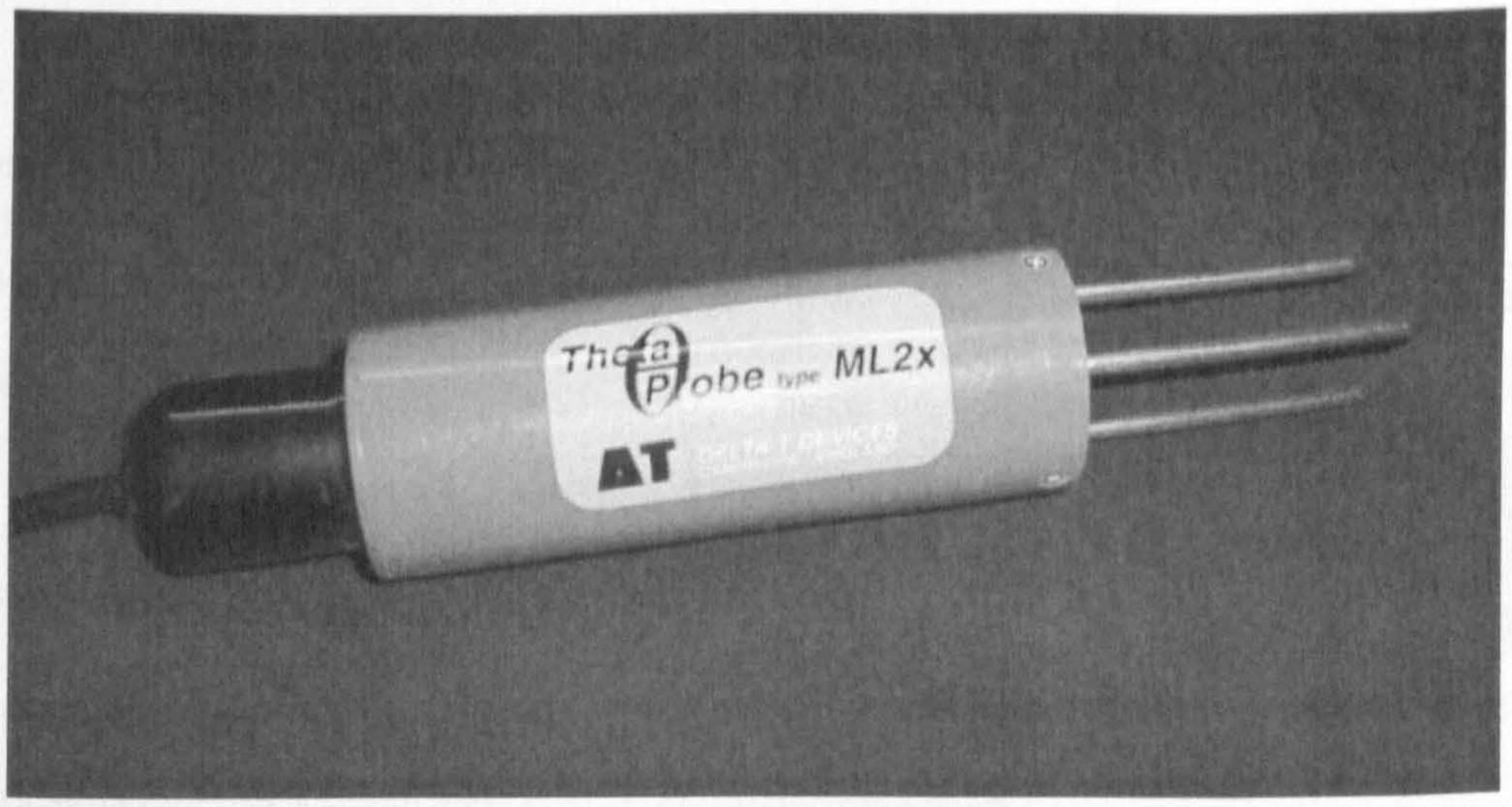

Figure 7.8 The theta probe used to measure the volumetric water content of the sand targets immediately prior to penetration.

In fieldwork, one or more theta probes are usually attached to data logging equipment and buried in the ground to monitor the changes in ground moisture over time. Burying the theta probe in the target might have affected the penetrometry so the target materials were prepared in a rigid plastic cylindrical container (diameter 320 mm and depth 350 mm) with seven regularly spaced sampling points drilled into the sidewall of the container. Water content was then measured directly by gently pushing the theta probe rods into the target at these points, taking a measurement and then retracting them. Adjacent sampling points were offset from each other on the side of the container to further minimise localised target disturbance (Figure 7.9) Two target materials were used: coarse grained Leighton Buzzard DA 16/30 and fine grained RH T sand which was prepared in five successive locked density layers as described previously.

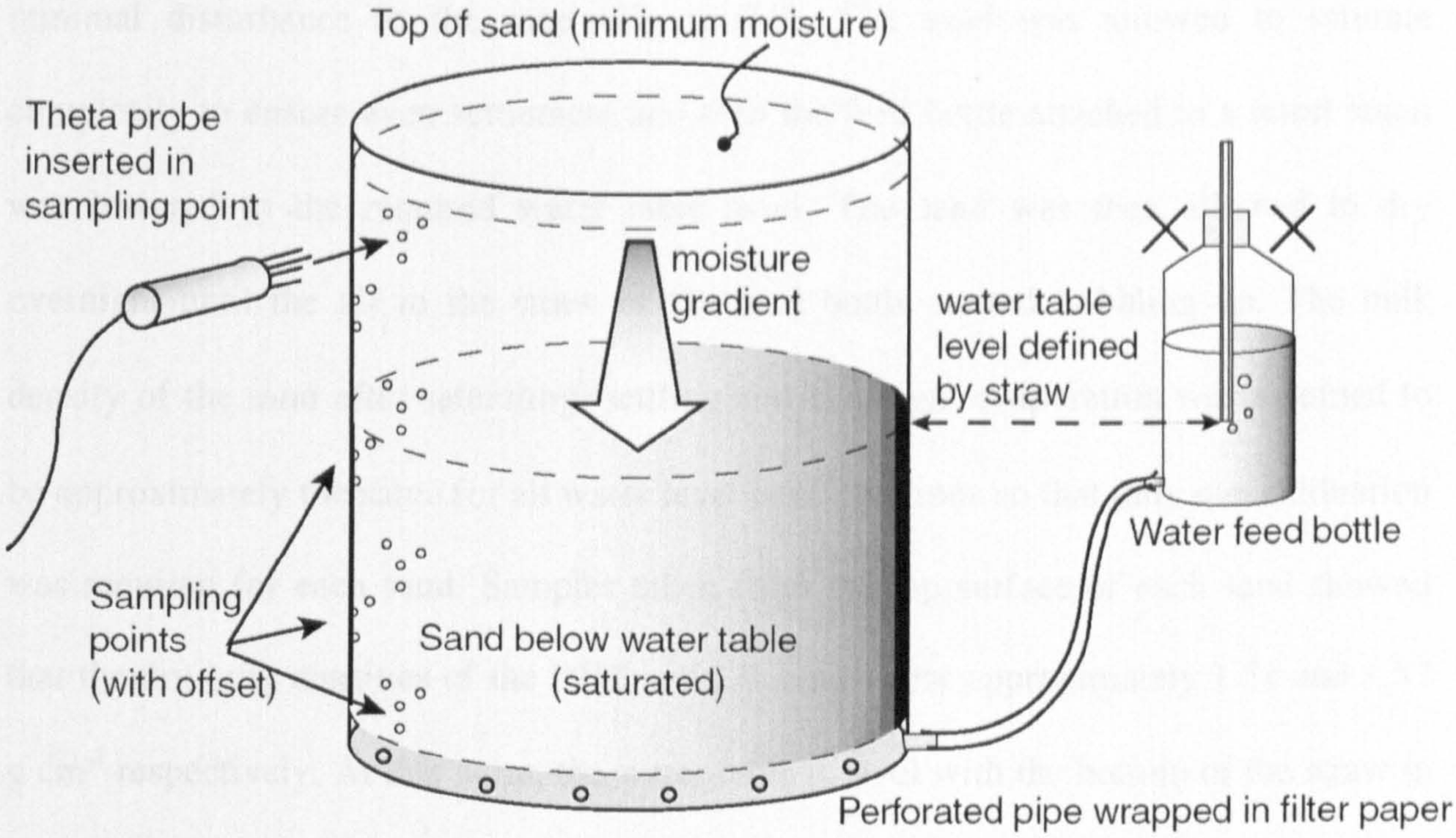

Figure 7.9 Producing a moisture gradient in sand with minimum disturbance using a siphon principle. Moisture content is measured prior to each drop using a Theta probe inserted into the sides of the container. Sampling points were offset to minimise sand disturbance.

Initial experiments with the new target container introduced the water by pouring it onto the surface until saturation was reached and then allowing the ensemble to dry out overnight. While similar to the way water is deposited on Earth and also with the way liquid methane might have been deposited at the Titan landing site, this approach proved unrepeatable as the mechanical action of the water on the surface compressed the upper layers of the sand, forcing trapped air to bubble up. A more repeatable method (Dr. Richard Whalley, personal communication) is to allow the water to be introduced into the sand from below by capillary action. This has also been used in an investigation to measure elastic wave velocities in saturated sand (Velea *et al.*, 2000). A hole was first drilled into the bottom of the sidewall of the container to accommodate a bulkhead connector and then a perforated rubber hose wrapped in filter paper was coiled up inside the bottom of the bucket and attached to the inside of this connector. The sand was loosely poured into the container and a feed bottle was used to introduce gently water into the bottom of the container through the perforated hose and filter paper causing

minimal disturbance to the sand (Figure 7.9). The sand was allowed to saturate completely to ensure even settlement and then the feed bottle attached to a retort stand was lowered to the required water table level. The sand was then allowed to dry overnight until the air in the straw of the feed bottle started bubbling up. The bulk density of the sand after saturating, settling and overnight evaporation was assumed to be approximately the same for all water level configurations so that only one calibration was required for each sand. Samples taken from the top surface of each sand showed that the dry bulk densities of the RHT and LB sands were approximately 1.51 and 1.57 g cm^{-3} respectively. At this point, the water table is level with the bottom of the straw in the feed bottle. This produces, by capillary action, a moisture gradient between the water table and the surface that can be controlled by adjusting the water table. Prior to filling the bucket with the sand and water, the sampling point holes were externally covered with thin packaging tape. Immediately before the drop, this tape was punctured by the theta probe rods, a measurement taken, and the holes were quickly resealed with tape. This simple method proved effective with at worst, a few drops of water being lost. Due to the time-consuming target preparation and subsequent necessity to allow each sand to dry completely before they could be used to prepare a new wet target, only four wet drops were carried out into each of the two sands. The water table levels were measured from the bottom of the target container (height 350 mm) at 150, 200, 250, and 350 mm (i.e. saturated sand).

7.4.2 Theta probe operating principles

A 100 MHz signal is transmitted to the soil via the probe's array of rods. The impedance measured across the array of rods is dependent on the dielectric constant and the ionic conductivity of the soil. The effect of this second factor is minimised using the

high 100 MHz signal frequency such that the measured impedance is affected mainly by the apparent dielectric constant of the soil (Gaskin and Miller, 1996). Water has a considerably higher dielectric than soil or air (~81 compared to 3-5 for soil and 1 for air). This implies that the dielectric constant for a given soil is largely determined by the water content. The probe outputs an analogue DC voltage between 0 and 1 V which is related to the soil dielectric constant and hence, when correctly calibrated, to the soil moisture content.

7.4.3 Soil specific calibration of the theta probe

In order to give accurate values of volumetric moisture content, a calibration of the theta probe was necessary for the two different sands. A soil specific calibration is needed to relate the probe's output voltage to the soil dielectric constant, ε, and in turn to its volumetric moisture content, θ_v. The relationship between the theta probe voltage output, V, and the square root of the soil's dielectric constant has been found to be given empirically by (Delta-T, 1999):

$$\sqrt{\varepsilon} = 1.07 + 6.4V - 6.4V^2 + 4.7V^3 \qquad \textbf{(Equation 7.2)}$$

and the relationship between this dielectric constant and the volumetric moisture content is given by an equation of the form (Delta-T, 1999):

$$\sqrt{\varepsilon} = a_0 + a_1\theta_v \qquad \textbf{(Equation 7.3)}$$

where a_0 and a_1 are coefficients that need to be determined from the calibration. A sample of damp soil was collected with minimal disturbance from the target surface using the sharp edged sampling cylinder. The theta probe rods were gently inserted into this sample and the probe's voltage output, V_w, was recorded. The wet weight, W_w, and volume, L, were also recorded. Using equation 7.2, a wet value for the dielectric constant, ε_w, was calculated. The sample was oven dried overnight in the same way as

used in the grain size analysis, and then weighed (W_0). The theta probe output, V_0, of this dried sample ($\theta \approx 0$) was then used in equation 7.2, and a value of $\sqrt{\varepsilon_0}$ was calculated. This is equal to the coefficient a_0. The volumetric water content, θ_W, of the original sample was then calculated:

$$\theta_w = \frac{(W_w - W_0)}{L} \qquad \textbf{(Equation 7.4)}$$

and the other coefficient, a_1, is given by:

$$a_1 = \frac{\sqrt{\varepsilon_w} - \sqrt{\varepsilon_0}}{\theta_w} \qquad \textbf{(Equation 7.5)}$$

Inserting Equation 7.2 into Equation 7.3 and rearranging now allows the water content of any sample to be found from the theta probe output (Delta-T, 1999):

$$\theta = \frac{\left(1.07 + 6.4V - 6.4V^2 + 4.7V^3\right) - a_0}{a_1} \qquad \textbf{(Equation 7.6)}$$

The graph in Figure 7.10 shows the resulting calibration curves for the two sands relating the Theta probe output to the soil moisture. This was used to create approximate sand-water moisture characteristic curves for each drop (described later).

7.4.4 Measurement accuracy

The manufacturer of the ML2x theta probe asserts an achievable measurement accuracy of ±0.05 and ±0.06 m^3m^{-3} for a generalised and soil-specific calibration respectively (Delta-T, 1999). In practice however, this is unlikely to be achieved in this wetted sand experiment for several reasons; although both sands are likely to be reasonably homogenous with the packing technique used, this is not guaranteed as it will depend on the rate water is introduced. Furthermore a large source of measurement error is the extent that the sand is disturbed by insertion and removal of the probe rods which inevitably leads to some liquid loss.

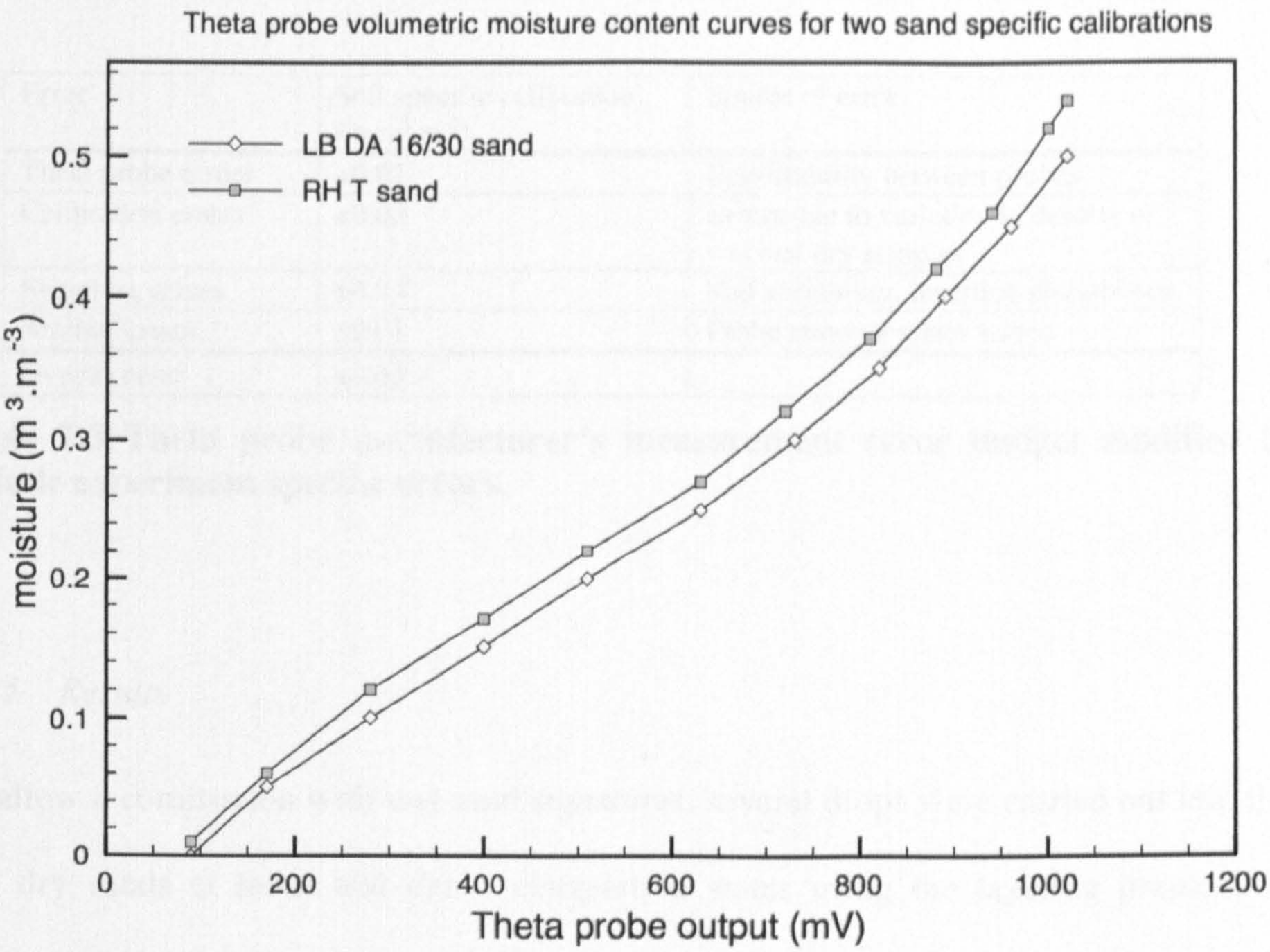

Figure 7.10 Soil-specific calibration curves for the two sands

In normal usage, the probe would be 'installed' in the soil to be tested and left to record moisture readings at various intervals using a data logger thus avoiding further soil disturbance. Another source of error is in the calibration, which relies of obtaining a moisture measurement from a sample in its wet and dry states. This is easy for a cohesive moist sand, however once the sand has dried it looses rigidity and will collapse leading to a change in density which affects the moisture measurements. For this purpose the wet sand sample was collected in a plastic container that held the sample together when dry for the second moisture measurement to be made however some shrinkage was noted. The probe's error measurement budget must be modified to account for these factors. Table 7.3 gives sufficient estimates of the new errors.

Error	Soil specific calibration (in $m^3.m^{-3}$)	Source of error
Theta probe errors	±0.01	Repeatability between probes
Calibration errors	±0.03	Errors due to variation in density of wet and dry samples
Sampling errors	±0.04	Soil variability, insertion disturbance
Sealing losses	±0.01	Probe removal water losses
Overall error	±0.05	

Table 7.3 Theta probe manufacturer's measurement error budget modified to include experiment specific errors.

7.4.5 Results

To allow a comparison with wet sand signatures, several drops were carried out into the two dry sands at loose and dense compaction states using the layering preparation technique described in section 3.5. Examining the signatures (Figure 7.11 and Figure 7.12) shows that when dry, the two sands have similar shaped signatures although the initial 'tip entry' peak is larger in the coarser sand.

The coarser grained LB sand generally has a higher penetration resistance than the finer RH T sand and as would expected, the compacted state of each sand has greater mechanical strength than the loose state. Once water is introduced into these sands even in small quantities, their penetrometry signatures change considerably and in different ways. Examining the finer RH T sand, Figure 7.13 shows the signatures for the water table configurations tested.

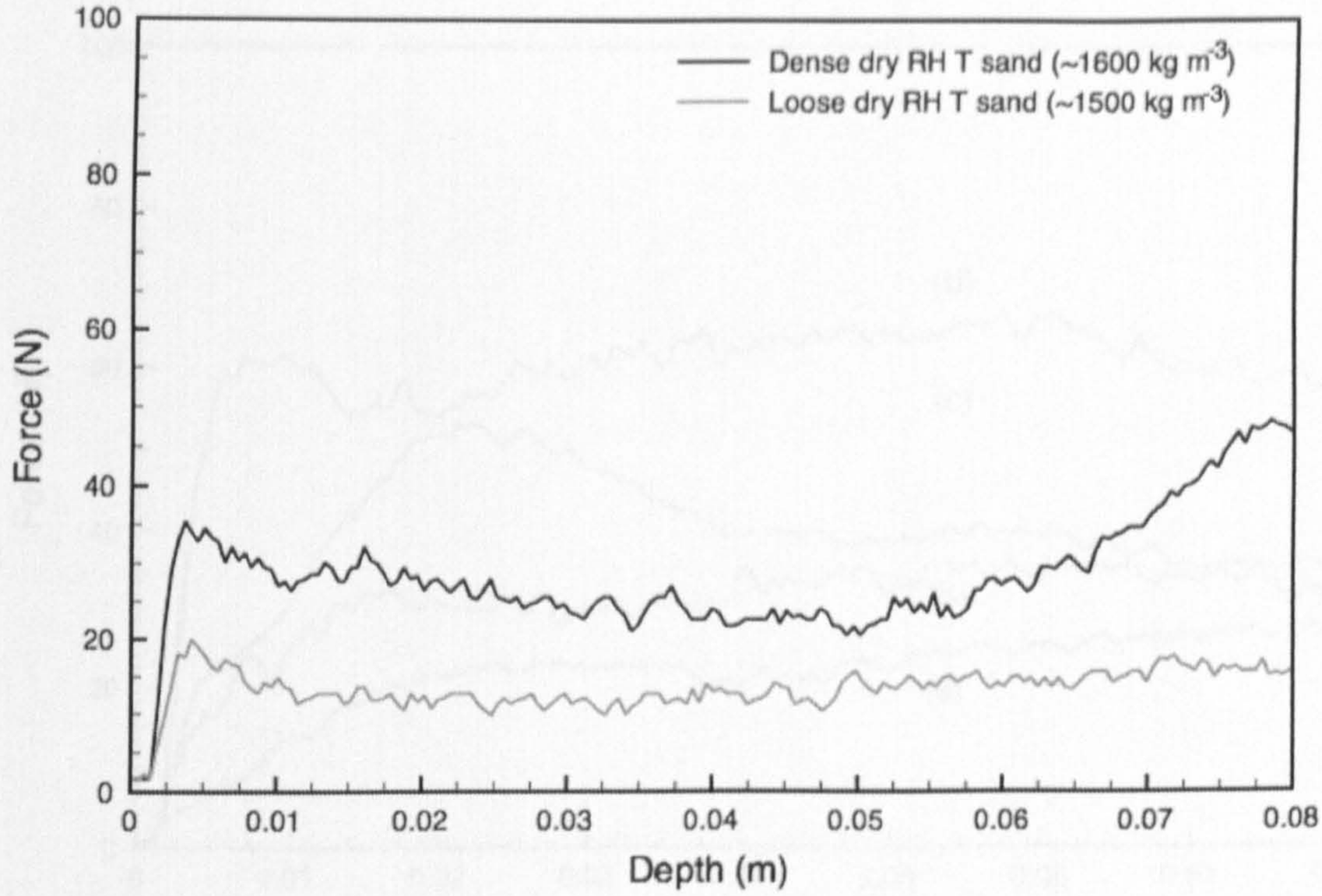

Figure 7.11 Penetrometry signatures for dry RH T sand in two densities. Impact at 4.6 m s^{-1}

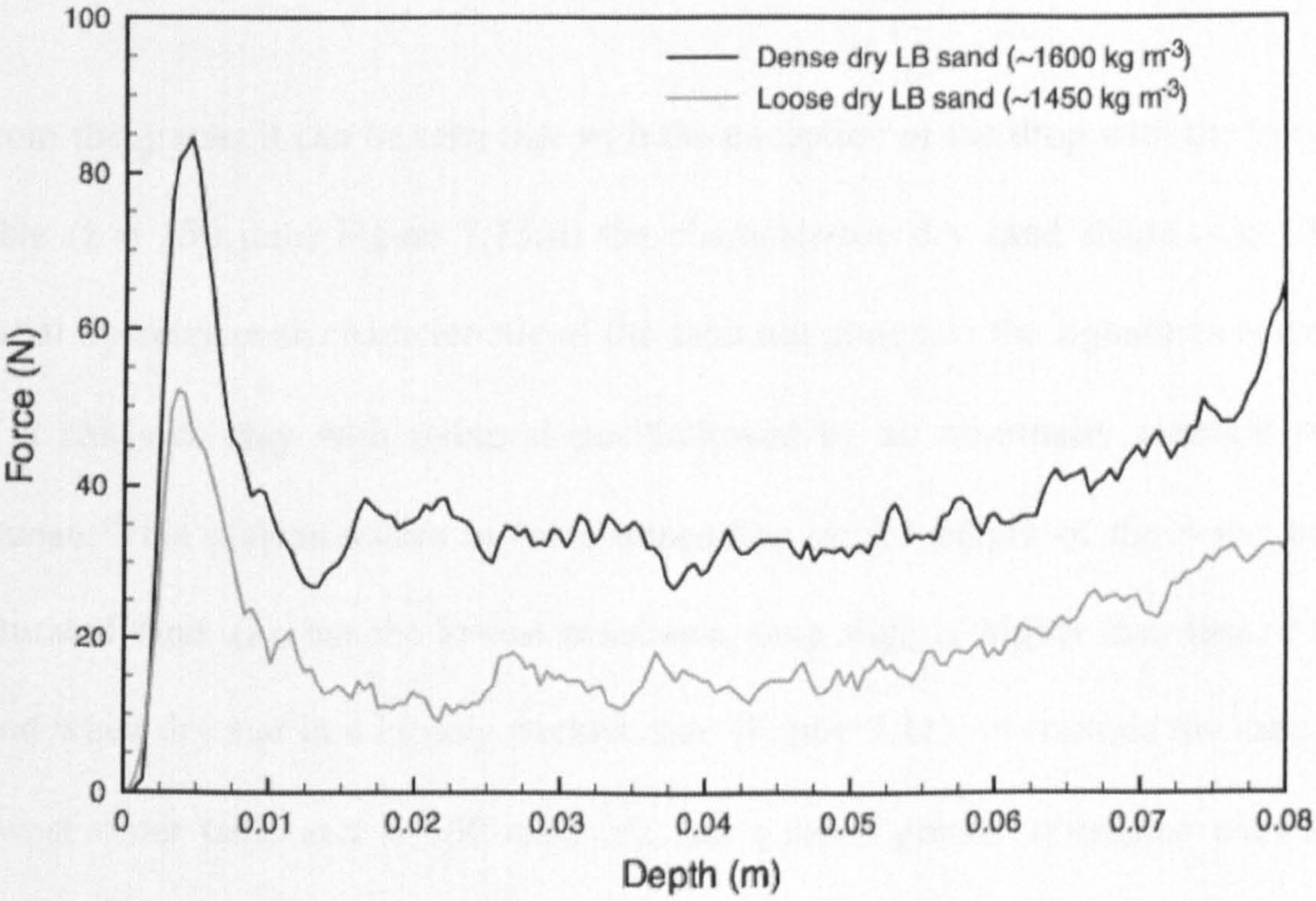

Figure 7.12 Signatures for dry LB sands in loose and dense states showing noticeably greater tip entry impact peaks than those seen in finer RH T sand above.

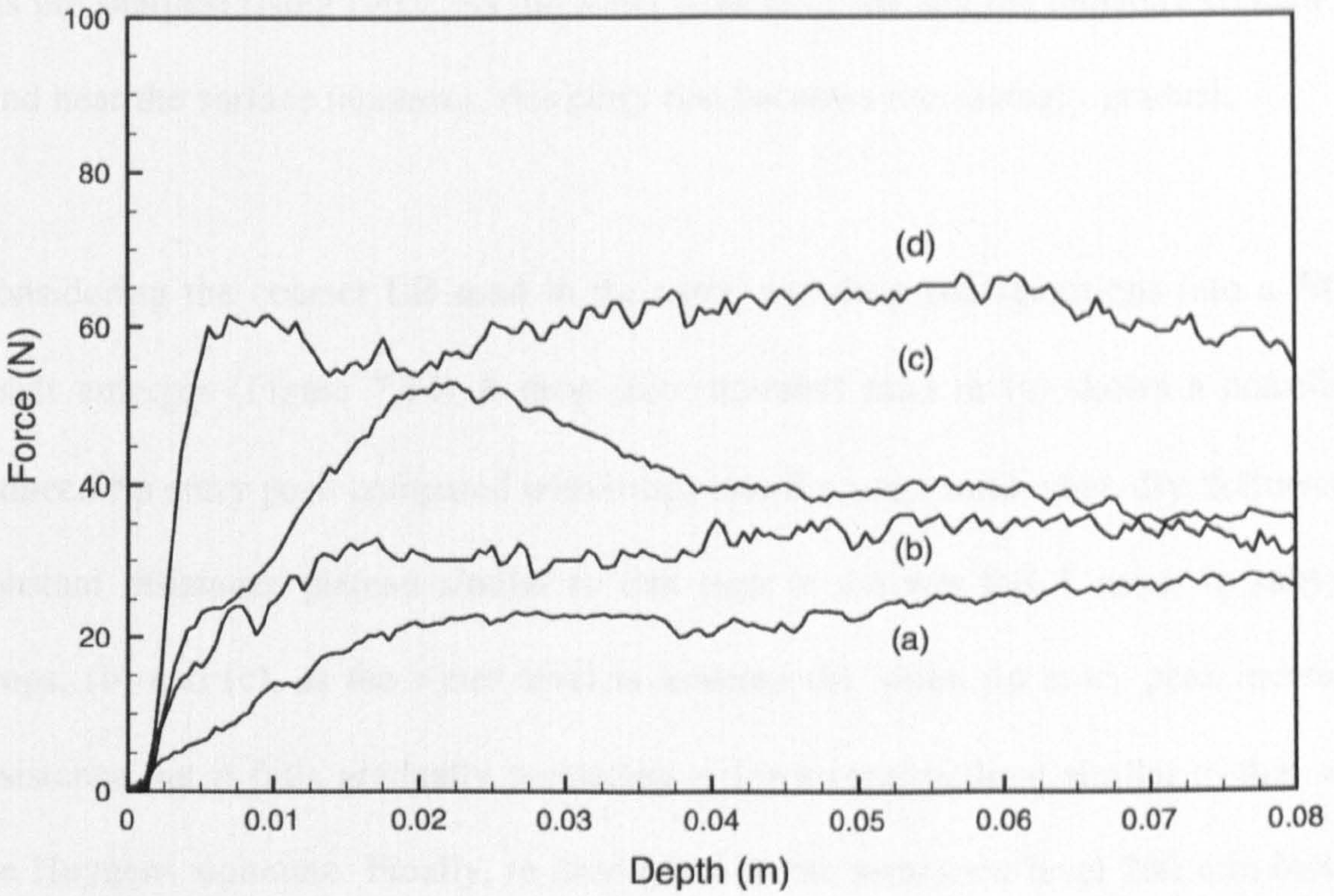

Figure 7.13 RH T sand with water penetrometry signatures for (a) saturated sand (water table at surface z = 350 mm) (b) water table at z = 250 mm (c) water table at z = 200 mm (d) water table at z = 150 mm.

From the graphs it can be seen that with the exception of the drop with the lowest water table (z = 150 mm) Figure 7.13(d) the characteristic dry sand shape is not seen; the initial tip entry peak characteristic of the sand has gone and the signatures resemble that of a cohesive clay with rising slopes followed by an essentially constant resistance plateau. This plateau varies in force depending on the height of the water table. The saturated sand, (a), has the lowest resistance, only slightly higher than that of the same sand when dry and in a loosely packed state (Figure 7.11). In contrast the sand with the lowest water table at z = 150 mm, (d), has a much greater resistance with a plateau phase nearly twice that of the same sand in the dry dense state. The tip entry peak also returns in this signature. The entry rise of each signature also varies with the moisture content of the sand. The sand with lowest water table and therefore driest surface, (d),

has the sharpest rising force. As the water table is raised and the moisture content of the sand near the surface increases, this entry rise becomes increasingly gradual.

Considering the coarser LB sand in the same wet drop configurations into a different result emerges (Figure 7.14) A drop into saturated sand in (a) shows a considerably reduced tip entry peak compared with drops into the same sand when dry, followed by a constant resistance plateau similar to that seen in the wet RH T sand. In subsequent drops, (b) and (c), as the water level is lowered the initial tip entry peak increases in resistance but it falls gradually producing a downward gradient similar to that seen in the Huygens signature. Finally, in drop (d) with the saturation level 200 mm below the target surface, the sand starts to behave as if in the dry state again, with a slightly more pronounced tip-entry peak and a gradual increase in resistance with depth in the plateau phase. These signatures show that small quantities of water can change the signatures of both sands in a distinct way from their dry state signatures and, these changes are noticeable within only a few centimetres of penetration.

A complete theory of the behaviour of liquid as a binder between grains is not available at present (Fournier *et al.*, 2005); however, the behaviour seen in the penetrometry signatures can be explained in part by capillary action. The water table level in the experiments gives the approximate level at which the sand is completely saturated; however voids between the grains of sand act like small capillary tubes and draw water upward due to surface tension.

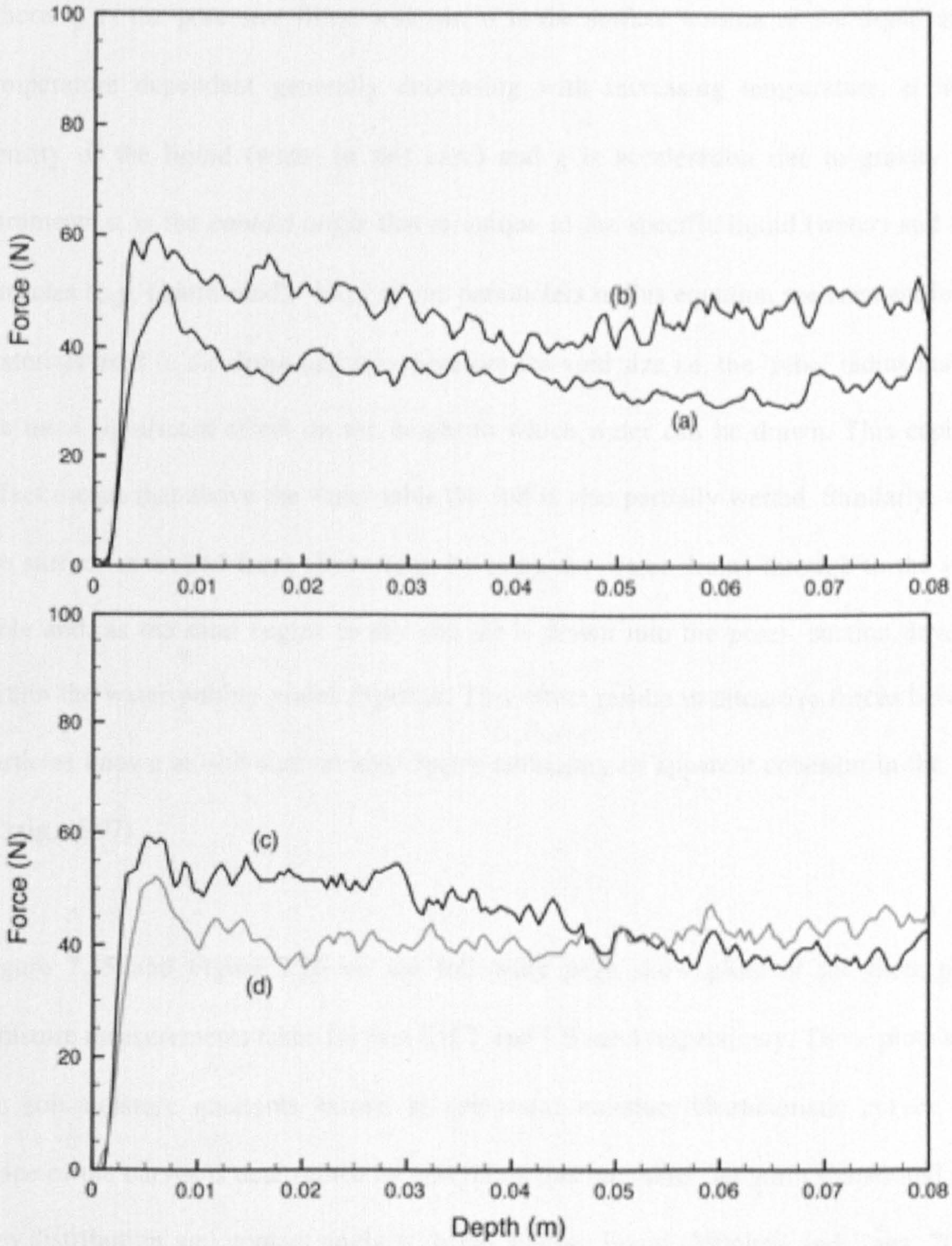

Figure 7.14 Wet LB sand penetrometry signatures for (a) saturated sand (water table at surface z = 350 mm) (b) water table at z = 250 mm (c) water table at z = 200 mm (d) water table at z = 150 mm.

The height, h, to which water rises above the water table is determined by (Terzaghi and Peck, 1967):

$$h = \frac{2\sigma\cos\alpha}{\rho g r_p} \qquad \textbf{(Equation 7.7)}$$

where r_p is the pore size filled with air, σ is the surface tension of the liquid and is temperature dependent generally decreasing with increasing temperature, ρ is the density of the liquid (water in this case) and g is acceleration due to gravity. The parameter α is the *contact angle* that is unique to the specific liquid (water) and solid particles (e.g. quartz sand). Most of the parameters in this equation are constant for the materials used in the drops and it is therefore the void size i.e. the 'tube' radius that has the most significant effect on the height to which water can be drawn. This capillary effect means that above the water table the soil is also partially wetted. Similarly, when the surface is wetted from above (e.g. by rain), the water drains through to the water table and, as the sand begins to dry and air is drawn into the pores, suction develops within the water pulling grains together. This effect results in attractive forces between particles known as soil suction and creates temporary or apparent cohesion in the sand (Craig, 1997).

Figure 7.15 and Figure 7.16 on the following page show plots of the theta probe moisture measurements taken for wet RH T and LB sand respectively. These plots show the soil-moisture gradients known as soil-water moisture characteristic curves. The shape of the curves is determined by several factors including the grain shapes and their size distribution and contact angle with the wetting liquid (Mitchell and Soga, 2005). However a key factor it is the pore size distribution of the soil, which will markedly affect the sand-water moisture characteristic curves (Hillel, 1971). In the region closely above the water table, liquid still completely coats the sand grains and the material is in the funicular state (Figure 7.17b).

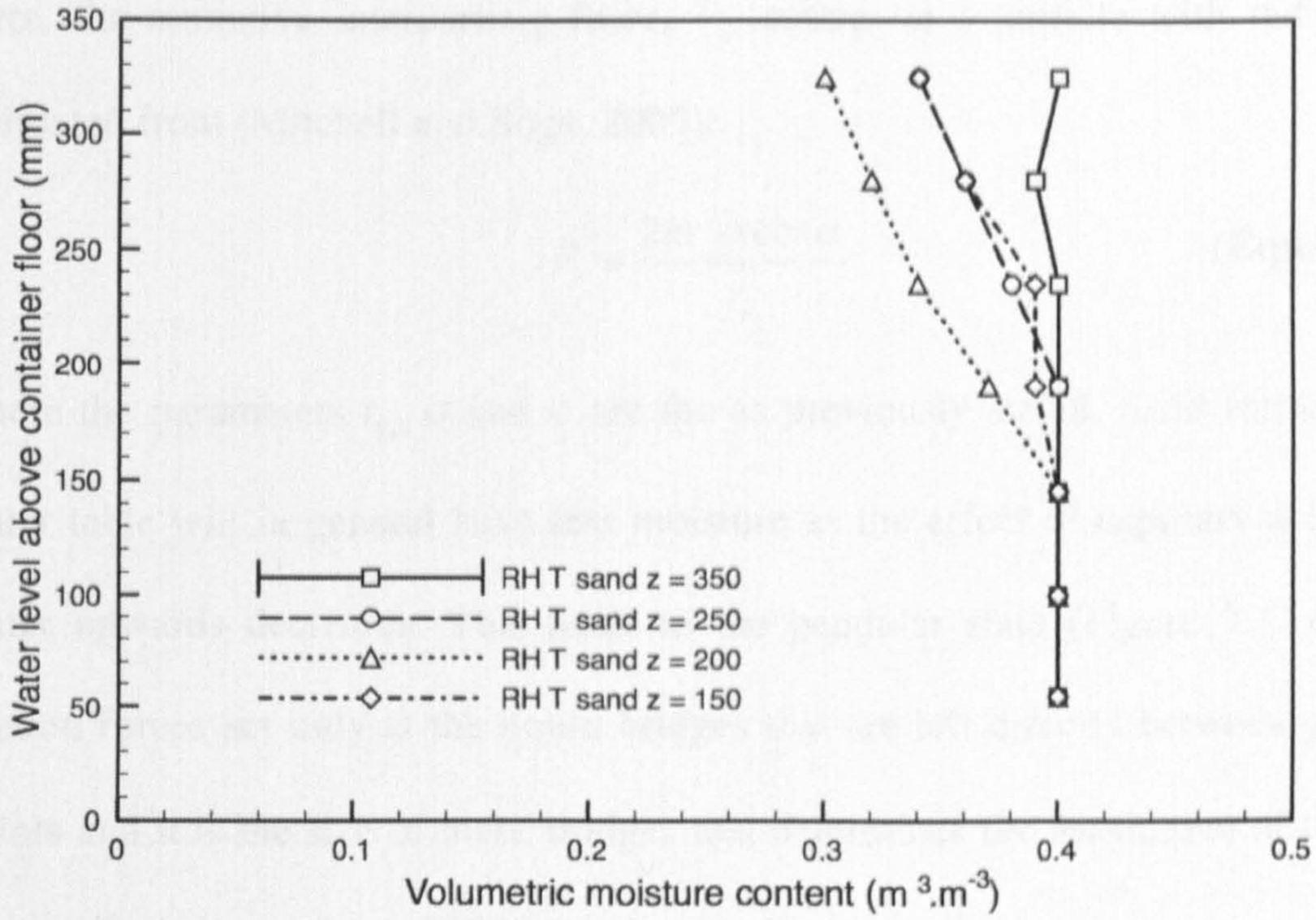

Figure 7.15 Soil-water moisture characteristic curves for RH T sand with water table at different heights, z, above the target container floor. Volumetric moisture content is given on the abscissa. For all water table levels there is a gradual decrease in moisture content nearer the surface. Legend line lengths give representative moisture measurement error magnitude.

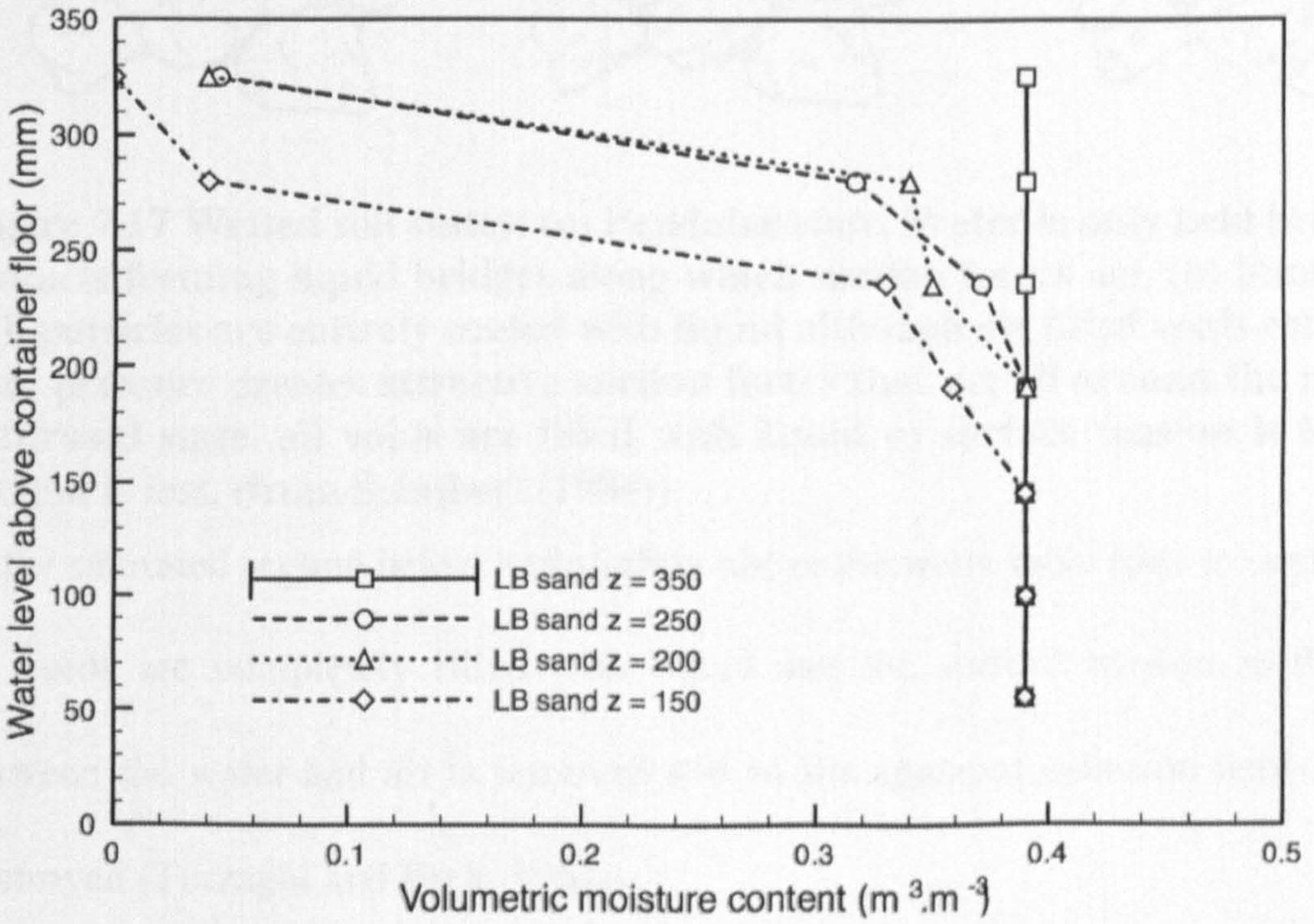

Figure 7.16 Soil-water moisture characteristic curves for LB sand with water table at different heights, z, above the target container floor. Moisture content declines rapidly above water table level except for the saturated target (z = 350 mm). Legend line lengths give representative moisture measurement error magnitude.

Here, the attractive interparticle force, F_c, acting on a particle with radius r can be estimated from (Mitchell and Soga, 2005):

$$F_c = \frac{2\pi r^2 \sigma \cos\alpha}{r_p} \qquad \textbf{(Equation 7.8)}$$

where the parameters $r_{p,}$, σ and α are the as previously stated. Sand further above the water table will in general have less moisture as the effect of capillary action drawing water upwards decreases. This leads to the pendular state (Figure 7.17a) where the suction forces act only at the liquid bridges that are left directly between grain contact points and it is the size of these bridges that determines the magnitude of the attractive force (Mitchell and Soga, 2005).

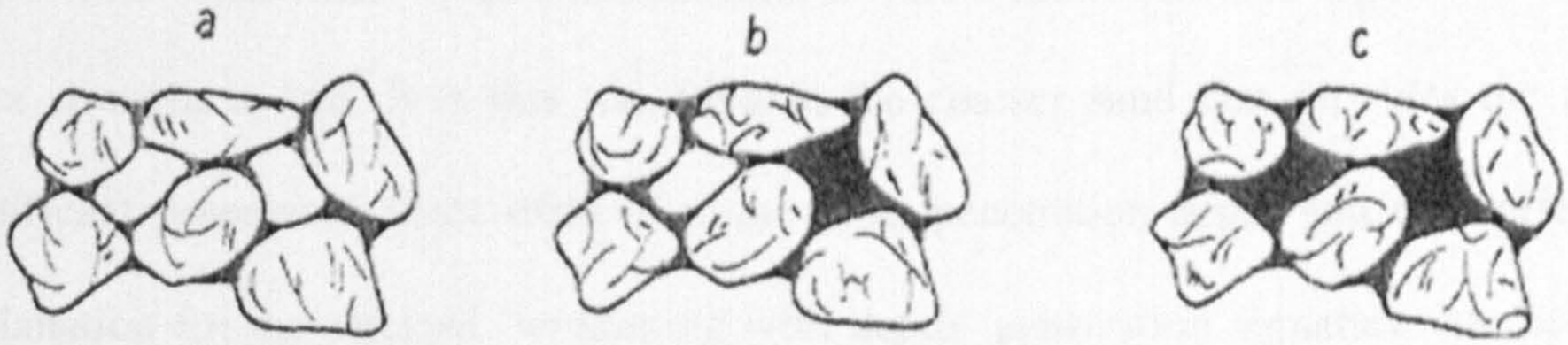

Figure 7.17 Wetted soil states: (a) Pendular state. Water is only held between grain contacts forming liquid bridges along which suction forces act. (b) Funicular state. Soil particles are entirely coated with liquid although air filled voids exist. Negative pore pressure creates attractive suction forces that act all around the particles. (c) Saturated state. all voids are filled with liquid so surface tension is lost and soil suction is lost. (from Schubert (1984))

In the saturated regime below and slightly above the water table (due to capillary action), all voids are completely filled with liquid and the surface tension at the boundary between the water and air is removed and so the apparent cohesion between grains is destroyed (Terzaghi and Peck, 1967).

In the case of the fine-grained RH T sand, the voids are narrow and capillary action therefore draws water significantly above the water table. This gives a more gradual changing moisture gradient in the sand which is reflected in the penetrometry signatures

of each water table configuration with the loss of the tip entry peak being replaced by a more gradual clay-like rise and subsequent constant force plateau. In contrast, the capillary action is more limited in the LB sand with its coarser voids. The signature of the lowest water table configuration (z = 150 mm) had surface sand that was nearly dry, with little moisture drawn up, and its signature is therefore slightly higher in absolute force than the dry dense sand due to apparent cohesion although the tip entry peak is greatly reduced. The saturated sand has no apparent cohesion and therefore is also similar, with the exception of a smaller tip-entry peak, to the signature in dry sand. The remaining two signatures both show downward trends similar to that seen in stage 3 of the Huygens signature, produced by the penetrometer passing from the cohesive regime where small quantities of liquid add strength toward a more saturated regime where the extra strength is lost. It is this transition in the coarser sand that provides the most significant downward force trend over the short penetration depth and may offer an explanation for the unusual 'weakening with depth' penetration signature returned on impacting the surface of Titan.

7.4.6 Discussion

The results presented above show the ACC-E penetrometer response to fine and coarse grained sands with carefully controlled quantities of moisture ranging from saturated to a surface that is almost dry. These signatures show how the addition of even small quantities of water between the grains of sand can dramatically change the penetrometry signature even over a short penetration distance, in some cases more than doubling the average penetration resistance compared to the same sand in a dry state.

While the penetration signatures from this experiment are interesting, further drops would have been beneficial. This was not possible due the time required to set up each water table configuration, allow the require moisture level to be reached and completely dry out each sand afterwards before preparing another drop. Bulk densities of each of the target sands were assumed to be constant by using the same preparation technique throughout. While this is only approximately true, it is valid assumption as sampling shows the sands were all in medium to dense packing states. The approximately constant bulk density therefore allowed the same moisture calibration to be used for the moisture states of both sands. Improvements could be made to moisture sampling in the experiment by using multiple theta probes permanently inserted into the side of the target container which would be useful for determining when the required moisture state has been reached and also eliminate any water loses from having to insert and remove a single probe. Furthermore, the experiment used water as a binder between the sand grains and measured water content using a theta probe. On Titan a binding fluid if present is likely to be methane or a mixture of methane and ethane which unlike water are non-polar making a theta probe useless at detecting their presence.

7.5 An interpretation of the surface material at the Huygens landing site

This chapter has analysed the signature returned from the Huygens landing site and put forward various possibilities to explain its shape. The analogue work points to the intriguing possibility of a thin coating on the substrate material with weaker mechanical properties than terrestrial snow, but this is tenuous, and impossible to identify from the ACC-E penetrometry signature alone.

The closest matching analogue drop shifted horizontally, but not rescaled vertically, to align with the third stage of the Huygens signature on which it is overlaid is shown in

Figure 7.18. This is LB sand with a water table at z = 200 mm (150 mm below the target surface). The Titan force drops more than 20 N over a short penetration depth of ~4.5 cm while this best analogue match barely achieves this over the penetrometer's full length of 8 cm. Table 7.4 compares the key statistics from the Titan drop with the drops into wetted sand and shows how significant the reduction in penetration resistance is. To demonstrate the significance of this downward trend in identifying a Titan surface analogue material, the author has used over 50 drops into natural analogue materials prepared in the laboratory to create a simple classification map shown in Figure 7.19. The gradient of the downward trend together with another parameter, the mean peak to trough amplitude (discussed in chapter 4) of any granularity, if present, highlight the unique nature of the Titan substrate material.

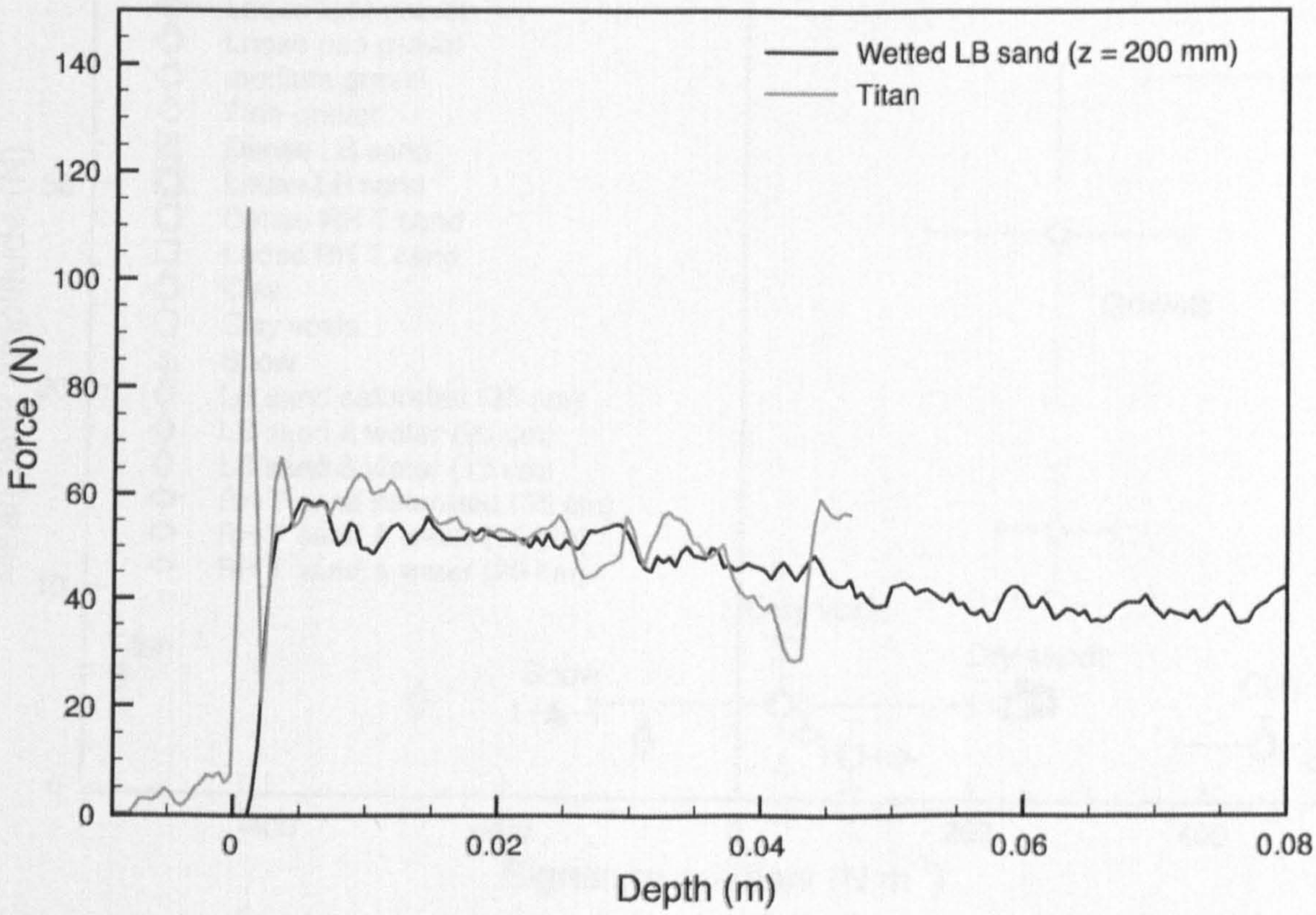

Figure 7.18 Titan penetrometry data shifted horizontally (but not scaled vertically) to allow the third stage to overlie the signature of a drop into wet LB sand with a water table at z = 200 mm, 150 mm below the surface of the sand. This is the closest analogue match to the Titan data with similar force and characteristic downward trend.

Signature	Mean force (N)	Gradient (N m^{-1})	Mean peak-trough amplitude (N)	Comments
Titan (stage 3)	51.33	-525.15	5.53	Flight data
RH T sand and water				
Water table height z = 150 mm	60.77	59.46	3.03	
z = 200 mm	79.01	497.29	1.84	
z = 250 mm	32.44	77.46	4.18	
z = 350 mm	23.22	138.20	1.90	Saturated sand
LB sand and water				
Water table height z=150 mm	41.34	57.21	4.36	Surface dry to touch
z=200 mm	44.47	-272.75	4.54	Closest Titan analogue match
z=250 mm	46.49	-49.15	4.88	
z=350 mm	34.25	-80.89	2.84	Saturated sand

Table 7.4 Three key statistics for drops into the wetted sands and third stage of Titan signature. Water table heights are from the bottom of the target container (350 mm height).

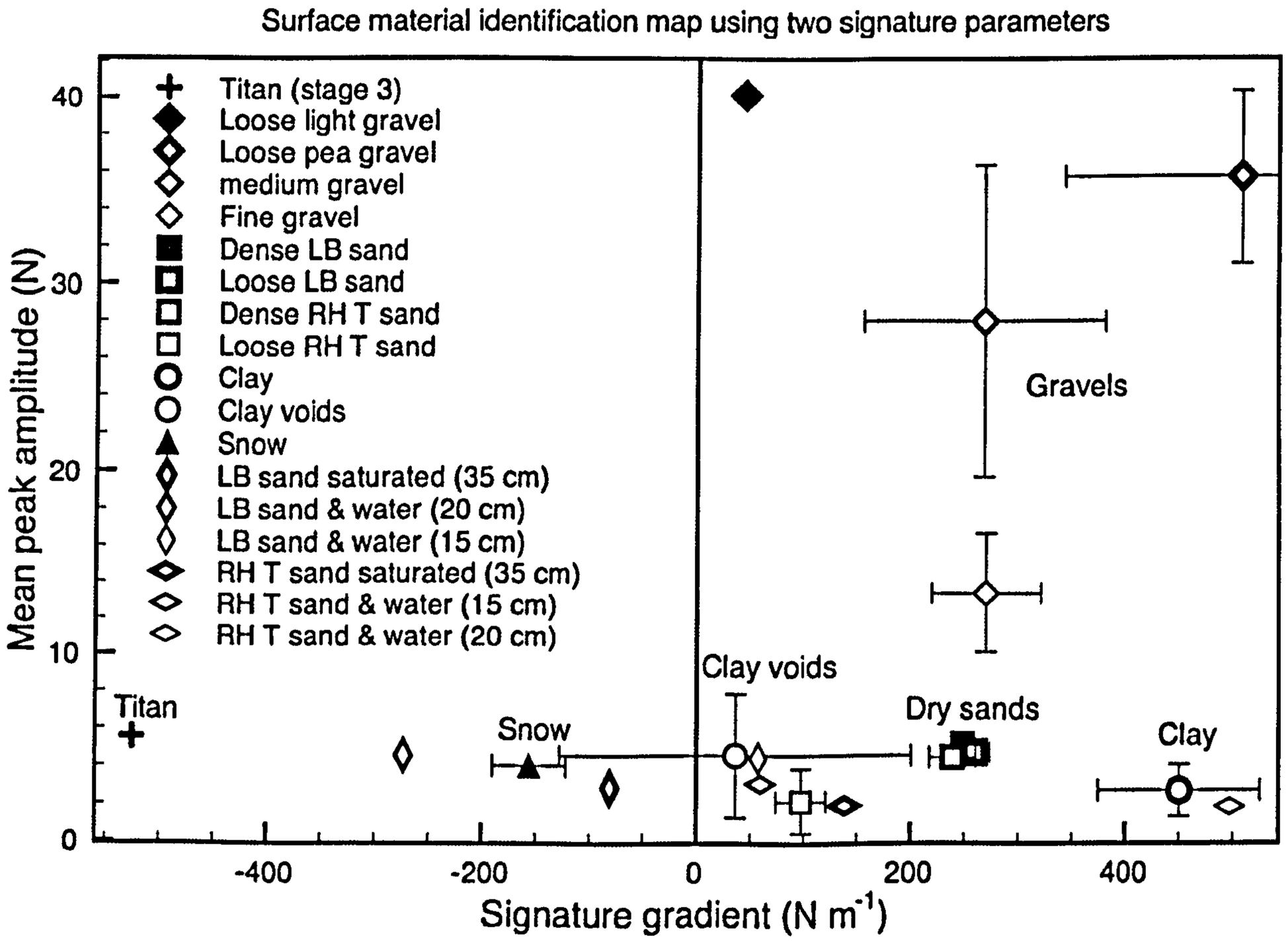

Figure 7.19 Surface material identification map using two key signature parameters. Parameters exclude the first 1 cm 'tip entry' of signature for comparative purposes with the Huygens third stage of signature. Where multiple drops of an analogue are available averages have been taken and standard errors are shown. Note the marked difference of the flight data's signature gradient to that of the Earth analogues (see text).

This identification map shows that even the closest terrestrial analogue match for this substrate material, a gradient wetted coarse sand, while close to matching the mean peak-trough undulations in the signature caused by granularity, is still some way from matching the degree of loss of strength with depth. This cannot be explained by Titan's reduced gravity compared to penetrometry drops carried out on Earth as the flight data's signature gradient is negative. The effect of gravity acts to compress underlying material which would cause a positive signature gradient (and for the small depth penetrated this would be negligible). It must also be noted that these analogues used water as their interstitial fluid that has a viscosity at room temperature ~5 times greater and a density approximately twice that which liquid methane would have on Titan's surface (Collins, 2005). These factors, together with the currently unknown contact angle between water ice and methane at Titan surface temperature, are likely to affect cohesive behaviour between any tentative ice grains. In addition to the observation of a detected increase in methane concentration by the probe sitting on the surface and thermal modelling work that support a damp surface (Lorenz *et al.*, 2006; Niemann *et al.*, 2005), recent work has suggested that methane/nitrogen/ethane rain may be a possibility at the Huygens landing site surface possibly supplying the necessary liquid (Graves *et al.*, 2008).

Applying the same method used to estimate a grain size of the various sites tested on Chesil beach in Chapter 5, an estimate of the Titan substrate material grain size can be made, assuming spherical grains that consist only of water ice which, at Titan's surface temperature, has a density of 0.93 g cm^{-3} (Collins, 2005). Using the empirical relationship found in Chapter 4 for spherical beads (Equation 4.5) together with the mean peak to trough force measured in the signature, 5.53 N, gives a mean particle mass

of 0.003g. Using the relationship between particle diameter and particle mass together with the water ice grain density, gives an upper limit on the mean grain diameter of ~2 mm :

$$d_{particle} = 2\left(\frac{3M}{4\pi\rho}\right)^{\frac{1}{3}} = 2\left(\frac{3\times(0.003)}{4\pi\times(0.93)}\right)^{\frac{1}{3}} \sim 0.2cm$$

(Equation 7.9)

This mean size of substrate ice grains provides a reasonable estimate given the very limited quantity of flight data available, and characterizes the grains as 'sand' according to the Udden-Wentworth grain size classification scale (see section 3.8.1). Furthermore, the limited experiments into liquid nitrogen frozen ice pebbles of various masses has demonstrated that a direct impact with a small 16 mm diameter spherical ice pebble of mass ~2g is capable of producing a similar magnitude impact spike to that seen in the Titan signature. This size of pebble is at the lower size limit for which DISR have complete rock counts and must therefore be considered part of the substrate. A small pebble impact is consistent with the surface simulation which yields an ~80% probability that the penetrometer's first surface contact was with the substrate rather than a larger 'rock' of the size seen in the surface images.

8 Conclusions and further work

This thesis has investigated the ability of a small, simple sensor to provide valuable scientific information from an *in situ* measurement of a planetary surface. It has been motivated by the successful landing, for the first time, of a probe on the unknown surface of Titan. The author's involvement with the project started immediately prior to the landing and coincided with the beginning of a time of rapid progress in the understanding of the nature of Titan's atmosphere and surface and how the two interact.

8.1 Final discussion

The development of a portable drop rig and laser based velocity system has allowed the collection of a sizeable catalogue of surface analogue signatures. Laboratory work has included a number of controlled experiments involving targets made from artificial spherical grains of various densities to explore penetrometry signature features and to derive an empirical relationship between signature peaks and the average masses of the grains impacting the penetrometer tip. Signatures have been investigated in both the time and frequency domain and this work has shown that spectra can be used to identify graded target materials, but drops at slower speeds suggest that collecting the signatures at higher sampling rates would improve the information content and improve material characterisation.

The analysis of fieldwork signatures from five separate sites on the sourthern coast of England has demonstrated that despite the penetrometer's limited length it has the capacity to reveal clearly subsurface structure complementing other more complex instruments such as a camera. Various natural sedimentary textural features, first

examined in artificial laboratory targets, were readily identified within the field penetrometry signatures. When combined with information from other instrumentation, this ability can help infer the environmental processes that have acted on the surface. Several modelling avenues were investigated with varying degrees of success, leading to the application of a physical penetrometry model to laboratory data. This model was extended to allow the fitting of layered targets.

Finally, in chapter 7 more specific experiments were carried out to help provide a possible interpretation of the signature returned from the Huygens landing site. It addressed the important question of whether the surface is wet. Preliminary experiments to identify the presence of distributed moisture in sands suggest that the surface may be damp and somewhat cohesive with a grain size similar to coarse sand. If dampness is confirmed, this would suggest that precipitation is active in the area or, that surface liquids have flowed recently possibly depositing the pebbles seen in the DISR surface images. The validity of the short signature returned from the moon's surface has been considered and through critical reasoning it is believed that the signature is legitimate although this is impossible to prove conclusively. An instrument is however only as good as the data it collects and in the case of the ACC-E penetrometer, it would certainly have been desirable to have had more. It is recommended that the future use of penetrometers for space application must consider either multiple fixed penetrometers or a single mobile one, attached to a rover for example. In the former case, this would of course be constrained by mass and power budget limits; however three devices fixed in a symmetrical arrangement on the probe foredome would not only have confirmed (by comparison) their correct operation on impact and given an indication of the horizontal variability of the surface, but may also have helped identify the probe's tilt immediately

prior to surface impact, an issue that caused considerable discussion within the SSP team and wider Huygens scientific community (Karkoschka *et al.*, 2007). In all cases where possible, a longer penetrometer would also be advantageous.

8.2 Further work

The experiment on distributed moisture in sands is thought provoking; however, further experiments would be useful, first to confirm the findings of this investigation, but also to examine the effect on the signatures of granular material with interstitial fluids of lower viscosities, surface tensions and different liquid-material contact angles. It may be difficult to quantify the amount of any such fluid within the target; however in the first instance the author would consider an improved experiment using water at a range of temperatures which can still be measured by a theta probe. At 90°C water has a viscosity of 0.315×10^{-3} Pa s and a surface tension of 0.061 N m^{-1}, closer to liquid methane at Titan temperatures (0.184×10^{-3} Pa s and 0.017 N m^{-1}respectively) (Escobedo and Mansoori, 1996). As was seen in chapter 7 the surface tension plays an important role in capillary action, which in turn affects the soil-liquid moisture characteristic curves the effect of which may be seen in these further experiments. The lower surface tension of the liquid, in a similar way to the methane on Titan, should also give weaker attractive interparticle forces between grains, although the effect of the different liquid-material contact angles would need to be considered. Furthermore, a lower viscosity interstitial liquid is able to escape the material pores more easily and therefore a decrease in the measured penetration force might be expected with increasing water temperature.

The high-speed photography session and quarter space technique provided fascinating insights into the movement of material in the vicinity of the penetrometer tip. This

powerful tool could be useful when compared with the output from the penetrometer and may help explain effects such as the tip entry peak in bead impacts and the 'smearing out' of layered targets.

Finally, further fieldwork would be important to validate any laboratory findings. It would be useful to study a wider range of sites whose surfaces have been shaped by different geological processes.

8.3 Concluding remarks

Titan is one of the most mysterious and intriguing bodies in our Solar System, yet strangely Earth-like with its own liquid cycle much like the hydrological cycle. Recent discoveries using the Cassini Radar of large lakes or seas in the polar regions and 'sand' dunes at lower latitudes have highlighted the diverse nature of its surface (Lorenz, 2006; Stofan *et al.*, 2007). Exploration will continue, with new and exciting discoveries waiting to be made. The author has had the privilege to analyse the end product of many years of effort of numerous, dedicated workers.

REFERENCES AND APPENDICES

References

Ahlenbrandt, T. S. (1979). Textural parameters in eolian deposits. *Geological survey paper* 1052: 21-52.

Allen, W. A., Mayfield, E. B., Morrison, H. L. (1957). Dynamics of a projectile penetrating sand. *Journal of Applied Physics* 28: 370-376.

Almedeij, J. H. and Diplas, P. (2003). Bedload transport in gravel-bed streams with unimodal sediment. *Journal of Hydraulic Engineering* 129: 896-904.

Anderson, W. W., Ahrens, T. J., Gibson, A., Scott, R. and Suzuki, K. (1996). Emplacement of penetrators into planetary surfaces. *Journal of Geophysical Research* 101: 21,137-121,149.

Bailey, J. E. (1997). An impact penetrometer for planetary surfaces. *Undergraduate Report, Physics with Space Science and Systems.* University of Kent.

Ball, A. J. and Lorenz, R. D. (1999). Penetrometry of extraterrestrial surfaces: A historical overview. In: Kömle, N. I., Kargl, G., Ball, A. J. and Lorenz, R. D. (Eds.), *Penetrometry in the solar system.* Osterreichischen Akademie der Wissenschaften, Graz, Austria

Bentley, J. P. (1983). Principles of measurement systems. Longman, London

Bird, M. K., Dutta-Roy, R., Heyl, M., Allison, M., Asmar, S. W., Folkner, W. M., Preston, R. A., Atkinson, D. H., Edenhofer, P., Plettemeier, D., Wohlmuth, R., Less, L. and Tyler, G. L. (2002). The Huygens doppler wind experiment, Titan winds derived from probe radio frequency measurements. *Space Science Reviews* 104: 613-640.

Blackwelder, E. (1940). The hardness of ice. *American Journal of Science* 238: 61-62.

Blott, S. J. and Pye, K. (2001). GRADISTAT: A grain size distribution and statistics package for the analysis of unconsolidated sediments. *Earth Surface Processes and Landforms* 26: 1237-1248.

Boguslavskii, Y., Drabkin, S. and Salman, A. (1996). Analysis of vertical projectile penetration in granular soils. *Journal of Physics* 29: 905-916.

Brooke, D. and Wynne, R. J. (1988). Signal processing, principles and applications. Edward Arnold, London

Brown, R. H., Baines, K. H., Bellucci, G., Bibring, J. P., Buratti, B. J., Capaccioni, F., Cerroni, P., Clark, R. N., Coradini, A. and Cruikshank, D. P. (2004). The Cassini Visual and Infrared Mapping Spectrometer (VIMS) investigation. *Space Science Reviews* 115: 111-168.

Butterfield, R. and Mahmoud, M. A. (1989). A fourier analysis of oscillating forces measured on a penetrometer in sand. *Journal of Sound and Vibration* 198: 335-342.

Campbell, D. B., Black, G. J., Carter, L. M. and Ostro, S. J. (2003). Planetary Science: Radar evidence for liquid surfaces on Titan. *Science* 302: 431-433.

Carr, A. P., Gleason, R. and King, A. (1970). Significance of pebble size and shape in sorting by waves. *Sedimentary Geology* 4: 89-101.

Carrier, W. D., Olhoeft, G. R. and Mendell, W. (1991). Physical properties of the lunar surface. In: Heiken, G. H., Vaniman, D. T. and French, B. M. (Eds.), *Lunar Sourcebook*. Cambridge University Press, Cambridge.

Cassel, D. K., Kachinoski, R. G. and Topp, G. C. (1994). Practical considerations for using a TDR cable tester. *Soil Technology* 7: 113-126.

Chatfield, C. (2004). The analysis of time series, an introduction. Chapman & Hall/CRC, London.

Cherkasov (1968b). Determination of the lunar density and mechanical strength of the surface layer of lunar soil at the landing site of the Luna 13 probe. *Kosmicheskie Issledovaniya (in Russian)* 5: 746-757.

Cho, G., Dodds, J. and Santamarina, J. C. (2006). Particle shape effects on packing density, stiffness, and strength: natural and crushed sands. *Journal of Geotechnical and Geoenvironmental Engineering* 132: 591-602.

Christensen, E. M., Batterson, S. A., Benson, H. E., Chandler, C. E., Jones, R. H., Scott, R. F., Shipley, E. N., Sperling, F. B. and Sutton, G. H. (1966). Lunar surface mechanical properties. *Nasa technical report 32-1023*.

Collins, G. C. (2005). Relative rates of fluvial bedrock incision on Titan and Earth *Geophysical Research Letters* 32: L22202.

Coustenis, A. and Taylor, F. (1999). Titan, the Earth-like moon. World Scientific Publishing Company.

Craig, R. F. (1997). Soil mechanics. Chapman & Hall, London.

Delta-T (1999). ThetaProbe soil moisture sensor type ML2x user manual. Delta-T Devices Ltd., Cambridge.

Diggle, P. J. (1990). Time series: a biostatistical introduction. Oxford University Press, Oxford.

Dyer, K. R. (1986). Coastal and estuarine sediment dynamics. John Wiley & Sons, New York.

Elachi, C., Im, E., Roth, L. and Werner, C. L. (1991). Cassini Titan radar mapper. *Proceedings of the IEEE* 79: 867-880.

Eriksson, A. I. (2000). Spectral Analysis. In: Paschmann, G. and Daly, P. W. (Eds.), *Analysis methods for multi-spacecraft data*: ISSI/ESA Scientific Report SR-001.

Farrel, D. A. and Greacen, E. L. (1966). Resistance to penetration of fine probes in compressible soil. *Australian Journal of Soil Research* 4: 1-17.

Ferri, F., Angrilli, F., Bianchini, G., Fulchignoni, M. and Team, H. (2002). Huygens atmospheric structure instrument of Huygens probe on Cassini Mission. *Acta Astronautica* 50: 249-255.

Flaser, F. M. (1983). Oceans on Titan? *Science* 221: 55-57.

Forrestal, M. J. and Luk, V. K. (2007). Penetration into soil targets. *International Journal of Impact Engineering* 12: 427-444.

Fournier, Z., Geromichalos, D., Herminghaus, S., Kohonen, M. M., Mugele, F., Scheel, M., Schulz, M., Schulz, B., Schier, C., Seemann, R. and Skudelny, A. (2005). Mechanical properties of wet granular materials. *Journal of Physics Condensed Matter* 17: S477-S502.

Fuchs, O. P. (1963). Impact phenomena. *AIAA Journal* 1: 2124-2126.

Fujii, Y. (2006). Optical method for accurate force measurement: dynamic response evaluation of an impact hammer. *Optical Engineering* 45: 023002.

Fujii, Y. and Fujimoto, H. (1999). Proposal for an impulse response evaluation method for force transducers. *Measurement Science and Technology* 10: N31-N33.

Fulchignoni, M., Ferri, F., Angrilli, F., Ball, A. J., Bar-Nun, A., Barucci, M. A., Bettanini, C., Bianchini, G., Borucki, W., Colombatti, G., Coradini, M., Coustenis, A., Debei, S., Falkner, P., Fanti, G., Flamini, E., Gaborit, V., Grard, R., Hamelin, M., Harri, A. M., Hathi, B., Jernej, I., Leese, M. R., Lehto, A., Lion Stoppato, P. F., López-Moreno, J. J., Mäkinen, T., Mcdonnell, J. A. M., Mckay, C. P., Molina-Cuberos, G., Neubauer, F. M., Pirronello, V., Rodrigo, R., Saggin, B., Schwingenschuh, K., Seiff, A., Simões, F., Svedhem, H., Tokano, T., Towner, M. C., Trautner, R., Withers, P. and Zarnecki, J. C. (2005). In situ measurements of the physical characteristics of Titan's environment. *Nature* 438: 785-791.

Garry, J. R. C., Towner, M. C., Ball, A. J., Zarnecki, J. C. and Marcou, G. (1999). The effect of ambient pressure and impactor geometry on low speed penetration of unconsolidated materials. *Advances in Space Research* 23: 1229-1234.

Gaskin, G. J. and Miller, J. D. (1996). Measurement of soil water content using a simplified impedence measuring technique. *Journal of Agricultural Engineering Research* 63: 153-160.

Glaser, D., Bartlett, P., Zacny, K. and Gorevan, S. (2006). A review of penetrometers for subsurface access on small solar system bodies. *Spacecraft Reconnaissance of Asteroid and Comet Interiors workshop,* Lunar and Planetary Institute, Santa Cruz, California.

Gottman, J. M. (1981). Time-series analysis, A comprehensive introduction for social scientists. Cambridge University Press, Cambridge.

Granger, R. A. (1995). Fluid mechanics. Dover Press, London.

Griffen, M. D. and French, J. R. (2004). Space vehicle design. American Institute of Aeronautics and Astronautics.

Griffith, C. A. (1993). Evidence for surface heterogeneity on Titan. *Nature* 364: 511.

Griffith, C. A., Owen, T., Geballe, T. R., Rayner, J. and Rannou, P. (2003). Evidence for the exposure of water ice on Titan's surface. *Science* 300: 628-629.

Griffith, C. A., Owen, T. and Wagener, R. (1991). Titan's surface and troposphere, investigated with ground-based, near-infrared observations. *Icarus* 93: 362-378.

Hagermann, A., Rosenberg, P. D., Towner, M. C., Garry, J. R. C., Svedhem, H., Leese, M. R., Hathi, B., Lorenz, R. D. and Zarnecki, J. C. (2007). Speed of sound measurements and the methane abundance in Titan's atmosphere. *Icarus* 189: 538-543.

Hillel, D. (1971). Soil and water: physical principles and processes. Academic Press, New York.

Huang, A. B. and Hsu, H. H. (2005). Cone penetration tests under simulated field conditions. *Geotechnique* 55: 345-354.

Ip, W. H. (1993). The new Titan's hydrogen torus. *Advances in Space Research* 13: 335-339.

Israël, G., Cabane, M., Brun, J.-F., Niemann, H. B., Way, S. H., Riedler, W., Steller, M., Raulin, F. and Coscia, D. (2002). Huygens probe aerosol collector pyrolyser experiment. *Space Science Reviews* 104: 433-468.

Jaeger, H. M. and Nagel, S. R. (1992). Physics of the granular state. *Science* 255: 1523-1531.

Jeans, J. (1925) In: The dynamical theory of gases. 4th Edition. Republished by Dover Press 1954.

Jones, M. P. (1987). Applied mineralogy: A quantitative approach. Graham & Trotman, London.

Kaiser, K. L. and Palmer, K. I. (2007). Cable transient voltages due to microphonics. *Journal of Electrostatics* 65: 723-727.

Kargl, G., Keller, T. and Kömle, N. I. (1999). Interpretation of penetrometry experiments. In: Kömle, N. I., Kargl, G., Ball, A. J. and Lorenz, R. D. (Eds.), *Penetrometry in the Solar System.* Verlag der Österreichischen Akademie der Wissenschaft, Graz, Austria.

Kargl, G., Macher, W., Ball, A. J., Towner, M. C. and Mcdonnell, J. A. M. (2005). Huygens data calibration report. Institute fur Weltraumforschung, Graz, Austria.

Kargl, G., Zohrer, A., Kömle, N. I., Ball, A. J., Ringrose, T. J., Paton, M. D., Atkinson, K. R., Towner, M. C. and Kapper, K. L. (2005). The detection of small-scale structures in planetary surface materials with ground-penetrating instruments. *Proceedings of the 3rd International Planetary Probe Workshop,* Anavyssos, Attica, Greece.

Karkoschka, E., Tomasko, M. G., Doose, L. R., See, C., Mcfarlane, E. A., Schröder, S. E. and Rizk, B. (2007). DISR imaging and the geometry of the descent of the Huygens probe within Titan's atmosphere. *Planetary and Space Science* 55: 1896-1935.
Keller, H. U., Grieger, B., Küppers, M., Schröder, S. E., Skorov, Y. V. and Tomasko, M. G. (2008). The properties of Titans surface at the Huygens landing site from DISR observations. *Planetary and Space Science* 56: 728-752.

Keller, H. U., Grieger, B., Küppers, M., Schröder, S. E., Skorov, Y. V. and Tomasko, M.G. (2008). The properties of Titan's surface at the Huygens landing site from DISR observations. *Planetary and Space Science* 56: 728-752.

Kemurdzhian, A. L., Brodskii, P. N., Gromov, V. V., Grushin, V. P., Kiselev, I. E., Kozlov, G. V., Mitskevich, A. V., Perminov, V. G., Sologub, P. S., Stepanov, A. D., Turbobinskii, A. V., Turchaninov, V. N. and N., Y. E. (1983). Preliminary results of detemining the physical properties of the soil of Venus by the Soviet automatic stations Venera 13 and Venera 14. *Kosmicheskie Issledovaniya (in Russian)* 21: 323-330.
Khare, B. N. and Sagan, C. (1973). Red clouds in reducing atmospheres. *Icarus* 20: 311-321.

Komar, P. D. (1998). Beach Processes and sedimentation. Prentice Hall, New Jersey, USA.

Kömle, N. I., Ball, A. J., Kargl, G., Keller, T., Macher, W., Thiel, M., Stöcker, J. and Rohe, C. (2001). Impact penetrometry on a comet nucleus - interpretation of laboratory data using penetration models. *Planetary and Space Science* 49: 575-598.

Kömle, N. I., Ball, A. J., Kargl, G., Stöcker, J., Thiel, M., Jolly, H. S., Dziruni, M. and Zarnecki, J. C. (1997). Using the anchoring device of a comet lander to determine surface mechanical properties. *Planetary and Space Science* 45: 1515-1538.

Kömle, N. I., Kargl, G. and Ball, A. J. (2001). Determination of physical properties of planetary sub-surface layers by artificial impacts and penetrometry. *Advances in Space Research* 28: 1539-1549.

Kress, M. E. and Mckay, C. P. (2004). Formation of methane in comet impacts: Implications for Earth, Mars, and Titan. *Icarus* 168: 475-483.

Kuiper, G. P. (1944). Titan: a satellite with an atmosphere. *Astrophysical Journal* 100: 329-332.

Lambe, T. W. (1951). Soil testing for engineers. John Wiley & Sons, New York.

Lebreton, J. P. and Matson, D. L. (2002). The Huygens probe: science, payload and mission Overview. *Space Science Reviews* 104: 59-99.

Lebreton, J. P., Witasse, O., Sollazzo, C., Blancquaert, T., Couzin, P., Schipper, A., Jones, J. B., Matson, D. L., Gurvits, L. I., Atkinson, D. H., Kazeminejad, B. and Pérez-Ayúcar, M. (2005). An overview of the descent and landing of the Huygens probe on Titan. *Nature*: 758-764.

Leeder, M. R. (1982). Sedimentology: process and product. Allen & Unwin, London.

Legget, R. F. and Hatheway, A. W. (1988). Geology and engineering. McGraw-Hill, London.

Lemmon, M. T., Karkoschka, E. and Tomasko, M. (1993). Titan's rotation: surface feature observed. *Icarus* 103: 329.

Levin, J. and Fox, J. A. (1991). Elementary statistics in social research. Harper Collins, New York.

Lewis, D. W. (1984). Practical sedimentology. Hutchinson Ross Publishing Company, New York.

Lindal, G. F., Wood, G. E., Hotz, H. B., Sweetnam, D. N., Eshleman, V. R. and Tyler, G. L. (1983). The atmosphere of Titan: an analysis of the Voyager 1 radio occultation measurements. *Icarus* 53: 348-363.

Liu, C. and Ahrens, T. J. (1999). Penetration depth time history measurement method. In: Furnish, M. D., Chhabildas, L. C. and Hixson, R. S. (Eds.), *Shock compression of condensed matter* CP505: 1039-1042.

Lorenz, R. D. (1994). Huygens Surface Science Package internal penetrometer (ACC-E) subsystem specification document. University of Kent and Canterbury.

Lorenz, R. D. (1994a). Exploring the surface of Titan. Thesis, University of Kent at Canterbury.

Lorenz, R. D. (2006). The Sand Seas of Titan: Cassini RADAR Observations of Longitudinal Dunes. *Science* 312: 724-726.

Lorenz, R. D. and Ball, A. J. (1999). Review of impact penetration tests and theories. In: Kömle, N. I., Kargl, G., Ball, A. J. and Lorenz, R. D. (Eds.), *Penetrometry in the solar system*. Osterreichischen Akademie der Wissenschaften, Graz, Austria.

Lorenz, R. D., Bannister, M., Daniell, P. M. and Krysinski, Z. (1994). An impact penetrometer for a landing spacecraft. *Measurement Science and Technology* 5: 1033.

Lorenz, R. D., Hathi, B., Leese, M. R., Garry, J. R. C. and Zarnecki, J. C. (1999). The Huygens SSP penetrometer: An update. In: Kömle, N. I., Kargl, G., Ball, A. J. and Lorenz, R. D. (Eds.), *Penetrometry in the solar system*. Osterreichischen Akademie der Wissenschaften, Graz, Austria.

Lorenz, R. D. and Lunine, J. I. (2005). Titans surface before Cassini. *Planetary and Space Science* 53: 557-576.

Lorenz, R. D., Niemann, H. B., Harpold, D. N., Way, S. H. and Zarnecki, J. C. (2006). Titan's damp ground: Constraints on Titan surface thermal properties from the temperature evolution of the Huygens GCMS inlet. *Meteoritics & Planetary Science* 41: 1705-1714.

Lorenz, R. D. and Shandera, S. E. (2002). Target effects during penetrator emplacement: heating, triboelectric charging, and mechanical disruption. *Planetary and Space Science* 50: 163-179.

Lunine, J. I. and Stevenson, D. J. (1983). Ethane ocean on Titan. *Science* 222: 1229-1230.

Lunne, T., Robertson, P. K. and Powell, J. J. M. (1997). Cone penetration testing in geotechnical practice. Spon Press, New York.

Mccarty, J. L., Carden, H. D. (1962). Impact characteristics of various materials obtained by an acceleration-time-history technique applicable to evaluating remote targets. *Nasa technical note TN D-1269,* Langley Research Center, Hampton, USA.

Mcdonough, T. R. and Brice, N. M. (1973a). New kind of ring around saturn. *Nature* 242: 513.

Mitchell, J. K., Bromwell, L. G., Carrier, W. D., Costes, N. C. and Scott, R. F. (1971). Apollo 14 preliminary science report. NASA SP-272.

Mitchell, J. K., Bromwell, L. G., David Carrier, W., Costes, N. C. and Scott, R. (1972). Soil mechanical properties of the Apollo 14 site. *Journal of Geophysical Research* 77: 5641-5664.

Mitchell, J. K., Carrier, W. D., Costes, N. C., Houston, W. N. and Scott, R. F. (1973). Surface soil variability and stratigraphy at the Apollo 16 site. *Lunar Science Conference,* 2437-2445. Geochimica et Cosmochima Acta.

Mitchell, J. K. and Soga, K. (2005). Fundamentals of soil behaviour. John Wiley & Sons, New York.

Mitra, S. K. and Kaiser, J. F. (1993). Handbook for digital signal processing. John Wiley & Sons, New York.

Mitzutani, H. (1999). Introduction. In: Kömle, N. I., Kargl, G., Ball, A. J. and Lorenz, R. D. (Eds.), *Penetrometry in the solar system.* Osterreichischen Akademie der Wissenschaften, Graz, Austria.

Muhleman, D. O., Grossman, A. W. and Butler, B. J. (1995). Radar investigations of Mars, Mercury, and Titan. *Annual Review of Earth and Planetary Sciences* 23: 337.

National Physical Laboratory (NPL) Dynamic force calibration. Internet site hosted by the National Physical Laboratory at http://www.npl.co.uk/server.php?show=ConWebDoc.2108, retrieved 14/07/07.

Nesje, A. and Dahl, S. O. (2000) Glaciers and environmental change. Arnold Press, London.

Nichols, G. (1998). Sedimentology and stratigraphy. Blackwell Science, Oxford.

Niemann, H. B., Atreya, S. K., Bauer, S. J., Biemann, K., Block, B., Carignan, G. R., Donahue, T. M., Frost, R. L., Gautier, D., Haberman, J. A., Harpold, D. N., Hunten, D. M., Israël, G., Lunine, J. I., Mauersberger, T. C., Owen, T., Raulin, F., Richards, J. E. and Way, S. H. (2002). The Gas Chromatograph Mass Spectrometer for the Huygens probe. *Space Science Reviews* 104: 553-591.

Niemann, H. B., Atreya, S. K., Bauer, S. J., Carignan, G. R., Demick, J. E., Frost, R. L., Gautier, D., Haberman, J. A., Harpold, D. N., Hunten, D. M., Israël, G., Lunine, J. I., Kasprzak, W. T., Owen, T. C., Paulkovich, M., Raulin, F., Raaen, E. and Way, S. H. (2005). The abundances of constituents of Titan's atmosphere from the GCMS instrument on the Huygens probe. *Nature* 438: 779-784.

Ohlsen, H. J. (1992). Sensing of aggregate size by means of a horizontal mini-penetrometer. *Soil & Tillage Research* 24: 79-94.

Paton, M. D. (2005). Penetrometery of NEO's and other solar system bodies. Thesis, Planetary and Space Sciences Research Institute, Open University, Milton Keynes.

Paton, M. D., Ball, A. J., Green, S. F., Hall, C., Mucklow, M. E. T. and Zarnecki, J. C. (2004). Laboratory simulation of a spacecraft landing on a near-Earth asteroid. *1st Hayabusa Symposium,* Tokyo: Astronomical Society of the Pacific Conference Series.

Perko, H. A. (2007). Geotechnical techniques used in planetary exploration. *Geotechnical Practice Publication*: 109-119.

Porco, C. C., West, R. A., Squyres, S., Mcewen, A., Thomas, P., Murray, C. D., Delgenio, A., Ingersoll, A. P., Johnson, T. V. and Neukum, G. (2004). Cassini imaging science: instrument characteristics and anticipated scientific investigations at Saturn. *Space Science Reviews* 115: 363-497.

Rages, K., Pollack J. B., (1983). Vertical distribution of scattering hazes in Titan's upper atmosphere. *Icarus* 55: 1983.

Richter, L., Anderson, R. C., Li, R. and Lindemann, R. (2005). Inferences of strength of Martian soil deposits along MER rover traverses from evaluations of vehicle sinkages as observed in wheel tracks. *th International Conference of the International Society for Terrain-Vehicle Systems (ISTVS), Hayama, Japan*

Richter, L., Coste, P., Gromov, V., Kochan, H., Pinna, S. and Richter, H. E. (2001). Development of the "planetary underground tool" subsurface soil sampler for the Mars express "Beagle 2" lander. *Advances in Space Research* 28: 1225-1230.

Sagan, C. (1972). The greenhouse of Titan. *Icarus* 18: 649-656.

Sagan, C. and Dermott, S. F. (1982). The tides in the seas of Titan. *Nature* 300: 731-733.

Samuels, M. L. (1989). Statistics for the life sciences. Prentice Hall, London.
Schubert, H. (1984). Capillary forces - modelling and application in particulate technology. *Powder Technology* 37: 105-116.

Schultz, P. H., Ernst, C. M. and Anderson, J. L. (2005). Expectations for crater size and photometric evolution from the Deep Impact collision. *Space Science Reviews* 117: 207-239.

Schwartz, M. and Shaw, L. (1975). Signal processing, discrete spectral analysis, detection, and estimation. McGraw-Hill.

Seiferlin, K., Hagermann, A., Banaszkiewicz, M. and Spohn, T. (1999). Using penetrators as thermal probes: the Mupus case. In: Kömle, N. I., Kargl, G., Ball, A. J. and Lorenz, R. D. (Eds.), *Penetrometry in the solar system*. Osterreichischen Akademie der Wissenschaften, Graz, Austria.

Smith, P. H., Lemmon, M. T., Lorenz, R. D., Sromovsky, L. A., Caldwell, J. J. and Allison, M. D. (1996). Titan's Surface Revealed by HST Imaging. *Icarus* 119: 336-349.
Smrekar, S., Catling, D., Lorenz, R., Magalhaes, J., Moersch, J., Morgan, P., Murray, B., Presley-Holloway, M., Yen, A. and Zent, A. (1999). Deep Space 2: The Mars microprobe mission. *Journal of Geophysical Research* 104: 27,013-27,030.

SSP team (1995). ACC-E calibration notes (internal document). University of Kent & Canterbury.

Stevenson, D. J. (1990). Triton and Titan: The behaviour of Ices more volatile than water. *Planetary Geology and Geophysics abstracts, Nasa techical memorandum*: 65-66.

Stevenson, D. J. (1992). Interior of Titan. *In proceedings symposium on Titan, European. Space Agency Special publication* SP-338: 29-33.

Stofan, E. R., Elachi, C., Lunine, J. I., Lorenz, R., Stiles, B., Mitchell, K. L., Ostro, S. J., Soderblum, L., Wood, C., Zebker, H., Wall, S., Janssen, M., Kirk, R. L., Lopes, R., Paganelli, F., Radebaugh, J., Wye, L., Anderson, Y., Allison, M., Boehmer, R., Callahan, P., Encrenaz, P., Flamini, E., Francescetti, G., Gim, Y., Hamilton, G., Hensley, S., Johnson, W. T. K., Kelleher, K., Muhleman, D. O., Paillou, P., Picardi, G., Posa, F., Roth, L., Seu, R., Shaffer, S., Vetrella, S. and West, R. A. (2007). The lakes of Titan. *Nature* 445: 61-64.

Stone, M. B., Barry, R., Bernstein, D. P., Pelc, M. D., Tsui, Y. K. and Schiffer, P. (2004). Local jamming via penetration of a granular medium. *Physical Review E - Statistical, Nonlinear, and Soft Matter Physics* 70: 41301-41311

Stone, M. B., Bernstein, D. P., Barry, R., Pelc, M. D., Tsui, Y. K. and Schiffer, P. (2004). Getting to the bottom of a granular medium. *Nature* 427: 503-504.

Surkov, Y. A. and Kremnev, R. S. (1998). Mars-96 mission: Mars exploration with the use of penetrators. *Planetary and Space Science* 46: 1689-1696.
Terzaghi, K. and Peck, R. B. (1967). Soil mechanics in engineering practice. John Wiley & Sons, New York.

Tomasko, M. G., Archinal, B. A., Becker, T. L., Bezare, Bushroe, M. W., Combes, M., Cook, D. A., Coustenis, A., De Bergh, C., Dafoe, L. E., Doose, L. R., Douté, S., Eibl, A., Engel, S., Gliem, F., Grieger, B., Holso, K., Howington-Kraus, E., Karkoschka, E., Keller, H. U., Kirk, R. L., Kramm, R., Küppers, M., Lanagan, P., Lellouch, E., Lemmon, M. T., Lunine, J. I., Mcfarlane, E. A., Moores, J., Prout, G. M., Rizk, B., Rosiek, M. R., Rueffer, P., Schröder, S. E., Schmitt, B., See, C., Smith, P. H., Soderblom, L. A., Thomas, N. and West, R. A. (2005). Rain, winds and haze during the Huygens probe's descent to Titan's surface. *Nature*: 765-778.

Tomasko, M. G., Buchhauser, D., Bushroe, M. W., Dafoe, L. E., Doose, L. R., Eibl, A., Fellows, C., Farlane, E. M., Prout, G. M., Pringle, M. J., Rizk, B., See, C., Smith, P. H. and Tsetsenekos, K. (2002). The Descent Imager/Spectral Radiometer (DISR) experiment on the Huygens entry probe of Titan. *Space Science Reviews* 104: 469-551.

Towner, M. C., Garry, J. R., Lorenz, R. D., Hagermann, A., Hathi, B., Svedhem, H., Clark, B. C., Leese, M. R. and Zarnecki, J. C. (2006). Physical properties of Titans surface at the Huygens landing site from the Surface Science Package Acoustic Properties sensor (API-S). *Icarus* 185: 457-465.

Tucker, M. E. (2001). Sedimentary rocks in the field. John Wiley & Sons, New York.

Vaz, C. M., Bassoi, L. H. and Hopmans, J. W. (2001). Contribution of water content and bulk density to field soil penetration resistance as measured by a combined cone penetrometer-TDR probe. *Soil and Tillage Research* 60: 35-42.

Velea, D., Shields, F. D. and Sabatier, J. M. (2000). Elastic wave velocities in partially saturated Ottawa sand: experimental results and modeling. *Soil Science Society of America Journal* 64: 1226-1233.

Wang, W. L. (1971). Low velocity projectile penetration. *ASCE J Soil Mech Found Div* 97: 1635-1655.

Wentworth, C. K. (1922). A scale of grade and class terms for clastic sediments. *Journal of Geology* 30: 377-392.

West, I. M. (2007). Studland and the South Haven Peninsula; geology of the Wessex coast of southern England. Internet site hosted by Southampton University, http://www.soton.ac.uk/~imw/index.htm, retrieved 20/03/08.

West, R. A., Brown, M. E., Salinas, S. V., Bouchez, A. H. and Roe, H. G. (2005). No oceans on Titan from the absence of a near-infrared specular reflection. *Nature* 436: 670-672.

Whalley, W. R., to, J., Kay, B. D., Whitmore, A. P. (2006). Prediction of the penetrometer resistance of soils with models with few parameters. *Geoderma* 137: 370-377

Whiteley, G. M. and Dexter, A. R. (1982). Forces required to displace individual particles within beds of similar particles. *Journal of Agricultural Engineering Research* 27: 215-225.

Willet, D. M. (1994). Calibration of Cassini SSP penetrometer. University of Kent & Canterbury.

Wilson, K. (1960). The time factor in the development of dune soils at South Haven Peninsula, Dorset. *The Journal of Ecology* 48: 341-359.

Yang, Y. and Davidson-Arnott, R. G. D. (2005). Rapid measurement of surface moisture content on a beach. *Journal of Coastal Research* 23: 447-452.

Yung, Y. L. and Allen, M. (1984). Photochemistry of the atmosphere of Titan: comparison between model and observations. *Astrophysical Journal* 55: 465-506.

Zarnecki, J. C., Banaszkiewicz, M., Bannister, M., Boynton, W. V., Challenor, P. G., Clark, B. C., Daniell, P. M., Delderfield, J., English, M. A., Fulchignoni, M., Garry, J. R., Geake, J. E., Green, S. F., Hathi, B., Jaroslawski, S., Leese, M. R., Lorenz, R. D., Mcdonnell, J. A. M., Merryweather-Clarke, N., Mill, C. S., Miller, R. J., Newton, G., Parker, D. J., Rabbetts, P., Svedhem, H., Turner, R. F. and Wright, M. J. (1997). The Huygens Surface Science Package. In: Wilson, A. (Ed.), *Huygens. science, payload and mission*: European Space Agency.

Zarnecki, J. C., Leese, M. R., Garry, J. R., Ghafoor, N. and Hathi, B. (2002). Huygens Surface Science Package. *Space Science Reviews* 104: 591-609.

Zarnecki, J. C., Leese, M. R., Hathi, B., Ball, A. J., Hagermann, A., Towner, M. C., Lorenz, R. D., Mcdonnell, J. A. M., Green, S. F., Patel, M. R., Ringrose, T. J., Rosenberg, P. D., Atkinson, K. R., Paton, M. D., Banaszkiewicz, M., Clark, B. C., Ferri, F., Fulchignoni, M., Ghafoor, N. A. L., Kargl, G., Svedhem, H., Delderfield, J., Grande, M., Parker, D. J., Challenor, P. G. and Geake, J. E. (2005). A soft solid surface on Titan as revealed by the Huygens Surface Science Package. *Nature* 438: 792-795.

Zöhrer, A., Kargl, G (2005). Finite element modelling of penetration tests into Martian analogue materials. *Proceedings 3rd International Planetary Probe Workshop*, Anavyssos, Greece.

Zou, R. P. and Yu, A. B. (1995). The packing of spheres in a cylindrical container: The thickness effect. *Chem. Eng. Sci.* 50: 1504-1507.

Appendix A: Program descriptions

The table below provides a brief description of the main programs written by the author during the course of his studies. Due to their length a copy of all code is held on a PSSRI disk share at the Open University and also by the author.

Program	Description
cal.m	Program used for calibration with air track.
rockhit.m	Simulates impact with the Titan surface based on rock data from DISR cameras
data_c.m	Reads in laboratory ACC-E data and applies transfer function. Reads laser data and converts to speed. Outputs combined laser and force signature file of type .ash for use with penstat.m or outputs separate files .sig and .spd for use with the hemi models.
hemi2.m	Layered target model based on earlier work by Anderson *et al.* (1996) and Kömle *et al.* (1997)
penstat.m	Signature analysis program. Provides simple descriptive statistics of signatures.

Appendix B: Penetrometry drop summary

The following table summarises over 150 drops carried out by the author using the free drop rig. Data are kept by the author and on the PSSRI disc share space at the Open University. Individual drops can be found in the relevant containing file within the containing folder indicated. Specific details of each drop are kept in an index sheet with each file.

Containing folder	Containing file(s)	Description
BEADS	1MMGBLAST.xls	1mm glass beads
	STEELSHOT2MM.xls	2 mm steel shot
	4MMGBLAST.xls	4 mm glass beads
	4MMGB_FGLASS_BOTTOM_EFFECTS.xls	4 mm glass beads bottom effects
	4MMGB_CONTAINER.xls	4 mm glass beads edge effects
	PLASTICBEADS4MM.xls	4 mm plastic beads
	STEELSHOT5MM.xls	5 mm steel shot
	6MMGBLAST.xls	6 mm glass beads
	6MMPLASTICBEADS.xls	6 mm plastic beads
	POLYSTYRENE_BEADS.xls	Polystyrene beads
	8MMGBLAST.xls	8 mm glass beads
	8MMGB_SPEED_LAST.xls	8 mm glass bead velocity drops
	PLASTICBEADS8MM.xls	8 mm plastic beads
	GBSANDSURROUND	Glass beads with sand boundary
	GLASSBEADS_SORTING.xls	Glass bead mixtures
CLAY	CLAY.xls	Clay drops
	CLAY_VOIDS.xls	Clay void drops
CRUST	SUGAR_GLASS_CRUST.xls	Sugar glass crust on sand
FIELDWORK	ABBOTSBURY.xls	Abbotsbury fieldwork drops
	BURTON BRADSTOCK.xls	Burton Bradstock fieldwork drops
	STUDLAND.xls	Studland fieldwork drops
	WEST BAY.xls	West Bay fieldwork drops
	WEST BEXINGTON.xls	West Bexington fieldwork drops
FOAMGLAS	FOAMGLAS.xls	Foamglas drops
	FOAMGLAS4MODEL.xls	Foamglas drops for hemi models
GRAVEL	COARSE_LIGHT_GRAVEL.xls	Coarse light gravel drops
	FINE_GRAVEL.xls	Fine gravel drops
	MEDIUM_PEA_GRAVEL.xls	Pea gravel drops
	MEDIUM_FINE_GRAVEL.xls	Medium gravel drops
ICE PEBBLES	ICE_PEBBLES.xls	Liquid nitrogen frozen ice pebble drops

SAND	LOOSE_LB_SAND.xls	Loosely compacted LB DA16/30 drops
	DENSE_LB_SAND.xls	As above densely compacted
	LOOSE_RHT_SAND.xls	Loosely compacted RH T sand
	DENSE_RHT_SAND.xls	As above densely compacted
SNOW	SNOW.xls	Snow drops
WET SAND	WATER_SAND_LB.xls	Wet LB DA16/30 sand drops
	WATER_SAND_RHT.xls	Wet RHT sand drops